5-10-2017

A Mathematical Model for β1-adrenergic Regulation of the Mouse Ventricular Myocyte Contraction

Paula D. Mullins
Georgia State University

A MATHEMATICAL MODEL FOR β_1-ADRENERGIC REGULATION OF THE MOUSE VENTRICULAR MYOCYTE CONTRACTION

by

PAULA MULLINS

Under the Direction of Vladimir E. Bondarenko, PhD

ABSTRACT

The β_1-adrenergic signaling system is one of the most important systems regulating heart function. Activation of this system leads to an increased heart rate, which can be beneficial during exercise, but can lead to cardiac hypertrophy and heart failure with continuous over-stimulation. In this dissertation, we have developed two comprehensive mathematical models of mouse ventricular myocyte contraction. The first model is based on a previously published mathematical model of action potential and Ca^{2+} handling mechanism of the mouse cardiac cell that are not modulated by the β_1-adrenergic signaling system. The model was verified with experimental data on mouse myocyte contraction at room temperature. In the model, we implement simplified sarcomere length variability and indirect modulation of the tropomyosin transition rates by Ca^{2+} and troponin. The resulting model describes well steady-state force-

calcium relationships, dependence of contraction force on sarcomere length, time course of contraction force and myocyte shortening, frequency dependence of contraction force and cellular contraction, and experimentally measured derivatives of myocyte length variation. We emphasize the importance of including variable sarcomere length in the model for ventricular myocyte contraction and investigate the differences in contraction force and cell shortening for epicardial and endocardial ventricular myocytes. The second model of the mouse ventricular myocyte contraction includes a more advanced description of the forces involved in myocyte contraction (active, passive, viscous, and flexible forces) and the β_1-adrenergic signaling system. The model was verified by the simulation of major experimental protocols on measurements of steady-state force-calcium relationships, crossbridge release rate (k_{rel}) and force development rate (k_{df}), force-velocity relationship, and force redevelopment rate (k_{tr}). It also reproduces quite well frequency and isoproterenol dependencies for $[Ca^{2+}]_i$ transients, total contraction force, and sarcomere shortening. The resulting mathematical model reveals the mechanisms of increased contraction force and myocyte shortening upon stimulation of β_1-adrenergic receptors. The developed mathematical models can be used further for simulations of contraction of ventricular myocytes from genetically modified mice and myocytes from mice which have developed chronic cardiac diseases.

INDEX WORDS: Contraction force, Sarcomere shortening, Crossbridge kinetics, Phosphorylation, Troponin I, Myosin binding protein C

A MATHEMATICAL MODEL FOR β_1-ADRENERGIC REGULATION OF THE MOUSE VENTRICULAR MYOCYTE CONTRACTION

by

PAULA MULLINS

A Dissertation Submitted in Partial Fulfillment of the Requirements for the Degree of

Doctor of Philosophy

in the College of Arts and Sciences

Georgia State University

2017

A MATHEMATICAL MODEL FOR β_1-ADRENERGIC REGULATION OF THE MOUSE VENTRICULAR MYOCYTE CONTRACTION

by

PAULA MULLINS

Committee Chair: Vladimir E. Bondarenko

Committee: Igor Belykh

Yaroslav Molkov

Alexandra Smirnova

Electronic Version Approved:

Office of Graduate Studies

College of Arts and Sciences

Georgia State University

May 2017

DEDICATION

To my loving and supportive parents, Joyce and Harold.

ACKNOWLEDGEMENTS

First, I would like thank my sister, Pamela Rose, for the Figures in Chapter 1. She clearly received all of the artistic genes in my family. While preparing the figures she probably learned more about contractile proteins than she ever wanted to know, but in so doing, she has saved my readers from having to decipher illustrations of my own.

I would also like to thank my friends and colleagues who have been such a help to me throughout my graduate studies at Georgia State University. Linda deCamp, Nilay Manzagol, Kelvin Rozier, and Sutandra Sarkar have been particularly helpful with feedback, encouragement, tips, and materials for the courses I have taught. I am also thankful to Deniz Alaçam, Linda deCamp, Xiuxiu He, Kelvin Rozier, and Brent Woodbridge, foremost for their friendship, but also for our discussions and collaborations in various Applied Math and Bioinformatics courses. Each of these friends has influenced my education and been a blessing in my life.

I would also like to thank all of the professors I have had at GSU. I am especially grateful to the professors in the Bioinformatics concentration who have inspired me with their research and encouraged me in my own. In particular, I would like to thank Dr. Igor Belykh, who introduced me to Mathematical Biology and first suggested that I pursue my doctorate. I would also like to thank Dr. Alexandra Smirnova, who was instrumental in my decision to apply to the Ph.D. program, and who suggested me to Dr. Bondarenko as a graduate assistant. In addition, I appreciate Dr. Belykh, Dr. Smirnova, and Dr. Yaroslav Molkov giving of their time to serve on my dissertation committee.

Finally, and most significantly, I would like to thank my advisor, Dr. Vladimir Bondarenko. He has had the patience of a saint as I have worked with concepts from Physics,

Chemistry and Biology that were distant memories from courses decades ago. He has helped me to catch up on many of the vast advances that have been made in cardiac research and micro-cellular biology in the years since I received my undergraduate degree. On a personal level, the past few years have been difficult for my family. Life has thrown us some curveballs. I will forever be grateful to Dr. Bondarenko for his understanding and encouragement in the midst of these challenges. Without his patient persistence and encouragement, this dissertation would not have been possible.

TABLE OF CONTENTS

LIST OF TABLES

LIST OF FIGURES

1 INTRODUCTION

Heart disease is the number one cause of death in the United States [1]. A common way to treat heart disease is through pharmacological interventions and implanted devices. A comprehensive knowledge of the basic physiological processes that occur at the cellular level is required for proper treatment of cardiac disease states. While experimental studies of cardiac cells are the primary source of knowledge on cardiac physiology, mathematical models are useful supplementary tools in understanding the mechanisms behind heart function in health and disease. In this chapter, we review the basic physiology of cardiac cell contraction and the current state of mathematical modeling of cardiac cellular contraction.

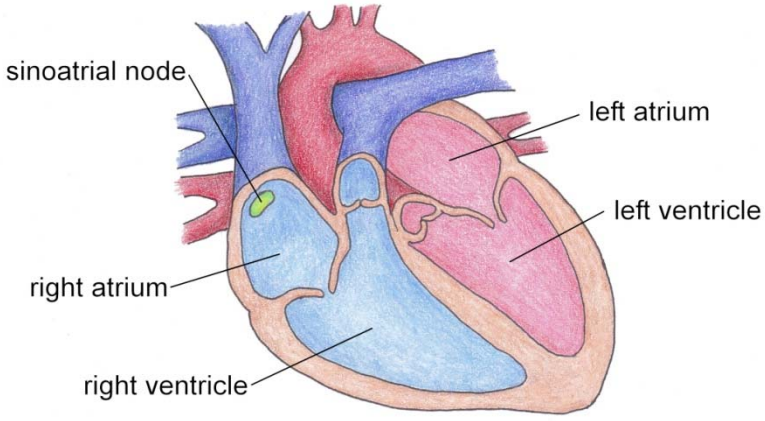

Figure 1.1 Diagram of the heart.

1.1 Physiological background

The heart is made up of several distinct regions, with different roles in the overall function of the organ. Because of their different roles, the regions have different types of cells. Some of the major components of the heart are the sinoatrial node, the left and right atrium, and the left and right ventricles (Fig. 1.1). The sinoatrial node, located on the right atrium, is the pacemaker of the heart. It sends electrical signals to the rest of the heart by means of Purkinje

fibers. The atria are the upper chambers of the heart, into which blood flows from the body. The blood is then pumped into the larger, lower chambers, called ventricles. From the ventricles, blood is pumped back out to the rest of the body. Due to their major role in heart contraction, the model presented in this paper is of contraction in ventricular cells.

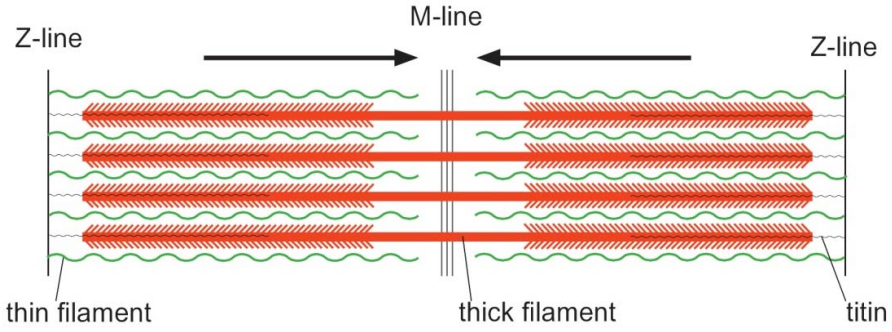

Figure 1.2 Schematic diagram of cardiac sarcomeres.

Thick filaments are composed primarily of myosin, attached to the Z-line by titin. Thin filaments contain actin, tropomyosin, and troponin complex. When the myosin heads change conformation, the thin filaments move toward the M line, causing a contraction.

1.1.1 Myofilaments and contraction

Cellular contraction is achieved through the interaction of contractile proteins in myofilaments. Myofilaments account for a significant amount of the volume in mammalian cardiac cells. In mouse hearts, for example, they account for approximately half of the cell volume [2]. Each myofilament is comprised of a series of thick and thin filaments (Fig. 1.2) which interact to generate cell movement and contraction. A sarcomere is a section of the myofilament between two consecutive Z-lines. The thick filaments are composed of myosin, titin, and myosin binding protein C (MyBP-C), while the thin filaments are composed of actin, tropomyosin (Tm), and troponin complex (TnI, TnC, and TnT) (Fig. 1.3). The globular heads of the myosin proteins protrude from the thick filament and bind to the actin on the thin filaments to form crossbridges. When myosin hydrolyzes ATP, the myosin head changes conformation, pulling the thin filament toward the M line and causing a contraction. In its resting state,

however, tropomyosin blocks the myosin binding sites on actin (Fig. 1.4A). When calcium (Ca^{2+}) binds to TnC, the tropomyosin protein shifts enough to uncover the binding sites and allow crossbridges to form (Fig. 1.4B). In this way, Ca^{2+} regulates cardiac contraction.

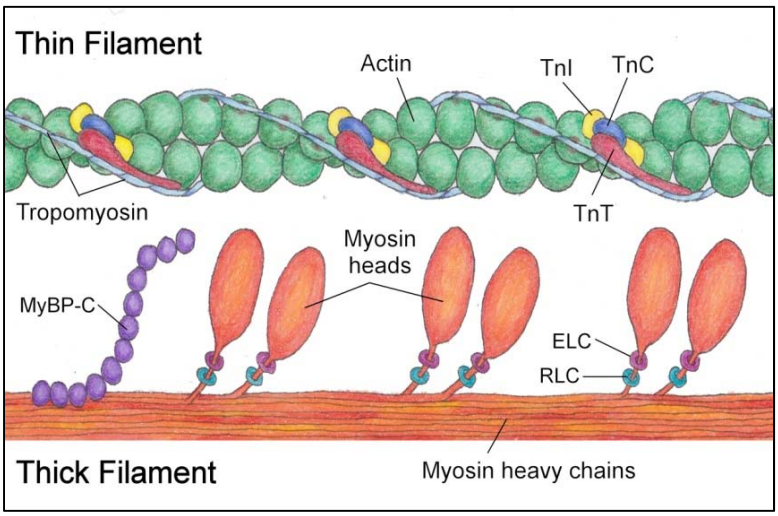

Figure 1.3 Thin and thick filament structure.

Tropomyosin and actin each form two strands which are interwoven to form the thin filament (top). The troponin complex consists of three subunits: troponin T (TnT), troponin C (TnC), and troponin I (TnI). The strand of the thick filament (bottom) is made primarily of the rod-like myosin tails (heavy chains). The myosin heads, which are attached to the heavy chains by the regulatory light chain (RLC) and essential light chain (ELC), protrude from the thick filament. Myosin binding protein C (MyBP-C) is typically spaced along the thick filament such that three pairs of myosin heads are located between consecutive MyBP-C molecules.

1.1.2 Phosphorylation of contractile proteins

In muscle cells, contractions are primarily regulated by intracellular Ca^{2+} levels, but there are other changes to contractile proteins which can affect the formation or disassociation of crossbridges. One such change is phosphorylation [3]. Phosphorylation is the addition of a negatively charged phosphate group to a protein. The addition of this group can change the structure of the protein, which can change the function of the protein [4]. While phosphorylation can occur to most of the contractile proteins, only TnI, MyBP-C, and the myosin regulatory light chain (RLC) are phosphorylated and dephosphorylated fast enough to influence contractions [3]. However, of these three, only TnI and MyBP-C are phosphorylated by protein kinase A (PKA), a

component of the β_1-adrenergic signaling system, so they are the only two whose phosphorylation is included in our contraction model.

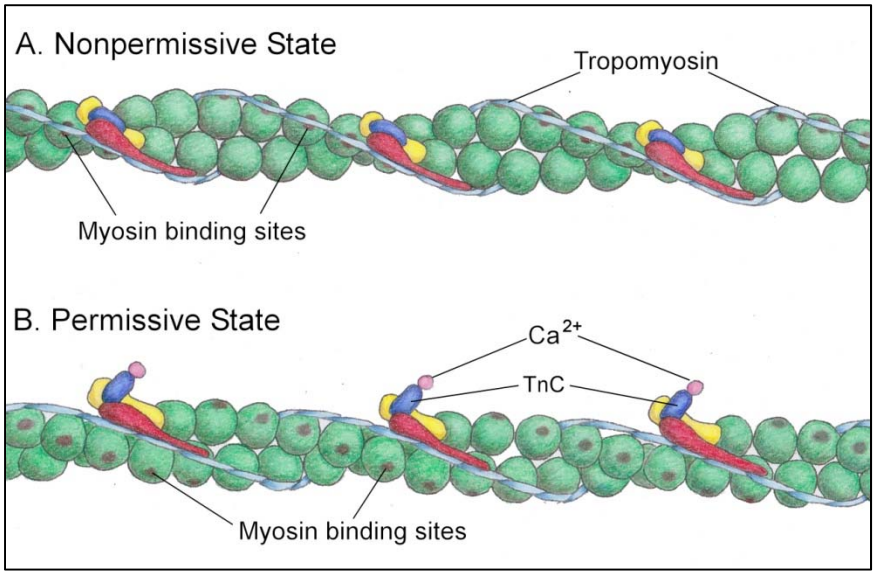

Figure 1.4 Two conformations of the thin filament.

(A) In the nonpermissive state, tropomyosin is blocking the myosin binding sites on actin. (B) In the permissive state, Ca^{2+} is bound to TnC, causing tropomyosin to shift so that the myosin binding sites are exposed.

1.1.2.1 Troponin I

Troponin I is the subunit of troponin complex which binds to actin and is a target of PKA [2]. Activation of the β_1-adrenergic signaling system increases the percentage of phosphorylated TnI from a baseline level of ~40% to a saturation level of ~80% [5, 6]. Multiple studies have shown that the phosphorylation of TnI decreases Ca^{2+} sensitivity [7-9], but Robertson *et al.* [7] found that the major effect of TnI phosphorylation was on the unbinding rate of Ca^{2+}. While investigating the role of phosphorylation of TnI versus MyBP-C on crossbridge kinetics, Kentish *et al.* [8] found that it is TnI phosphorylation by PKA that increases relaxation rates.

1.1.2.2 Myosin binding protein C

Myosin binding protein C is a protein located on the thick filament of a sarcomere. MyBP-C molecules are spaced along the thick filament such that there are three sets of myosin

heads between them (Fig. 1.4) [10, 11]. MyBP-C's role in crossbridge mechanics is still relatively unknown, but its phosphorylation has been found to be important in maintaining sarcomere structure and normal cardiac function [12]. Mutations of MyBP-C are the most common genetic cause of hypertrophic cardiomyopathies, with 150 different mutations of the MyBP-C gene having been found to be linked to cardiomyopathies [10].

PKA-activated phosphorylation of MyBP-C accelerates crossbridge kinetics, decreases Ca^{2+} sensitivity, and enhances relaxation [13]. Tong *et al*. [14] found that changes in stretch-activated contraction kinetics were due to phosphorylation of MyBP-C, not TnI, while the changes in the steady state force-Ca^{2+} relationship were primarily due to TnI phosphorylation. More recent experimental data, however, has shown that both MyBP-C and TnI make approximately equal contribution to the change in steady-state force-Ca^{2+} relationships [15].

1.1.3 The β_1-adrenergic signaling system

The β_1-adrenergic signaling system is one of the primary signaling systems in the body. Activation of this system sends epinephrine (adrenaline) and norepinephrine (noradrenaline) throughout the body initiating what is often called the "fight or flight" response, which includes increased heart rate, blood pressure, and cardiac contractility. In ventricular myocytes, stimulation of the β_1-adrenoreceptors (β_1-ARs) by a β_1-adrenergic agonist (isoproterenol) sets off a sequence of events (see [16]) which leads downstream to the activation of PKA. PKA phosphorylates several cardiac proteins, including TnI and MyBP-C (see Section 1.1.2).

1.2 Mathematical models of cardiac cells

1.2.1 *Modeling cardiac electrical activity and Ca^{2+} dynamics*

The first cardiac cell models were of Purkinje cells. Because these cells have currents similar to neural cells (sodium and potassium currents), the first models were based on the 1952

Hodgkin-Huxley (H-H) model of a neuron [17]. Like the H-H model, the 1962 Noble model [18] included a differential equation for the membrane current (I_m) comprised of three ionic currents, sodium (I_{Na}), potassium (I_K), and the anion (leak) current (I_{An}):

$$I_m = C_m \frac{dE_m}{dt} + I_{Na} + I_K + I_{An}, \tag{1.1}$$

where C_m is the membrane capacity, t is the time, and E_m is the membrane potential. Each individual ionic current was expressed as the ionic conductance (g_{Na}, g_K, and g_{An}) times the difference in the membrane potential and the ionic equilibrium potential (E_{Na}, E_K, and E_{An}):

$$I_{Na} = g_{Na}\left(E_m - E_{Na}\right) \tag{1.2}$$

$$I_K = g_K\left(E_m - E_K\right) \tag{1.3}$$

$$I_{An} = g_{An}\left(E_m - E_{An}\right) \tag{1.4}$$

An explanation of the non-linear differential equations of the gating variables related to the conductances, and how they have been modified from the H-H equations, can be found in [18]. At that time there was little experimental knowledge about the role of Ca^{2+} in cardiac cells, therefore, the 1962 Noble model [18] did not include a Ca^{2+} current. One important change from the H-H model was that Noble described potassium (K^+) dynamics using two currents, a fast inward and a slow outward current, each with their own conductances (g_{K1} and g_{K2}, respectively). The addition of a slow outward current allowed the model to reproduce the long plateau in the action potential. Unfortunately, the model was flawed because it was based on flawed experimental data [19].

As experiments became more precise and more detail was discovered about the components of cardiac cells, the cardiac models became increasingly complex. In 1975, the McAllister-Noble-Tsien model of a Purkinje cell [20] extended the Noble model to include five

more currents. They introduced a secondary inward current (i_{si}) partially carried by Ca^{2+}, a transient outward chloride current (i_{qr}), replaced the outward K^+ current (I_{K1}) with two K^+ currents (i_{x1} and i_{x2}), and replaced the single leak (anion) current with three background ionic currents: an inward current ($i_{Na,b}$) and two outward currents (i_{K1} and $i_{Cl,b}$).

The 1985 DiFrancesco-Noble Purkinje model [21] made several important additions to the modeling of cardiac cells. Among those improvements were the addition of time-dependent intracellular Na^+, Ca^{2+}, and K^+ concentrations, time-dependent extracellular K^+ concentration, the Na^+-K^+ exchange pump current (i_p), and the Na^+/Ca^{2+} exchange current (i_{NaCa}). It also modeled the movement of Ca^{2+} through the sarcoplasmic reticulum (SR) by the SR Ca-ATPase (SERCA) from the cytosol into the network sarcoplasmic reticulum (NSR), from the NSR to the junctional sarcoplasmic reticulum (JSR) through diffusion, and release from the JSR by Ca^{2+} induced Ca^{2+} release (CICR) [19]. This description of intracellular Ca^{2+} cycling becomes particularly important in the description of cellular contraction.

1.2.2 *Modeling ventricular cells*

Much of the current research on cardiac cells focuses on ventricular cells. Abnormalities in ventricular action potential duration (APD) are believed to be the leading cause of fatal cardiac arrhythmias. For this reason, modeling ventricular cells has become particularly important [22].

In 1977, Beeler and Reuter introduced the first model of a cardiac ventricular cell [23]. It was based primarily on the McAllister-Noble-Tsien Purkinje cell model, using H-H type descriptions for membrane currents. Like the McAllister-Noble-Tsien Purkinje cell model, they included currents i_{K1}, i_{x1}, i_{Na}, i_{Ca}, and i_s, however, they did not believe the experimental evidence for ventricular cells supported the existence of two more time-activated outward currents or the

dynamic chloride current, so they did not included i_{K2}, i_{x2} , or i_{Cl} in their ventricular cell model. They also omitted the i_{Na} current, including its effects in the i_s current [23].

As cardiac cell modeling advanced, most of the models became species and region specific. One benefit of this specificity was that modelers could attempt to better fit types of data that varied between species (such as the APD) and make more reliable model predictions for cellular behavior. Despite being designed as species specific, most models could be modified to account for differences in species data. The Luo-Rudy (L-R) ventricular cardiac action potential (AP) models from the early 1990's marked a significant step forward [24-26]. These guinea pig myocyte models were based on an extensive amount of data, including data from single cell and single channel experiments. This allowed the authors to update existing ion current descriptions, as well as introduce additional currents. The Luo-Rudy phase 2 dynamic AP model [24, 25] included many of the processes important to intracellular Ca^{2+} transients, such as the Na^+/Ca^{2+} exchanger (I_{NaCa}), a non-specific Ca^{2+} activated current ($I_{ns(Ca)}$), a sarcolemmal Ca^{2+} pump ($I_{p(Ca)}$), buffering of Ca^{2+} ions in the myoplasm and SR, and movement of Ca^{2+} through the SR (I_{up}, I_{tr}, I_{leak}, and I_{rel}). The inclusion of these processes allowed the dynamic L-R 2 model to incorporate variable ionic concentrations, particularly Ca^{2+}, which they noted could be the basis for future excitation-contraction models [24]. In addition, Luo and Rudy published their model equations so others were able to implement their model. Because of these innovations, the L-R 2 model [24, 25] has become the most used ventricular myocyte model [19].

Other models which introduced important Ca^{2+} handling processes were the 1998 Jafri-Rice-Winslow (JRW) model [27] and the 1999 Winslow *et al*. model [28]. Among other innovations, the JRW model introduced a subspace region for local control of CICR. The

Winslow *et al*. model, which was the first canine model, was able to model Ca^{2+} mediated AP prolongation in tachycardia-induced heart failure [19].

The 2004 Bondarenko *et al*. model [29] was the first mouse ventricular cell model. Mice and rats have a significantly shorter APD than larger species, with no plateau. This difference makes the electrophysiological models of other species more difficult to adapt to the mouse, the most used species in genetic research. The Bondarenko *et al*. model was the first to describe the short, "triangular" AP of mice, and included both apex and septum cells. This model was also the first to simulate Ca^{2+} fluxes and describe a comprehensive Markov model for the L-type Ca^{2+} channel.

1.2.3 Modeling the beta adrenergic signaling system

Early cardiac cell experiments and models, such as those discussed above, focused on electrical activity and Ca^{2+} dynamics. Recently there has been a research focus on protein signaling systems such as the α- and β-adrenergic and CaMKII-mediated signaling systems, which modulate various cell activity [16]. The β_1-adrenergic signaling system has been of particular note as it causes the most prominent effects on cardiac cells and is a target for pharmacological interventions such as "beta-blockers".

Comprehensive mathematical models of the β_1-adrenergic system in ventricular cells have been developed for various species [16, 30-33]. The 2003 Saucerman *et al*. model [30] of rat ventricular myocytes was the first such model. This model included two PKA targets, phospholamban and the L-type Ca^{2+} channel. The 2004 Saucerman-McCulloch model [31] for rabbit ventricular myocytes included additional PKA targets: slow delayed rectifier K^+ current (I_{Ks}), ryanodine receptors, and troponin I. The Yang-Saucerman model [33] extended the

previous Saucerman models to mouse ventricular myocytes, focusing on Ca^{2+} dynamics [16], but it did not describe the effects of β_1-adrenoreceptor activation on the mouse action potential.

Heijman *et al*. [34] developed a canine ventricular myocyte model which included three signaling systems: the β_1- and β_2-adrenergic and the CaMKII-mediated signaling systems. This compartmentalized model included both biochemical and electrophysiological parts and was extensively verified by experimental data. Like the Heijman *et al*. model [34], the Bondarenko mouse ventricular myocyte model [16] is compartmentalized, containing three subcellular compartments: caveolae, extracaveolae, and cytosol. Compartmentalization is important due to the localization of the components of the various signaling systems [35-38]. The Bondarenko model [16] contains the β_1-adrenergic signaling system, but has been extended in the Rozier-Bondarenko model [39] to include the β_2-adrenergic signaling system.

1.2.4 *Modeling cardiac contraction*

The basis of our current understanding of crossbridge kinetics can be traced back at least to Huxley [40]. He proposed the sliding of two filaments, one of myosin and one of actin, to cause a contraction. He mentioned "side-pieces", now known to be myosin heads, which could slide along the actin filament, combining temporarily with the actin filament. In his mathematical model [40] of striated muscle contraction, he included two crossbridge states, attached and detached, which he described by partial differential equations. In addition, he included the role of ATP in his model, but not Ca^{2+} activation.

However, it is now understood that Ca^{2+} plays an integral role in crossbridge formation in cardiac muscle cells. With the advances in the modeling of Ca^{2+} transients, more physiologically accurate contraction models were able to be developed. The 1996 Negroni-Lascano contraction model [41], while based on the Huxley model, introduced the effects of Ca^{2+} kinetics and

sarcomere dynamics on crossbridge structure and mechanics. The Ca^{2+} kinetics were described by a four state system: TnC without bound Ca^{2+} (T), TnC with bound Ca^{2+} but no crossbridges (TCa), TnC with bound Ca^{2+} and crossbridges (TCa*), and TnC without bound Ca^{2+} but with crossbridges (T*).

In 1999, Rice *et al*. [42] examined various Markov models for tropomyosin states based on the number of crossbridges and whether Ca^{2+} was bound to TnC. States with bound Ca^{2+} were considered permissive states (P), the states without Ca^{2+} were considered nonpermissive (N) (see Fig. 1.4). The models the authors considered ranged from four to six tropomyosin states. In three of the models, transitions from N to P were modulated by a two troponin states. Using the models with multiple crossbridges, Rice *et al*. [42] examined the effects of various mechanisms to describe crossbridge cooperativity.

A more comprehensive model of cardiac cell contraction, which included a description of active, passive, viscous, and flexible forces was developed by Rice *et al*. [43] in 2008. They introduced a four-state crossbridge model that included nonpermissive and permissive states, but distinguished between weakly bound and strongly bound crossbridge states. The model reproduced multiple experimental protocols on the steady-state force-Ca^{2+} relationship, force-velocity relationship, time behavior of force and sarcomere shortening, and rate of force redevelopment, k_{tr}, as a function of normalized force. The 2008 Rice *et al*. model [43] was species specific for rat and rabbit ventricular myocytes.

The Mullins-Bondarenko model [44] was developed in 2013 to describe mouse ventricular myocyte contraction (see Chapter 2). The model is based on the Bondarenko *et al*. [29] model of action potential and Ca^{2+} dynamics in mouse ventricular myocytes, but has a simplified description of sarcomere shortening using Hooke's law. The model describes well the

contraction of ventricular myocytes from two heart regions, the epicardium and endocardium. It emphasizes the importance of variable sarcomere length in the description of contraction force. The results of the model simulations fit well the experimental data on the steady-state force-Ca^{2+} relationship, time course of contraction force and sarcomere shortening, and frequency dependence of contraction force and myocyte shortening.

The effects of the β_1-adrenergic signaling system on ventricular contraction was studied by Land *et al*. [45] in 2013. The authors used modifications of the model parameters from their previous mathematical model of mouse ventricular contraction [46] to include the effects of stimulation of the β_1-adrenergic receptors parametrically, however, the biochemical part of the signaling system was not incorporated. The resulting model was used to simulate tension development without and with stimulation of β_1-ARs. The authors [45] concluded that in control their model produced realistic tension development, while upon stimulation with isoproterenol the simulated tension was greater than that measured experimentally.

More recently, Negroni *et al*. [47] developed a detailed mathematical model for the β_1-adrenergic regulation of rabbit ventricular myocyte contraction. This model was based on the Negroni-Lascano contraction model [48] and the Soltis-Saucerman model of β_1-adrenergic signaling in rabbit ventricular myocytes [49]. The model described the effects of activation of β_1-ARs on the steady-state force-Ca^{2+} relationship, the stiffness-frequency relationship, force-velocity dependence, and stretch-activation of the contraction force. The authors compared the results of their simulations to the corresponding experimental data. While the Negroni *et al*. model [47] described the effects of stimulation of β_1-ARs, it had limitations in that the model was developed based on experimental data from multiple species, including frog, guinea pig, rabbit, ferret, cat, and mouse.

1.3 Purpose of the study

While multiple models were developed for myocyte contraction, including mouse ventricular myocyte contraction [46], the models were not investigated with respect to stimulations of different frequencies, nor did they describe the effects of cellular heterogeneity or variable sarcomere length. The existing cardiac contraction models also have a limited ability to simulate the effects of β_1-adrenergic signaling on ventricular myocyte contraction. The β_1-adrenergic contraction models were only developed for rabbit ventricular myocytes, but a model for the mouse ventricular cell, which has much shorter action potential and different Ca^{2+} dynamics, was absent.

Therefore, in this dissertation, we develop two mathematical models of mouse ventricular myocyte contraction. The first model is based on a comprehensive mathematical model of the action potential and Ca^{2+} dynamics in mouse ventricular myocytes [29] and addresses the questions about the effects of stimulation frequencies, variable sarcomere lengths, and cellular heterogeneity on the myocyte contraction. The second model is designed to describe the β_1-adrenergic signaling system and its effects on mouse ventricular myocyte contraction. It also simulates a broad set of the experimental protocols for measurements of steady-state force-Ca^{2+} relationships, crossbridge release rate (k_{rel}) and force development rate (k_{df}), force-velocity relationship, and force redevelopment rate (k_{tr}).

2 A SIMPLIFIED MATHEMATICAL MODEL OF THE MOUSE VENTRICULAR MYOCYTE CONTRACTION

2.1 Introduction

Cardiac cell functions include the interaction of several major subsystems, including those responsible for the generation of electrical activity, Ca^{2+} dynamics, and cardiac contraction. Experimental data from diseased hearts or obtained at fast pacing rates show that the changes in one of the subsystems can lead to abnormal behavior in others. For example, dysfunction of the L-type Ca^{2+} channel, as in Timothy syndrome when the channel's inactivation is significantly reduced, affects Ca^{2+} handling in cardiac cells [50, 51] resulting in cardiac arrhythmias. Heterogeneities in cellular electrical activities in the heart, dysfunction of K^+ channels, or acidosis can also produce pro-arrhythmic behavior, such as action potential propagation block, re-entry, Ca^{2+} alternans, and irregular contractions [52, 53]. In particular, instability of Ca^{2+} dynamics (alternans) can lead to action potential alternans [54] and alternans in mechanical contraction [55]. Therefore, understanding interactions of the major cardiac cell subsystems and mechanisms of their pro-arrhythmic activity is of great importance.

Myocyte contraction is a complex process which involves activation of ionic currents (Fig. 2.1A), including L-type Ca^{2+} current (I_{CaL}), through which Ca^{2+} enters the cell and causes Ca^{2+} release (J_{rel}) from the intracellular Ca^{2+} store, the sarcoplasmic reticulum [56]. High intracellular Ca^{2+} concentration ($[Ca^{2+}]_i$) leads to an increase in Ca^{2+} bound by intracellular proteins (troponin, calmodulin) and changes the myofilament configuration, resulting in force development. Force generation involves conformational changes in thick (myosin) and thin (actin, tropomyosin, and troponin) filaments resulting in an increase in their overlap. Myosin represents a polypeptide chain with globular heads, which constitute crossbridges that interact

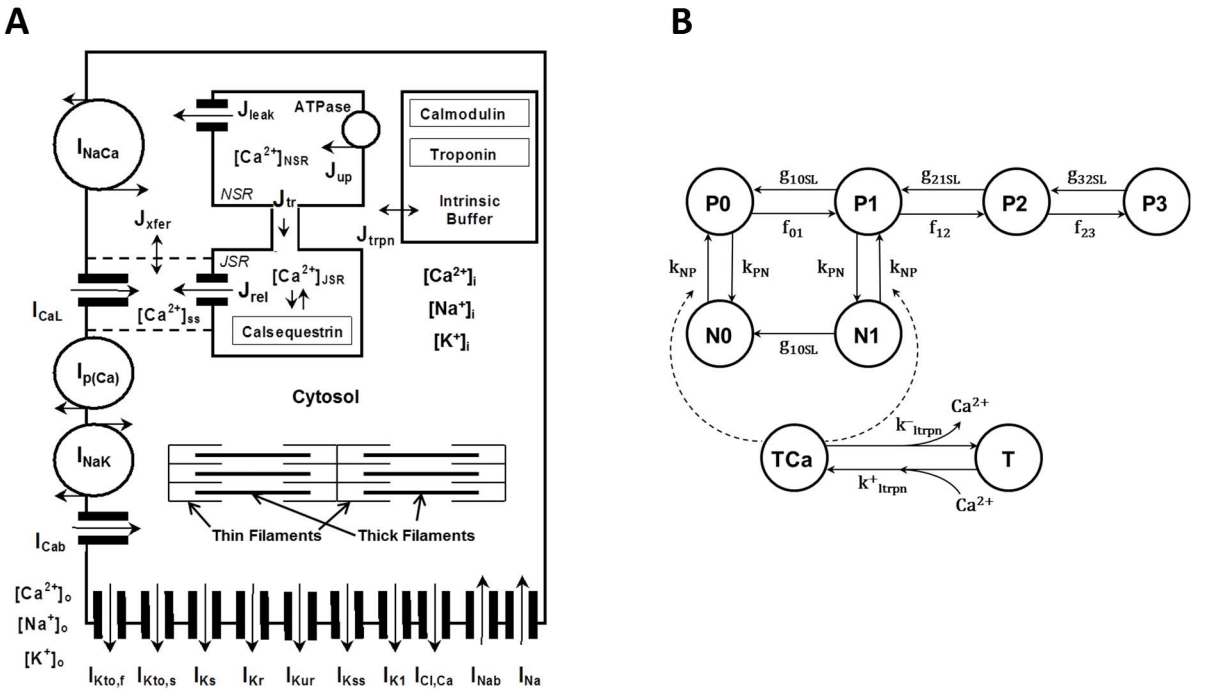

Figure 2.1 Schematic diagram of the mouse model cell and Markov model for force generation.

(A) Mouse model ionic currents and Ca^{2+} fluxes as presented by Bondarenko *et al.* [29]. Transmembrane currents are the fast Na^+ current (I_{Na}), the L-type Ca^{2+} current (I_{CaL}), the sarcolemmal Ca^{2+} pump ($I_{p(Ca)}$), the Na^+/Ca^{2+} exchanger (I_{NaCa}), the rapidly recovering transient outward K^+ current ($I_{Kto,f}$), the slowly recovering transient outward K^+ current ($I_{Kto,s}$), the rapid delayed rectifier K^+ current (I_{Kr}), the ultrarapidly activating delayed rectifier K^+ current (I_{Kur}), the noninactivating steady-state voltage activated K^+ current (I_{Kss}), the time-independent K^+ current (I_{K1}), the slow delayed rectifier K^+ current (I_{Ks}), the Na^+/K^+ pump (I_{NaK}), the Ca^{2+}-activated chloride current ($I_{Cl,Ca}$), the Ca^{2+} and Na^+ background currents (I_{Cab} and I_{Nab}). I_{stim} is the external stimulation current. The Ca^{2+} fluxes within the cell are uptake of Ca^{2+} from the cytosol to the network sarcoplasmic reticulum (SR) (J_{up}), Ca^{2+} release from the junctional SR (J_{rel}), Ca^{2+} flux from the network SR (NSR) to junctional SR (JSR) (J_{tr}), Ca^{2+} leak from the SR to the cytosol (J_{leak}), Ca^{2+} flux from the subspace volume to the bulk myoplasm (J_{xfer}), Ca^{2+} flux to troponin (J_{trpn}). The model includes Ca^{2+} buffering by troponin and calmodulin in the cytosol and by calsequestrin in the SR. $[Ca^{2+}]_i$, $[Na^+]_i$, and $[K^+]i$ are the intracellular Ca^{2+}, Na^+, and K^+ concentrations in cytosol; $[Ca^{2+}]_o$, $[Na^+]_o$, and $[K^+]_o$ are the extracellular Ca^{2+}, Na^+, and K^+ concentrations. Contraction force (F_{contr}) develops due to interaction of thin and thick filaments in the cytosol. (B) State diagram of the Markov model for the force generation in mouse cardiac myofilaments [42]. Top states describe cross-bridge formation, bottom states describe Ca^{2+} binding to troponin. P0, P1, P2, and P3 are the permissive states; N0 and N1 are the nonpermissive states. TCa is Ca^{2+} bound troponin; T is unbound troponin. (Figure reproduced from [44])

with thin filaments. Thin filaments are composed of long tropomyosin polypeptide chains, on which globular actin molecules aggregate in a double-stranded helix with crossbridge binding sites. In a non-active configuration, troponin blocks crossbridge binding sites (Fig. 1.4). Upon Ca^{2+} binding to troponin, troponin-tropomyosin complex exposes crossbridge binding sites

which interact with myosin globular heads, thereby creating weak bonds. ATP molecules bound to actin release a phosphate group and transform weak bonds into strong bonds. This transformation results in a change of crossbridge conformation to a bent position and forces thick filaments to slide relative to thin filaments.

Because of the complexity of the contraction mechanism, most mathematical models use a significantly simplified description of this process [57]. They explore the Huxley two-state crossbridge model [40], extend it to a larger number of crossbridge states, and include direct and indirect interaction with troponin and variable sarcomere lengths [42, 57]. Such simplified description, for example, does not involve energy metabolism and interaction with mitochondria. The crossbridge models are further incorporated into cellular models, which include electrical activity, comprehensive Ca^{2+} dynamics [43, 46, 58], and energy metabolism [59, 60].

In this chapter, we developed a new electromechanical model for mouse ventricular myocyte contraction at room temperature (298°K, or +25°C) [44]. We employed previously published models for action potential and Ca^{2+} dynamics in mouse ventricular myocytes [29, 61-63], which were also developed for room temperature (298°K, or +25°C), and incorporated a myocyte contraction model from Rice *et al.* [42]. These models were successfully employed for simulations of proarrhythmic activities in mouse cardiac cells and tissues [62, 63]. In addition, in the Rice *et al.* [42] model, we implemented a simplified sarcomere length variation during twitch. We also explored the effects of heterogeneity of the electrical activity and Ca^{2+} dynamics in epicardial and endocardial cells on the contraction force generation and cell shortening. The resulting model was adjusted to fit experimental data on mouse ventricular cell contraction. Our model successfully reproduces steady-state force-calcium relationships for different sarcomere lengths; time courses of the Ca^{2+} transients, developed force, and cellular shortening; peak force-

frequency and cell shortening-frequency relationships; and time-to-peak force and time-to-50% force relaxation. We also investigated and emphasized the importance of using variable sarcomere lengths in models of myocyte contraction. In the simulations, we compared both the absolute value of the contraction force and cellular shortening, and their normalized dependencies to fit existing experimental data.

2.2 Methods

A mathematical model for mouse ventricular myocyte contraction is a natural extension of the Bondarenko *et al*. model [29] for action potential and Ca^{2+} dynamics in mouse ventricular myocytes, with model improvements from [61-63] (Fig. 2.1A), developed for room temperature (298°K, or +25°C). In this chapter, we explored mouse ventricular myocyte models from the epicardial and endocardial regions of the heart [63]. Endocardial cells have more prolonged action potentials and larger intracellular $[Ca^{2+}]_i$ transients compared to epicardial cells [63]. We incorporated the Rice *et al.* [42] contraction model 4 in our model of electrical activity and Ca^{2+} handling [29, 61-63] (See Appendix A) and adjusted model parameters to fit experimental data on myocyte contraction obtained for room temperatures.

The Rice *et al.* [42] model links Ca^{2+} dynamics and myocyte contraction (Fig. 2.1B). The model contains two nonpermissive tropomyosin states (N0 and N1) and four permissive tropomyosin states (P0, P1, P2, and P3). N0, N1, P0, P1, P2, and P3 are functions of time that describe probabilities of finding the model in that particular state. N0 is the rest state of the model, with no strongly bound crossbridges. When Ca^{2+} binds to the tropomyosin, it changes its conformation to a permissive state without strongly bound crossbridges (P0), which allows for strong binding of one (P1), two (P2), or three (P3) crossbridges. The model also includes one nonpermissive state with one strongly bound crossbridge even without a bound Ca^{2+} ion (N1).

All transition rates in the model are Ca^{2+}-independent, except for k_{NP}, which depends on the concentration of troponin with Ca^{2+} bound to a low-affinity binding site. Detailed analysis of several contraction models and the plausibility of different cooperative mechanisms was performed in [42]. The model which we adopted for the mouse ventricular myocyte contraction (Model 4 from [42]) gave the best fit to the existing experimental data for mice. The contraction model parameters for epicardial and endocardial cells are presented in Appendix A.

Contraction force F_{contr} (in mN/mm^2) was calculated using the equation [42]:

$$F_{contr} = -73.26\, F_{contrn}, \tag{2.1}$$

where

$$F_{contrn} = -\frac{P1 + N1 + 2(P2) + 3(P3)}{F_{\max}}, \tag{2.2}$$

$$F_{\max} = P1_{\max} + 2(P2_{\max}) + 3(P3_{\max}), \tag{2.3}$$

$$P1_{\max} = \frac{f_{01}(2g_{\min xb})(3g_{\min xb})}{\Sigma}, \tag{2.4}$$

$$P2_{\max} = \frac{f_{01}f_{12}(3g_{\min xb})}{\Sigma}, \tag{2.5}$$

$$P3_{\max} = \frac{f_{01}f_{12}f_{23}}{\Sigma}, \tag{2.6}$$

$$\Sigma = (g_{\min xb})(2g_{\min xb})(3g_{\min xb}) + f_{01}(2g_{\min xb})(3g_{\min xb}) + f_{01}f_{12}(3g_{\min xb}) + f_{01}f_{12}f_{23}, \tag{2.7}$$

$$f_{01} = 3f_{XB},\ f_{12} = 10f_{XB},\ f_{23} = 7f_{XB}. \tag{2.8}$$

In equation (2.1), F_{contrn} is the normalized contraction force, and the coefficient −73.26 was obtained from fitting absolute values of the steady-state and dynamic experimental forces. For simulating steady-state force-calcium relationships (F-Ca^{2+}), we used fixed values of the sarcomere lengths (SL), so that d(SL)/dt = 0, and changed intracellular Ca^{2+} concentration. We

simulated F-Ca^{2+} relationships for sarcomere lengths 1.9, 2.1, and 2.3 μm. In this case, F_{contrn} has time-independent magnitude.

For simulating twitch contraction, where F_{contrn} is time-dependent, we used Hooke's law, the linear relationship between contraction/relaxation force and cell shortening/extension:

$$SL = 0.8F_{contrn} + SL_0 \tag{2.9}$$

where SL_0 is the initial value of SL. In this case, sarcomere length becomes a function of time. We estimated the variable cell length by

$$L = L_0 \times \frac{SL}{SL_0} \tag{2.10}$$

where initial cell length L_0 = 100 μm. For all simulations in this chapter, we used extracellular Ca^{2+} concentration $[Ca^{2+}]_o$ = 2 mM.

The electromechanical cardiac cell models were stimulated with different frequencies using a stimulus current (I_{stim} = 80 pA/pF, τ_{stim} = 0.5 ms) for at least 200,000 ms to reach a quasi-steady state. Simulated data of intracellular $[Ca^{2+}]_i$ transients, myocyte contraction force F_{contr}, and sarcomere length SL on the interval from 192,000 to 200,000 ms were compared to extensive experimental data.

The model consists of 51 ordinary differential equations and multiple model parameters (see Appendix A). Differential equations were solved by fourth-order Runge-Kutta method with time step 0.0001 ms. The model was implemented as an original Intel FORTRAN 90 code, which was run under SUSE Linux on a Dell Precision Workstation T3500 (Intel Xeon Processor W3670, 3.2 GHz, 8 GB RAM). To determine the values of the model parameters, we ran simulations and compared key characteristics of myocyte $[Ca^{2+}]_i$ transients and contraction force to experimental data obtained from mice. We adjusted transition rates in the Markov model for tropomyosin until our simulations fit well the experimental data from multiple laboratories.

2.3 Results

2.3.1 Steady-state force-calcium relationships

We first simulated steady-state force-calcium relationships. Both epicardial and endocardial cell models demonstrated the same simulation data for the steady-state force, as the contraction model Rice *et al.* [42] depends on intracellular $[Ca^{2+}]_i$ concentration. Figure 2.2A shows the Ca^{2+}-dependence of the absolute value of contraction force obtained by Prabhakar *et al.* [64] for two different sarcomere lengths, 1.9 and 2.3 μm, from skinned mouse ventricular myocytes. For both cases, the force represents an increasing sigmoid function of calcium concentration. There is a relatively small increase in the saturation force from 48.8 to 57.2 mN/mm^2 when sarcomere length increases by about 20%, from 1.9 to 2.3 μm. Figure 2.2B shows simulation of the steady-state force-calcium relationships for three sarcomere lengths, 1.9, 2.1, and 2.3 μm. Our model is able to closely reproduce the saturating value of the force for corresponding sarcomere lengths. However, there are some differences between simulated and experimental data in sensitivity to external Ca^{2+}, as simulated force saturates at smaller values of Ca^{2+} concentrations. Such differences are due to a decrease in Ca^{2+} sensitivity of skinned compared to intact cardiac cells [2].

Our model is also able to reproduce a shift in Ca^{2+} sensitivity for steady-state force-calcium relationships shown for three sarcomere lengths (Fig. 2.2D). Such a shift can be clearly seen for normalized steady-state force-calcium relationships. Simulations show that an increase in sarcomere length leads to smaller half-saturation values of Ca^{2+} concentrations, demonstrating an increase in Ca^{2+} sensitivity (Fig. 2.2D). A similar shift in Ca^{2+} sensitivity is also observed experimentally for mouse cardiac cells (Fig. 2.2C) [64, 65].

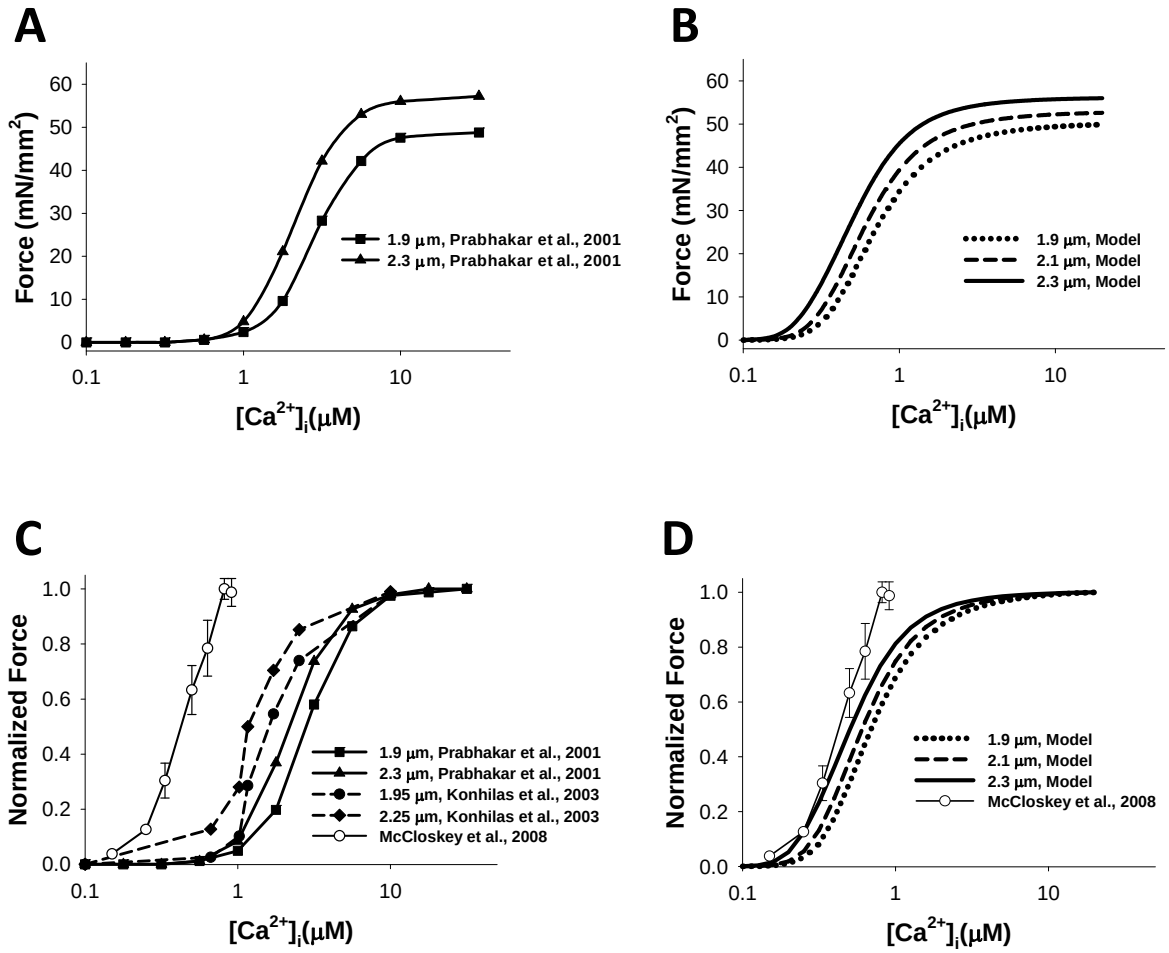

Figure 2.2 The steady-state force-$[Ca^{2+}]_i$ relationship.

The steady-state absolute force-$[Ca^{2+}]_i$ relationship (A and B) and the steady-state normalized force-$[Ca^{2+}]_i$ relationship (C and D). Experimental data from Prabhakar *et al*. [64] (SL = 1.9 and 2.3 μm) and Konhilas *et al*. [65] (SL = 1.95 and 2.25 μm), obtained with skinned myocytes, are shown in (A) and (C) with filled symbols; experimental data for non-skinned myocytes from [66] is shown by unfilled circles in (C) and (D). The model's simulations at various initial sarcomere lengths (SL = 1.9, 2.1, and 2.3 μm) are shown in (B) and (D). Simulated data for both epicardial and endocardial cells are the same. (Figure reproduced from [44])

In addition to the skinned mouse ventricular myocytes, our simulation data is also compared to the available experimental data on steady-state force-calcium relationships from intact cells, shown in Fig. 2.2 C and D with unfilled circles [66]. Figure 2.2D shows that our simulations are in good agreement with the experimental data. ICa_{50} and Hill coefficient *h*

obtained by fitting steady-state force-calcium relationships from McCloskey *et al.* [66] data with the function

$$F\left(\left[\mathrm{Ca}^{2+}\right]_{\mathrm{i}}\right)=F_{\min}+\frac{F_{\max}-F_{\min}}{1+\left(\left[\mathrm{Ca}^{2+}\right]_{\mathrm{i}}/\mathrm{ICa}_{50}\right)^{h}} \tag{2.11}$$

are 0.4 μM $[Ca^{2+}]_i$ and 3.05, respectively. Fitting our simulation data gives ICa_{50} 0.68, 0.59, and 0.49 μM $[Ca^{2+}]_i$ and Hill coefficients 2.30, 2.33, and 2.25, for sarcomere lengths 1.9, 2.1, and 2.3 μM, respectively.

Table 2.1 Experimental conditions for measurements of contraction force, cell shortening, and $[Ca^{2+}]_i$ transients and corresponding simulated conditions.

Reference	Temperature, ◦C	Sarcomere length, μm	$[Ca^{2+}]_o$ mM	Stimulation freq., Hz	$[Ca^{2+}]_i$ indicator
Gao *et al*. **[67]**	20-22	2.1-2.2	2.0	0.5	Fura-2
Kirchhefer *et al*. **[68]**	Room	No data	2.0	0.5	
Kogler *et al*. **[69]**	22-23	2.1-2.2	2.0	0.5	Fura-2
McCloskey *et al*. **[70]**	22	2.1	2.0	0.5	Fura-2
Stuyvers *et al*. **[71]**	25	2.0-2.1	2.0	1.0	
Fentzke *et al*. **[72]**	22-23	2.3			
Huang *et al*. **[73]**	Room	2.3	0.5	0.5	
Jones *et al*. **[74]**	25		2.0		Fluo-3
Simulation, this chapter	25	2.1	2.0	0.5	

Table reproduced from [44]

2.3.2 Dynamic behavior of contraction force

To test the ability of our model to reproduce time behavior of the contraction force developed by mouse ventricular myocytes, we first stimulated the model cells with a constant frequency of 0.5 Hz. The time course of force in epicardial and endocardial cell simulations is plotted in Fig. 2.3A by red solid and dashed lines, respectively. As endocardial cells show larger $[Ca^{2+}]_i$ transients than epicardial cells, we obtained that the former develops stronger contraction force and larger shortening than the latter. The time behavior of the contraction forces obtained experimentally is shown by black solid lines with symbols [67, 69-71]. There are significant

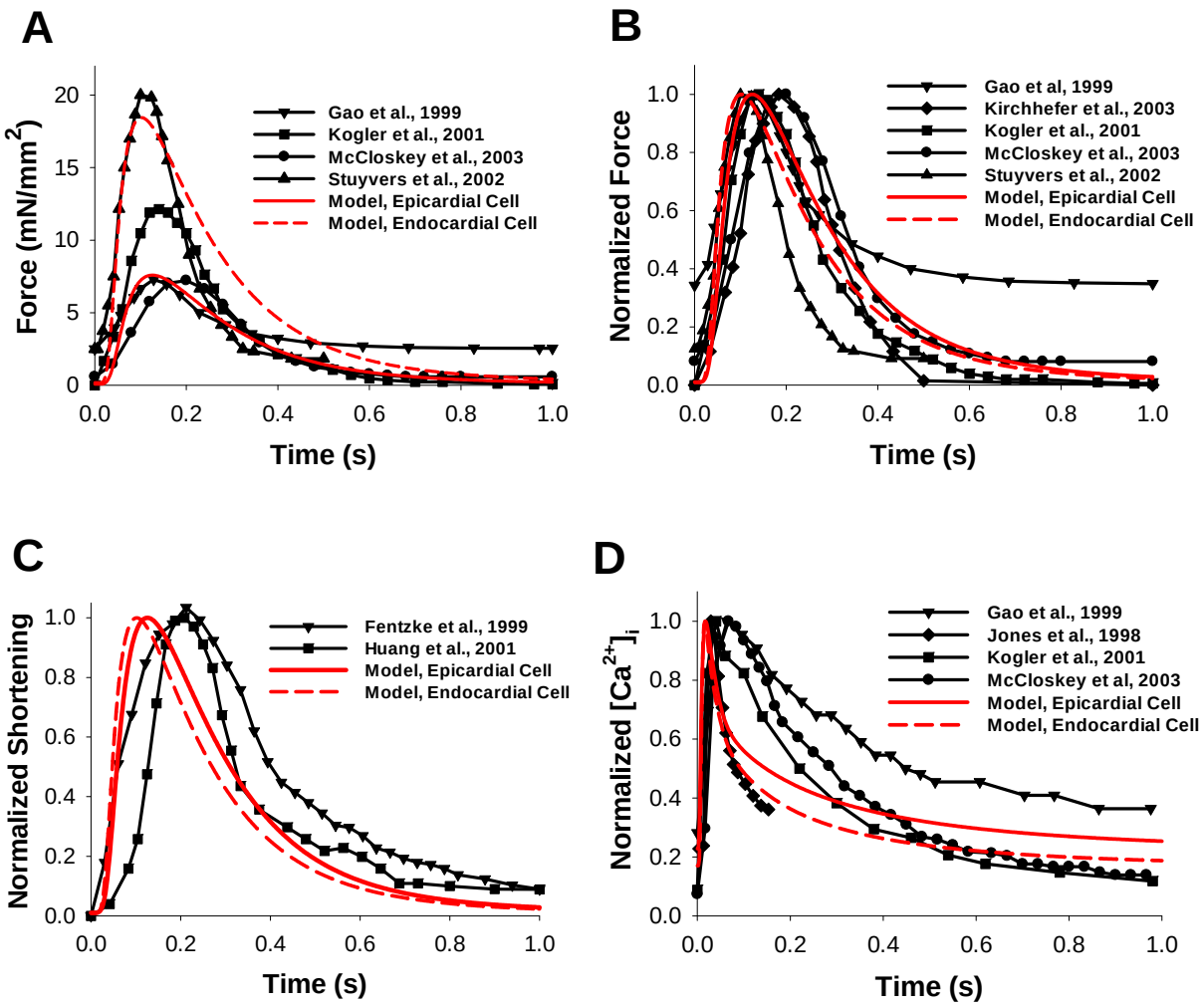

Figure 2.3 Contraction force, myocyte shortening, and $[Ca^{2+}]_i$ transients.

The time course force (in mN/mm^2) (A) and normalized force (B) simulated by the model for epicardial (red solid lines) and endocardial (red dashed lines) cells are compared with experimental data from Stuyvers *et al*. [71], Gao *et al*. [67], Kirchhefer *et al*. [68], Kogler *et al*. [69], and McCloskey *et al*. [70]. (C) Normalized shortening as a function of time. Simulation data is shown by red solid (epicardial cell) and red dashed (endocardial cell) lines, experimental data from Fentzke *et al*. [72] and Huang *et al*. [73] are shown by lines with symbols. (D) Normalized $[Ca^{2+}]_i$ transients as functions of time. The model simulation (red solid and red dashed lines for epicardial and endocardial cells, respectively) is compared to experimental data from Gao *et al*. [67], Jones *et al*. [74], Kogler *et al*. [69], and McCloskey *et al*. [70] (lines with symbols). For comparison, the initial sarcomere length in the model simulation is set to 2.1 µm, extracellular $[Ca^{2+}]_i$ concentration is 2 mM, and the frequency is 0.5 Hz, the frequency used most in the experimental data (see Table 2.1). (Figure reproduced from [44])

differences in the experimental data obtained from different experimental groups on the time behavior of force, both in peak values and residual forces (Table 2.1). Comparison of the time behavior of normalized simulated and experimental forces, both for epicardial and endocardial

cells, shows a clear similarity in the time-to-peak values and relaxation of the simulated forces (Fig. 2.3B) [67-71].

Our model includes changes in sarcomere length during myocyte contraction. The time behavior of normalized sarcomere shortening for simulated cells is shown in Fig. 2.3C by red solid and dashed lines for epicardial and endocardial cells, respectively. The models did not show large differences in time-to-peak shortening and relaxation times. They closely reproduced myocyte shortening obtained in different experiments with mice (solid lines with symbols in Fig. 2.3C) [72, 73]. For comparison of the time scales of contraction force and Ca^{2+} dynamics, we also plotted the time courses of the simulated and experimental intracellular Ca^{2+} transients by red lines and black solid lines with symbols in Fig. 2.3D, respectively. In each case, there is a delay in force development following the peak of the Ca^{2+} transient (compare times to peaks in Fig. 2.3 B and D).

2.3.3 Force-frequency relationships

In order to investigate force-frequency relationships, we also stimulated model cells with different frequencies ranging from 0.25 to 2.0 Hz. Frequency dependencies of intracellular Ca^{2+} transients, contraction force, and cell shortening are shown in Fig. 2.4. Our simulated peak $[Ca^{2+}]_i$-frequency relationship (red solid and dashed lines in Fig. 2.4A) is within the variability of experimental data (solid lines with symbols in Fig. 2.4A) [70, 71, 75, 76]. Note that the simulated amplitudes of $[Ca^{2+}]_i$ transients for epicardial and endocardial cells are verified by the experimental data obtained by Dilly *et al.* [77] (Fig. 2.4D). The models were able to reproduce peak contraction force-frequency relationships for mouse ventricular myocytes in the frequency range from 0.5 to 2.0 Hz (Fig. 2.4B). The experimental data shows biphasic behavior of the peak force, with a decrease from 0.25 to 0.5-1.0 Hz, followed by an increase from 1.0 to 2.0 Hz [70],

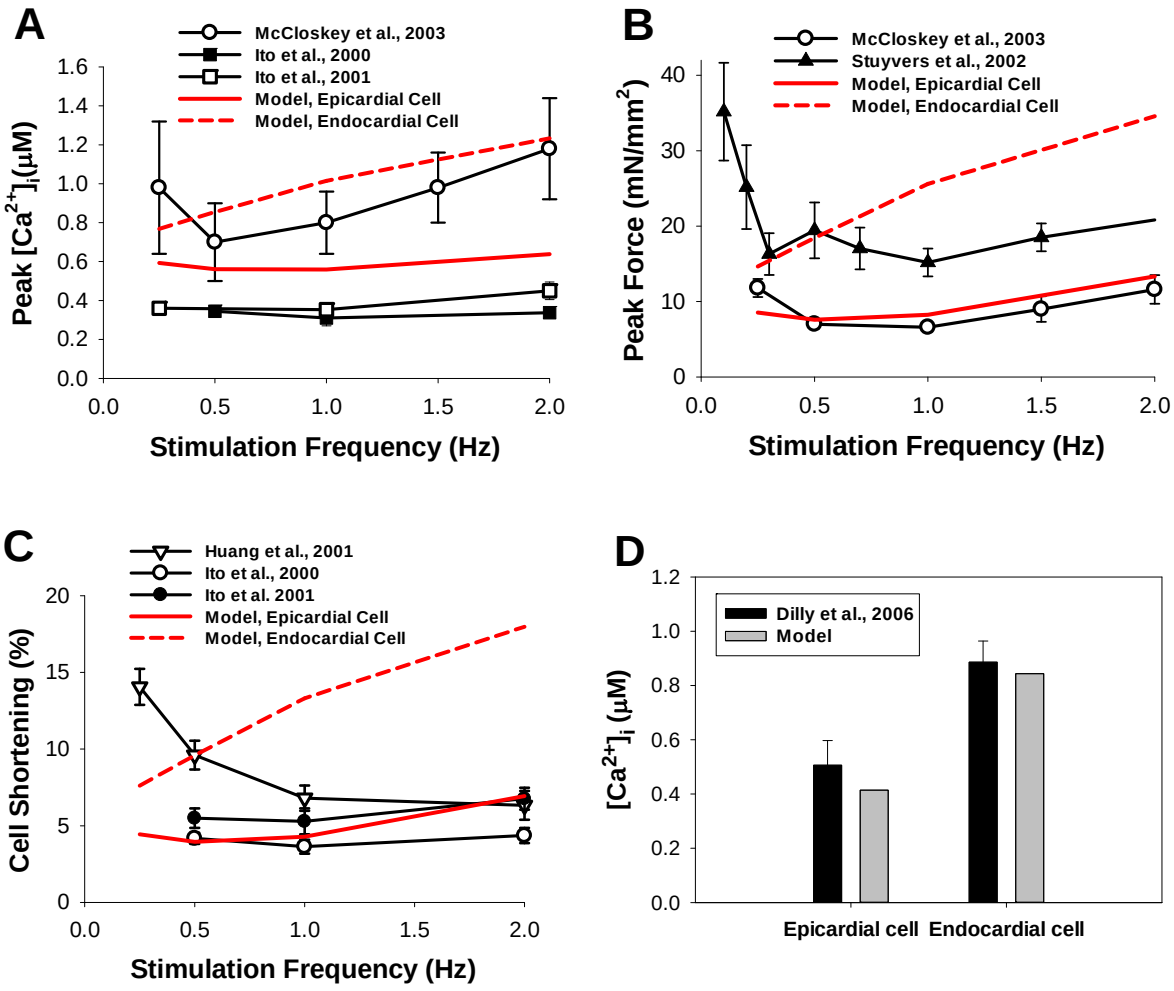

Figure 2.4 Stimulation frequency dependence.

(A) Peak $[Ca^{2+}]_i$.(B) Peak force. (C) Cell shortening. The simulation data is shown by red solid (epicardial cell) and red dashed (endocardial cell) lines. The modeling results are compared to data from Ito *et al.* [75, 76] (A), McCloskey *et al.* [70] (A and B), and Huang *et al.* [73] (C). The initial SL for the simulation is 2.1 μm. (D) Experimental (black bars [77]) and simulated (gray bars) intracellular $[Ca^{2+}]_i$ transients obtained for epicardial and endocardial cells at stimulation frequency 1 Hz. (Figure reproduced from [44])

with a clear minimum in force-frequency relationships (however, see data of Ito *et al.* [76] where the minimum is less apparent). Our model reproduced such biphasic behavior of the force-frequency relationships for epicardial cells. Peak contraction force for endocardial cells increases with stimulation frequency.

Finally, we were able to simulate peak lengthening-frequency relationships (red lines in Fig. 2.4C). While some experimental data shows consistent decrease in cellular shortening

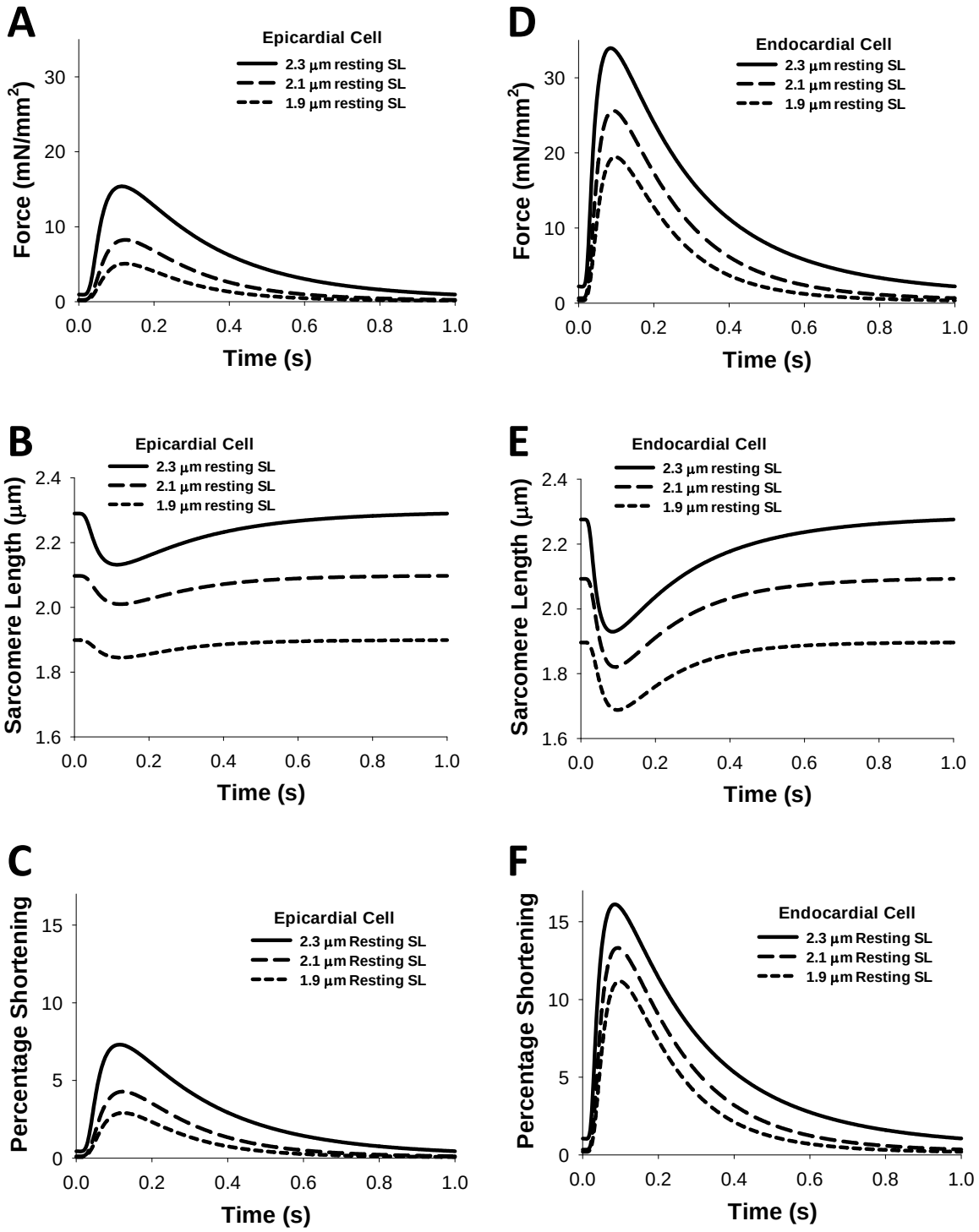

Figure 2.5 Time course of the contraction force, sarcomere length, and percentage of shortening for epicardial and endocardial cells for different sarcomere lengths.

Simulations with different resting sarcomere lengths (SL0 = 1.9, 2.1, and 2.3 μm) show a significant difference in the magnitude of the contraction force (A, D), sarcomere length (B, E) and percentage of sarcomere length shortening (C, F). The stimulation frequency for each simulation is 1 Hz. Simulations are performed for epicardial (A, B, C) and endocardial (D, E, F) cells. (Figure reproduced from [44])

with frequency [73], other data follows biphasic behavior [75, 76] (solid lines with symbols in Fig. 2.4C). Our modeling data demonstrates biphasic behavior in cell shortening for epicardial cells, which is consistent with the biphasic behavior of the contraction force and $[Ca^{2+}]_i$ transients (red solid lines in Fig. 2.4 A, B and C). Model endocardial cells show only an increase in cell shortening as well as in $[Ca^{2+}]_i$ (red dashed lines in Fig. 2.4 A and C, respectively).

Simulated time courses for contraction forces, sarcomere lengths, and sarcomere shortenings for three different resting sarcomere lengths (1.9, 2.1, and 2.3 μm) for epicardial and endocardial cells are shown in Fig. 2.5. As seen from the figure, an increase in the resting sarcomere length increases twitch force and relative sarcomere shortening. Similar behavior is also observed experimentally and from simulation of others [43, 46]. At comparable sarcomere lengths, the endocardial cells develop larger contraction force and sarcomere shortening than the epicardial cells (Fig. 2.5).

2.3.4 Constant versus variable sarcomere length

While steady-state simulations show that peak force is dependent on the initial sarcomere length, there is also a dynamic relationship between force and sarcomere length. Our models use a variable SL when calculating the transition rate from non-permissive to permissive states, as well as in the detachment rates in permissive states. To see the effect of using a variable SL in the transition rate equations, we ran simulations in which a constant SL replaced the variable SL in the calculation of the normalized sarcomere length

$$SL_{\text{norm}} = \frac{SL - 1.3\mu\text{m}}{2.3\mu\text{m} - 1.3\mu\text{m}} \tag{2.12}$$

which is used in the detachment rates and transition rates in the Markov model (Fig. 2.1B)

$$g_{10SL} = g_{xbSL}, \quad g_{21SL} = 2g_{xbSL}, \quad g_{32SL} = 3g_{xbSL}, \tag{2.13}$$

$$k_{NP} = k_{PN}\left(\frac{[LTRPNCa]}{[LTRPNCa]_{tot}\,K_{half}}\right)^{Ntm}, \tag{2.14}$$

$$g_{xbSL} = g_{minxb}\left(2-\left(SL_{norm}\right)^{1.6}\right), \tag{2.15}$$

$$K_{half} = 1/\left(1+\frac{K_{Ca}}{1.5\mu\mathrm{M}-SL_{norm}\times 1.0\mu\mathrm{M}}\right), \tag{2.16}$$

$$Ntm = 5+3\,SL_{norm}, \tag{2.17}$$

where $K_{Ca} = k^{-}_{ltrpn}/k^{+}_{ltrpn}$, and the constants can be found in Appendix A.

Figure 2.6A shows force development in epicardial cells at a stimulation rate of 1 Hz in the simulation using a constant SL (dashed line) versus the simulation using a variable SL (solid line) (see also Fig. 2.6B). Data for endocardial cells displays similar behavior and is shown in Fig. 2.6 C and D. The peak force when using a constant SL is clearly higher, while the residual force appears to be about the same. However, simulations run at various frequencies show that the peak and residual force when using a constant SL (Fig. 2.7E) is always higher than corresponding forces when a variable SL is used (Fig. 2.7C). Even though there is a difference in the magnitude of force, the frequency dependence of peak force when using a constant SL (black dashed line in Fig. 2.7F) is similar to the frequency dependence when a variable SL is used (black solid line in Fig. 2.7F). For comparison, Fig. 2.7 B and D show simulated data on cell shortening and contraction force at different stimulation frequencies for endocardial cells, using variable sarcomere length (data on constant SL is not shown). As seen from the figures, both peak contraction force and cell shortening are larger for the endocardial cells than the epicardial cells. In both cases, constant and variable SL, we observed a decrease in time-to-peak and time to 50% relaxation rate for the contraction force with an increase of stimulation frequency starting

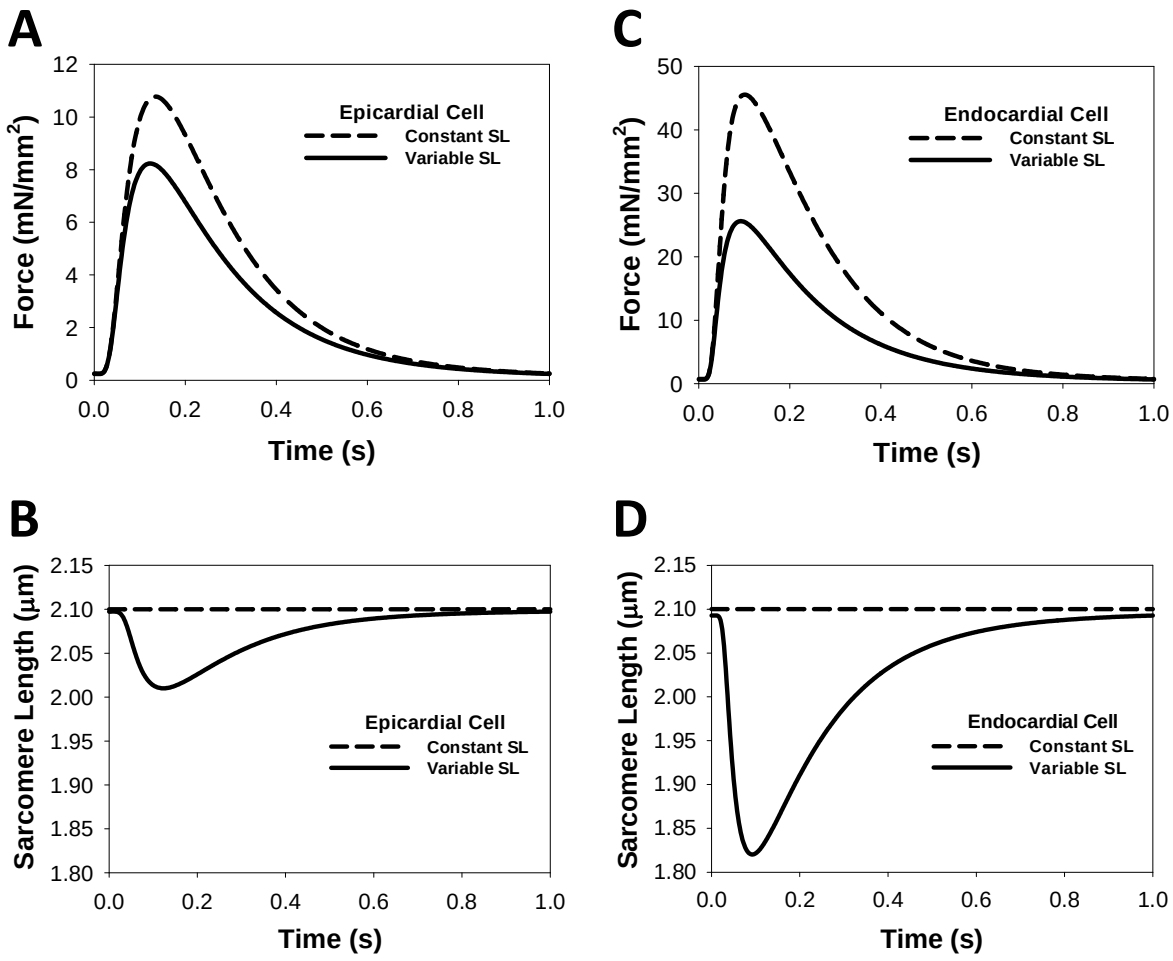

Figure 2.6 The effects of constant and variable sarcomere lengths on the contraction force development and myocyte shortening.

(A) Force development for the models with variable (solid line) and constant (dashed line) sarcomere lengths. Changing the SL from variable to a constant (B, D) does not change $[Ca^{2+}]_i$ transients, but changes contraction force (A, C). The initial SL for each simulation is 2.1 μm with a stimulation frequency of 1 Hz. Simulation data shows an increase in force, both for epicardial (A) and endocardial (C) cells, when variable SL is replaced by constant SL. (Figure reproduced from [44])

from 0.5 Hz. A similar increase in the residual contraction force at the larger stimulation frequencies is also observed experimentally [78].

2.3.5 Frequency dependence of dL/dt and dF/dt

The frequency dependencies of the peak force and cell shortening are shown in Fig. 2.4. As might be expected, dL/dt and dF/dt also showed frequency dependence. Simulated time

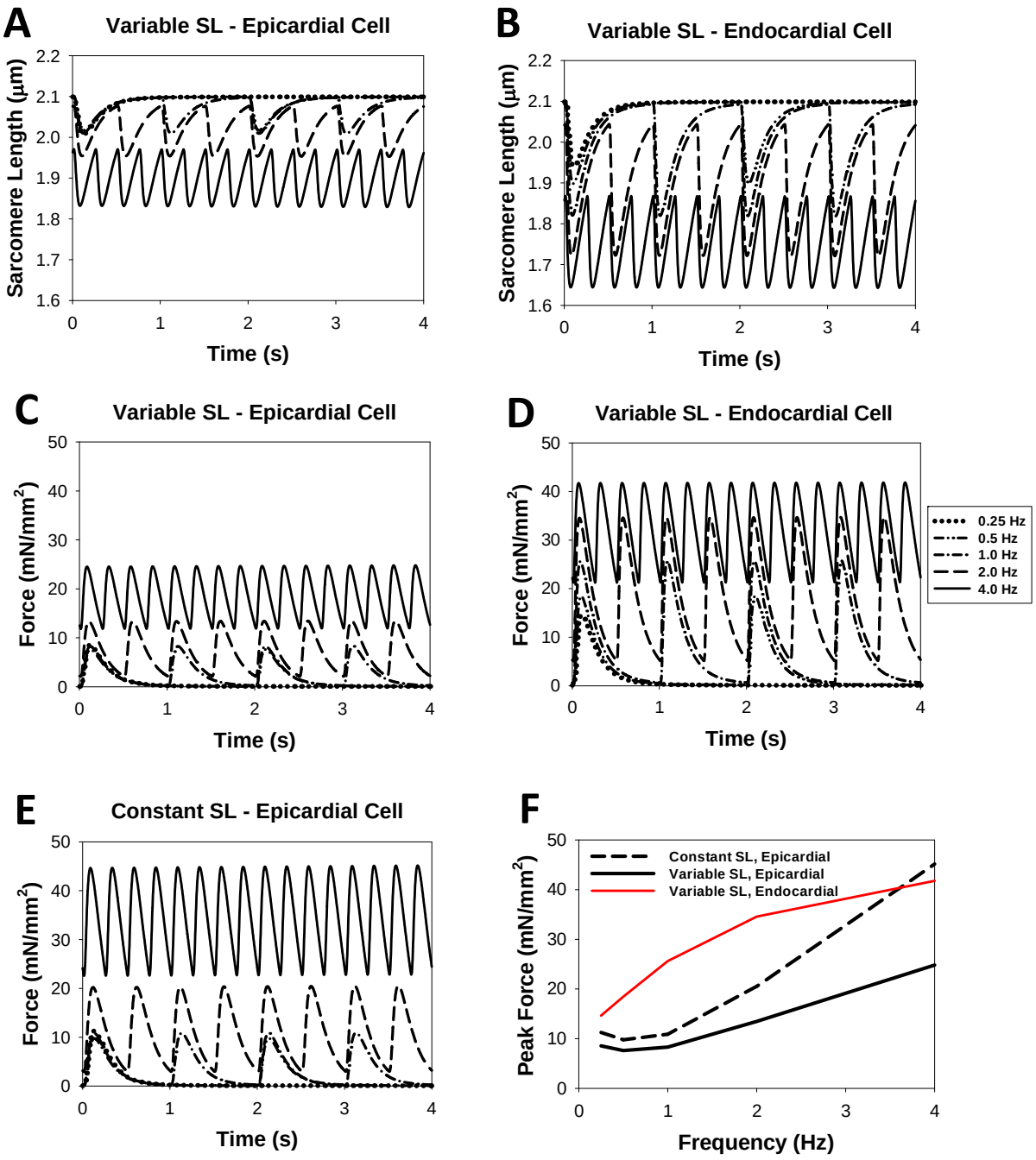

Figure 2.7 The effects of stimulation frequency on the time behavior of sarcomere length and contraction force for epicardial and endocardial cells.

The time courses of the SL (A and B) and contraction force (C, D, and E) over a four second interval are shown at different stimulation frequencies for epicardial (A, C, and E) and endocardial (B and D) cells. The simulation data with constant SL is shown only for epicardial cells, as the data for endocardial cells is similar. The frequency dependence of force for an epicardial cell when a variable SL parameter is used is not as pronounced as the frequency dependence of force when a constant SL parameter is used (C and E). The initial SL for each simulation is 2.1 μm, but the residual force for higher frequencies leads to significant shortening (A and B). Frequency dependence of peak force for epicardial and endocardial cells with variable SL and for epicardial cell with constant SL is shown in (F). (Figure reproduced from [44])

courses for dL/dt (Fig. 2.8 A and B) and dF/dt (Fig. 2.8 C and D) are shown for various frequencies from 0.25 Hz to 4.0 Hz, both for epicardial (Fig. 2.8 A and C) and endocardial (Fig. 2.8 B and D) cells. A negative dL/dt value indicates cell shortening during a contraction, while a positive dL/dt corresponds to relaxation. A positive dF/dt indicates the increase in force during a contraction, while a negative dF/dt corresponds to relaxation. The epicardial cell demonstrated a monotonic increase in the magnitudes of peak values for dL/dt and dF/dt in the frequency range from 0.25 to 4 Hz (Fig. 2.8 A and C). In contrast, the endocardial cell showed biphasic behavior in the peak magnitudes of the derivatives: an increase when the stimulation frequency changes from 0.25 to 2 Hz, and a decrease in the frequency range from 2 to 4 Hz (Fig. 2.8 B and D).

The frequency relationship for $+dL/dt_{max}$ (solid lines) and $-dL/dt_{max}$ (dashed lines) is shown in Fig. 2.9A. Both values showed biphasic behavior. For the epicardial cell, $+dL/dt_{max}$ and $-dL/dt_{max}$ decreased at stimulation frequencies from 0.25 to 0.5 Hz, and then increased for stimulation frequencies up to 4 Hz. For the endocardial cell, $+dL/dt_{max}$ and $-dL/dt_{max}$ increased at stimulation frequencies from 0.25 to 2 Hz, and then decreased for stimulations frequencies up to 4 Hz. When compared to the experimental data, our model tended to show, on average, peak contraction rates approximately equal to experimental data (open symbols). However, the model showed somewhat slower relaxation, thus lower values of $+dL/dt_{max}$, than experimental data (solid symbols) [73, 79, 80].

Figure 2.9B shows the frequency relationship for $+dF/dt_{max}$ (solid lines) and $-dF/dt_{max}$ (dashed lines). As with corresponding values for $+dL/dt_{max}$ and $-dL/dt_{max}$, the $+dF/dt_{max}$ and $-dF/dt_{max}$ showed biphasic behavior for both epicardial and endocardial cells.

To compare experimental and simulated data quantitatively, we plotted experimental and simulated results on time-to-peak and time-to-50% relaxation of the contraction force and

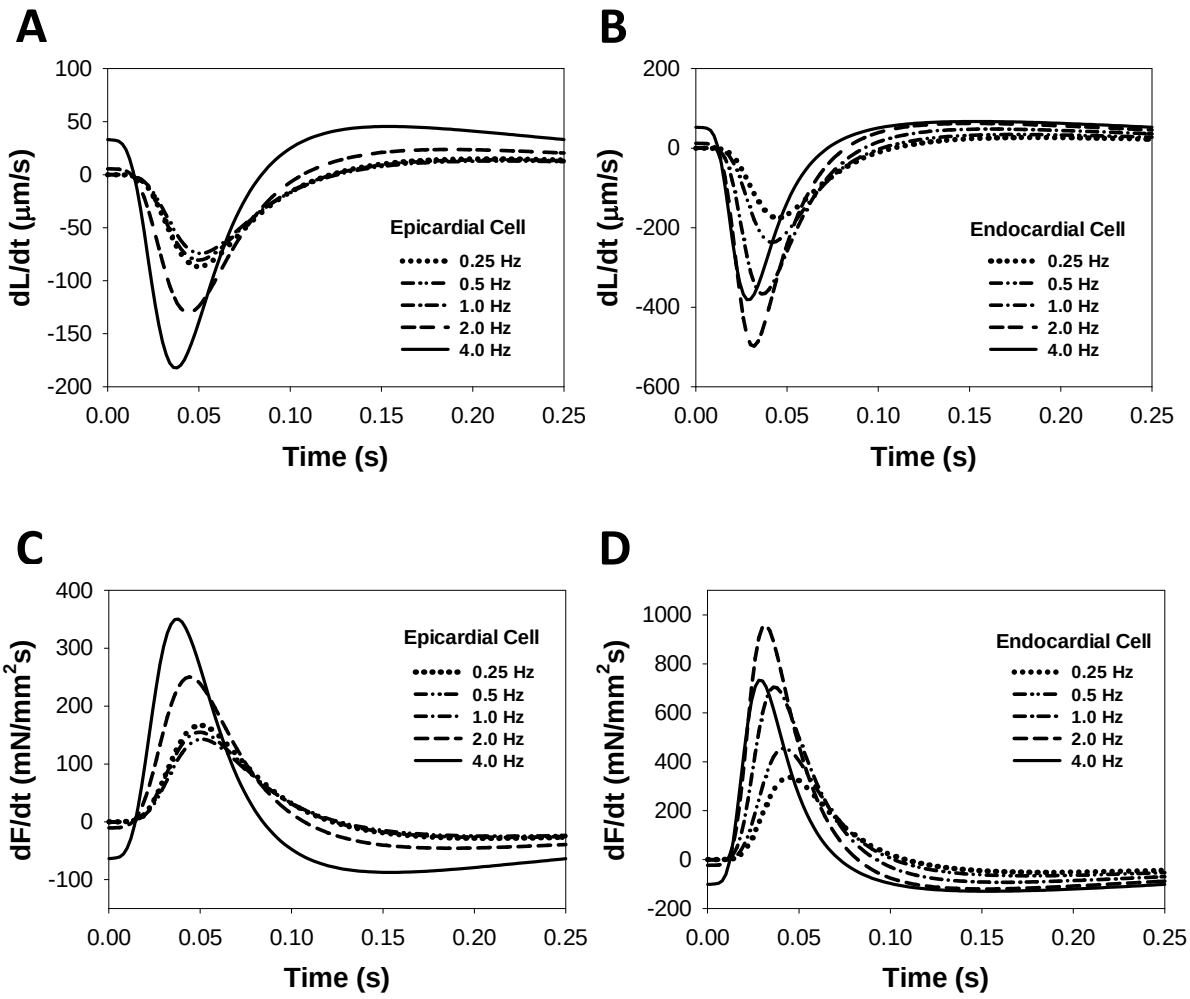

Figure 2.8 Time behavior of dL/dt and dF/dt for different stimulation frequencies.

Simulated time course of the rates of cellular shortening dL/dt (A, B) and contraction force dF/dt (C, D) during twitches for epicardial (A, C) and endocardial (B, D) cells. For epicardial cells, the largest values of $\pm dL/dt_{max}$ and $\pm dF/dt_{max}$ are observed at a relatively fast stimulation frequency of 4 Hz (solid lines in (A) and (C)). For endocardial cells, the largest values of $\pm dL/dt_{max}$ and $\pm dF/dt_{max}$ occur in the frequency interval from 1 to 4 Hz (dashed lined in (B) and (D)). (Figure reproduced from [44])

intracellular $[Ca^{2+}]_i$ transients in Fig. 2.10. Simulated data are shown for both epicardial and endocardial cells (black and red, respectively, in Fig. 2.10 B and D). Simulated data for time-to-peak force showed good agreement with the experimental data (compare Fig. 2.10 B and A), while time-to-50% relaxation were somewhat longer in the simulated data than those obtained in the experiments (compare Fig. 2.10 D and C). Experimental data for time-to-peak and time-to-50% relaxation of $[Ca^{2+}]_i$ transients were somewhat longer than those from simulations, but the

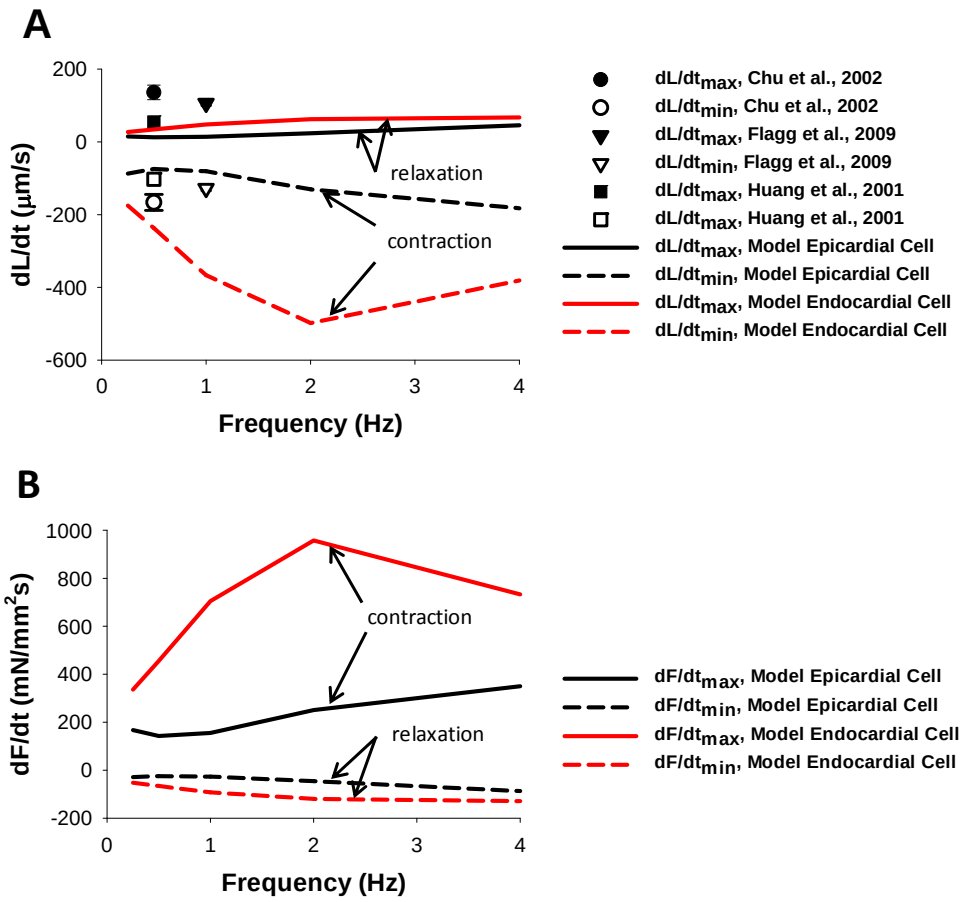

Figure 2.9 Frequency dependence of dL/dt_{max} and dF/dt_{max}.

(A) The simulated frequency dependencies of $(+dL/dt)_{max}$ (solid lines) and $(-dL/dt)_{max}$ (dashed lines). Experimental data from Chu *et al*. [80], Flagg *et al*. [79], and Huang *et al*. [73] are shown by symbols. We consider $(-dL/dt)$ to correspond to cell shortening. (B) The simulated frequency dependence of $(+dF/dt)_{max}$ (solid lines) and $(-dF/dt)_{max}$ (dashed lines). We consider $(+dF/dt)$ to correspond to contraction. The initial SL for the simulations in (A) and (B) is 2.1 µm. Data for epicardial and endocardial cells are shown in black and red, respectively. (Figure reproduced from [44])

50% relaxation of $[Ca^{2+}]_i$ transients were somewhat longer than those from simulations, but the simulated time-to-50% relaxations approached the experimental values at larger frequencies. Epicardial and endocardial cells showed similar simulated values for time-to-peak and time-to-50% relaxation of $[Ca^{2+}]_i$ transients, and for time-to-50% relaxation of contraction force. However, there were moderate differences between the cells for time-to-peak of the contraction force (Fig. 2.10B).

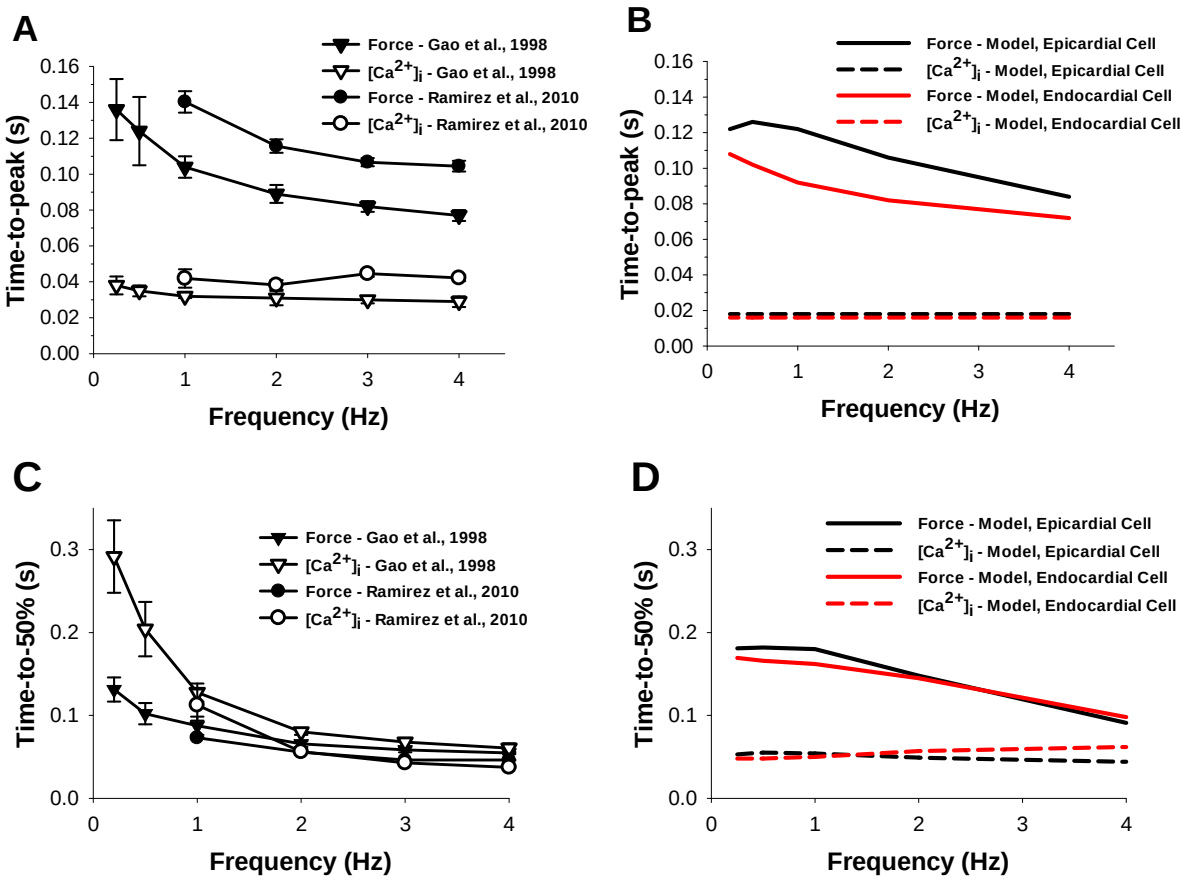

Figure 2.10 Time-to-peak and time-to-50% relaxation of the contraction force and $[Ca^{2+}]_i$ transients as function of stimulation frequency.

Experimental (A) and simulated (B) frequency dependencies of time-to-peaks for intracellular $[Ca^{2+}]_i$ transients and contraction force, and experimental (C) and simulated (D) frequency dependencies of time-to-50% relaxations for intracellular $[Ca^{2+}]_i$ transients and contraction force. Experimental data are obtained by Gao *et al*. ([67], triangles) and Ramirez-Correa *et al*. ([81], circles). Unfilled and filled symbols are used for intracellular $[Ca^{2+}]_i$ transients and contraction force, respectively. Simulation data for contraction force and intracellular $[Ca^{2+}]_i$ transients are shown by solid and dashed lines, respectively, and data for epicardial and endocardial cells are shown in black and red, respectively. (Figure reproduced from [44])

2.4 Discussion

In this chapter, we developed a new model for mouse ventricular myocyte contraction. This model is based on previously published models for epicardial and endocardial cells [29, 61-63], which include a comprehensive description of action potential, ionic currents, and Ca^{2+} dynamics. For a description of myocyte contraction, we adopted Model 4 developed by Rice *et al.* [42] by fitting experimental data on contraction for mice.

Mice demonstrate much faster heartbeats than many other species. Their contraction rate is about 10 beats per second [82], which is, for example, faster than the rabbit (4 Hz, [83]) and human (1 Hz, [84]) heart contraction rates. In addition, the action potential duration in mouse ventricular myocytes is also much shorter (APD_{50} ~ 4.5 ms in mice [29] versus ~200 ms in rabbits [43] and ~300-400 ms in humans [85]). These differences suggest different time characteristics for contraction in mouse, compared to human or rabbit, ventricular myocytes.

In a mouse cardiac cell, at moderate stimulation rates, an increase in action potential is followed by an increase in $[Ca^{2+}]_i$ and a delayed increase in force. The peak value of Ca^{2+} transient occurs after almost complete repolarization of action potential. In addition, peak contraction force appears after a significant decline of $[Ca^{2+}]_i$. Our model replicates this relationship. Figure 2.11 shows normalized values for epicardial action potential (solid line), $[Ca^{2+}]_i$ (dashed line), and force (dotted line) over a 0.5 second interval for a simulation at 1 Hz. In larger species, such as rabbit, time scaling of the action potential, $[Ca^{2+}]_i$ and contraction force transients is different (Fig. 9 in [43]). For rabbits, $[Ca^{2+}]_i$ transient, in significant part, overlaps with the action potential and contraction force transient, while the peak sequence is the same as in mice.

Mouse ventricular myocytes, unlike other species, demonstrate biphasic frequency dependence of intracellular $[Ca^{2+}]_i$ transient and peak force [70, 71] (however, see data of Ito *et al.* [76] where biphasic behavior is less apparent). Stuyvers *et al.* [71] suggested a qualitative mechanism which explains this biphasic behavior based on frequency-dependent Ca^{2+} dynamics. The minimum occurs at the crossroad of the descending frequency trend of the Ca^{2+} load into the sarcoplasmic reticulum during diastole and ascending trend in Ca^{2+} entry into the cell through L-type Ca^{2+} channels. They used a simplified description of Ca^{2+} dynamics for mouse ventricular

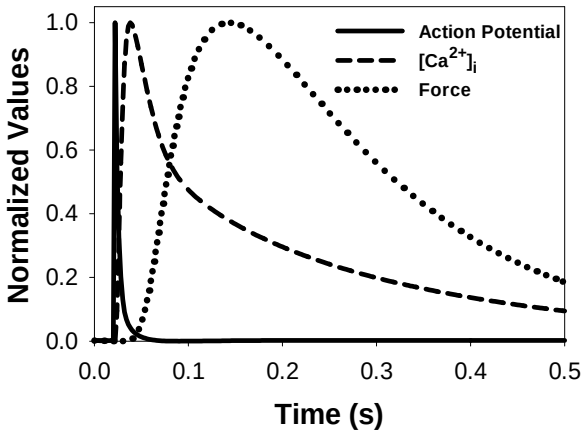

Figure 2.11 Scaling action potential, $[Ca^{2+}]_i$ transient, and force in the model for mouse ventricular myocyte contraction.

The simulation used an initial SL of 2.1 μm and a stimulation frequency of 1 Hz. In mouse ventricular myocytes, Ca^{2+} transient develops after action potential repolarization is almost complete. After that, the contraction force develops with time delay due to Ca^{2+} binding to troponin and troponin-induced changes in contractile proteins. (Figure reproduced from [44])

myocytes. Our model for an epicardial cell, which includes a comprehensive description of the electrical activity and Ca^{2+} dynamics in mouse ventricular myocytes during cell twitch, was also able to reproduce this physiological phenomenon. In our model, myocyte contraction force is related to Ca^{2+} dynamics through the Markov model for crossbridge kinetics. While both peak $[Ca^{2+}]_i$ transients and peak contraction force show minimum values as functions of stimulation frequency, these minimum frequency values are slightly different (Fig. 2.4). This trend is also confirmed by the experimental data of McCloskey *et al.* [66].

However, our model for the endocardial cell does not show biphasic behavior in the frequency-dependence of both peak $[Ca^{2+}]_i$ transients and peak contraction force. There is also some experimental data in which non-monotonic increase in peak $[Ca^{2+}]_i$ transients and myocyte shortening in mice is less apparent: even saturation and decrease in myocyte shortening amplitude at relatively large stimulation frequencies occurred [76]. Our model for the endocardial cell, at least qualitatively, reproduced saturation and even decrease in sarcomere

shortening and contraction force amplitude at 4 Hz stimulation (Fig. 2.7 B and D). This effect can be explained by the larger peak and diastolic values of $[Ca^{2+}]_i$ transients in endocardial cells compared to epicardial cells, which shift the operation interval of intracellular Ca^{2+} towards a smaller slope in force-calcium relationships (Fig. 2.2D).

While there are no specific experimental studies of contraction force and cell shortening in mouse epicardial and endocardial ventricular myocytes, there are a few studies of the differences in action potentials and Ca^{2+} handling in these cells [77, 86]. The studies show that the endocardial cells demonstrate significantly larger $[Ca^{2+}]_i$ transients, and our modeling predicts larger contraction force and shortening in these ventricular myocytes.

Our electromechanical model for mouse ventricular myocyte contraction includes a variable sarcomere length during cell contraction, the effect that occurs in most experiments. Simulations with variable sarcomere length produced significantly smaller contraction force than the simulations with constant sarcomere length despite the same time course and amplitude of $[Ca^{2+}]_i$ transient during twitch. This suggests the importance of the inclusion of cell shortening in the model for cardiac myocyte contraction. Note that a similar result was obtained with a more complex model of Rice *et al.* [43], developed for rabbit ventricular myocytes, who also studied the effects of variable and fixed sarcomere length on the force development.

Several models for cardiac myocyte contraction have been developed to date [42, 43, 46, 58, 60] (see also review [57]). Earlier models did not include sarcomere shortening during twitch [42, 58, 60]. They are primarily focused on simplification of the description of crossbridge kinetics, their dependence on Ca^{2+} dynamics, and careful reproduction of the existing experimental data on steady-state and dynamic force-calcium relationships. Most of these models have limitations due to this and other simplifications.

Rice *et al.* [42] investigated five Markov models describing contraction mechanisms in cardiac myocytes. Two of the models consisted of four tropomyosin states and transitions between them (N0, N1, P0, and P1, see Fig. 2.1B). These models differed by the mechanisms of modulation of the transition rates (in Fig. 2.1B they are defined as k_{NP} and k_{PN}). In Model 1, rates k_{NP} and k_{PN} were independent of the developed force, while in Model 2 the rates depended on the developed force. In both models, Ca^{2+} binding to troponin directly affected tropomyosin shifting, i.e., rates k_{NP} and k_{PN}. Model 3 included an indirect connection of the Ca^{2+} binding to troponin and tropomyosin shifting, as shown by dashed arrows in Fig. 2.1B (see also [42]), and only four states (N0, N1, P0, and P1). Models 4 and 5 were extended to up to three crossbridge bindings, which resulted in four permissive tropomyosin states, P0, P1, P2, and P3, (Fig. 2.1B and [42]). The only difference between Models 4 and 5 was the modulation of the k^{-}_{ltrpn} rate by generated force. Because Model 4 and Model 5 yielded an approximately equal description of myocyte contraction, we implemented Model 4 in our electrophysiological model, as Model 5 led to unstable solutions.

Our model of mouse ventricular myocyte contraction also has some limitations due to the simplification of the biophysical mechanism of contraction. In particular, the model uses a simplified description of the relationships between contraction force and cellular shortening in the form of Hooke's law, while the real dependence is more complicated [43]. It does not describe the effects of cellular shortening on Ca^{2+} transients, as does the 2008 model of Rice *et al.* [43]; however, this effect is relatively small. Also, our model, as most other models, does not take into account intracellular spatial inhomogeneities of Ca^{2+} concentration and crossbridge binding sites.

Nevertheless, despite the limitations, our electromechanical model of mouse ventricular myocyte contraction was extensively verified by experimental data obtained for mice. It reproduced reasonably well a significant amount of the existing experimental data. The model can be used for cells from two different regions of the heart (epicardium and endocardium). As with most other models, it uses a simplified description of the contraction force generation. We employed a six-state Markov model for tropomyosin dynamics and separate Ca^{2+} binding to troponin to describe force development. More comprehensive models will be necessary to develop a better simulation of more extended experimental data sets.

For supporting information, see the model summary in Appendix A.

3 A MATHEMATICALMODEL OF β_1–ADRENERGIC REGULATION OF MOUSE VENTRICULAR MYOCYTE CONTRACTION

3.1 Introduction

Multiple experimental protocols have been developed to study mechanisms of cardiac myocyte contraction and isolate the stages of this process. These include measurements of steady-state force-calcium relationships, the crossbridge release rate (k_{rel}), force development rate (k_{df}), force-velocity relationship, and force redevelopment rate (k_{tr}), which were performed with skinned cardiac cells [15, 87, 88]. In addition, frequency and isoproterenol dependencies for $[Ca^{2+}]_i$ transients, total contraction force, and sarcomere shortening were measured with non-skinned cardiac cells [67, 70, 75, 76, 81, 89-95].

Cardiac myocyte contraction is modulated by the β_1-adrenergic signaling system and its components, the activation of which significantly increases contraction force, sarcomere shortening, and speeds up contraction relaxation [91, 92]. Experimental data demonstrate that it is the phosphorylation of two contractile proteins, TnI and MyBP-C, that causes the major effects of β_1-adrenoreceptor activation on myocyte contraction [15, 87]. While the experimental investigations have led to the development of mathematical models that allow for detailed description of myocyte contraction, only a few models include the effects of activation of β_1-adrenergic signaling. Land *et al*. [45] used modifications of their model parameters to include the effects of stimulation of the β_1-adrenergic receptors, however, there was no detailed description of the biochemical reactions involved in the β_1-adrenergic signaling system. More recently, a detailed mathematical model was developed for the β_1-adrenergic regulation of rabbit ventricular myocytes [47] that included modeling of biochemical reactions. However, the model gave qualitative, rather than quantitative, agreement with the experimental data, perhaps because

the model was developed based on data from multiple species, including mice, which have a significantly different repolarization mechanism and different Ca^{2+} dynamics.

In this chapter, we developed a new comprehensive mathematical model of the β_1-adrenergic regulation of mouse ventricular myocyte contraction, which was verified by experimental data obtained from mice. Our model is based on a model of the β_1-adrenergic signaling system in mouse ventricular cells [16] and models for myocyte contraction [42-44]. In this new model, we incorporated phosphorylation of MyBP-C, as well as the effect of phosphorylation of TnI and MyBP-C on crossbridge attachment and detachment rates and on the viscosity coefficient. With the resulting model, we were able to simulate major experimental protocols without and with stimulation of the β_1-adrenergic signaling system. These protocols included measurements of steady-state force-calcium relationships, force-velocity relationship, and rates k_{rel}, k_{df}, and k_{tr}. We also simulated frequency and isoproterenol dependencies for $[Ca^{2+}]_i$ transients, total contraction force, and sarcomere shortening. The fit of the simulations to the experimental data suggests that the increased contraction force and myocyte shortening upon stimulation of β_1-ARs is primarily due to the increased $[Ca^{2+}]_i$ transients and phosphorylation of TnI and MyBP-C resulting from activation of the β_1-adrenergic signaling system. The new mathematical model can also be modified to simulate ventricular myocyte contraction in genetically modified mice modeling chronic cardiac diseases.

3.2 Methods

3.2.1 Model development

To develop this model, we modified the Bondarenko model [16], which describes action potential, Ca^{2+} dynamics, and the biochemical part of the β_1-adrenergic signaling system (Fig. 3.1), to include active contraction force from [42, 44], passive and flexible contraction forces

from [43], and modified viscous force based on the description by Rice *et al*. [43]. A detailed description of the Bondarenko model is given elsewhere [16, 96]. In this chapter we focused on the model development for myocyte contraction.

Our mathematical model is based exclusively on experimental data obtained from mice. During model development we used data from multiple laboratories so that our model would fall within the range of an "average" set of experimental data. Due to the modular structure of the original Bondarenko model [16], we were able to add modules for MyBP-C phosphorylation and myocyte contraction without affecting the parameters for existing modules. First we added the MyBP-C module, and fit parameters to experimental data for MyBP-C phosphorylation. Next we added the contraction module, and fit parameters to match experimental contraction data for control conditions. As we simulated new protocols (described in the remainder of Section 3.2) and compared the results to the corresponding experimental data, we were able to identify the contributions of active, passive, viscous, and flexible force and refine the parameters accordingly. To account for changes in contraction characteristics due to stimulation of the β_1-adrenergic system, we introduced factors to adjust several rates and constants due to TnI and MyBP-C phosphorylation. We repeated the parameter fitting process for the contraction module, focusing only on parameters for the introduced factors. When experimental data was available for the independent effects of TnI versus MyBP-C phosphorylation in a particular protocol, we adjusted the parameters accordingly; otherwise we adjusted the parameters such that TnI and MyBP-C affected the rate equally.

3.2.2 Active contraction force

The active force portion of the model is based on force generated from crossbridges. We used our previous Markov model of six tropomyosin states (see Chapter 2, Fig. 2.1B), with

modifications of the rate constants and the equation for active contraction force. Time behavior of the tropomyosin states is described by the same differential equations as in Chapter 2 [44]. These equations and the contraction model parameters are presented in Appendix B.

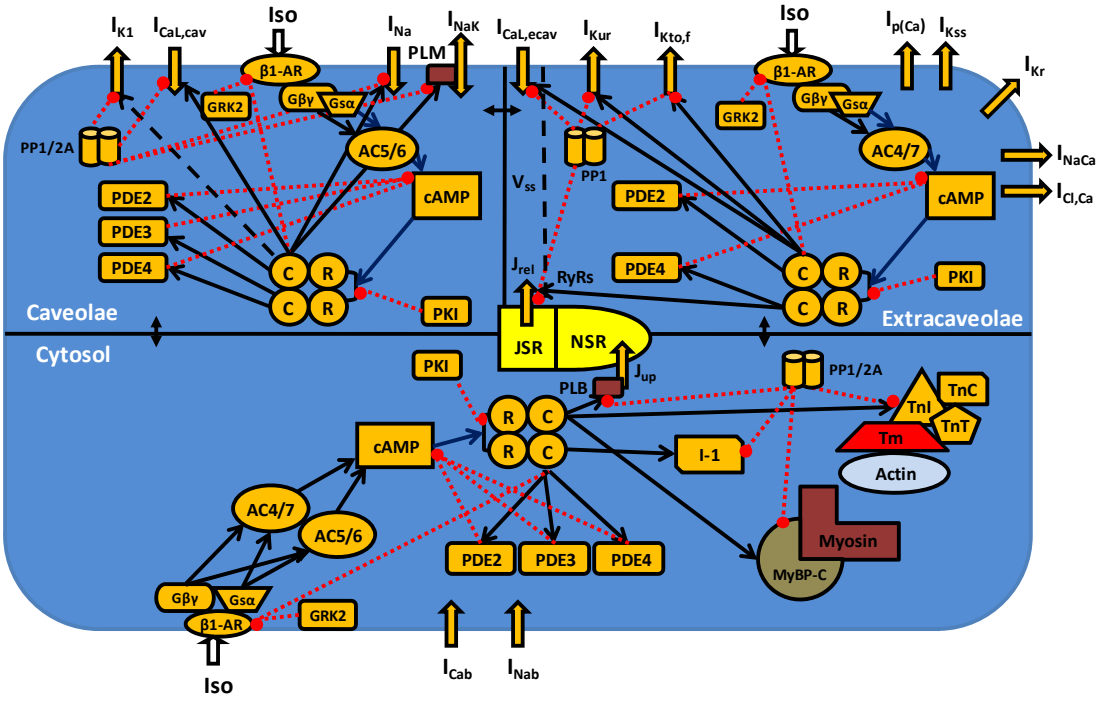

Figure 3.1 Schematic diagram of the β_1-adrenergic regulation of the mouse ventricular myocyte contraction.

The model cell contains three intracellular compartments in the β_1-adrenergic signaling system: caveolae, extra-caveolae, and cytosol. The subspace volume (V_{ss}) is located in the caveolae domain. Transmembrane currents are the time-independent K^+ current (I_{K1}), the L-type Ca^{2+} current ($I_{CaL,cav}$ and $I_{CaL,ecav}$), the fast Na^+ current (I_{Na}), the Na^+/K^+ pump [I_{NaK}, regulated by phospholemman(PLM)], the ultrarapidly activating delayed rectifier K^+ current (I_{Kur}), the rapidly recovering transient outward K^+ current ($I_{Kto,f}$), the sarcolemmal Ca^{2+} pump ($I_{p(Ca)}$), the noninactivating steady-state voltage activated K^+ current (I_{Kss}), the rapid delayed rectifier K^+ current (I_{Kr}), the Na^+/Ca^{2+} exchanger (I_{NaCa}), the Ca^{2+}-activated chloride current ($I_{Cl,Ca}$), the Ca^{2+} and Na^+ background currents (I_{Cab} and I_{Nab}). The Ca^{2+} fluxes within the cell are uptake of Ca^{2+} from the cytosol to the network sarcoplasmic reticulum (NSR) by the SERCA pump (J_{up}) and the Ca^{2+} release from the junctional sarcoplasmic reticulum (JSR) through the ryanodine receptors (RyRs) (J_{rel}). The components of the β_1-adrenergic signaling system are the β_1-adrenergic receptors (β_1-AR); α- and βγ-subunits of stimulatory G-protein ($G_{s\alpha}$ and $G_{\beta\gamma}$); G-protein-coupled receptor kinase of type 2 (GRK2); adenylyl cyclases of type 5/6 or 4/7 (AC5/6 or AC4/7, respectively); cyclic AMP (cAMP); regulatory (R) and catalytic (C) subunit of protein kinase A (PKA) holoenzyme; phosphodiesterases of type 2, 3, or 4 (PDE2, PDE3, or PDE4, respectively); inhibitor-1 (I-1); protein kinase A inhibitor (PKI); and protein phosphatases of type 1 and 2A (PP1 and PP2A). Stimulatory links are shown by black arrows and inhibitory links are shown by red dashed lines with circles. The contractile proteins are actin; myosin; myosin binding protein C (MyBP-C); troponin I, C and T (TnI, TnC and TnT, respectively); and tropomyosin (Tm). They are localized in the cytosolic compartment. Two of these (TnI and MyBP-C) are substrates of the β_1-adrenergic signaling system.

Active contraction force F_{contr} (in mN/mm^2) was calculated using the equation:

$$F_{contr} = 58.0\, F_{contrn}, \tag{3.1}$$

where

$$F_{contrn} = \frac{P1 + N1 + 2(P2) + 3(P3)}{F_{\max}}, \tag{3.2}$$

$$F_{\max} = P1_{\max} + 2(P2_{\max}) + 3(P3_{\max}), \tag{3.3}$$

$$P1_{\max} = \frac{f_{01}(2g_{\min xb})(3g_{\min xb})}{\Sigma}, \tag{3.4}$$

$$P2_{\max} = \frac{f_{01}f_{12}(3g_{\min xb})}{\Sigma}, \tag{3.5}$$

$$P3_{\max} = \frac{f_{01}f_{12}f_{23}}{\Sigma}, \tag{3.6}$$

$$\Sigma = (g_{\min xb})(2g_{\min xb})(3g_{\min xb}) + f_{01}(2g_{\min xb})(3g_{\min xb}) + f_{01}f_{12}(3g_{\min xb}) + f_{01}f_{12}f_{23}, \tag{3.7}$$

$$f_{01} = 15f_{XB}, f_{12} = 30f_{XB}, f_{23} = 7f_{XB}. \tag{3.8}$$

In equation (3.1), F_{contrn} is the normalized contraction force, and the coefficient 58.0 was obtained from fitting absolute values of the steady-state and dynamic experimental forces.

Experimental data show that active contraction force is regulated by Ca^{2+} transients and activation of the β_1-adrenergic signaling system. Two major proteins are involved in the force modulation, TnI and MyBP-C. Activation of β_1-ARs results in an increased level of phosphorylation of TnI and MyBP-C which changes the transition rates between tropomyosin states.

TnI phosphorylation is described by a differential equation developed by Bondarenko [16]:

$$\frac{df_{TnI,p}^{cyt}}{dt} = \frac{k_{TnI\_PKA}\cdot[C]^{cyt}\cdot(1-f_{TnI,p}^{cyt})}{K_{TnI\_PKA}+(1-f_{TnI,p}^{cyt})} - \frac{k_{TnI\_PP2A}\cdot[PP2A]^{cyt}\cdot f_{TnI,p}^{cyt}}{K_{TnI\_PP2A}+f_{TnI,p}^{cyt}}, \tag{3.9}$$

where $f_{TnI,p}^{cyt}$ is the fraction of phosphorylated TnI, k_{TnI_PKA} is the rate of TnI phosphorylation by PKA, k_{TnI_PP2A} is the rate of TnI dephosphorylation by PP2A, K_{TnI_PKA} is the relative affinity for TnI phosphorylation by PKA, K_{TnI_PP2A} is the relative affinity for TnI dephosphorylation by PP2A, $[C]^{cyt}$ is the cytosolic concentration of catalytic subunit of PKA, and $[PP2A]^{cyt}$ is the cytosolic concentration of protein phosphatase of type 2A (see Appendix B).

Similarly, we describe phosphorylation of MyBP-C by the following differential equation:

$$\frac{df_{MyBPC,p}^{cyt}}{dt} = \frac{k_{MyBPC\_PKA}\cdot[C]^{cyt}\cdot(1-f_{MyBPC,p}^{cyt})}{K_{MyBPC\_PKA}+(1-f_{MyBPC,p}^{cyt})} - \frac{k_{MyBPC\_PP}\cdot\left([PP1]^{cyt}+[PP2A]^{cyt}\right)\cdot f_{MyBPC,p}^{cyt}}{K_{MyBPC\_PP}+f_{MyBPC,p}^{cyt}}, \quad (3.10)$$

where $f_{MyBPC,p}^{cyt}$ is the fraction of phosphorylated MyBP-C, k_{MyBPC_PKA} is the rate of MyBP-C phosphorylation by PKA, k_{MyBPC_PP} is the rate of MyBP-C dephosphorylation by PP1 and PP2A, K_{MyBPC_PKA} is the relative affinity for MyBP-C phosphorylation by PKA, K_{MyBPC_PP} is the relative affinity for MyBP-C dephosphorylation by PP1 and PP2A, and $[PP1]^{cyt}$ is the cytosolic concentration of protein phosphatase of type 1, (see Appendix B).

Model parameters for equation (3.10) were adjusted to fit experimental data on phosphorylation of MyBP-C. Figure 3.2A demonstrates simulated and experimental increases of phosphorylation levels of MyBP-C due to an activation of β_1-ARs. Experimental data [97-99] show a significant level of phosphorylation of MyBP-C (~55-60%) without stimulation of β_1-ARs, which is in line with our modeling value of 57.5% phosphorylation. Upon activation of β_1-ARs, the experimental phosphorylation level of MyBP-C increased 1.65-1.8 fold [97-99], which is close to our simulated 1.64 fold. In addition, we simulated kinetics of MyBP-C

phosphorylation, shown in Fig. 3.2B. Our simulation data fits well the experimental data of Verduyn *et al*. [99].

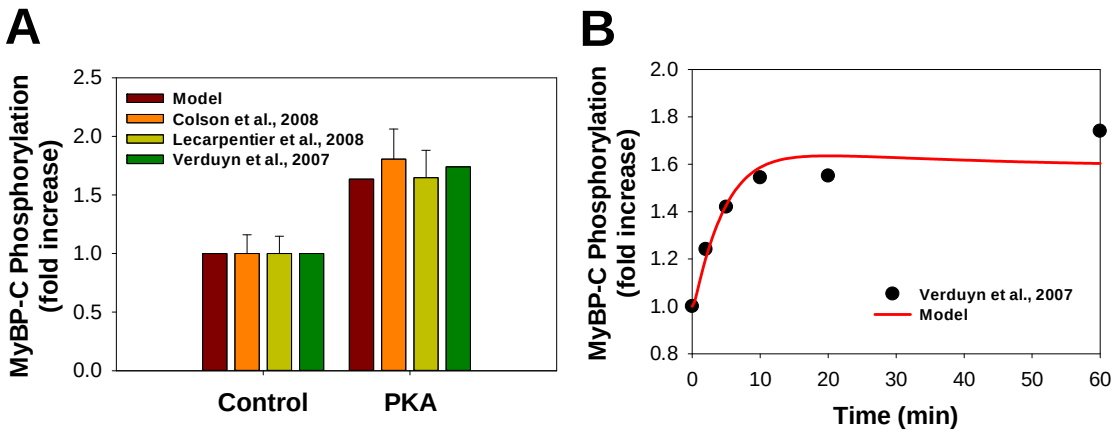

Figure 3.2 MyBP-C phosphorylation levels.

(A) Maximum MyBP-C phosphorylation levels of model simulations and experimental data [97-99] without (Control) and with (PKA) β_1-adrenergic stimulation. Values have been normalized to control values for comparison. Simulation data was obtained by stimulation with 10 µM isoproterenol to achieve maximum effect. (B) The time-course of MyBP-C phosphorylation by fold increase. The model simulation was obtained by stimulation with 10 µM isoproterenol (shown by the solid line) and is compared to experimental data from Verduyn *et al*. [99] (shown by symbols).

Activation of the β_1-adrenergic system increases detachment rates and decreases attachment rates. In our model this effect is accomplished by the modulation of rate constants, f_{XB} and g_{minxb}, using the level of phosphorylation of TnI and MyBP-C, as shown below:

$$f_{XB} = f_{XB0}\left(1+0.45\left(f_{TnI,p}^{cyt}-0.364\right)\right)^{-1}\left(1+1.5\left(f_{MyBPC,p}^{cyt}-0.575\right)\right)^{-1}, \tag{3.11}$$

$$g_{minxb} = g_{minxb0}\left(1+0.3\left(f_{TnI,p}^{cyt}-0.364\right)\right)\left(1+1.0\left(f_{MyBPC,p}^{cyt}-0.575\right)\right), \tag{3.12}$$

where the numbers 0.364 and 0.575 reflect the unstimulated phosphorylation levels of TnI and MyBP-C, respectively, and f_{XB0} and g_{minxb0} are given in Appendix B.

3.2.3 Passive contraction force

Passive contraction force is similar to that developed by Rice *et al*. [43]. It includes titin- and collagen-related components:

$$F_{passive}\left(SL\right)=F_{titin}\left(SL\right)+F_{collagen}\left(SL\right), \tag{3.13}$$

where

$$F_{titin}\left(SL\right)=\begin{cases} PCon_{titin}\left(\exp\left(PExp_{titin}\left(SL-SL_{rest}\right)\right)-1\right) & \text{if} \quad SL\geq SL_{rest} \\ -PCon_{titin}\left(\exp\left(PExp_{titin}\left(SL_{rest}-SL\right)\right)-1\right) & \text{if} \quad SL<SL_{rest} \end{cases} \tag{3.14}$$

$$F_{collagen}\left(SL\right)=\begin{cases} PCon_{collagen}\left(\exp\left(PExp_{collagen}\left(SL-SL_{collagen}\right)\right)-1\right) & \text{if} \quad SL\geq SL_{collagen} \\ 0 & \text{if} \quad SL<SL_{collagen} \end{cases} \tag{3.15}$$

Constants in Eqs. (3.14) and (3.15) are given in Appendix B.

Because experimental data by Najafi *et al*. [100] shows that passive contraction force is very weakly modulated by PKA, and the magnitude of the passive force is relatively small compared to the active force, we did not include the effects of stimulation of β_1-ARs on the passive force in this model.

3.2.4 Viscous force

In our model, we implemented viscous force, which contains two terms, one with linear and one with quadratic dependence on the sarcomere shortening velocity v:

$$F_{visc}=-visc\cdot v\left(1-a_{fx}\cdot v\right), \tag{3.16}$$

where $visc$ is the linear viscosity coefficient and a_{fx} is the additional parameter responsible for nonlinearity.

This form of the viscous force can be derived from the Hill equation relating force and muscle velocity [101] (see Appendix C for details):

$$\left(v+b\right)\left(F+a\right)=b\left(F_0+a\right). \tag{3.17}$$

Solution of this equation with respect to F/F_0 gives:

$$\frac{F}{F_0} = \frac{1 - \dfrac{av}{bF_0}}{1 + \dfrac{v}{b}}. \tag{3.18}$$

In equation (3.18), the numerator is a linear function of v, which reflects a decrease in F/F_0 with shortening velocity. The term v/b in the denominator changes this behavior to hyperbolic. Experimental data on the dependence of shortening velocity on the relative force for mice [88] demonstrates that the deviation from linearity is quite small, which suggests that the ratio v/b in the denominator is also small. Using the Taylor expansion of the denominator, we obtain:

$$\frac{F}{F_0} \approx \left(1 - \frac{av}{bF_0}\right)\left(1 - \frac{v}{b}\right). \tag{3.19}$$

Equation (3.19) can be presented in the form

$$\frac{F}{F_0} \approx 1 - \left(\frac{a}{bF_0} + \frac{1}{b}\right)v + \left(\frac{a}{b^2 F_0}\right)v^2, \tag{3.20}$$

which includes both linear and quadratic dependence of the force on the muscle shortening velocity, which was implemented in our model.

Experimental data by Sadayappan *et al*. [88] also shows that the shortening velocity increases upon stimulation of the β_1-adrenergic signaling system. To simulate these effects, we implemented modulation of *visc* and a_{fx} by phosphorylated fractions of TnI and MyBP-C:

$$visc = visc_0 \left(1 + 0.33\left(f^{cyt}_{TnI,p} - 0.364\right)\right)^{-1} \left(1 + 1.1\left(f^{cyt}_{MyBPC,p} - 0.575\right)\right)^{-1}, \tag{3.21}$$

$$a_{fx} = a_{fx0} \left(1 + 0.2\left(f^{cyt}_{TnI,p} - 0.364\right)\right)^{-1} \left(1 + 0.6\left(f^{cyt}_{MyBPC,p} - 0.575\right)\right)^{-1}, \tag{3.22}$$

in which parameters were obtained to fit the experimental data by Sadayappan *et al*. [88] ($visc_0$ and a_{fx0} are given in Appendix B).

3.2.5 Flexible force

We used the expression of the flexible forces as proposed by Rice *et al*. [43]

$$F_{flex} = KSE\left(SL - SL_0\right), \tag{3.23}$$

where parameter KSE = 1.0.

3.2.6 Sarcomere shortening

Unlike our Chapter 2 model, where sarcomere shortening was calculated using Hooke's law and active contraction force only, sarcomere (SL) shortening in this model is described using Newton's second law represented in the form of two first-order differential equations:

$$\frac{dv}{dt} = \frac{F_{contrn} + F_{passive} + F_{visc} + F_{flex}}{mass}, \tag{3.24}$$

$$\frac{dSL}{dt} = -v. \tag{3.25}$$

Here, *mass* is the model parameter related to sarcomere mass.

3.2.7 Method of simulation

The cardiac cell model was stimulated with different frequencies using a stimulus current (I_{stim} = 80 pA/pF, τ_{stim} = 1.0 ms) for at least 300,000 ms to reach a quasi-steady state. Simulated data of intracellular $[Ca^{2+}]_i$ transients, myocyte contraction force, and sarcomere length SL on the interval from 296,000 to 300,000 ms were compared to extensive experimental data.

The model consists of 150 ordinary differential equations (see Appendix B), which were solved by the fourth-order Runge-Kutta method. In order to decrease computing time, the differential equations for four "fast" variables ($[Ca^{2+}]_{ss}$ and RyR states P_{O1}, P_{C1p}, and P_{O1p}) were solved with a time step of 0.000002 ms, but the differential equations for all remaining variables were solved with two different time steps. The 0.000002 ms time step was used during the first 10 milliseconds after the initiation of the stimulus current, but a larger time step, 0.0001 ms, was

used otherwise. For the force-velocity simulations with isoproterenol and frequency dependence simulations with isoproterenol, all time steps were decreased by a factor of 10. The model was implemented as an original Intel FORTRAN 90 code, which was run under SUSE Linux on a Dell Precision Workstation T3500 (Intel Xeon Processor W3670, 3.20 GHz, 8 GB RAM).

3.3 Results

We used several mathematical models as templates for the development of our model of the β_1-adrenergic regulation of mouse ventricular myocyte contraction. These included a model of the β_1-adrenergic signaling system in mouse ventricular cells [16] and models for myocyte contraction [42-44]. The resulting model allowed for simulation of major experimental protocols designed for studying cardiac myocyte contraction without and with stimulation of the β_1-adrenergic signaling system.

Experimental data demonstrated that the phosphorylation of two contractile proteins, TnI and MyBP-C, cause the major effects of β_1-AR stimulation on cardiac myocyte contraction [15, 102]. The Bondarenko model of the β_1-adrenergic signaling system in mouse ventricular myocytes [16] included a description of phosphorylation of TnI, as it was involved in the modulation of Ca^{2+} dynamics. In the current model, we developed equations to describe phosphorylation of MyBP-C (see Appendix B). Figure 3.2 shows simulated and experimental data on MyBP-C phosphorylation upon stimulation of the β_1-adrenergic signaling system. Experimental data shows that the MyBP-C phosphorylation level increased 1.6-1.8 fold after application of PKA. Our model replicated this increase well when stimulated with a maximum concentration (10 μM) of isoproterenol (Fig. 3.2A). In addition, we were able to simulate the time course of MyBP-C phosphorylation, which is shown in Fig. 3.2B. Simulated phosphorylation kinetics are consistent with the experimental data from Verduyn *et al*. [99].

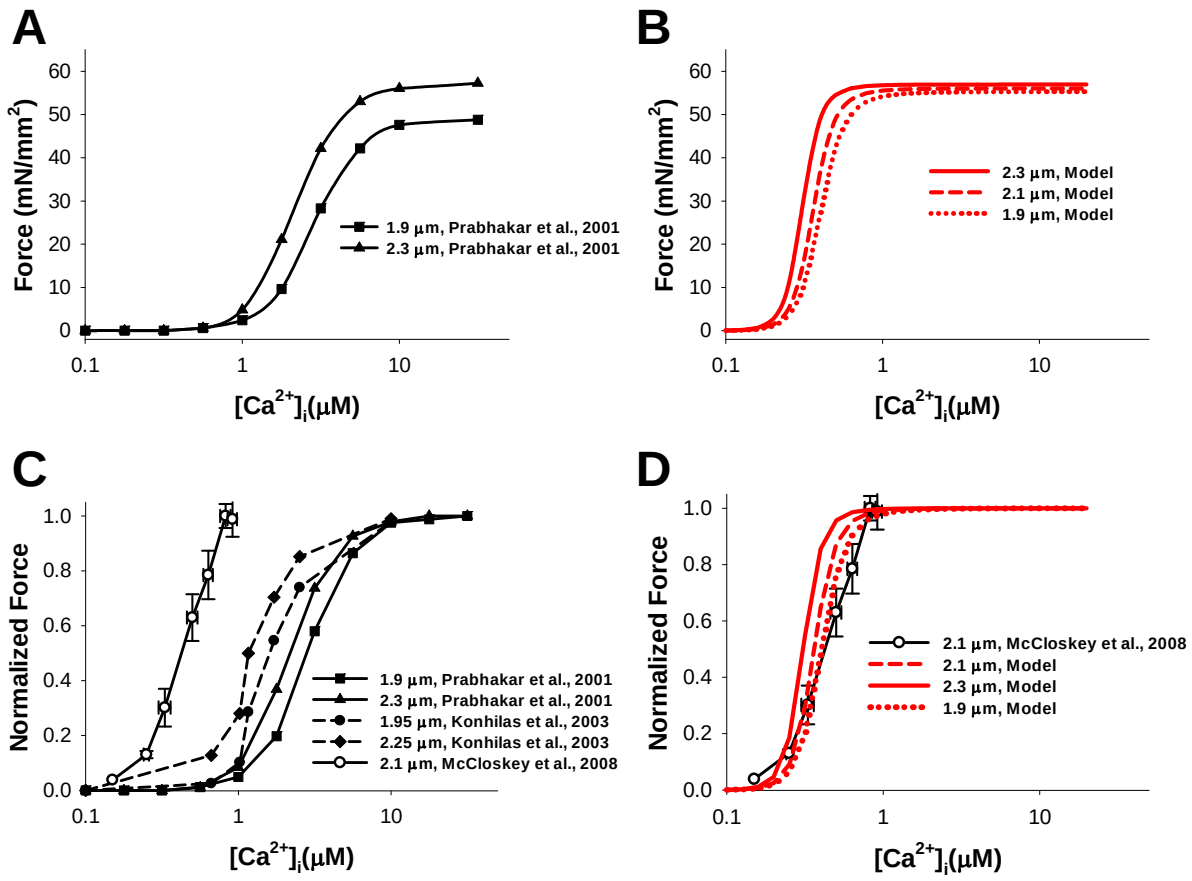

Figure 3.3 The steady-state force-$[Ca^{2+}]_i$ relationship for various sarcomere lengths.

The steady-state absolute force-$[Ca^{2+}]_i$ relationship (A and B) and the normalized steady-state force-$[Ca^{2+}]_i$ relationship (C and D) for different sarcomere lengths (SL). Experimental data obtained with skinned myocytes [64, 65] are shown in (A) and (C) with filled symbols; experimental data obtained with non-skinned myocytes [66] are shown in (C) and (D) with unfilled symbols. The model's simulations at various initial SL lengths are shown in red in (B) and (D).

The first protocol we simulated using our model was the steady-state active force-$[Ca^{2+}]_i$ relationship for differing SL lengths (Fig. 3.3). Sarcomeres with a larger resting length show both an increase in absolute force and an increase in $[Ca^{2+}]_i$ sensitivity. These increases can be seen in both the experimental data and model simulations (Fig. 3.3 A and B, respectively). Our simulations model well the maximum absolute force for a 2.3 μm sarcomere, but the reduction in maximum force for shorter sarcomeres is not as large as the experimental data for Prabhakar *et al*. [64]. Figure 3.3 C and D show the normalized force-$[Ca^{2+}]_i$ relationship. The experimental

data for Prabhakar *et al*. [64] and Konhilas *et al*. [65], which are from skinned myocytes, show a lower $[Ca^{2+}]_i$ sensitivity than the model simulations. However, the $[Ca^{2+}]_i$ sensitivity in our model matches well the data for McCloskey *et al*. [66], which are from non-skinned myocytes. In addition, our model matches well the experimental increase in $[Ca^{2+}]_i$ sensitivity when sarcomere length increases. The ratio of half-activation $[Ca^{2+}]_i$ concentrations estimated from the experimental data by Prabhakar *et al*. [64] is equal to 1.31 when sarcomere length changes from 1.9 to 2.3 μm. The ratio estimated from the experimental data by Konhilas *et al*. [65] is equal to 1.29 when sarcomere length changes from 1.95 to 2.25 μm. Our simulations give the ratio 1.33 when sarcomere length changes from 1.9 to 2.3 μm, which is close to the experimental ratios (Fig. 3.3 C and D).

Activation of the β_1-adrenergic signaling system decreases $[Ca^{2+}]_i$ sensitivity of the active force. Experimental data for the normalized force-$[Ca^{2+}]_i$ relationship without and with activation with PKA (Fig. 3.4A) show this decrease in $[Ca^{2+}]_i$ sensitivity. The experimental ratio of the half-activation $[Ca^{2+}]_i$ values for the active force with and without application of PKA is estimated as 1.47±0.05 (mean±SE) based on the experimental data sets [15, 72, 88, 103, 104]. Experimental data were obtained for the sarcomere lengths ranging from 2.1 to 2.3 μm. Our corresponding simulated half-activation $[Ca^{2+}]_i$ ratios obtained upon stimulation with and without 10 μM isoproterenol are equal to 1.66, 1.51, and 1.36 for sarcomere lengths 1.9, 2.1, and 2.3 μm, respectively (Fig. 3.4B).

Our model was able to reproduce a second experimental protocol: stretch-activated force kinetics in response to a small (~1%) stretch of the sarcomere (Fig. 3.5). This protocol was designed to determine two critical rates, k_{rel} and k_{df}, that characterize contraction force [87]. The rate k_{rel} characterizes the rate of crossbridges detachment during phase 2 and the rate k_{df}

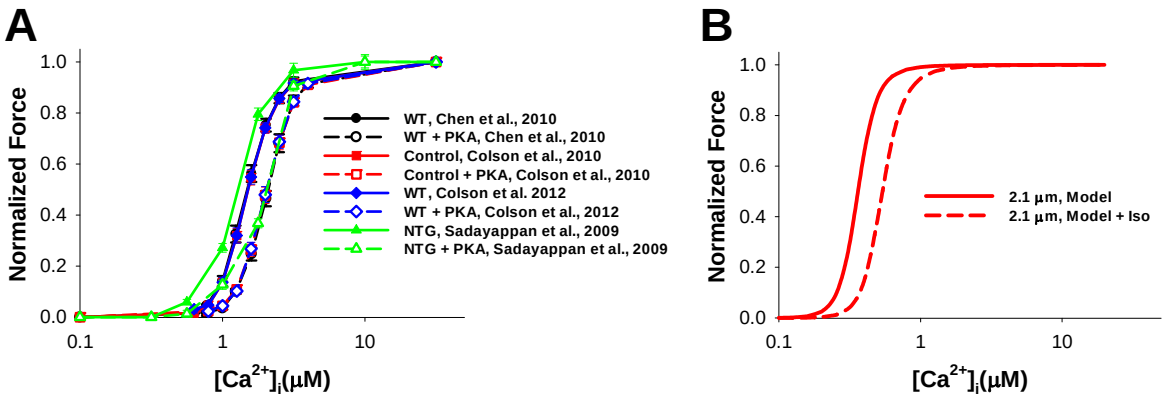

Figure 3.4 The effect of β_1-adrenergic stimulation on the normalized steady-state force-$[Ca^{2+}]_i$ relationship.

(A) Experimental data for controls are shown with solid lines and symbols. Experimental data using stimulation with PKA are shown with dashed lines and unfilled symbols [15, 88, 103, 104]. (B) Model simulations without and with β_1-adrenergic stimulation (10 μM isoproterenol) are shown with solid and dashed lines, respectively. The model replicates the decrease in calcium sensitivity, which results from β_1-adrenergic stimulation. Simulated sarcomere length is 2.1 μm.

represents the rate of the force development after the stretch (phase 3 in Fig. 3.5B) [87]. To simulate this experiment, we first applied a $[Ca^{2+}]_i$ to achieve about 50% of maximum active force. Then, at time moment 3000 ms, we stretched the sarcomere length by 1%, from 2.1 μm to 2.12 μm. To simulate the crossbridge detachment during abrupt stretch, we multiplied parameter g_{minxb} by the factor

$$1+1.4\exp[-(t-3000.0)(1+0.3(f_{TnI,p}^{cyt}-0.364))(1+1.0(f_{MyBPC,p}^{cyt}-0.575))/6.0].$$

This factor determines an abrupt increase in the g_{minxb} rate at t = 3000 ms that decreases exponentially in time with characteristic time constant 6.0 ms to ensure almost complete cross-bridges detachment within approximately 20 ms. In addition, this time constant is modulated by phosphorylation of TnI and MyBP-C, as it is observed experimentally.

As a result of this stretch, the force sharply increased (phase 1) and decreased (phase 2), and then redeveloped to a larger steady-state value (phase 3) (Fig. 3.5 A and B). This kind of behavior is also observed experimentally [87]. In the experiments, application of PKA resulted in

an increase of both k_{rel} and k_{df}. Our simulations were able to reproduce these changes (dashed lines in Fig. 3.5 A and B). Simulated and experimental values of k_{rel} and k_{df} without and with stimulation of the β_1-adrenergic signaling system are shown in Fig. 3.5 C and D. Our model reproduced well the rate of crossbridge detachment k_{rel} in stimulated and unstimulated cardiac cells (Fig. 3.5C), as well as the rate of force development k_{df} in the stimulated cell; however, the simulated value of k_{df} in the unstimulated cell was lower than the experimental value (Fig. 3.5D).

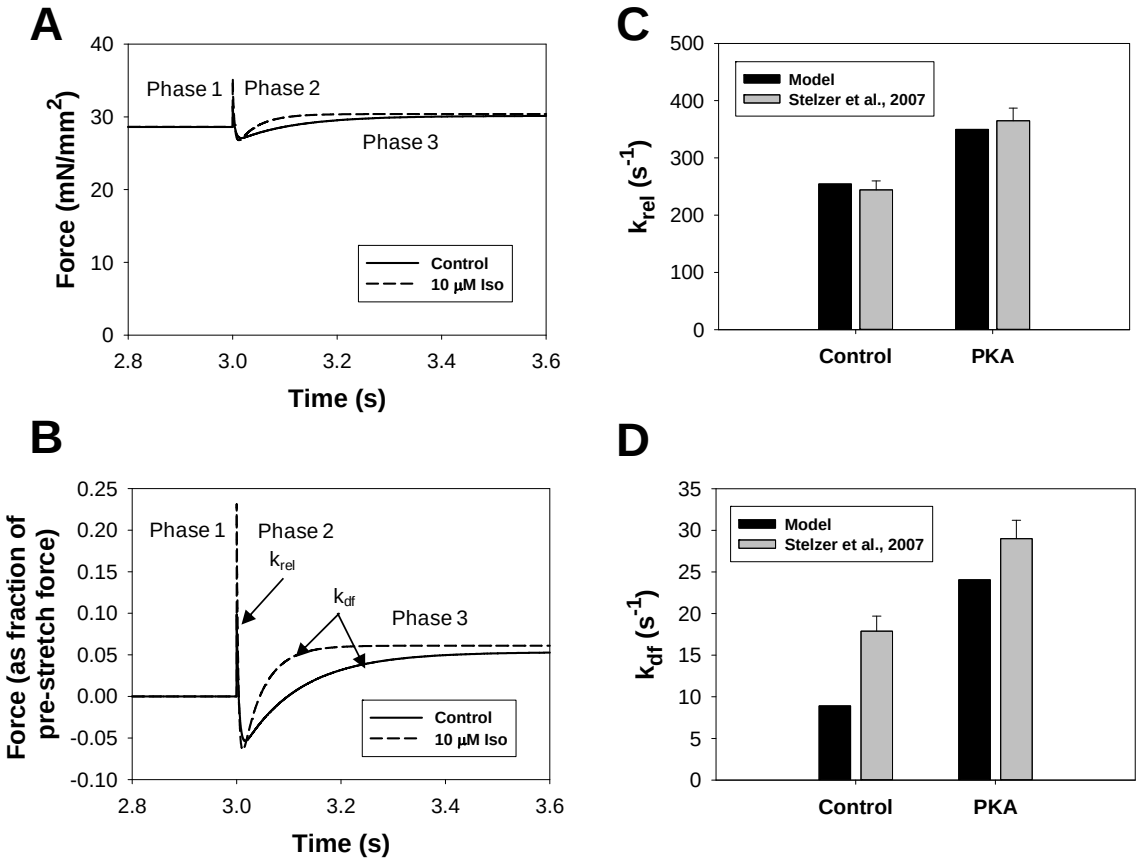

Figure 3.5 The stretch activation protocol.

In this protocol, contraction force was activated by 0.361 and 0.545 μM of $[Ca^{2+}]_i$ for control and 10 μM isoproterenol, respectively, which approximately corresponds to ~50% of the maximum active force. Then the sarcomere was stretched by 1% of its length from the 3rd to 5th seconds. (A) The simulated time courses of the absolute force without and with β_1-adrenergic stimulation are shown with solid and dashed lines, respectively. Initial sarcomere length is 2.1 μm. (B) Time behavior of the force as fraction of pre-stretched force. (C) The simulated (black bars) crossbridge release rate k_{rel} without (Control) and with (PKA) stimulation of β_1-adrenergic signaling system is compared to the experimental data Stelzer *et al*. [87] (gray bars). (D) The simulated (black bars) force development rate k_{df} without (Control) and with (PKA) stimulation of β_1-adrenergic signaling system is compared to the experimental data Stelzer *et al*. [87] (gray bars).

The third major experimental protocol we simulated with our model was a force-velocity protocol. In this protocol, the active force was first maximally activated with 2 μM of $[Ca^{2+}]_i$. At 1000 ms the $[Ca^{2+}]_i$ was changed to simulate an afterload ranging from 0.0 to 1.0 of the maximum force. The afterload force was increased from 0.0 to 1.0 of the maximum force in 0.1 steps during successive trials. The velocity of sarcomere shortening was determined on the interval from 1005 to 1020 ms, where the change in sarcomere length is approximately linear as a function of time. Figure 3.6 A and B show the changes in sarcomere length during the force-velocity protocol as a function of time for the afterload forces from 0.0 to 1.0 of the maximum force for control conditions (Fig. 3.6A) and after stimulation with 10 μM isoproterenol (Fig. 3.6B). It can be seen that isoproterenol accelerated sarcomere shortening at all values of afterload force. The comparison of the simulated and experimental sarcomere shortening velocity at different afterloads without and with stimulation of the β_1-adrenergic signaling system is shown in Fig. 3.6C. The simulated data fit well the experimental data obtained by Sadayappan *et al*. [88] for mouse ventricular myocytes. In addition, the model was able to reproduce the experimental data on the effects of PKA on the cardiac muscle power output defined as the product of the force and the sarcomere shortening velocity [88] (Fig. 3.6D).

Finally, we simulated ventricular myocyte behavior during a fourth major experimental protocol, one which determines the rate of force redevelopment, k_{tr}. For this purpose, the myocyte was activated with different concentrations of $[Ca^{2+}]_i$ from 0.1 to 8.0 μM. The cell was first held at a sarcomere length of 2.1 μm for 2000 ms. At time moment 2000 ms the sarcomere length was reduced to the steady-state sarcomere length for that $[Ca^{2+}]_i$ concentration. After 20 ms, the sarcomere was stretched back to 2.1 μm. The time course of force was then fitted with an exponential function to obtain k_{tr}. (The steady-state sarcomere length for each $[Ca^{2+}]_i$

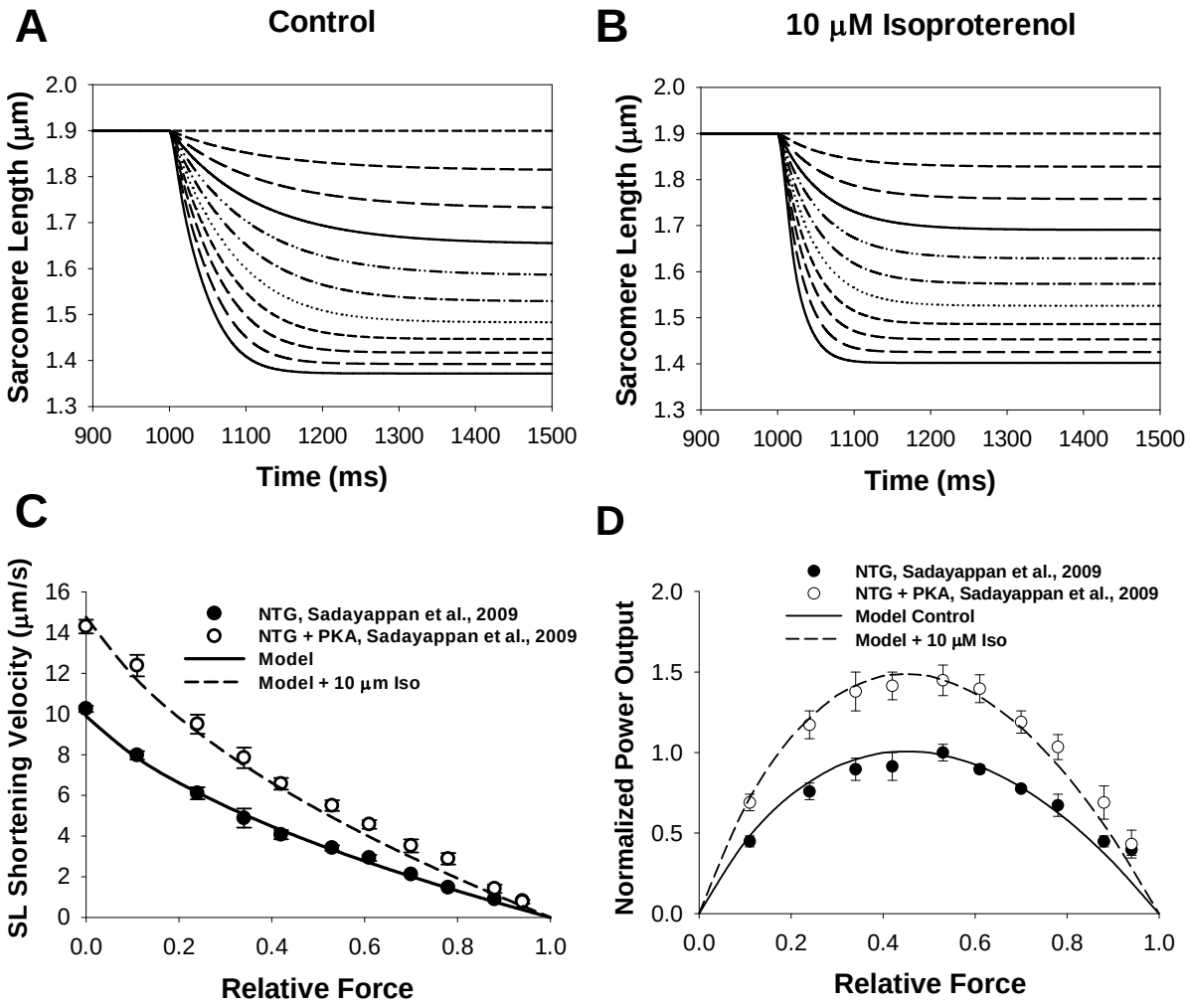

Figure 3.6 The force-velocity protocol.

The time courses of SL are shown during the force-velocity protocol without and with beta adrenergic stimulation (A and B, respectively). During this protocol, the active force was maximally activated with 2 μM of $[Ca^{2+}]_i$. The afterload force was changed from 0.0 to 1.0 of the maximum force in 0.1 steps at 1000 ms. The velocity of sarcomere shortening is determined on the interval from 1005 to 1020 ms, where the change in sarcomere length is approximately linear as a function of time. The force-velocity relationship (C) and power output (D) from the model simulations (shown by lines) are compared to data from Sadayappan *et al*. [88] (shown by symbols). Model simulations without and with β_1-adrenergic stimulation are shown in (C) and (D) by solid and dashed lines, respectively. Experimental data without and with β_1-adrenergic stimulation are shown by filled and unfilled symbols, respectively.

was obtained by a separate simulation of the model behavior for 4000 ms at that $[Ca^{2+}]_i$.) Figure 3.7 shows the absolute and normalized values of k_{tr} as functions of the relative force, which was determined by $[Ca^{2+}]_i$ concentration. Experimental data shows that k_{tr} increased with relative force up to a maximum value both without and with application of PKA. Application of PKA

increased the magnitudes of k_{tr} at all relative forces. Our simulations reproduced these dependencies in general. Simulations of k_{tr} without β_1-adrenergic stimulation demonstrated good agreement with the experimental data. However, our simulations with β_1-adrenergic stimulation by 10 μM isoproterenol showed somewhat higher values for k_{tr}.

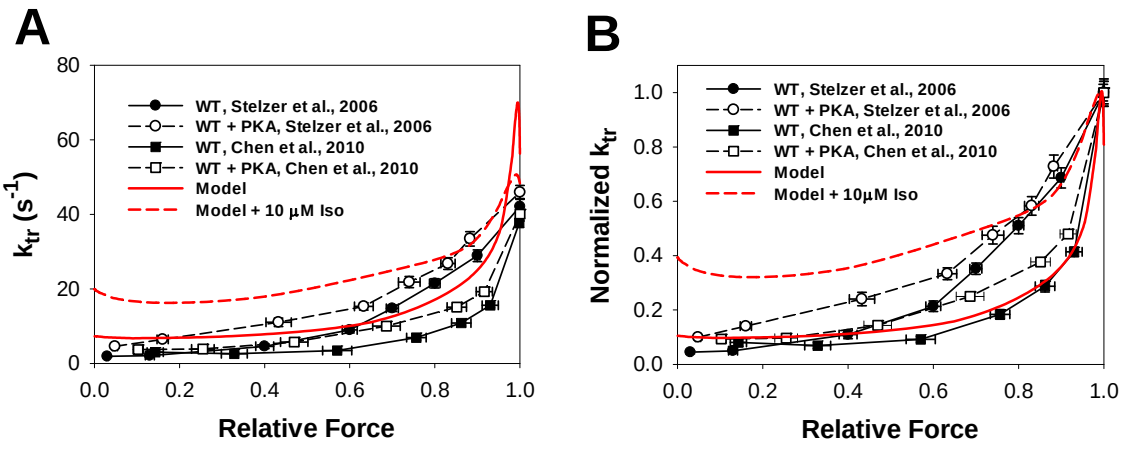

Figure 3.7 k_{tr} and normalized k_{tr} values as a function of relative force.

The k_{tr} and normalized k_{tr} values are shown as a function of relative force (A and B, respectively) without and with β_1-adrenergic stimulation (solid and dashed lines, respectively). The myocyte was activated with different concentrations of $[Ca^{2+}]_i$ from 0.1 to 8.0 μM. At time moment 2000 ms the sarcomere length was reduced from 2.1 μm to the steady-state value for a given $[Ca^{2+}]_i$ concentration for 20 ms and then stretched back to 2.1 μm. Time course of the force was fitted with an exponential function to obtain k_{tr}. Model simulations without and with stimulation with 10 μM isoproterenol are shown in red. Experimental data without and with PKA stimulation [15, 105] are shown in black with filled and unfilled symbols, respectively.

To investigate the effects of β_1-adrenergic stimulation on $[Ca^{2+}]_i$ transients, total contraction force, and sarcomere shortening, we simulated electrical stimulation of the ventricular myocyte model with I_{stim} = 80 pA/pF and τ_{stim} = 1.0 ms at 1 Hz without and with application of 1 μM isoproterenol (Fig. 3.8). Simulations showed a significant increase in the magnitude of $[Ca^{2+}]_i$ transients, total contraction force, and sarcomere shortening after stimulation of β_1-adrenoceptors (Fig. 3.8 A-C). In addition, they showed faster rates of activation and relaxation. We compared the increases of model cell activities stimulated at 0.5 Hz to experimental data obtained at stimulation frequencies ranging from 0.5 to 4.0 Hz (Fig. 3.8 D-F).

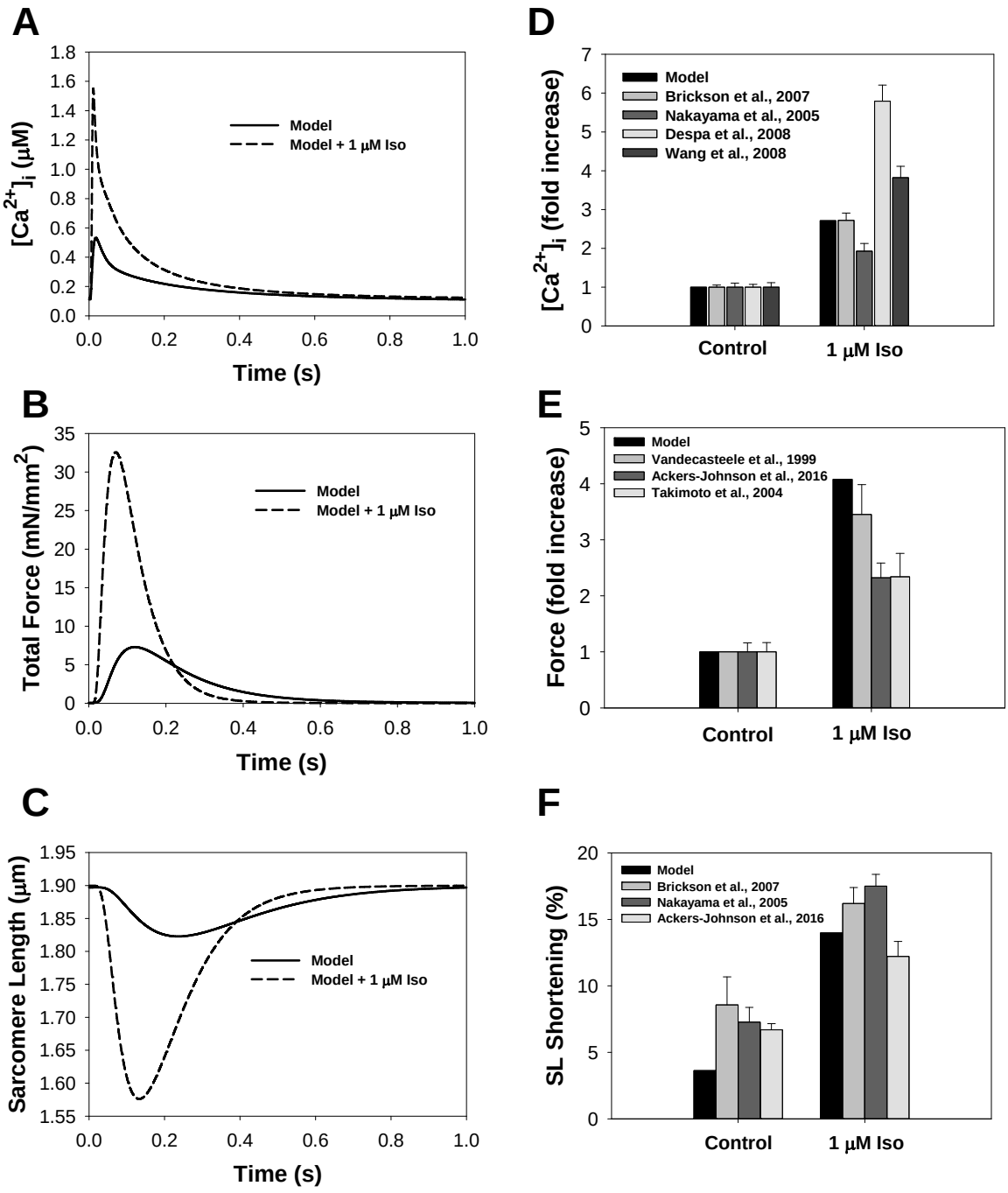

Figure 3.8 Time course of $[Ca^{2+}]_i$, contraction force, and sarcomere length.

The simulated time course of $[Ca^{2+}]_i$ (A), contraction force (B), and sarcomere length (C) without and with β_1-adrenergic stimulation by 1 μM isoproterenol are shown by solid and dashed lines, respectively. The simulated increases in peak $[Ca^{2+}]_i$ (D), peak force (E), and percentage shortening (F) resulting from β_1-adrenergic stimulation are compared to experimental data [89, 92, 94, 95, 102, 106, 107] without and with β_1-adrenergic stimulation. The values for $[Ca^{2+}]_i$ and force are normalized to control peak values. The model stimulation frequency for (A), (B), and (C) is 1 Hz. The model stimulation frequency for (D), (E), and (F) is 0.5 Hz. Experimental measurements were obtained at 0.5 Hz for Brickson *et al*. [102] and Nakayama *et al*. [92]; 1 Hz for Wang *et al*. [107]; 2 Hz for Despa *et al*. [106] and Ackers-Johnson *et al*. [89]; and 4 Hz for Vandecasteele *et al*. [95] and Takimoto *et al*. [94].

Upon activation of the β_1-adrenergic signaling system, simulated $[Ca^{2+}]_i$ transients increased by 2.7 fold, while the increases in the experimental data ranged from 1.9 to 5.8 fold (Fig. 3.8D). Similarly, the simulated increase in the total force was 4.1, which is similar to the experimental data, which ranged from 2.3 to 3.5 fold (Fig. 3.8E). Finally, our model showed an increase in fractional sarcomere shortening from 3.6% to 14.0% before and after application of 1 μM isoproterenol, respectively. Simulation data with β_1-adrenergic stimulation is in line with the experimental data (ranging from 12.2% to 17.5%), but sarcomere shortening for control is somewhat smaller than in this set of experimental data (6.7% to 8.6%). Better agreement was obtained with another set of experimental data for control (ranging from 2.3% to 5.5% at 0.5 Hz, Fig. 3.9B), but those experiments did not include measurements of the effects of β_1-adrenergic stimulation.

Our model reproduced quite well the frequency dependencies of the peak $[Ca^{2+}]_i$ transients, peak total force, and sarcomere shortening (Fig. 3.9). Both simulations and experimental data showed bi-phasic frequency dependence of $[Ca^{2+}]_i$ transients (Fig. 3.9A). Simulations of the peak force demonstrated biphasic behavior, as well; however, some experimental data showed bi-phasic frequency dependence with saturation in contraction force at frequencies from 2 to 4 Hz (Fig. 3.9B). Finally, our simulations of sarcomere shortening showed tri-phasic behavior as stimulation frequency increased from 0.25 to 4.0 Hz (Fig. 3.9C). These simulation results are close to the experimental data in terms of shortening magnitude, but some experimental data demonstrated only bi-phasic dependencies.

Finally, we simulated the behavior of peak $[Ca^{2+}]_i$ transients, peak total force, and sarcomere shortening as functions of isoproterenol (Fig. 3.10). Our simulations showed a somewhat larger increase in peak $[Ca^{2+}]_i$ transients with isoproterenol concentration than the

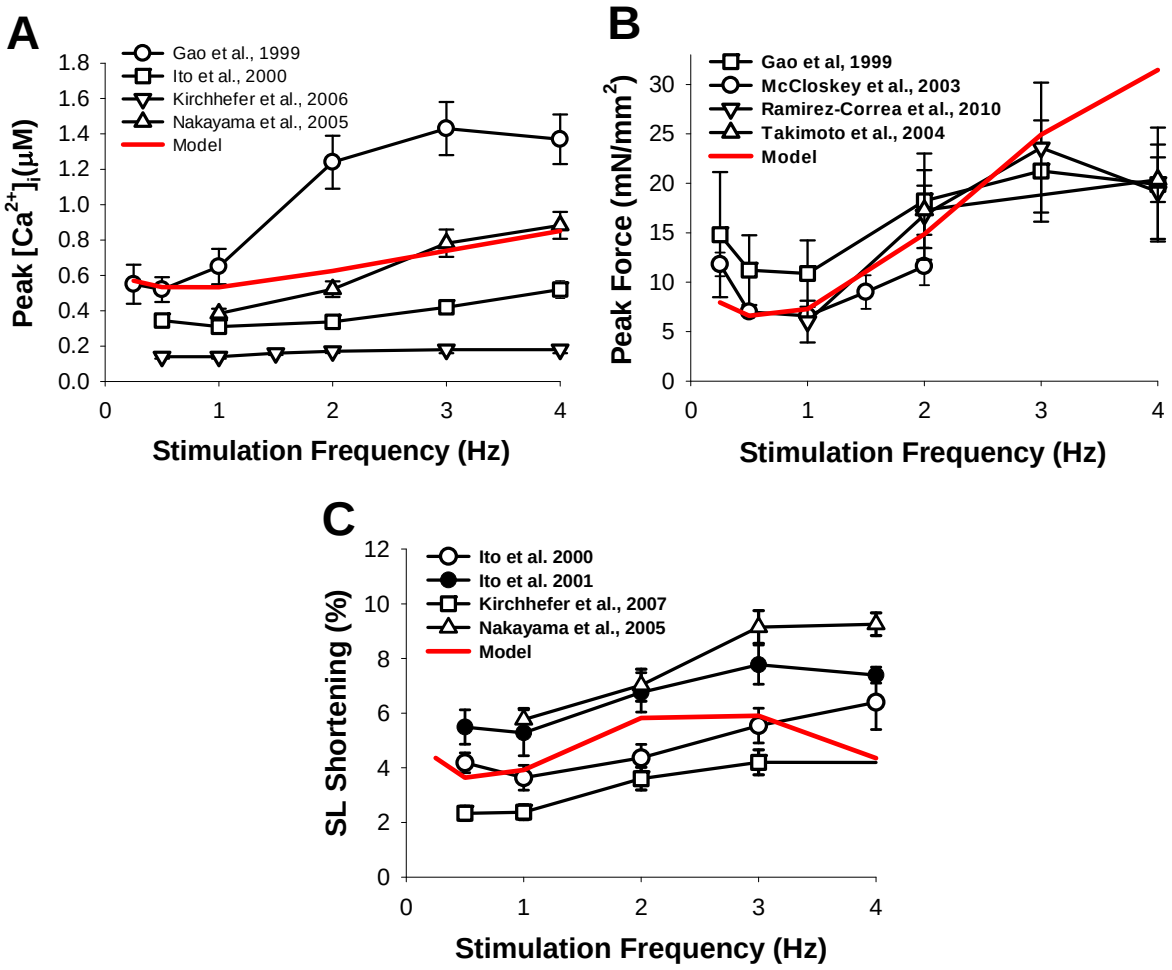

Figure 3.9 Frequency dependence of peak $[Ca^{2+}]_i$, peak force, and cell shortening.

The simulated frequency dependence of peak $[Ca^{2+}]_i$ (A), peak force (B), and cell shortening (C) (shown in red) are compared to experimental data [67, 70, 75, 76, 81, 90-92, 94] (shown in black). The initial SL for the model simulation is 1.9 μm.

experimental values (Fig. 3.10A). However, we have only one experiment available in which isoproterenol dependence of peak $[Ca^{2+}]_i$ transients was measured; other experimental data obtained specifically at 1 μM isoproterenol shows better agreement with our simulations (Fig. 3.8D). Our simulation of the isoproterenol dependence of peak force is also quite close to the experimental data (Fig. 3.10B), taking into account the accuracy of the force measurements. Simulated sarcomere shortening is within the range of the experimental data (Fig. 3.10C).

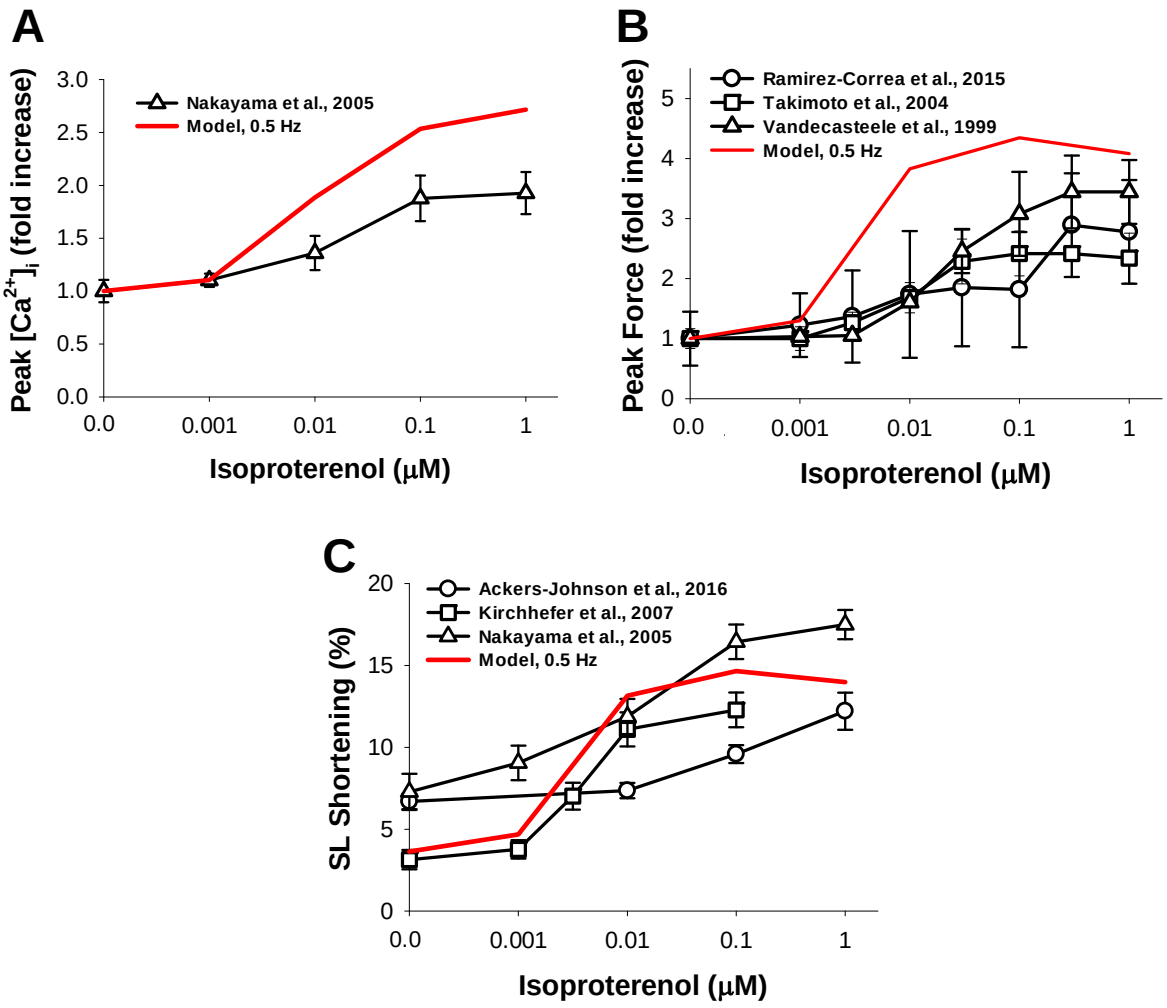

Figure 3.10 Isoproterenol dependence of peak $[Ca^{2+}]_i$, peak force, and cell shortening.

The simulated isoproterenol dependence of peak $[Ca^{2+}]_i$ (A), peak force (B), and cell shortening (C) (shown in red) are compared to experimental data [89, 91-95] (shown in black). The values for peak $[Ca^{2+}]_i$ (A) and peak force (B) are normalized to control values. The initial SL for the model simulation is 1.9 μm with a stimulation frequency of 0.5 Hz. Experimental measurements were obtained at 0.5 Hz for Nakayama *et al*. [92], Kirchhefer *et al*. [91] and Ramirez-Correa *et al*. [93]; 2 Hz for Ackers-Johnson *et al*. [89]; and 4 Hz for Takimoto *et al*. [94] and Vandecasteele *et al*. [95].

Thus, in this chapter, we developed a new mathematical model of the β_1-adrenergic regulation of mouse ventricular myocyte contraction that was able to simulate major experimental protocols on measurements of steady-state force-calcium relationships, crossbridge release rates (k_{rel}) and force development (k_{df}), force-velocity relationship, and force

redevelopment (k_{tr}). It also reproduced quite well frequency and isoproterenol dependencies for $[Ca^{2+}]_i$ transients, total contraction force, and sarcomere shortening.

3.4 Discussion

3.4.1 Recent progress in mathematical modeling of cardiac myocyte contraction

Mathematical modeling of cardiac myocyte contraction has a long history. Multiple cardiac contraction models have been developed since the early work of Huxley [40]. The most popular models were developed by Negroni and Lascano [41], Rice *et al*. [42], and Rice *et al*. [43]. Many of these are implemented in cellular contraction models that include a description of action potential and Ca^{2+} dynamics.

The 1999 Rice *et al*. model [42] was implemented in several cardiac cellular models, including one for guinea pig ventricular myocytes [58] and one for mouse ventricular myocytes [44]. The 2000 Rice *et al*. model [58] focused mostly on modeling short-term interval-force relations, which was found to result from the interplay of the ryanodine receptor adaptation and the SR Ca^{2+} load, with additional contributions of the membrane currents and myofilament activation. Mullins and Bondarenko [44] adopted Rice *et al*. [42] Model 4 to simulate mouse ventricular myocyte contraction with the inclusion of sarcomere shortening. They were able to reproduce steady-state force-Ca^{2+} relationships, dependence of contraction force on the sarcomere length, time course of contraction force and myocyte shortening, and frequency dependence of contraction force and myocyte shortening. The 2008 Rice *et al*. model [43] was implemented in rat and rabbit ventricular myocyte models, and in a canine ventricular myocyte model by Campbell *et al*. [108].

Our new mathematical model of mouse ventricular myocyte contraction synthesizes several previously developed models of mouse ventricular myocytes [16, 96] and cardiac

myocyte contraction [42-44]. We used a recent mouse ventricular myocyte model that includes descriptions of action potential, Ca^{2+} dynamics, and the β_1-adrenegic signaling system [16, 96] to incorporate a modified three-crossbridge model from Rice *et al*. [42], and passive and flexible forces from Rice *et al*. [43]. In this paper, we also proposed a new description of viscous force that includes both linear and nonlinear viscosity. The resulting model reproduced quantitatively major experimental data on ventricular myocyte contraction obtained from mice.

3.4.2 The effects of β_1-adrenergic stimulation on cardiac cell contraction

Experimental data demonstrates that activation of the β_1-adrenergic signaling system results in stronger active contraction force, decrease in Ca^{2+}-sensitivity of the steady-state force-Ca^{2+} relationship, and accelerated force development and relaxation [89, 103]. These effects are mostly due to phosphorylation of troponin I and myosin binding protein C, which affect Ca^{2+} sensitivity of the contraction force, crossbridge attachment and detachment rates, viscosity, rate of force redevelopment, and the power of cardiac output [88, 105].

Previously, a mathematical model of the β_1-adrenergic regulation of the rabbit ventricular myocyte contraction was developed [47], which was based on the contraction model of Negroni and Lascano [48] and the Soltis-Saucerman model of β_1-adrenergic signaling [49]. The model described the effects of β_1-adrenergic stimulation on myocyte contraction mostly qualitatively, to demonstrate the direction of its effects rather than their magnitude. In addition, the simulation data were compared not only to those obtained from rabbit cardiac cells, but also from ventricular myocytes of other species [47].

Our mathematical model of the β_1-adrenergic regulation of the mouse ventricular myocyte contraction was developed based on data obtained from a single species (mouse). We simulated major experimental contraction protocols for measurements of steady-state force-

calcium relationships, crossbridge release rate (k_{rel}) and force development rate (k_{df}), force-velocity relationship, and force redevelopment rate (k_{tr}). Most of the simulation data compares quite well with the experiments (e.g., steady-state force-Ca^{2+} relationship, force-velocity relationship, power output as a function of the relative force). Our model implements the effects of β_1-adrenergic signaling through the phosphorylation of TnI and MyBP-C, and their effects on the transition rates between tropomyosin states and on viscous force. These modulations allowed for the simulation of all experimental protocols described in this study.

3.4.3 Model limitations

Although our mathematical model of the β_1-adrenergic regulation of mouse ventricular myocyte contraction describes well a number of experimental protocols, it has several limitations. One limitation is that we used the model of an epicardial ventricular cell, however, the experimental data used for the model development does not discriminate between the epicardial and endocardial cell types. We also used data obtained from different laboratories which varied significantly in the magnitude of force, Ca^{2+} sensitivity, and sensitivity to isoproterenol. Lastly, in our model we only implemented the β_1-adrenergic signaling system, which can potentially interact with β_2-adrenergic and CaMKII-mediated signaling systems.

For supplemental information, see the model summary in Appendix B.

4 CONCLUSIONS

Thus, in this dissertation, we developed two mathematical models of mouse ventricular myocyte contraction. The first model was based on a comprehensive model of the action potential and Ca^{2+} dynamics in mouse ventricular myocytes that is not modulated by the β_1-adrenergic signaling system. In the model, we used a simplified description of the contraction force and sarcomere shortening. The resulting model fit well experimental data on steady-state force-calcium relationships, dependence of the contraction force on the sarcomere length, time course of the contraction force and myocyte shortening, frequency dependence of the contraction force and cellular contraction, and experimentally measured derivatives of the myocyte length variation. We emphasized the importance of the inclusion of variable sarcomere length into a model for ventricular myocyte contraction, and we investigated the differences in contraction force and cell shortening for epicardial and endocardial ventricular myocytes.

The second, more comprehensive mathematical model of the mouse ventricular myocyte contraction included regulation of the contraction by the β_1-adrenergic signaling system through phosphorylation of troponin I and myosin binding protein C. The model was based on experimental data obtained from mice and described well major experimental protocols on ventricular contraction (steady-state force-Ca^{2+} relationship, stretch-activated force development, force-velocity relationship, power output as a function of relative force, the rate of force redevelopment as a function of relative force, the effects of isoproterenol on the magnitude of contraction force and sarcomere shortening, and frequency and isoproterenol-dependence of contraction force and sarcomere shortening). The model can be used as a template for mathematical models of β_1-adrenergic regulation of contraction in other cell types and cells from other species, as well as for the interpretation of experimental data obtained from mice.

REFERENCES

1. Kochanek KD, Murphy SL, Xu J, and Tejada-Vera B. Deaths: Final Data for 2014. *Natl Vital Stat Rep*, 65:1-122, 2016.

2. Bers DM, *Excitation-contraction coupling and cardiac contractile force*. 2nd ed. Developments in cardiovascular medicine. 2001, Dordrecht ; Boston: Kluwer Academic Publishers.

3. England PJ. Cardiac function and phosphorylation of contractile proteins. *Philosophical Transactions of the Royal Society B: Biological Sciences*, 302:83-90, 1983.

4. Alberts B, *Molecular biology of the cell*. 5th ed. 2008, New York: Garland Science.

5. Li L, Desantiago J, Chu G, Kranias EG, and Bers DM. Phosphorylation of phospholamban and troponin I in beta-adrenergic-induced acceleration of cardiac relaxation. *Am J Physiol Heart Circ Physiol*, 278:H769-779, 2000.

6. Karczewski P, Bartel S, and Krause EG. Differential sensitivity to isoprenaline of troponin I and phospholamban phosphorylation in isolated rat hearts. *Biochem J*, 266:115-122, 1990.

7. Robertson SP, Johnson JD, Holroyde MJ, Kranias EG, Potter JD, and Solaro RJ. The effect of troponin I phosphorylation on the Ca2+-binding properties of the Ca2+-regulatory site of bovine cardiac troponin. *J Biol Chem*, 257:260-263, 1982.

8. Kentish JC, McCloskey DT, Layland J, Palmer S, Leiden JM, Martin AF, and Solaro RJ. Phosphorylation of troponin I by protein kinase A accelerates relaxation and crossbridge cycle kinetics in mouse ventricular muscle. *Circ Res*, 88:1059-1065, 2001.

9. Yasuda S, Coutu P, Sadayappan S, Robbins J, and Metzger JM. Cardiac transgenic and gene transfer strategies converge to support an important role for troponin I in regulating relaxation in cardiac myocytes. *Circ Res*, 101:377-386, 2007.

10. Barefield D and Sadayappan S. Phosphorylation and function of cardiac myosin binding protein-C in health and disease. *J Mol Cell Cardiol*, 48:866-875, 2010.

11. Gruen M, Prinz H, and Gautel M. cAPK-phosphorylation controls the interaction of the regulatory domain of cardiac myosin binding protein C with myosin-S2 in an on-off fashion. *FEBS Lett*, 453:254-259, 1999.

12. Sadayappan S, Gulick J, Osinska H, Martin LA, Hahn HS, Dorn GW, 2nd, Klevitsky R, Seidman CE, Seidman JG, and Robbins J. Cardiac myosin-binding protein-C phosphorylation and cardiac function. *Circ Res*, 97:1156-1163, 2005.

13. Decker RS, Decker ML, Kulikovskaya I, Nakamura S, Lee DC, Harris K, Klocke FJ, and Winegrad S. Myosin-binding protein C phosphorylation, myofibril structure, and contractile function during low-flow ischemia. *Circulation*, 111:906-912, 2005.

14. Tong CW, Stelzer JE, Greaser ML, Powers PA, and Moss RL. Acceleration of crossbridge kinetics by protein kinase A phosphorylation of cardiac myosin binding protein C modulates cardiac function. *Circ Res*, 103:974-982, 2008.

15. Chen PP, Patel JR, Rybakova IN, Walker JW, and Moss RL. Protein kinase A-induced myofilament desensitization to Ca(2+) as a result of phosphorylation of cardiac myosin-binding protein C. *J Gen Physiol*, 136:615-627, 2010.

16. Bondarenko VE. A compartmentalized mathematical model of the beta1-adrenergic signaling system in mouse ventricular myocytes. *PLoS One*, 9:e89113, 2014.

17. Hodgkin AL and Huxley AF. A quantitative description of membrane current and its application to conduction and excitation in nerve. *J Physiol*, 117:500-544, 1952.

18. Noble D. A modification of the Hodgkin--Huxley equations applicable to Purkinje fibre action and pace-maker potentials. *J Physiol*, 160:317-352, 1962.

19. Winslow RL, Cortassa S, O'Rourke B, Hashambhoy YL, Rice JJ, and Greenstein JL. Integrative modeling of the cardiac ventricular myocyte. *Wiley Interdiscip Rev Syst Biol Med*, 3:392-413, 2011.

20. McAllister RE, Noble D, and Tsien RW. Reconstruction of the electrical activity of cardiac Purkinje fibres. *J Physiol*, 251:1-59, 1975.

21. DiFrancesco D and Noble D. A model of cardiac electrical activity incorporating ionic pumps and concentration changes. *Philos Trans R Soc Lond B Biol Sci*, 307:353-398, 1985.

22. Demir SS. Computational modeling of cardiac ventricular action potentials in rat and mouse: review. *Jpn J Physiol*, 54:523-530, 2004.

23. Beeler GW and Reuter H. Reconstruction of the action potential of ventricular myocardial fibres. *J Physiol*, 268:177-210, 1977.

24. Luo CH and Rudy Y. A dynamic model of the cardiac ventricular action potential. I. Simulations of ionic currents and concentration changes. *Circ Res*, 74:1071-1096, 1994.

25. Luo CH and Rudy Y. A dynamic model of the cardiac ventricular action potential. II. Afterdepolarizations, triggered activity, and potentiation. *Circ Res*, 74:1097-1113, 1994.

26. Luo CH and Rudy Y. A model of the ventricular cardiac action potential. Depolarization, repolarization, and their interaction. *Circ Res*, 68:1501-1526, 1991.

27. Jafri MS, Rice JJ, and Winslow RL. Cardiac Ca2+ dynamics: the roles of ryanodine receptor adaptation and sarcoplasmic reticulum load. *Biophys J*, 74:1149-1168, 1998.

28. Winslow RL, Rice J, Jafri S, Marban E, and O'Rourke B. Mechanisms of altered excitation-contraction coupling in canine tachycardia-induced heart failure, II: model studies. *Circ Res*, 84:571-586, 1999.

29. Bondarenko VE, Szigeti GP, Bett GC, Kim SJ, and Rasmusson RL. Computer model of action potential of mouse ventricular myocytes. *Am J Physiol Heart Circ Physiol*, 287:H1378-1403, 2004.

30. Saucerman JJ, Brunton LL, Michailova AP, and McCulloch AD. Modeling beta-adrenergic control of cardiac myocyte contractility in silico. *J Biol Chem*, 278:47997-48003, 2003.

31. Saucerman JJ and McCulloch AD. Mechanistic systems models of cell signaling networks: a case study of myocyte adrenergic regulation. *Prog Biophys Mol Biol*, 85:261-278, 2004.

32. Kuzumoto M, Takeuchi A, Nakai H, Oka C, Noma A, and Matsuoka S. Simulation analysis of intracellular Na+ and Cl- homeostasis during beta 1-adrenergic stimulation of cardiac myocyte. *Prog Biophys Mol Biol*, 96:171-186, 2008.

33. Yang JH and Saucerman JJ. Phospholemman is a negative feed-forward regulator of Ca2+ in beta-adrenergic signaling, accelerating beta-adrenergic inotropy. *J Mol Cell Cardiol*, 52:1048-1055, 2012.

34. Heijman J, Volders PG, Westra RL, and Rudy Y. Local control of beta-adrenergic stimulation: Effects on ventricular myocyte electrophysiology and Ca(2+)-transient. *J Mol Cell Cardiol*, 50:863-871, 2011.

35. Balijepalli RC, Foell JD, Hall DD, Hell JW, and Kamp TJ. Localization of cardiac L-type Ca(2+) channels to a caveolar macromolecular signaling complex is required for beta(2)-adrenergic regulation. *Proc Natl Acad Sci U S A*, 103:7500-7505, 2006.

36. Best JM and Kamp TJ. Different subcellular populations of L-type Ca2+ channels exhibit unique regulation and functional roles in cardiomyocytes. *J Mol Cell Cardiol*, 52:376-387, 2012.

37. Rybin VO, Xu X, Lisanti MP, and Steinberg SF. Differential targeting of beta -adrenergic receptor subtypes and adenylyl cyclase to cardiomyocyte caveolae. A mechanism to functionally regulate the cAMP signaling pathway. *J Biol Chem*, 275:41447-41457, 2000.

38. Scriven DR, Asghari P, Schulson MN, and Moore ED. Analysis of Cav1.2 and ryanodine receptor clusters in rat ventricular myocytes. *Biophys J*, 99:3923-3929, 2010.

39. Rozier K and Bondarenko VE. Distinct physiological effects of beta1- and beta2-adrenoceptors in mouse ventricular myocytes: Insights from a compartmentalized mathematical model. *Am J Physiol Cell Physiol*:ajpcell 00273 02016, 2017.

40. Huxley AF. Muscle structure and theories of contraction. *Prog Biophys Biophys Chem*, 7:255-318, 1957.

41. Negroni JA and Lascano EC. A cardiac muscle model relating sarcomere dynamics to calcium kinetics. *J Mol Cell Cardiol*, 28:915-929, 1996.

42. Rice JJ, Winslow RL, and Hunter WC. Comparison of putative cooperative mechanisms in cardiac muscle: length dependence and dynamic responses. *Am J Physiol*, 276:H1734-1754, 1999.

43. Rice JJ, Wang F, Bers DM, and de Tombe PP. Approximate model of cooperative activation and crossbridge cycling in cardiac muscle using ordinary differential equations. *Biophys J*, 95:2368-2390, 2008.

44. Mullins PD and Bondarenko VE. A mathematical model of the mouse ventricular myocyte contraction. *PLoS One*, 8:e63141, 2013.

45. Land S, Louch WE, Niederer SA, Aronsen JM, Christensen G, Sjaastad I, Sejersted OM, and Smith NP. Beta-adrenergic stimulation maintains cardiac function in Serca2 knockout mice. *Biophys J*, 104:1349-1356, 2013.

46. Land S, Niederer SA, Aronsen JM, Espe EK, Zhang L, Louch WE, Sjaastad I, Sejersted OM, and Smith NP. An analysis of deformation-dependent electromechanical coupling in the mouse heart. *J Physiol*, 590:4553-4569, 2012.

47. Negroni JA, Morotti S, Lascano EC, Gomes AV, Grandi E, Puglisi JL, and Bers DM. beta-adrenergic effects on cardiac myofilaments and contraction in an integrated rabbit ventricular myocyte model. *J Mol Cell Cardiol*, 81:162-175, 2015.

48. Negroni JA and Lascano EC. Simulation of steady state and transient cardiac muscle response experiments with a Huxley-based contraction model. *J Mol Cell Cardiol*, 45:300-312, 2008.

49. Soltis AR and Saucerman JJ. Synergy between CaMKII substrates and beta-adrenergic signaling in regulation of cardiac myocyte Ca(2+) handling. *Biophys J*, 99:2038-2047, 2010.

50. Splawski I, Timothy KW, Sharpe LM, Decher N, Kumar P, Bloise R, Napolitano C, Schwartz PJ, Joseph RM, Condouris K, Tager-Flusberg H, Priori SG, Sanguinetti MC, and Keating MT. Ca(V)1.2 calcium channel dysfunction causes a multisystem disorder including arrhythmia and autism. *Cell*, 119:19-31, 2004.

51. Bader PL, Faizi M, Kim LH, Owen SF, Tadross MR, Alfa RW, Bett GC, Tsien RW, Rasmusson RL, and Shamloo M. Mouse model of Timothy syndrome recapitulates triad of autistic traits. *Proc Natl Acad Sci U S A*, 108:15432-15437, 2011.

52. Orchard CH, McCall E, Kirby MS, and Boyett MR. Mechanical alternans during acidosis in ferret heart muscle. *Circ Res*, 68:69-76, 1991.

53. London B, Baker LC, Petkova-Kirova P, Nerbonne JM, Choi BR, and Salama G. Dispersion of repolarization and refractoriness are determinants of arrhythmia phenotype in transgenic mice with long QT. *J Physiol*, 578:115-129, 2007.

54. Fox JJ, McHarg JL, and Gilmour RF, Jr. Ionic mechanism of electrical alternans. *Am J Physiol Heart Circ Physiol*, 282:H516-530, 2002.

55. Valverde CA, Mundina-Weilenmann C, Reyes M, Kranias EG, Escobar AL, and Mattiazzi A. Phospholamban phosphorylation sites enhance the recovery of intracellular Ca2+ after perfusion arrest in isolated, perfused mouse heart. *Cardiovasc Res*, 70:335-345, 2006.

56. Keener JP and Sneyd J, *Mathematical physiology II. System Physiology*. 2nd ed. Interdisciplinary applied mathematics. 2009, New York, NY: Springer.

57. Trayanova NA and Rice JJ. Cardiac electromechanical models: from cell to organ. *Front Physiol*, 2:43, 2011.

58. Rice JJ, Jafri MS, and Winslow RL. Modeling short-term interval-force relations in cardiac muscle. *Am J Physiol Heart Circ Physiol*, 278:H913-931, 2000.

59. Matsuoka S, Sarai N, Jo H, and Noma A. Simulation of ATP metabolism in cardiac excitation-contraction coupling. *Prog Biophys Mol Biol*, 85:279-299, 2004.

60. Cortassa S, Aon MA, O'Rourke B, Jacques R, Tseng HJ, Marban E, and Winslow RL. A computational model integrating electrophysiology, contraction, and mitochondrial bioenergetics in the ventricular myocyte. *Biophys J*, 91:1564-1589, 2006.

61. Petkova-Kirova PS, London B, Salama G, Rasmusson RL, and Bondarenko VE. Mathematical modeling mechanisms of arrhythmias in transgenic mouse heart overexpressing TNF-alpha. *Am J Physiol Heart Circ Physiol*, 302:H934-952, 2012.

62. Bondarenko VE and Rasmusson RL. Simulations of propagated mouse ventricular action potentials: effects of molecular heterogeneity. *Am J Physiol Heart Circ Physiol*, 293:H1816-1832, 2007.

63. Bondarenko VE and Rasmusson RL. Transmural heterogeneity of repolarization and Ca2+ handling in a model of mouse ventricular tissue. *Am J Physiol Heart Circ Physiol*, 299:H454-469, 2010.

64. Prabhakar R, Boivin GP, Grupp IL, Hoit B, Arteaga G, Solaro RJ, and Wieczorek DF. A familial hypertrophic cardiomyopathy alpha-tropomyosin mutation causes severe cardiac hypertrophy and death in mice. *J Mol Cell Cardiol*, 33:1815-1828, 2001.

65. Konhilas JP, Irving TC, Wolska BM, Jweied EE, Martin AF, Solaro RJ, and de Tombe PP. Troponin I in the murine myocardium: influence on length-dependent activation and interfilament spacing. *J Physiol*, 547:951-961, 2003.

66. McCloskey DT, Turcato S, Wang GY, Turnbull L, Zhu BQ, Bambino T, Nguyen AP, Lovett DH, Nissenson RA, Karliner JS, and Baker AJ. Expression of a Gi-coupled receptor in the heart causes impaired Ca2+ handling, myofilament injury, and dilated cardiomyopathy. *Am J Physiol Heart Circ Physiol*, 294:H205-212, 2008.

67. Gao WD, Perez NG, Seidman CE, Seidman JG, and Marban E. Altered cardiac excitation-contraction coupling in mutant mice with familial hypertrophic cardiomyopathy. *J Clin Invest*, 103:661-666, 1999.

68. Kirchhefer U, Neumann J, Bers D, Buchwalow I, Fabritz L, Hanske G, Justus I, Riemann B, Schmitz W, and Jones L. Impaired relaxation in transgenic mice overexpressing junctin. *Cardiovascular Research*, 59:369-379, 2003.

69. Kogler H, Soergel DG, Murphy AM, and Marban E. Maintained contractile reserve in a transgenic mouse model of myocardial stunning. *Am J Physiol Heart Circ Physiol*, 280:H2623-2630, 2001.

70. McCloskey DT, Turnbull L, Swigart P, O'Connell TD, Simpson PC, and Baker AJ. Abnormal myocardial contraction in alpha(1A)- and alpha(1B)-adrenoceptor double-knockout mice. *J Mol Cell Cardiol*, 35:1207-1216, 2003.

71. Stuyvers BD, McCulloch AD, Guo J, Duff HJ, and ter Keurs HEDJ. Effect of stimulation rate, sarcomere length and Ca2+on force generation by mouse cardiac muscle. *The Journal of Physiology*, 544:817-830, 2002.

72. Fentzke RC, Buck SH, Patel JR, Lin H, Wolska BM, Stojanovic MO, Martin AF, Solaro RJ, Moss RL, and Leiden JM. Impaired cardiomyocyte relaxation and diastolic function in transgenic mice expressing slow skeletal troponin I in the heart. *J Physiol*, 517 (Pt 1):143-157, 1999.

73. Huang L, Wolska BM, Montgomery DE, Burkart EM, Buttrick PM, and Solaro RJ. Increased contractility and altered Ca^{2+} transients of mouse heart myocytes conditionally expressing PKCbeta. *Am J Physiol Cell Physiol*, 280:C1114-1120, 2001.

74. Jones LR, Suzuki YJ, Wang W, Kobayashi YM, Ramesh V, Franzini-Armstrong C, Cleemann L, and Morad M. Regulation of Ca2+ signaling in transgenic mouse cardiac myocytes overexpressing calsequestrin. *J Clin Invest*, 101:1385-1393, 1998.

75. Ito K, Yan X, Tajima M, Su Z, Barry WH, and Lorell BH. Contractile reserve and intracellular calcium regulation in mouse myocytes from normal and hypertrophied failing hearts. *Circ Res*, 87:588-595, 2000.

76. Ito K, Yan X, Feng X, Manning WJ, Dillmann WH, and Lorell BH. Transgenic expression of sarcoplasmic reticulum Ca^{2+} atpase modifies the transition from hypertrophy to early heart failure. *Circ Res*, 89:422-429, 2001.

77. Dilly KW, Rossow CF, Votaw VS, Meabon JS, Cabarrus JL, and Santana LF. Mechanisms underlying variations in excitation-contraction coupling across the mouse left ventricular free wall. *J Physiol*, 572:227-241, 2006.

78. Kushnir A, Shan J, Betzenhauser MJ, Reiken S, and Marks AR. Role of CaMKIIdelta phosphorylation of the cardiac ryanodine receptor in the force frequency relationship and heart failure. *Proc Natl Acad Sci U S A*, 107:10274-10279, 2010.

79. Flagg TP, Cazorla O, Remedi MS, Haim TE, Tones MA, Bahinski A, Numann RE, Kovacs A, Schaffer JE, Nichols CG, and Nerbonne JM. Ca2+-independent alterations in diastolic sarcomere length and relaxation kinetics in a mouse model of lipotoxic diabetic cardiomyopathy. *Circ Res*, 104:95-103, 2009.

80. Chu G, Carr AN, Young KB, Lester JW, Yatani A, Sanbe A, Colbert MC, Schwartz SM, Frank KF, Lampe PD, Robbins J, Molkentin JD, and Kranias EG. Enhanced myocyte contractility and Ca^{2+} handling in a calcineurin transgenic model of heart failure. *Cardiovasc Res*, 54:105-116, 2002.

81. Ramirez-Correa GA, Cortassa S, Stanley B, Gao WD, and Murphy AM. Calcium sensitivity, force frequency relationship and cardiac troponin I: critical role of PKA and PKC phosphorylation sites. *J Mol Cell Cardiol*, 48:943-953, 2010.

82. Mohler PJ, Schott JJ, Gramolini AO, Dilly KW, Guatimosim S, duBell WH, Song LS, Haurogne K, Kyndt F, Ali ME, Rogers TB, Lederer WJ, Escande D, Le Marec H, and Bennett V. Ankyrin-B mutation causes type 4 long-QT cardiac arrhythmia and sudden cardiac death. *Nature*, 421:634-639, 2003.

83. Preckel B, Mullenheim J, Moloschavij A, Thamer V, and Schlack W. Xenon administration during early reperfusion reduces infarct size after regional ischemia in the rabbit heart in vivo. *Anesth Analg*, 91:1327-1332, 2000.

84. Jouven X, Empana JP, Schwartz PJ, Desnos M, Courbon D, and Ducimetiere P. Heart-rate profile during exercise as a predictor of sudden death. *N Engl J Med*, 352:1951-1958, 2005.

85. Glukhov AV, Fedorov VV, Lou Q, Ravikumar VK, Kalish PW, Schuessler RB, Moazami N, and Efimov IR. Transmural dispersion of repolarization in failing and nonfailing human ventricle. *Circ Res*, 106:981-991, 2010.

86. Brunet S, Aimond F, Li H, Guo W, Eldstrom J, Fedida D, Yamada KA, and Nerbonne JM. Heterogeneous expression of repolarizing, voltage-gated K+ currents in adult mouse ventricles. *J Physiol*, 559:103-120, 2004.

87. Stelzer JE, Patel JR, Walker JW, and Moss RL. Differential roles of cardiac myosin-binding protein C and cardiac troponin I in the myofibrillar force responses to protein kinase A phosphorylation. *Circ Res*, 101:503-511, 2007.

88. Sadayappan S, Gulick J, Klevitsky R, Lorenz JN, Sargent M, Molkentin JD, and Robbins J. Cardiac myosin binding protein-C phosphorylation in a {beta}-myosin heavy chain background. *Circulation*, 119:1253-1262, 2009.

89. Ackers-Johnson M, Li PY, Holmes AP, O'Brien SM, Pavlovic D, and Foo RS. A simplified, Langendorff-free method for concomitant isolation of viable cardiac myocytes and nonmyocytes from the adult mouse heart. *Circ Res*, 119:909-920, 2016.

90. Kirchhefer U, Hanske G, Jones LR, Justus I, Kaestner L, Lipp P, Schmitz W, and Neumann J. Overexpression of junctin causes adaptive changes in cardiac myocyte Ca(2+) signaling. *Cell Calcium*, 39:131-142, 2006.

91. Kirchhefer U, Klimas J, Baba HA, Buchwalow IB, Fabritz L, Huls M, Matus M, Muller FU, Schmitz W, and Neumann J. Triadin is a critical determinant of cellular Ca cycling and contractility in the heart. *Am J Physiol Heart Circ Physiol*, 293:H3165-3174, 2007.

92. Nakayama M, Yan X, Price RL, Borg TK, Ito K, Sanbe A, Robbins J, and Lorell BH. Chronic ventricular myocyte-specific overexpression of angiotensin II type 2 receptor results in intrinsic myocyte contractile dysfunction. *Am J Physiol Heart Circ Physiol*, 288:H317-327, 2005.

93. Ramirez-Correa GA, Frazier AH, Zhu G, Zhang P, Rappold T, Kooij V, Bedja D, Snyder GA, Lugo-Fagundo NS, Hariharan R, Li Y, Shen X, Gao WD, Cingolani OH, Takimoto E, Foster DB, and Murphy AM. Cardiac troponin I Pro82Ser variant induces diastolic dysfunction, blunts beta-adrenergic response, and impairs myofilament cooperativity. *J Appl Physiol (1985)*, 118:212-223, 2015.

94. Takimoto E, Soergel DG, Janssen PM, Stull LB, Kass DA, and Murphy AM. Frequency- and afterload-dependent cardiac modulation in vivo by troponin I with constitutively active protein kinase A phosphorylation sites. *Circ Res*, 94:496-504, 2004.

95. Vandecasteele G, Eschenhagen T, Scholz H, Stein B, Verde I, and Fischmeister R. Muscarinic and beta-adrenergic regulation of heart rate, force of contraction and calcium current is preserved in mice lacking endothelial nitric oxide synthase. *Nat Med*, 5:331-334, 1999.

96. Grinshpon M and Bondarenko VE. Simulation of the effects of moderate stimulation/inhibition of the beta1-adrenergic signaling system and its components in mouse ventricular myocytes. *Am J Physiol Cell Physiol*, 310:C844-856, 2016.

97. Colson BA, Bekyarova T, Locher MR, Fitzsimons DP, Irving TC, and Moss RL. Protein kinase A-mediated phosphorylation of cMyBP-C increases proximity of myosin heads to actin in resting myocardium. *Circ Res*, 103:244-251, 2008.

98. Lecarpentier Y, Vignier N, Oliviero P, Guellich A, Carrier L, and Coirault C. Cardiac Myosin-binding protein C modulates the tuning of the molecular motor in the heart. *Biophys J*, 95:720-728, 2008.

99. Verduyn SC, Zaremba R, van der Velden J, and Stienen GJ. Effects of contractile protein phosphorylation on force development in permeabilized rat cardiac myocytes. *Basic Res Cardiol*, 102:476-487, 2007.

100. Najafi A, Sequeira V, Helmes M, Bollen IA, Goebel M, Regan JA, Carrier L, Kuster DW, and Van Der Velden J. Selective phosphorylation of PKA targets after beta-adrenergic receptor stimulation impairs myofilament function in Mybpc3-targeted HCM mouse model. *Cardiovasc Res*, 110:200-214, 2016.

101. Hill AV. The heat of shortening and the dynamic constants of muscle. *Proc R Soc Lond B*, 126:136-195, 1938.

102. Brickson S, Fitzsimons DP, Pereira L, Hacker T, Valdivia H, and Moss RL. In vivo left ventricular functional capacity is compromised in cMyBP-C null mice. *Am J Physiol Heart Circ Physiol*, 292:H1747-1754, 2007.

103. Colson BA, Locher MR, Bekyarova T, Patel JR, Fitzsimons DP, Irving TC, and Moss RL. Differential roles of regulatory light chain and myosin binding protein-C phosphorylations in the modulation of cardiac force development. *J Physiol*, 588:981-993, 2010.

104. Colson BA, Patel JR, Chen PP, Bekyarova T, Abdalla MI, Tong CW, Fitzsimons DP, Irving TC, and Moss RL. Myosin binding protein-C phosphorylation is the principal mediator of protein kinase A effects on thick filament structure in myocardium. *J Mol Cell Cardiol*, 53:609-616, 2012.

105. Stelzer JE, Fitzsimons DP, and Moss RL. Ablation of myosin-binding protein-C accelerates force development in mouse myocardium. *Biophys J*, 90:4119-4127, 2006.

106. Despa S, Tucker AL, and Bers DM. Phospholemman-mediated activation of Na/K-ATPase limits [Na]i and inotropic state during beta-adrenergic stimulation in mouse ventricular myocytes. *Circulation*, 117:1849-1855, 2008.

107. Wang H, Kohr MJ, Wheeler DG, and Ziolo MT. Endothelial nitric oxide synthase decreases beta-adrenergic responsiveness via inhibition of the L-type Ca2+ current. *Am J Physiol Heart Circ Physiol*, 294:H1473-1480, 2008.

108. Campbell SG, Flaim SN, Leem CH, and McCulloch AD. Mechanisms of transmurally varying myocyte electromechanics in an integrated computational model. *Philos Trans R Soc A*, 366:3361-3380, 2008.

109. Hilal-Dandan R, Kanter JR, and Brunton LL. Characterization of G-protein signaling in ventricular myocytes from the adult mouse heart: differences from the rat. *J Mol Cell Cardiol*, 32:1211-1221, 2000.

110. Post SR, Hilal-Dandan R, Urasawa K, Brunton LL, and Insel PA. Quantification of signalling components and amplification in the beta-adrenergic-receptor-adenylate cyclase pathway in isolated adult rat ventricular myocytes. *Biochem J*, 311 (Pt 1):75-80, 1995.

111. Freedman NJ, Liggett SB, Drachman DE, Pei G, Caron MG, and Lefkowitz RJ. Phosphorylation and desensitization of the human beta 1-adrenergic receptor. Involvement of G protein-coupled receptor kinases and cAMP-dependent protein kinase. *J Biol Chem*, 270:17953-17961, 1995.

112. Gao X, Sadana R, Dessauer CW, and Patel TB. Conditional stimulation of type V and VI adenylyl cyclases by G protein betagamma subunits. *J Biol Chem*, 282:294-302, 2007.

113. Zimmermann G and Taussig R. Protein kinase C alters the responsiveness of adenylyl cyclases to G protein alpha and betagamma subunits. *J Biol Chem*, 271:27161-27166, 1996.

114. Iancu RV, Ramamurthy G, Warrier S, Nikolaev VO, Lohse MJ, Jones SW, and Harvey RD. Cytoplasmic cAMP concentrations in intact cardiac myocytes. *Am J Physiol Cell Physiol*, 295:C414-422, 2008.

115. Bode DC, Kanter JR, and Brunton LL. Cellular distribution of phosphodiesterase isoforms in rat cardiac tissue. *Circ Res*, 68:1070-1079, 1991.

116. Osadchii OE. Myocardial phosphodiesterases and regulation of cardiac contractility in health and cardiac disease. *Cardiovasc Drugs Ther*, 21:171-194, 2007.

117. Mongillo M, Tocchetti CG, Terrin A, Lissandron V, Cheung YF, Dostmann WR, Pozzan T, Kass DA, Paolocci N, Houslay MD, and Zaccolo M. Compartmentalized phosphodiesterase-2 activity blunts beta-adrenergic cardiac inotropy via an NO/cGMP-dependent pathway. *Circ Res*, 98:226-234, 2006.

118. Beavo JA, Bechtel PJ, and Krebs EG. Activation of protein kinase by physiological concentrations of cyclic AMP. *Proc Natl Acad Sci U S A*, 71:3580-3583, 1974.

119. Dao KK, Teigen K, Kopperud R, Hodneland E, Schwede F, Christensen AE, Martinez A, and Doskeland SO. Epac1 and cAMP-dependent protein kinase holoenzyme have similar cAMP affinity, but their cAMP domains have distinct structural features and cyclic nucleotide recognition. *J Biol Chem*, 281:21500-21511, 2006.

120. El-Armouche A, Wittkopper K, Degenhardt F, Weinberger F, Didie M, Melnychenko I, Grimm M, Peeck M, Zimmermann WH, Unsold B, Hasenfuss G, Dobrev D, and Eschenhagen T. Phosphatase inhibitor-1-deficient mice are protected from catecholamine-induced arrhythmias and myocardial hypertrophy. *Cardiovasc Res*, 80:396-406, 2008.

121. Chu G, Luo W, Slack JP, Tilgmann C, Sweet WE, Spindler M, Saupe KW, Boivin GP, Moravec CS, Matlib MA, Grupp IL, Ingwall JS, and Kranias EG. Compensatory mechanisms associated with the hyperdynamic function of phospholamban-deficient mouse hearts. *Circ Res*, 79:1064-1076, 1996.

122. Bers DM and Stiffel VM. Ratio of ryanodine to dihydropyridine receptors in cardiac and skeletal muscle and implications for E-C coupling. *Am J Physiol*, 264:C1587-1593, 1993.

123. Despa S, Bossuyt J, Han F, Ginsburg KS, Jia LG, Kutchai H, Tucker AL, and Bers DM. Phospholemman-phosphorylation mediates the beta-adrenergic effects on Na/K pump function in cardiac myocytes. *Circ Res*, 97:252-259, 2005.

APPENDICES

Appendix A Chapter 2 Model Summary

Membrane Potential

$$\frac{dV}{dt} = -\frac{1}{C_m}(I_{CaL} + I_{p(Ca)} + I_{NaCa} + I_{Cab} + I_{Na} + I_{Nab} + I_{NaK} + I_{Kto,f} + I_{Kto,s} + I_{K1} + I_{Ks} + I_{Kur} + I_{Kss} + I_{Kr} + I_{Cl,Ca} - I_{stim}) \quad \text{(A.1)}$$

Calcium Dynamics

Calcium Concentration

$$\frac{d[Ca^{2+}]_i}{dt} = B_i \left\{ J_{leak} + J_{xfer} - J_{up} - J_{trpn} - \left(I_{Cab} - 2I_{NaCa} + I_{p(Ca)}\right)\frac{A_{cap}C_m}{2V_{myo}F} \right\} \quad \text{(A .2)}$$

$$\frac{d[Ca^{2+}]_{ss}}{dt} = B_{ss} \left\{ J_{rel}\frac{V_{JSR}}{V_{ss}} - J_{xfer}\frac{V_{myo}}{V_{ss}} - I_{CaL}\frac{A_{cap}C_m}{2V_{ss}F} \right\} \quad \text{(A .3)}$$

$$\frac{d[Ca^{2+}]_{JSR}}{dt} = B_{JSR}\{J_{tr} - J_{rel}\} \quad \text{(A .4)}$$

$$\frac{d[Ca^{2+}]_{NSR}}{dt} = \{J_{up} - J_{leak}\}\frac{V_{myo}}{V_{NSR}} - J_{tr}\frac{V_{JSR}}{V_{NSR}} \quad \text{(A .5)}$$

$$B_i = \left\{ 1 + \frac{[CMDN]_{tot}K_m^{CMDN}}{(K_m^{CMDN} + [Ca^{2+}]_i)^2} \right\}^{-1} \quad \text{(A .6)}$$

$$B_{ss} = \left\{ 1 + \frac{[CMDN]_{tot}K_m^{CMDN}}{(K_m^{CMDN} + [Ca^{2+}]_{ss})^2} \right\}^{-1} \quad \text{(A .7)}$$

$$B_{JSR} = \left\{ 1 + \frac{[CSQN]_{tot}K_m^{CSQN}}{(K_m^{CSQN} + [Ca^{2+}]_{JSR})^2} \right\}^{-1} \quad \text{(A .8)}$$

Calcium Fluxes

$$J_{rel} = v_1(P_{O1} + P_{O2})([Ca^{2+}]_{JSR} - [Ca^{2+}]_{ss})P_{RyR} \quad \text{(A .9)}$$

$$J_{tr} = \frac{[Ca^{2+}]_{NSR} - [Ca^{2+}]_{JSR}}{\tau_{tr}} \quad \text{(A .10)}$$

$$J_{xfer} = \frac{[Ca^{2+}]_{ss} - [Ca^{2+}]_i}{\tau_{xfer}} \quad \text{(A .11)}$$

$$J_{leak} = v_2([Ca^{2+}]_{NSR} - [Ca^{2+}]_i) \quad \text{(A .12)}$$

$$J_{up} = v_3 \frac{[Ca^{2+}]_i^2}{K_{m,up}^2 + [Ca^{2+}]_i^2} \quad \text{(A .13)}$$

$$J_{trpn} = k_{htrpn}^+[Ca^{2+}]_i([HTRPN]_{tot} - [HTRPNCa]) - k_{htrpn}^-[HTRPNCa] + k_{ltrpn}^+[Ca^{2+}]_i([LTRPN]_{tot} - [LTRPNCa]) - k_{ltrpn}^-[LTRPNCa] \quad \text{(A .14)}$$

$$\frac{dP_{RyR}}{dt} = -0.04P_{RyR} - 0.1\frac{I_{CaL}}{I_{CaL,\max}}e^{-\frac{(V+5.0)^2}{648.0}} \quad \text{(A .15)}$$

Calcium Buffering

$$\frac{d[LTRPNCa]}{dt} = k_{ltrpn}^+[Ca^{2+}]_i\{[LTRPN]_{tot} - [LTRPNCa]\} - k_{ltrpn}^-[LTRPNCa] \quad \text{(A .16)}$$

$$\frac{d[HTRPNCa]}{dt} = k_{htrpn}^+[Ca^{2+}]_i\{[HTRPN]_{tot} - [HTRPNCa]\} - k_{htrpn}^-[HTRPNCa] \quad \text{(A .17)}$$

Ryanodine Receptors

$$\frac{dP_{O1}}{dt} = k_a^+[Ca^{2+}]_{ss}^n P_{C1} - k_a^- P_{O1} - k_b^+[Ca^{2+}]_{ss}^m P_{O1} + k_b^- P_{O2} - k_c^+ P_{O1} + k_c^- P_{C2} \quad \text{(A .18)}$$

$$P_{C1} = 1 - (P_{C2} + P_{O1} + P_{O2}) \quad \text{(A .19)}$$

$$\frac{dP_{O2}}{dt} = k_b^+ [Ca^{2+}]_{ss}^m P_{O1} - k_b^- P_{O2} \quad \text{(A .20)}$$

$$\frac{dP_{C2}}{dt} = k_c^+ P_{O1} - k_c^- P_{C2} \quad \text{(A .21)}$$

Calcium Currents

L-type Calcium Current

$$I_{CaL} = G_{CaL} O (V - E_{Ca,L}) \quad \text{(A .22)}$$

$$\frac{dO}{dt} = \alpha C_4 - 4\beta O + K_{pcb} I_1 - \gamma O + 0.001(\alpha I_2 - K_{pcf} O) \quad \text{(A .23)}$$

$$C_1 = 1 - (O + C_2 + C_3 + C_4 + I_1 + I_2 + I_3) \quad \text{(A .24)}$$

$$\frac{dC_2}{dt} = 4\alpha C_1 - \beta C_2 + 2\beta C_3 - 3\alpha C_2 \quad \text{(A .25)}$$

$$\frac{dC_3}{dt} = 3\alpha C_2 - 2\beta C_3 + 3\beta C_4 - 2\alpha C_3 \quad \text{(A .26)}$$

$$\frac{dC_4}{dt} = 2\alpha C_3 - 3\beta C_4 + 4\beta O - \alpha C_4 + 0.01(4K_{pcb}\beta I_1 - \alpha\gamma C_4) + 0.002(4\beta I_2 - K_{pcf} C_4) + 4\beta K_{pcb} I_3 - \gamma K_{pcf} C_4 \quad \text{(A .27)}$$

$$\frac{dI_1}{dt} = \gamma O - K_{pcb} I_1 + 0.001(\alpha I_3 - K_{pcf} I_1) + 0.01(\alpha\gamma C_4 - 4\beta K_{pcb} I_1) \quad \text{(A .28)}$$

$$\frac{dI_2}{dt} = 0.001(K_{pcf} O - \alpha I_2) + K_{pcb} I_3 - \gamma I_2 + 0.002(K_{pcf} C_4 - 4\beta I_2) \quad \text{(A .29)}$$

$$\frac{dI_3}{dt} = 0.001(K_{pcf} I_1 - \alpha I_3) + \gamma I_2 - K_{pcb} I_3 + \gamma K_{pcf} C_4 - 4\beta K_{pcb} I_3 \quad \text{(A .30)}$$

$$\alpha = 0.4 e^{(V+15.0)/15.0} \quad \text{(A .31)}$$

$$\beta = 0.13\, e^{-(V+15.0)/18.0} \quad \text{(A .32)}$$

$$\gamma = \frac{K_{pc,\max}[Ca^{2+}]_{ss}}{K_{pc,half} + [Ca^{2+}]_{ss}} \quad \text{(A .33)}$$

$$K_{pcf} = 2.5\ \text{ms}^{-1} \quad \text{(A .34)}$$

Calcium Pump Current

$$I_{p(Ca)} = I_{p(Ca)}^{\max} \frac{[Ca^{2+}]_i^2}{K_{m,p(Ca)}^2 + [Ca^{2+}]_i^2} \quad \text{(A .35)}$$

Na^+-Ca^{2+} Exchange Current

$$I_{NaCa} = k_{NaCa} \frac{1}{K_{m,Na}^3 + [Na^+]_0^3} \frac{1}{K_{m,Ca} + [Ca^{2+}]_0} \frac{1}{1 + k_{sat} e^{(\eta-1)VF/RT}} \times (e^{\eta VF/RT}[Na^+]_i^3[Ca^{2+}]_0 - e^{(\eta-1)VF/RT}[Na^+]_0^3[Ca^{2+}]_i) \quad \text{(A .36)}$$

Calcium Background Current

$$I_{Cab} = G_{Cab}(V - E_{CaN}) \quad \text{(A .37)}$$

$$E_{CaN} = \frac{RT}{2F} \ln\left(\frac{[Ca^{2+}]_0}{[Ca^{2+}]_i}\right) \quad \text{(A .38)}$$

Sodium Dynamics

Sodium Concentration

$$\frac{d[Na^+]_i}{dt} = -(I_{Na} + I_{Nab} + 3I_{NaCa} + 3I_{NaK}) \frac{A_{cap} C_m}{V_{myo} F} \quad \text{(A .39)}$$

Fast Sodium Current

$$I_{Na} = G_{Na} O_{Na} (V - E_{Na}) \quad \text{(A .40)}$$

$$E_{Na} = \frac{RT}{F} \ln\left(\frac{0.9[Na^+]_0 + 0.1[K^+]_0}{0.9[Na^+]_i + 0.1[K^+]_i}\right) \quad \text{(A .41)}$$

$$C_{Na3} = 1 - (O_{Na} + C_{Na1} + C_{Na2} + IF_{Na} + I1_{Na} + I2_{Na} + IC_{Na2} + IC_{Na3}) \quad \text{(A .42)}$$

$$\frac{dC_{Na2}}{dt} = \alpha_{Na11} C_{Na3} - \beta_{Na11} C_{Na2} + \beta_{Na12} C_{Na1} - \alpha_{Na12} C_{Na2} + \alpha_{Na3} IC_{Na2} - \beta_{Na3} C_{Na2} \quad \text{(A .43)}$$

$$\frac{dC_{Na1}}{dt} = \alpha_{Na12} C_{Na2} - \beta_{Na12} C_{Na1} + \beta_{Na13} O_{Na} - \alpha_{Na13} C_{Na1} + \alpha_{Na3} IF_{Na} - \beta_{Na3} C_{Na1} \quad \text{(A .44)}$$

$$\frac{dO_{Na}}{dt} = \alpha_{Na13} C_{Na1} - \beta_{Na13} O_{Na} + \beta_{Na2} IF_{Na} - \alpha_{Na2} O_{Na} \quad \text{(A .45)}$$

$$\frac{dIF_{Na}}{dt} = \alpha_{Na2} O_{Na} - \beta_{Na2} IF_{Na} + \beta_{Na3} C_{Na1} - \alpha_{Na3} IF_{Na} + \beta_{Na4} I1_{Na} - \alpha_{Na4} IF_{Na} + \alpha_{Na12} IC_{Na2} - \beta_{Na12} IF_{Na} \quad \text{(A .46)}$$

$$\frac{dI1_{Na}}{dt} = \alpha_{Na4} IF_{Na} - \beta_{Na4} I1_{Na} + \beta_{Na5} I2_{Na} - \alpha_{Na5} I1_{Na} \quad \text{(A .47)}$$

$$\frac{dI2_{Na}}{dt} = \alpha_{Na5} I1_{Na} - \beta_{Na5} I2_{Na} \quad \text{(A .48)}$$

$$\frac{dIC_{Na2}}{dt} = \alpha_{Na11} IC_{Na3} - \beta_{Na11} IC_{Na2} + \beta_{Na12} IF_{Na} - \alpha_{Na12} IC_{Na2} + \beta_{Na3} C_{Na2} - \alpha_{Na3} IC_{Na2} \quad \text{(A .49)}$$

$$\frac{dIC_{Na3}}{dt} = \beta_{Na11} IC_{Na2} - \alpha_{Na11} IC_{Na3} + \beta_{Na3} C_{Na3} - \alpha_{Na3} IC_{Na3} \quad \text{(A .50)}$$

$$\alpha_{Na11} = \frac{3.802}{0.1027 e^{-(V+2.5)/17.0} + 0.20 e^{-(V+2.5)/150.0}} \quad \text{(A .51)}$$

$$\alpha_{Na12} = \frac{3.802}{0.1027 e^{-(V+2.5)/15.0} + 0.23 e^{-(V+2.5)/150.0}} \quad \text{(A .52)}$$

$$\alpha_{Na13} = \frac{3.802}{0.1027 e^{-(V+2.5)/12.0} + 0.25 e^{-(V+2.5)/150.0}} \quad \text{(A .53)}$$

$$\beta_{Na11} = 0.1917 e^{-(V+2.5)/20.3} \quad \text{(A .54)}$$

$$\beta_{Na12} = 0.20 e^{-(V-2.5)/20.3} \quad \text{(A .55)}$$

$$\beta_{Na13} = 0.22 e^{-(V-7.5)/20.3} \quad \text{(A .56)}$$

$$\alpha_{Na3} = 7.0 \times 10^{-7} e^{-(V+7.0)/7.7} \quad \text{(A .57)}$$

$$\beta_{Na3} = 0.0084 + 0.00002\,(V + 7.0) \quad \text{(A .58)}$$

$$\alpha_{Na2} = \frac{1.0}{0.188495 e^{-(V+7.0)/16.6} + 0.393956} \quad \text{(A .59)}$$

$$\beta_{Na2} = \alpha_{Na13}\alpha_{Na2}\alpha_{Na3} / (\beta_{Na13}\beta_{Na3}) \quad \text{(A .60)}$$

$$\alpha_{Na4} = \alpha_{Na2} / 1000.0 \quad \text{(A .61)}$$

$$\beta_{Na4} = \alpha_{Na3} \quad \text{(A .62)}$$

$$\alpha_{Na5} = \alpha_{Na2} / 95000 \quad \text{(A .63)}$$

$$\beta_{Na5} = \alpha_{Na3} / 50.0 \quad \text{(A .64)}$$

Background Sodium Current

$$I_{Nab} = G_{Nab}(V - E_{Na}) \quad \text{(A .65)}$$

Potassium Dynamics

Potassium Concentration

$$\frac{d[K^+]_i}{dt} = -(I_{Kto,f} + I_{Kto,s} + I_{K1} + I_{Ks} + I_{Kss} + I_{Kur} + I_{Kr} - 2I_{NaK}) \frac{A_{cap} C_m}{V_{myo} F} \quad \text{(A .66)}$$

Transient Outward Potassium Current $I_{Kto,f}$

$$I_{Kto,f} = G_{Kto,f} a_{to,f}^3 i_{to,f} (V - E_K) \quad \text{(A .67)}$$

$$E_K = \frac{RT}{F} \ln\left(\frac{[K^+]_0}{[K^+]_i}\right) \quad \text{(A .68)}$$

$$\frac{da_{to,f}}{dt} = \alpha_a (1 - a_{to,f}) - \beta_a a_{to,f} \quad \text{(A .69)}$$

$$\frac{di_{to,f}}{dt} = \alpha_i(1 - i_{to,f}) - \beta_i i_{to,f} \quad \text{(A .70)}$$

$$\alpha_a = 0.18064\, e^{0.03577(V+30.0)} \quad \text{(A .71)}$$

$$\beta_a = 0.3956\, e^{-0.06237(V+30.0)} \quad \text{(A .72)}$$

$$\alpha_i = \frac{0.000152 e^{-(V+13.5)/7.0}}{0.067083 e^{-(V+33.5)/7.0} + 1} \quad \text{(A .73)}$$

$$\beta_i = \frac{0.00095 e^{(V+33.5)/7.0}}{0.051335 e^{(V+33.5)/7.0} + 1} \quad \text{(A .74)}$$

Transient Outward Potassium Current $I_{Kto,s}$

$$I_{Kto,s} = G_{Kto,s} a_{to,s} i_{to,s} (V - E_K) \quad \text{(A .75)}$$

$$\frac{da_{to,s}}{dt} = \frac{a_{ss} - a_{to,s}}{\tau_{ta,s}} \quad \text{(A .76)}$$

$$\frac{di_{to,s}}{dt} = \frac{i_{ss} - i_{to,s}}{\tau_{ti,s}} \quad \text{(A .77)}$$

$$a_{ss} = 1/(1 + e^{-(V+22.5)/7.7}) \quad \text{(A .78)}$$

$$i_{ss} = 1/(1 + e^{(V+45.2)/5.7}) \quad \text{(A .79)}$$

$$\tau_{ta,s} = 0.493 e^{-0.0629V} + 2.058 \quad \text{(A .80)}$$

$$\tau_{ti,s} = 270.0 + \frac{1050.0}{1 + e^{(V+45.2)/5.7}} \quad \text{(A .81)}$$

Time-independent Potassium Current

$$I_{K1} = 0.3397 \left(\frac{[K^+]_0}{[K^+]_0 + 210.0} \right) \left(\frac{V - E_K}{1 + e^{0.0448(V - E_K)}} \right) + 0.0193V \quad \text{(A .82)}$$

Slow Delayed-Rectifier Potassium Current

$$I_{Ks} = G_{Ks} n_{Ks}^2 (V - E_K) \quad \text{(A .83)}$$

$$\frac{dn_{Ks}}{dt} = \alpha_n (1 - n_{Ks}) - \beta_n n_{Ks} \quad \text{(A .84)}$$

$$\alpha_n = \frac{0.00000481333(V + 26.5)}{1 - e^{-0.128(V+26.5)}} \quad \text{(A .85)}$$

$$\beta_n = 0.0000953333 e^{-0.038(V+26.5)} \quad \text{(A .86)}$$

Ultra-Rapidly Activating Delayed-Rectifier Potassium Current

$$I_{Kur} = G_{Kur} a_{ur} i_{ur} (V - E_K) \quad \text{(A .87)}$$

$$\frac{da_{ur}}{dt} = \frac{a_{ss} - a_{ur}}{\tau_{aur}} \quad \text{(A .88)}$$

$$\frac{di_{ur}}{dt} = \frac{i_{ss} - i_{ur}}{\tau_{iur}} \quad \text{(A .89)}$$

$$\tau_{aur} = \frac{6.1}{e^{0.0629(V+40.0)} + e^{-0.0629(V+40.0)}} + 2.058 \quad \text{(A .90)}$$

$$\tau_{iur} = 1200.0 - \frac{170.0}{1 + e^{(V+45.2)/5.7}} \quad \text{(A .91)}$$

Non-Inactivating Steady-State Potassium Current

$$I_{Kss} = G_{Kss} a_{Kss} (V - E_K) \quad \text{(A .92)}$$

$$\frac{da_{Kss}}{dt} = \frac{a_{ss} - a_{Kss}}{\tau_{Kss}} \quad \text{(A .93)}$$

$$\frac{di_{Kss}}{dt} = 0 \quad \text{(A .94)}$$

$$\tau_{Kss} = \frac{1235.5}{e^{0.0862(V+40.0)} + e^{-0.0862(V+40.0)}} + 13.17 \quad \text{(A .95)}$$

Rapid Delayed Rectifier Potassium Current (mERG)

$$I_{Kr} = O_K \cdot G_{Kr} \cdot \left[V - \frac{RT}{F} \ln\left(\frac{0.98[K^+]_o + 0.02[Na^+]_o}{0.98[K^+]_i + 0.02[Na^+]_i} \right) \right] \quad \text{(A .96)}$$

$$C_{K0} = 1 - (C_{K1} + C_{K2} + O_K + I_K) \quad \text{(A .97)}$$

$$\frac{dC_{K1}}{dt} = \alpha_{a0} C_{K0} - \beta_{a0} C_{K1} + k_b C_{K2} - k_f C_{K1} \quad \text{(A .98)}$$

$$\frac{dC_{K2}}{dt} = k_f C_{K1} - k_b C_{K2} + \beta_{a1} O_K - \alpha_{a1} C_{K2} \quad \text{(A .99)}$$

$$\frac{dO_K}{dt} = \alpha_{a1} C_{K2} - \beta_{a1} O_K + \beta_i I_K - \alpha_i O_K \quad \text{(A .100)}$$

$$\frac{dI_K}{dt} = \alpha_i O_K - \beta_i I_K \quad \text{(A .101)}$$

$$\alpha_{a0} = 0.022348 e^{0.01176V} \quad \text{(A .102)}$$

$$\beta_{a0} = 0.047002 e^{-0.0631V} \quad \text{(A .103)}$$

$$\alpha_{a1} = 0.013733 \ e^{0.038198V} \quad \text{(A .104)}$$

$$\beta_{a1} = 0.0000689 \ e^{-0.04178V} \quad \text{(A .105)}$$

$$\alpha_i = 0.090821 \ e^{0.023391(V+5.0)} \quad \text{(A .106)}$$

$$\beta_i = 0.006497 \ e^{-0.03268(V+5.0)} \quad \text{(A .107)}$$

Sodium-Potassium Pump Current

$$I_{NaK} = I_{NaK}^{\max} f_{NaK} \frac{1}{1 + (K_{m,Nai} / [Na^+]_i)^{3/2}} \frac{[K^+]_0}{[K^+]_0 + K_{m,Ko}} \quad \text{(A .108)}$$

$$f_{NaK} = \frac{1}{1 + 0.1245 e^{-0.1VF/RT} + 0.0365 \sigma e^{-VF/RT}} \quad \text{(A .109)}$$

$$\sigma = \frac{1}{7}(e^{[Na^+]_0/67300} - 1) \quad \text{(A .110)}$$

Calcium-Activated Chloride Current

$$I_{Cl,Ca} = G_{Cl,Ca} O_{Cl,Ca} \frac{[Ca^{2+}]_i}{[Ca^{2+}]_i + K_{m,Cl}} (V - E_{Cl}) \quad \text{(A .111)}$$

$$O_{Cl,Ca} = \frac{0.2}{1 + \exp[-(V - 46.7)/7.8]} \quad \text{(A .112)}$$

Contraction

Permissive states

$$\frac{dN0}{dt} = k_{PN} P0 + g_{10SL} N1 - k_{NP} N0 \quad \text{(A .113)}$$

$$\frac{dN1}{dt} = k_{PN} P1 - \left(k_{NP} + g_{10SL}\right) N1 \quad \text{(A .114)}$$

$$\frac{dP0}{dt} = g_{10SL} P1 + k_{NP} N0 - \left(k_{PN} + f_{01}\right) P0 \quad \text{(A .115)}$$

$$\frac{dP1}{dt} = g_{21SL} P2 + f_{01} P0 + k_{NP} N1 - \left(f_{12} + g_{10SL} + k_{PN}\right) P1 \quad \text{(A .116)}$$

$$\frac{dP2}{dt} = g_{32SL} P3 + f_{12} P1 - \left(f_{23} + g_{21SL}\right) P2 \quad \text{(A .117)}$$

$$\frac{dP3}{dt} = f_{23} P2 - g_{32SL} P3 \quad \text{(A .118)}$$

$$f_{01} = 3 f_{XB} \quad \text{(A .119)}$$

$$f_{12} = 10 f_{XB} \quad \text{(A .120)}$$

$$f_{23} = 7 f_{XB} \quad \text{(A .121)}$$

$$g_{10SL} = g_{xbSL} \tag{A .122}$$

$$g_{21SL} = 2g_{xbSL} \tag{A .123}$$

$$g_{32SL} = 3g_{xbSL} \tag{A .124}$$

$$g_{xbSL} = g_{minxb}\left(2 - \left(SL_{norm}\right)^{1.6}\right) \tag{A .125}$$

$$SL_{norm} = \frac{SL - 1.3\mu\text{m}}{2.3\mu\text{m} - 1.3\mu\text{m}} \tag{A .126}$$

$$SL = 0.8F_{contrn} + SL_0$$

$$k_{NP} = k_{PN}\left(\frac{\left[LTRPNCa\right]}{\left[LTRPNCa\right]_{tot} \times K_{half}}\right)^{Ntm} \tag{A .128}$$

$$Ntm = 5 + 3\ SL_{norm} \tag{A .129}$$

$$K_{half} = 1/\left(1 + \frac{K_{Ca}}{1.5\mu\text{M} - SL_{norm} \times 1.0\mu\text{M}}\right) \tag{A .130}$$

$$K_{Ca} = \frac{k_{ltrpn}^{-}}{k_{ltrpn}^{+}} \tag{A .131}$$

Contraction Force

$$F_{contr} = -73.26\ F_{contrn} \tag{A .132}$$

$$F_{contrn} = -\frac{P1 + N1 + 2\left(P2\right) + 3\left(P3\right)}{F_{\max}} \tag{A .133}$$

$$F_{\max} = P1_{\max} + 2\left(P2_{\max}\right) + 3\left(P3_{\max}\right) \tag{A .134}$$

$$P1_{\max} = \frac{f_{01}\left(2g_{\min xb}\right)\left(3g_{\min xb}\right)}{\Sigma} \tag{A .135}$$

$$P2_{\max} = \frac{f_{01} f_{12} \left(3 g_{\min xb}\right)}{\Sigma} \tag{A .136}$$

$$P3_{\max} = \frac{f_{01} f_{12} f_{23}}{\Sigma} \tag{A .137}$$

$$\Sigma = \left(g_{\min xb}\right)\left(2 g_{\min xb}\right)\left(3 g_{\min xb}\right) + f_{01}\left(2 g_{\min xb}\right)\left(3 g_{\min xb}\right) + f_{01} f_{12}\left(3 g_{\min xb}\right) + f_{01} f_{12} f_{23} \tag{A .138}$$

Model parameters

Cell Geometry Parameters

Parameter	Definition	Value
A_{cap}	Capacitive membrane area	1.534×10^{-4} cm^2
V_{myo}	Myoplasmic volume	25.84×10^{-6} µl
V_{JSR}	Junctional SR volume	0.12×10^{-6} µl
V_{NSR}	Network SR volume	2.098×10^{-6} µl
V_{ss}	Subspace volume	1.485×10^{-9} µl

Extracellular Ion Concentrations

Parameter	Definition	Value
$[K^+]_o$	Extracellular K^+ concentration	4,000 µM
$[Na^+]_o$	Extracellular Na^+ concentration	136,000 µM
$[Ca^{2+}]_o$	Extracellular Ca^{2+} concentration	2,000 µM

SR Parameters

Parameter	Definition	Value
v_1	Maximum RyR channel Ca^{2+} permeability (epicardial cell)	4.0 ms^{-1}
v_1	Maximum RyR channel Ca^{2+} permeability (endocardial cell)	2.9 ms^{-1}
v_2	Ca^{2+} leak rate constant from the NSR	1.74×10^{-5} ms^{-1}
v_3	SR Ca^{2+}-ATPase maximum pump rate	0.315 µM ms^{-1}
$K_{m,up}$	Half-saturation constant for SR Ca^{2+}-ATPase pump	0.5 µM
τ_{tr}	Time constant for transfer from NSR to JSR	20.0 ms
τ_{xfer}	Time constant for transfer from subspace to myoplasm	8.0 ms
k_a^+	RyR $P_{C1} - P_{O1}$ rate constant	0.006075 µM^{-4} ms^{-1}
k_a^-	RyR $P_{O1} - P_{C1}$ rate constant	0.07125 ms^{-1}
k_b^+	RyR $P_{O1} - P_{O2}$ rate constant	0.00405 µM^{-3} ms^{-1}

k_b^-	RyR $P_{O2} - P_{O1}$ rate constant	0.965 ms^{-1}
k_c^+	RyR $P_{O1} - P_{C2}$ rate constant	0.009 ms^{-1}
k_c^-	RyR $P_{C2} - P_{O1}$ rate constant	0.0008 ms^{-1}
n	RyR Ca^{2+} cooperativity parameter $P_{C1} - P_{O1}$	4
m	RyR Ca^{2+} cooperativity parameter $P_{O1} - P_{O2}$	3

L-type Ca^{2+} Channel Parameters

Parameter	Definition	Value
G_{CaL}	Specific maximum conductivity for L-type Ca^{2+} channel	0.2342 mS μF^{-1}
$E_{Ca,L}$	Reversal potential for L-type Ca^{2+} channel	52.0 mV
$K_{pc,max}$	Maximum time constant for Ca^{2+}-induced inactivation	0.11662 ms^{-1}
$K_{pc,half}$	Half-saturation constant for Ca^{2+}-induced inactivation	10.0 μM
K_{pcb}	Voltage-insensitive rate constant for inactivation	0.0005 ms^{-1}
$I_{CaL,max}$	Normalization constant for L-type Ca^{2+} current	7.0 pA pF^{-1}

Buffering Parameters

Parameter	Definition	Value
$[LTRPN]_{tot}$	Total myoplasmic troponin low-affinity site concentration	70.0 μM
$[HTRPN]_{tot}$	Total myoplasmic troponin high-affinity site concentration	140.0 μM
k^+_{htrpn}	Ca^{2+} on rate constant for troponin high-affinity sites	0.00237 μM^{-1} ms^{-1}
k^-_{htrpn}	Ca^{2+} off rate constant for troponin high-affinity sites	3.2×10^{-5} ms^{-1}
k^+_{ltrpn}	Ca^{2+} on rate constant for troponin low-affinity sites	0.0327 μM^{-1} ms^{-1}
k^-_{htrpn}	Ca^{2+} off rate constant for troponin low-affinity sites	0.0196 ms^{-1}
$[CMDN]_{tot}$	Total myoplasmic calmodulin concentration	50.0 μM
$[CSQN]_{tot}$	Total junctional SR calsequestrin concentration	15,000 μM
K_m^{CMDN}	Ca^{2+} half saturation constant for calmodulin	0.238 μM
K_m^{CSQN}	Ca^{2+} half saturation constant for calsequestrin	800.0 μM

Membrane Current Parameters

Parameter	Definition	Value
C_m	Specific membrane capacitance	1.0 μF cm^{-2}
F	Faraday's constant	96.5 C $mmol^{-1}$
T	Absolute temperature	298 K
R	Ideal gas constant	8.314 J mol^{-1} K^{-1}
k_{NaCa}	Scaling factor of Na^+-Ca^{2+} exchange (epicardial cell)	234.24 pA pF^{-1}
k_{NaCa}	Scaling factor of Na^+-Ca^{2+} exchange (endocardial cell)	131.76 pA pF^{-1}
$K_{m,Na}$	Na^+ half saturation constant for Na^+-Ca^{2+} exchange	87,500 μM

$K_{m,Ca}$	Ca^{2+} half saturation constant for Na^{+}-Ca^{2+} exchange	1,380 μM
k_{sat}	Na^{+}-Ca^{2+} exchange saturation factor at very negative potentials	0.1
η	Controls voltage dependence of Na^{+}-Ca^{2+} exchange	0.35
I^{max}_{NaK}	Maximum Na^{+}-K^{+} exchange current (epicardial cell)	0.704 pA pF^{-1}
I^{max}_{NaK}	Maximum Na^{+}-K^{+} exchange current (endocardial cell)	0.6952 pA pF^{-1}
$K_{m,Nai}$	Na^{+} half saturation constant for Na^{+}-K^{+} exchange current	21,000 μM
$K_{m,Ko}$	K^{+} half saturation constant for Na^{+}-K^{+} exchange current	1,500 μM
$I^{max}_{p(Ca)}$	Maximum Ca^{2+} pump current (epicardial cell)	0.085 pA pF^{-1}
$I^{max}_{p(Ca)}$	Maximum Ca^{2+} pump current (endocardial cell)	0.0595 pA pF^{-1}
$K_{m,p(Ca)}$	Ca^{2+} half saturation constant for Ca^{2+} pump current	0.5 μM
G_{Cab}	Maximum background Ca^{2+} current conductance (epicardial cell)	0.000033 mS μF^{-1}
G_{Cab}	Maximum background Ca^{2+} current conductance (endocardial cell)	0.000017 mS μF^{-1}
G_{Na}	Maximum fast Na^{+} current conductance	13.0 mS μF^{-1}
G_{Nab}	Maximum background Na^{2+} current conductance	0.0026 mS μF^{-1}
$G_{Kto,f}$	Maximum transient outward K^{+} current conductance (epicardial cell)	0.3846 mS μF^{-1}
$G_{Kto,f}$	Maximum transient outward K^{+} current conductance (endocardial cell)	0.1939 mS μF^{-1}
G_{Ks}	Maximum slow delayed rectifier K^{+} current conductance	0.00575 mS μF^{-1}
$G_{Kto,s}$	Maximum transient outward K^{+} current conductance (epicardial cell)	0.0 mS μF^{-1}
G_{Kur}	Maximum ultra-rapidly delayed rectifier K^{+} current conductance (epicardial cell)	0.3424 mS μF^{-1}
G_{Kur}	Maximum ultra-rapidly delayed rectifier K^{+} current conductance (endocardial cell)	0.1405 mS μF^{-1}
G_{Kss}	Maximum non-inactivating steady-state K^{+} current conductance (apex)	0.0611 mS μF^{-1}
G_{Kr}	Maximum rapid delayed rectifier K^{+} current conductance	0.078 mS μF^{-1}
k_f	Rate constant for rapid delayed rectifier K^{+} current	0.023761 ms^{-1}
k_b	Rate constant for rapid delayed rectifier K^{+} current	0.036778 ms^{-1}
$G_{Cl,Ca}$	Maximum calcium-activated chloride current conductance	10.0 mS μF^{-1}
$K_{m,Cl}$	Half saturation constant for Ca^{2+}-activated chloride current	10.0 μM
E_{Cl}	Reversal potential for calcium-activated chloride current	–40.0 mV

Contraction Parameters

Parameter	Definition	Value
SL_0	Initial sarcomere length	2.1 μm
k_{PN}	Transition rate from permissive to non-permissive state	0.045 ms^{-1}
f_{XB}	Basic transition rate from weak to strong crossbridge	0.10 ms^{-1}
g_{minxb}	Minimum detachment rate from strong to weak crossbridge	0.14 ms^{-1}

Initial Conditions (epicardial cell)

Parameter	Definition	Value
t	Time	0.0 ms
V	Membrane potential	−76.3108 mV
$[Ca^{2+}]_i$	Myoplasmic Ca^{2+} concentration	0.128703 μM
$[Ca^{2+}]_{ss}$	Subspace SR Ca^{2+} concentration	0.128703 μM
$[Ca^{2+}]_{JSR}$	Junctional SR Ca^{2+} concentration	1125.08 μM
$[Ca^{2+}]_{NSR}$	Network SR Ca^{2+} concentration	1125.08 μM
$[LTRPNCa]$	Concentration Ca^{2+} bound low-affinity troponin-binding sites	12.3737 μM
$[HTRPNCa]$	Concentration Ca^{2+} bound high-affinity troponin-binding sites	126.707 μM
O	L-type Ca^{2+} channel conducting state	0.854831×10^{-11}
C_1	L-type Ca^{2+} channel closed state	0.993178
C_2	L-type Ca^{2+} channel closed state	0.680457×10^{-2}
C_3	L-type Ca^{2+} channel closed state	0.174826×10^{-4}
C_4	L-type Ca^{2+} channel closed state	0.199631×10^{-7}
I_1	L-type Ca^{2+} channel inactivated state	0.253348×10^{-10}
I_2	L-type Ca^{2+} channel inactivated state	0.318339×10^{-8}
I_3	L-type Ca^{2+} channel inactivated state	0.943466×10^{-8}
P_{C1}	Fraction of RyR channels in state P_{C1}	0.999714
P_{C2}	Fraction of RyR channels in state P_{C2}	0.263112×10^{-3}
P_{O1}	Fraction of RyR channels in state P_{O1}	0.233877×10^{-4}
P_{O2}	Fraction of RyR channels in state P_{O2}	0.209256×10^{-9}
C_{Na3}	Closed state of fast Na^+ channel	0.420023
C_{Na2}	Closed state of fast Na^+ channel	0.0267137
C_{Na1}	Closed state of fast Na^+ channel	0.723752×10^{-3}
O_{Na}	Open state of fast Na^+ channel	0.414576×10^{-5}
IF_{Na}	Fast inactivated state of fast Na^+ channel	0.893687×10^{-3}
$I1_{Na}$	Slow inactivated state 1 of fast Na^+ channel	0.124299×10^{-4}
$I2_{Na}$	Slow inactivated state 2 of fast Na^+ channel	0.909901×10^{-7}
IC_{Na2}	Close-inactivated state of fast Na^+ channel	0.0329860
IC_{Na3}	Close-inactivated state of fast Na^+ channel	0.518643
$[Na^+]_i$	Myoplasmic Na^+ concentration	14,564.6 μM
$[K^+]_i$	Myoplasmic K^+ concentration	143,419 μM
$a_{to,f}$	Gating variable for transient outward K^+ current	0.482630×10^{-2}
$i_{to,f}$	Gating variable for transient outward K^+ current	0.999945
n_{Ks}	Gating variable for slow delayed rectifier K^+ current	0.645626×10^{-3}
$a_{to,s}$	Gating variable for transient outward K^+ current	0.921658×10^{-3}
$i_{to,s}$	Gating variable for transient outward K^+ current	0.995756
a_{ur}	Gating variable for ultra-rapidly activating delayed rectifier K^+ current	0.921658×10^{-3}
i_{ur}	Gating variable for ultra-rapidly activating delayed rectifier K^+ current	0.995756

a_{Kss}	Gating variable for non-inactivating steady-state K^+ current	0.921658×10^{-3}
i_{Kss}	Gating variable for non-inactivating steady-state K^+ current	1.0
C_{K0}	*m*ERG channel closed state	0.996856
C_{K1}	*m*ERG channel closed state	0.156600×10^{-2}
C_{K2}	*m*ERG channel closed state	0.101174×10^{-2}
O_K	*m*ERG channel open state	0.450855×10^{-3}
I_K	*m*ERG channel inactivated state	0.115611×10^{-3}
P_{RyR}	Ca^{2+} release modulation factor	0.358438×10^{-13}
SL	Sarcomere length	2.096593 μm
N0	Nonpermissive tropomyosin with 0 crossbridges	0.998770
N1	Nonpermissive tropomyosin with 1 crossbridge	0.367612×10^{-4}
P0	Permissive tropomyosin with 0 crossbridges	0.112735×10^{-3}
P1	Permissive tropomyosin with 1 crossbridge	0.148856×10^{-3}
P2	Permissive tropomyosin with 2 crossbridges	0.408484×10^{-3}
P3	Permissive tropomyosin with 3 crossbridges	0.523108×10^{-3}

Appendix B Chapter 3 Model Summary

Biochemical part

Cell compartments

Parameter	Definition	Value	Reference
A_{cap}	Capacitive membrane area	1.534×10^{-4} cm^2	Bondarenko et al. [29]
V^{cell}	Cell volume	38.00×10^{-6} µl	Bondarenko et al. [29]
V^{cyt}	Cytosolic volume	25.84×10^{-6} µl	Bondarenko et al. [29]
V_{JSR}	Junctional SR volume	0.12×10^{-6} µl	Bondarenko et al. [29]
V_{NSR}	Network SR volume	2.098×10^{-6} µl	Bondarenko et al. [29]
V_{ss}	Subspace volume	1.485×10^{-9} µl	Bondarenko et al. [29]
V^{cav}	Caveolar volume	$0.02\times V_{cell}$	Heijman et al. [34]
V^{ecav}	Extracaveolar volume	$0.04\times V_{cell}$	Heijman et al. [34]

The protein P concentrations in the cell ($[P]^{cell}$), caveolae, extracaveolae, and cytosol

$$[\mathrm{P}]^{\mathrm{cav}} = \mathrm{f}_{\mathrm{P}}^{\mathrm{cav}} \cdot [\mathrm{P}]^{\mathrm{cell}} \cdot \frac{\mathrm{V}^{\mathrm{cell}}}{\mathrm{V}^{\mathrm{cav}}} \tag{B.1}$$

$$[\mathrm{P}]^{\mathrm{ecav}} = \mathrm{f}_{\mathrm{P}}^{\mathrm{ecav}} \cdot [\mathrm{P}]^{\mathrm{cell}} \cdot \frac{\mathrm{V}^{\mathrm{cell}}}{\mathrm{V}^{\mathrm{ecav}}} \tag{B.2}$$

$$[\mathrm{P}]^{\mathrm{cyt}} = (1 - \mathrm{f}_{\mathrm{P}}^{\mathrm{cav}} - \mathrm{f}_{\mathrm{P}}^{\mathrm{ecav}}) \cdot [\mathrm{P}]^{\mathrm{cell}} \cdot \frac{\mathrm{V}^{\mathrm{cell}}}{\mathrm{V}^{\mathrm{cyt}}} \tag{B.3}$$

β_1-adrenergic receptor module

Para-meter	Definition	Value	Reference
$[L]$	Ligand concentration	0…100 µM	
$[R_{\beta 1}]_{tot}$	Total β_1-adrenoceptor concentration	0.0103 µM	Hilal-Dandan et al. [109]
$\mathrm{f}_{\beta 1}^{cav}$	Fraction of β_1-adrenoceptors located in caveolae	0.01	Rybin et al. [37] Balijepalli et al. [35]
$\mathrm{f}_{\beta 1}^{ecav}$	Fraction of β_1-adrenoceptors located in extracaveolae	0.5	Rybin et al. [37] Balijepalli et al. [35]
$\mathrm{f}_{\beta 1}^{cyt}$	Fraction of β_1-adrenoceptors located in cytosol	$\mathrm{f}_{\beta 1}^{cyt} = 1 - \mathrm{f}_{\beta 1}^{cav} - \mathrm{f}_{\beta 1}^{ecav}$	Rybin et al. [37] Balijepalli et al. [35]
$[G_s]_{tot}$	Total concentration of G_s protein	2.054 µM	Post et al. [110]
f_{Gs}^{cav}	Fraction of G_s protein located in caveolae	0.4	Rybin et al. [37]

f_{Gs}^{ecav}	Fraction of G_s protein located in extracaveolae	0.4	Rybin et al. [37]
f_{Gs}^{cyt}	Fraction of G_s protein located in cytosol	$f_{Gs}^{cyt} = 1 - f_{Gs}^{cav} - f_{Gs}^{ecav}$	
$K_{\beta 1,L}$	Low affinity constant of β_1-adrenoceptor for isoproterenol	0.567 μM	Heijman et al. [34]
$K_{\beta 1,H}$	High affinity constant of β_1-adrenoceptor for isoproterenol	0.0617 μM	Heijman et al. [34]
$K_{\beta 1,C}$	Affinity constant of β_1-adrenoceptor for G_s protein	2.86 μM	Bondarenko [16]
k_{PKA+}	Rate of PKA phosphorylation of β_1-adrenoceptor	0.00081 μM^{-1} s^{-1}	Freedman et al. [111]
k_{PKA-}	Rate of PKA dephosphorylation of β_1-adrenoceptor	0.0002025 s^{-1}	Bondarenko [16]
k_{GRK2+}	Rate of GRK2 phosphorylation of β_1-adrenoceptor	0.000243 s^{-1}	Bondarenko [16]
k_{GRK2-}	Rate of GRK2 dephosphorylation of β_1-adrenoceptor	k_{PKA-}	Bondarenko [16]
$k_{act1,Gs}$	Activation rate for G_s by high affinity complex	4.9 s^{-1}	Heijman et al. [34]
$k_{act2,Gs}$	Activation rate for G_s by low affinity complex	0.26 s^{-1}	Heijman et al. [34]
$k_{hyd,Gs}$	Hydrolysis rate of $G_{s\alpha\text{-}GTP}$	0.8 s^{-1}	Saucerman et al. [30]
$k_{reas,Gs}$	Re-association rate for G_s	1200 μM^{-1} s^{-1}	Saucerman et al. [30]

Caveolae

$$[R_{\beta 1}]_{tot}^{cav} = f_{\beta 1}^{cav} \cdot [R_{\beta 1}]_{tot} \cdot \frac{V_{cell}}{V_{cav}} \tag{B.4}$$

$$[G_s]_{\alpha\beta\gamma}^{cav} = f_{Gs}^{cav} \cdot [G_s]_{tot} \cdot \frac{V_{cell}}{V_{cav}} - [G_s]_{\alpha,GTP}^{cav} - [G_s]_{\alpha,GDP}^{cav} \tag{B.5}$$

$$[R_{\beta 1}]_{np,tot}^{cav} = [R_{\beta 1}]_{tot}^{cav} - [R_{\beta 1}]_{PKA,tot}^{cav} - [R_{\beta 1}]_{GRK2,tot}^{cav} \tag{B.6}$$

$$a_{\beta 1}^{cav} = \frac{1}{K_{\beta 1,L}} \cdot \left(K_{\beta 1,L} + [L]\right) \cdot \left(K_{\beta 1,H} + [L]\right) \tag{B.7}$$

$$b_{\beta 1}^{cav} = [G_s]_{\alpha\beta\gamma}^{cav} \cdot \left(K_{\beta 1,H} + [L]\right) - [R_{\beta 1}]_{np,tot}^{cav} \cdot \left(K_{\beta 1,H} + [L]\right) + K_{\beta 1,C} \cdot K_{\beta 1,H} \left(1 + \frac{[L]}{K_{\beta 1,L}}\right) \tag{B.8}$$

$$c_{\beta 1}^{cav} = -[R_{\beta 1}]_{np,tot}^{cav} \cdot K_{\beta 1,C} \cdot K_{\beta 1,H} \tag{B.9}$$

$$[R_{\beta 1}]_{np,f}^{cav} = \frac{-b_{\beta 1}^{cav} + \sqrt{[b_{\beta 1}^{cav}]^2 - 4 \cdot a_{\beta 1}^{cav} \cdot c_{\beta 1}^{cav}}}{2 \cdot a_{\beta 1}^{cav}} \tag{B.10}$$

$$[G_s]_f^{cav} = \frac{[G_s]_{\alpha\beta\gamma}^{cav}}{1 + [R_{\beta 1}]_{np,f}^{cav} \left(\frac{1}{K_{\beta 1,C}} + \frac{[L]}{K_{\beta 1,C} \cdot K_{\beta 1,H}} \right)} \tag{B.11}$$

$$[LR_{\beta 1}]_{np}^{cav} = \frac{[L] \cdot [R_{\beta 1}]_{np,f}^{cav}}{K_{\beta 1,L}} \tag{B.12}$$

$$[R_{\beta 1} G_s]_{np}^{cav} = \frac{[R_{\beta 1}]_{np,f}^{cav} \cdot [G_s]_f^{cav}}{K_{\beta 1,C}} \tag{B.13}$$

$$[LR_{\beta 1} G_s]_{np}^{cav} = \frac{[L] \cdot [R_{\beta 1}]_{np,f}^{cav} \cdot [G_s]_f^{cav}}{K_{\beta 1,C} \cdot K_{\beta 1,H}} \tag{B.14}$$

$$\frac{d[R_{\beta 1}]_{PKA,tot}^{cav}}{dt} = k_{PKA+} \cdot [C]^{cav} \cdot [R_{\beta 1}]_{np,tot}^{cav} - k_{PKA-} \cdot [R_{\beta 1}]_{PKA,tot}^{cav} \tag{B.15}$$

$$\frac{d[R_{\beta 1}]_{GRK2,tot}^{cav}}{dt} = k_{GRK2+} \cdot \left([LR_{\beta 1}]_{np}^{cav} + [LR_{\beta 1} G_s]_{np}^{cav} \right) - k_{GRK2-} \cdot [R_{\beta 1}]_{GRK2,tot}^{cav} \tag{B.16}$$

$$\frac{d[G_s]_{\alpha,GTP}^{cav}}{dt} = k_{act2,Gs} \cdot [R_{\beta 1} G_s]_{np}^{cav} + k_{act1,Gs} \cdot [LR_{\beta 1} G_s]_{np}^{cav} - k_{hyd,Gs} \cdot [G_s]_{\alpha,GTP}^{cav} \tag{B.17}$$

$$\frac{d[G_s]_{\beta\gamma}^{cav}}{dt} = k_{act2,Gs} \cdot [R_{\beta 1} G_s]_{np}^{cav} + k_{act1,Gs} \cdot [LR_{\beta 1} G_s]_{np}^{cav} - k_{reas,Gs} \cdot [G_s]_{\beta\gamma}^{cav} \cdot [G_s]_{\alpha,GDP}^{cav} \tag{B.18}$$

$$\frac{d[G_s]_{\alpha,GDP}^{cav}}{dt} = k_{hyd,Gs} \cdot [G_s]_{\alpha,GTP}^{cav} - k_{reas,Gs} \cdot [G_s]_{\beta\gamma}^{cav} \cdot [G_s]_{\alpha,GDP}^{cav} \tag{B.19}$$

Extracaveolae

$$[R_{\beta 1}]_{tot}^{ecav} = \mathrm{f}_{\beta 1}^{ecav} \cdot [R_{\beta 1}]_{tot} \cdot \frac{V_{cell}}{V_{ecav}} \tag{B.20}$$

$$[G_s]_{\alpha\beta\gamma}^{ecav} = \mathrm{f}_{Gs}^{ecav} \cdot [G_s]_{tot} \cdot \frac{V_{cell}}{V_{ecav}} - [G_s]_{\alpha,GTP}^{ecav} - [G_s]_{\alpha,GDP}^{ecav} \tag{B.21}$$

$$[R_{\beta 1}]_{np,tot}^{ecav} = [R_{\beta 1}]_{tot}^{ecav} - [R_{\beta 1}]_{PKA,tot}^{ecav} - [R_{\beta 1}]_{GRK2,tot}^{ecav} \tag{B.22}$$

$$a_{\beta 1}^{ecav} = \frac{1}{K_{\beta 1,L}} \cdot \left(K_{\beta 1,L} + [L]\right) \cdot \left(K_{\beta 1,H} + [L]\right) \tag{B.23}$$

$$b_{\beta 1}^{ecav} = [G_s]_{\alpha\beta\gamma}^{ecav} \cdot \left(K_{\beta 1,H} + [L]\right) - [R_{\beta 1}]_{np,tot}^{ecav} \cdot \left(K_{\beta 1,H} + [L]\right) + K_{\beta 1,C} \cdot K_{\beta 1,H} \left(1 + \frac{[L]}{K_{\beta 1,L}}\right) \tag{B.24}$$

$$c_{\beta 1}^{ecav} = -[R_{\beta 1}]_{np,tot}^{ecav} \cdot K_{\beta 1,C} \cdot K_{\beta 1,H} \tag{B.25}$$

$$[R_{\beta 1}]_{np,f}^{ecav} = \frac{-b_{\beta 1}^{ecav} + \sqrt{[b_{\beta 1}^{ecav}]^2 - 4 \cdot a_{\beta 1}^{ecav} \cdot c_{\beta 1}^{ecav}}}{2 \cdot a_{\beta 1}^{ecav}} \tag{B.26}$$

$$[G_s]_f^{ecav} = \frac{[G_s]_{\alpha\beta\gamma}^{ecav}}{1 + [R_{\beta 1}]_{np,f}^{ecav} \left(\frac{1}{K_{\beta 1,C}} + \frac{[L]}{K_{\beta 1,C} \cdot K_{\beta 1,H}}\right)} \tag{B.27}$$

$$[LR_{\beta 1}]_{np}^{ecav} = \frac{[L] \cdot [R_{\beta 1}]_{np,f}^{ecav}}{K_{\beta 1,L}} \tag{B.28}$$

$$[R_{\beta 1} G_s]_{np}^{ecav} = \frac{[R_{\beta 1}]_{np,f}^{ecav} \cdot [G_s]_f^{ecav}}{K_{\beta 1,C}} \tag{B.29}$$

$$[LR_{\beta 1} G_s]_{np}^{ecav} = \frac{[L] \cdot [R_{\beta 1}]_{np,f}^{ecav} \cdot [G_s]_f^{ecav}}{K_{\beta 1,C} \cdot K_{\beta 1,H}} \tag{B.30}$$

$$\frac{d[R_{\beta 1}]_{PKA,tot}^{ecav}}{dt} = k_{PKA+} \cdot [C]^{ecav} \cdot [R_{\beta 1}]_{np,tot}^{ecav} - k_{PKA-} \cdot [R_{\beta 1}]_{PKA,tot}^{ecav} \tag{B.31}$$

$$\frac{d[R_{\beta 1}]_{GRK2,tot}^{ecav}}{dt} = k_{GRK2+} \cdot \left([LR_{\beta 1}]_{np}^{ecav} + [LR_{\beta 1} G_s]_{np}^{ecav}\right) - k_{GRK2-} \cdot [R_{\beta 1}]_{GRK2,tot}^{ecav} \tag{B.32}$$

$$\frac{d[G_s]_{\alpha,GTP}^{ecav}}{dt} = k_{act2,Gs} \cdot [R_{\beta 1} G_s]_{np}^{ecav} + k_{act1,Gs} \cdot [LR_{\beta 1} G_s]_{np}^{ecav} - k_{hyd,Gs} \cdot [G_s]_{\alpha,GTP}^{ecav} \tag{B.33}$$

$$\frac{d[G_s]_{\beta\gamma}^{ecav}}{dt} = k_{act2,Gs} \cdot [R_{\beta 1} G_s]_{np}^{ecav} + k_{act1,Gs} \cdot [LR_{\beta 1} G_s]_{np}^{ecav} - k_{reas,Gs} \cdot [G_s]_{\beta\gamma}^{ecav} \cdot [G_s]_{\alpha,GDP}^{ecav} \tag{B.34}$$

$$\frac{d[G_s]^{ecav}_{\alpha,GDP}}{dt} = k_{hyd,Gs}\cdot[G_s]^{ecav}_{\alpha,GTP} - k_{reas,Gs}\cdot[G_s]^{ecav}_{\beta\gamma}\cdot[G_s]^{ecav}_{\alpha,GDP} \tag{B.35}$$

Cytosol

$$[R_{\beta1}]^{cyt}_{tot} = \mathrm{f}^{cyt}_{\beta1}\cdot[R_{\beta1}]_{tot}\cdot\frac{V_{cell}}{V_{cyt}} \tag{B.36}$$

$$[G_s]^{cyt}_{\alpha\beta\gamma} = \mathrm{f}^{cyt}_{Gs}\cdot[G_s]_{tot}\cdot\frac{V_{cell}}{V_{cyt}} - [G_s]^{cyt}_{\alpha,GTP} - [G_s]^{cyt}_{\alpha,GDP} \tag{B.37}$$

$$[R_{\beta1}]^{cyt}_{np,tot} = [R_{\beta1}]^{cyt}_{tot} - [R_{\beta1}]^{cyt}_{PKA,tot} - [R_{\beta1}]^{cyt}_{GRK2,tot} \tag{B.38}$$

$$a^{cyt}_{\beta1} = \frac{1}{K_{\beta1,L}}\cdot\left(K_{\beta1,L}+[L]\right)\cdot\left(K_{\beta1,H}+[L]\right) \tag{B.39}$$

$$b^{cyt}_{\beta1} = [G_s]^{cyt}_{\alpha\beta\gamma}\cdot\left(K_{\beta1,H}+[L]\right) - [R_{\beta1}]^{cyt}_{np,tot}\cdot\left(K_{\beta1,H}+[L]\right) + K_{\beta1,C}\cdot K_{\beta1,H}\left(1+\frac{[L]}{K_{\beta1,L}}\right) \tag{B.40}$$

$$c^{cyt}_{\beta1} = -[R_{\beta1}]^{cyt}_{np,tot}\cdot K_{\beta1,C}\cdot K_{\beta1,H} \tag{B.41}$$

$$[R_{\beta1}]^{cyt}_{np,f} = \frac{-b^{cyt}_{\beta1} + \sqrt{[b^{cyt}_{\beta1}]^2 - 4\cdot a^{cyt}_{\beta1}\cdot c^{cyt}_{\beta1}}}{2\cdot a^{cyt}_{\beta1}} \tag{B.42}$$

$$[G_s]^{cyt}_{f} = \frac{[G_s]^{cyt}_{\alpha\beta\gamma}}{1+[R_{\beta1}]^{cyt}_{np,f}\left(\frac{1}{K_{\beta1,C}}+\frac{[L]}{K_{\beta1,C}\cdot K_{\beta1,H}}\right)} \tag{B.43}$$

$$[LR_{\beta1}]^{cyt}_{np} = \frac{[L]\cdot[R_{\beta1}]^{cyt}_{np,f}}{K_{\beta1,L}} \tag{B.44}$$

$$[R_{\beta1}G_s]^{cyt}_{np} = \frac{[R_{\beta1}]^{cyt}_{np,f}\cdot[G_s]^{cyt}_{f}}{K_{\beta1,C}} \tag{B.45}$$

$$[LR_{\beta1}G_s]^{cyt}_{np} = \frac{[L]\cdot[R_{\beta1}]^{cyt}_{np,f}\cdot[G_s]^{cyt}_{f}}{K_{\beta1,C}\cdot K_{\beta1,H}} \tag{B.46}$$

$$\frac{d[R_{\beta 1}]^{cyt}_{PKA,tot}}{dt} = k_{PKA+} \cdot [C]^{cyt} \cdot [R_{\beta 1}]^{cyt}_{np,tot} - k_{PKA-} \cdot [R_{\beta 1}]^{cyt}_{PKA,tot} \quad \text{(B.47)}$$

$$\frac{d[R_{\beta 1}]^{cyt}_{GRK2,tot}}{dt} = k_{GRK2+} \cdot \left([LR_{\beta 1}]^{cyt}_{np} + [LR_{\beta 1}G_s]^{cyt}_{np}\right) - k_{GRK2-} \cdot [R_{\beta 1}]^{cyt}_{GRK2,tot} \quad \text{(B.48)}$$

$$\frac{d[G_s]^{cyt}_{\alpha,GTP}}{dt} = k_{act2,Gs} \cdot [R_{\beta 1}G_s]^{cyt}_{np} + k_{act1,Gs} \cdot [LR_{\beta 1}G_s]^{cyt}_{np} - k_{hyd,Gs} \cdot [G_s]^{cyt}_{\alpha,GTP} \quad \text{(B.49)}$$

$$\frac{d[G_s]^{cyt}_{\beta\gamma}}{dt} = k_{act2,Gs} \cdot [R_{\beta 1}G_s]^{cyt}_{np} + k_{act1,Gs} \cdot [LR_{\beta 1}G_s]^{cyt}_{np} - k_{reas,Gs} \cdot [G_s]^{cyt}_{\beta\gamma} \cdot [G_s]^{cyt}_{\alpha,GDP} \quad \text{(B.50)}$$

$$\frac{d[G_s]^{cyt}_{\alpha,GDP}}{dt} = k_{hyd,Gs} \cdot [G_s]^{cyt}_{\alpha,GTP} - k_{reas,Gs} \cdot [G_s]^{cyt}_{\beta\gamma} \cdot [G_s]^{cyt}_{\alpha,GDP} \quad \text{(B.51)}$$

Adenylyl cyclase module

Para-meter	Definition	Value	Reference
$K_{m,ATP}$	Adenylyl cyclase affinity for ATP	340 μM	Bondarenko [16]
$[ATP]$	ATP concentration	5000 μM	Heijman et al. [34]
$[AC]_{tot}$	Total cellular AC concentration	0.02622 μM	Post et al. [110]
$f_{AC56,AC47}$	Fraction of AC that is of type 5 or 6	0.74	Heijman et al. [34]
f^{cav}_{AC56}	Fraction of AC5/6 located in caveolae	0.0875	Heijman et al. [34]
f^{ecav}_{AC47}	Fraction of AC4/7 located in extracaveolae space	0.1648	Heijman et al. [34]
$K^{AC56}_{m,Gs\alpha}$	AC5/6 affinity for $G_{s\alpha}$	0.0852 μM	Heijman et al. [34]
$h_{AC56,Gs\alpha}$	Hill coefficient for AC5/6 activation by $G_{s\alpha}$	1.357	Heijman et al. [34]
$V^{AC56}_{G\beta\gamma}$	Maximum amplification of AC5/6 by $G_{s\beta\gamma}$	1.430	Gao et al. [112]
$K^{AC56}_{m,Gs\beta\gamma}$	Affinity constant for $G_{s\beta\gamma}$ modulation of AC5/6	0.003793 μM	Gao et al. [112]
$h_{AC56,Gs\beta\gamma}$	Hill coefficient for $G_{s\beta\gamma}$ modulation of AC5/6	1.0842	Gao et al. [112]
$AC56_{basal}$	Basal AC5/6 activity	0.0377	Heijman et al. [34]
AF_{56}	Amplification factor for AC5/6	51.1335 s^{-1}	Bondarenko [16]
$K^{AC47}_{m,Gs\alpha}$	AC4/7 affinity for $G_{s\alpha}$	0.05008 μM	Zimmermann and Taussig [113]
$h_{AC47,Gs\alpha}$	Hill coefficient for AC4/7 activation by $G_{s\alpha}$	1.1657	Zimmermann and Taussig [113]
$V^{AC47}_{G\beta\gamma}$	Maximum amplification of AC4/7 by $G_{s\beta\gamma}$	1.3500	Zimmermann and Taussig [113]

$K_{m,Gs\beta\gamma}^{AC47}$	Affinity constant for $G_{s\beta\gamma}$ modulation of AC4/7	0.004466 μM	Zimmermann and Taussig [113]
$h_{AC47,Gs\beta\gamma}$	Hill coefficient for $G_{s\beta\gamma}$ modulation of AC4/7	0.8700	Zimmermann and Taussig [113]
$AC47_{basal}$	Basal AC4/7 activity	0.04725	Bondarenko [16]
AF_{47}	Amplification factor for AC4/7	9.283 s^{-1}	Bondarenko [16]

Caveolae

$$[AC56]^{cav} = \mathrm{f}_{AC56}^{cav} \cdot \mathrm{f}_{AC56,AC47} \cdot [AC]_{tot} \cdot \frac{V_{cell}}{V_{cav}} \tag{B.52}$$

$$k_{AC56}^{cav} = AF_{56} \cdot \left(AC56_{basal} + \frac{\left([G_s]_{\alpha,GTP}^{cav}\right)^{h_{AC56,Gs\alpha}}}{K_{m,Gs\alpha}^{AC56} + \left([G_s]_{\alpha,GTP}^{cav}\right)^{h_{AC56,Gs\alpha}}} \right) \cdot \left(1 + \frac{V_{G\beta\gamma}^{AC56} \cdot \left([G_s]_{\beta\gamma}^{cav}\right)^{h_{AC56,Gs\beta\gamma}}}{K_{m,Gs\beta\gamma}^{AC56} + \left([G_s]_{\beta\gamma}^{cav}\right)^{h_{AC56,Gs\beta\gamma}}} \right) \tag{B.53}$$

$$\frac{d[cAMP]_{AC56}^{cav}}{dt} = k_{AC56}^{cav} \cdot \frac{[AC56]^{cav} \cdot [ATP]}{K_{m,ATP} + [ATP]} \tag{B.54}$$

Extracaveolae

$$[AC47]^{ecav} = \mathrm{f}_{AC47}^{ecav} \cdot (1 - \mathrm{f}_{AC56,AC47}) \cdot [AC]_{tot} \cdot \frac{V_{cell}}{V_{ecav}} \tag{B.55}$$

$$k_{AC47}^{ecav} = AF_{47} \cdot \left(AC47_{basal} + \frac{\left([G_s]_{\alpha,GTP}^{ecav}\right)^{h_{AC47,Gs\alpha}}}{K_{m,Gs\alpha}^{AC47} + \left([G_s]_{\alpha,GTP}^{ecav}\right)^{h_{AC47,Gs\alpha}}} \right) \cdot \left(1 + \frac{V_{G\beta\gamma}^{AC47} \cdot \left([G_s]_{\beta\gamma}^{ecav}\right)^{h_{AC47,Gs\beta\gamma}}}{K_{m,Gs\beta\gamma}^{AC47} + \left([G_s]_{\beta\gamma}^{ecav}\right)^{h_{AC47,Gs\beta\gamma}}} \right) \tag{B.56}$$

$$\frac{d[cAMP]_{AC47}^{ecav}}{dt} = k_{AC47}^{ecav} \cdot \frac{[AC47]^{ecav} \cdot [ATP]}{K_{m,ATP} + [ATP]} \tag{B.57}$$

Cytosol

$$[AC56]^{cyt} = (1 - \mathrm{f}_{AC56}^{cav}) \cdot \mathrm{f}_{AC56,AC47} \cdot [AC]_{tot} \cdot \frac{V_{cell}}{V_{cyt}} \tag{B.58}$$

$$[AC47]^{cyt} = (1 - \mathrm{f}_{AC47}^{ecav}) \cdot (1 - \mathrm{f}_{AC56,AC47}) \cdot [AC]_{tot} \cdot \frac{V_{cell}}{V_{cyt}} \tag{B.59}$$

$$k_{AC56}^{cyt} = AF_{56} \cdot \left(AC56_{basal} + \frac{\left([G_s]_{\alpha,GTP}^{cyt}\right)^{h_{AC56,Gs\alpha}}}{K_{m,Gs\alpha}^{AC56} + \left([G_s]_{\alpha,GTP}^{cyt}\right)^{h_{AC56,Gs\alpha}}} \right) \cdot \left(1 + \frac{V_{G\beta\gamma}^{AC56} \cdot \left([G_s]_{\beta\gamma}^{cyt}\right)^{h_{AC56,Gs\beta\gamma}}}{K_{m,Gs\beta\gamma}^{AC56} + \left([G_s]_{\beta\gamma}^{cyt}\right)^{h_{AC56,Gs\beta\gamma}}} \right) \tag{B.60}$$

$$\frac{d[cAMP]_{AC56}^{cyt}}{dt} = k_{AC56}^{cyt} \cdot \frac{[AC56]^{cyt} \cdot [ATP]}{K_{m,ATP} + [ATP]} \tag{B.61}$$

$$k_{AC47}^{cyt} = AF_{47} \cdot \left(AC47_{basal} + \frac{\left([G_s]_{\alpha,GTP}^{cyt}\right)^{h_{AC47,Gs\alpha}}}{K_{m,Gs\alpha}^{AC47} + \left([G_s]_{\alpha,GTP}^{cyt}\right)^{h_{AC47,Gs\alpha}}} \right) \cdot \left(1 + \frac{V_{G\beta\gamma}^{AC47} \cdot \left([G_s]_{\beta\gamma}^{cyt}\right)^{h_{AC47,Gs\beta\gamma}}}{K_{m,Gs\beta\gamma}^{AC47} + \left([G_s]_{\beta\gamma}^{cyt}\right)^{h_{AC47,Gs\beta\gamma}}} \right) \tag{B.62}$$

$$\frac{d[cAMP]_{AC47}^{cyt}}{dt} = k_{AC47}^{cyt} \cdot \frac{[AC47]^{cyt} \cdot [ATP]}{K_{m,ATP} + [ATP]} \tag{B.63}$$

Phosphodiesterase module

Parameter	Definition	Value	Reference
$[IBMX]$	Concentration of IBMX	0…100 µM	
$h_{IBMX,PDE2}$	Hill coefficient for inhibition of PDE2 by IBMX	1.000	Bondarenko [16]
K_{PDE2}^{IBMX}	Affinity of IBMX for PDE2	29.50 µM	Bondarenko [16]
$h_{IBMX,PDE3}$	Hill coefficient for inhibition of PDE3 by IBMX	1.000	Bondarenko [16]
K_{PDE3}^{IBMX}	Affinity of IBMX for PDE3	5.100 µM	Bondarenko [16]
$h_{IBMX,PDE4}$	Hill coefficient for inhibition of PDE4 by IBMX	1.000	Bondarenko [16]
K_{PDE4}^{IBMX}	Affinity of IBMX for PDE4	16.200 µM	Bondarenko [16]
$k_{f,PDEp}$	Rate of phosphorylation of PDE3/4 by PKA	0.0196 μM^{-1} s^{-1}	Heijman et al. [34]
$k_{b,PDEp}$	Rate of dephosphorylation of PDE3/4 by PKA	0.0102 s^{-1}	Heijman et al. [34]
$\Delta_{k,PDE3/4}$	Increase in PDE3/4 activity after phosphorylation	3.0	Heijman et al. [34]
k_{PDE2}	Rate of cAMP hydrolysis by PDE2	20 s^{-1}	Iancu et al. [114]
$K_{m,PDE2}$	Affinity of PDE2 for cAMP	33 µM	Bode et al. [115]
k_{PDE3}	Rate of cAMP hydrolysis by PDE3	2.5 s^{-1}	Heijman et al. [34]
$K_{m,PDE3}$	Affinity of PDE3 for cAMP	0.44 µM	Bode et al. [115]
k_{PDE4}	Rate of cAMP hydrolysis by PDE4	3.5 s^{-1}	Bondarenko [16]
$K_{m,PDE4}$	Affinity of PDE4 for cAMP	1.4 µM	Bondarenko [16]
$f_{PDE,part}$	Fraction of total PDE located in the particulate fraction	0.2	Osadchii [116]
$r_{part,PDE2,PDE3}$	Ratio of PDE2 and PDE3 activities in particulate fraction	0.570	Mongillo et al. [117]

$r_{part,PDE3,PDE4}$	Ratio of PDE3 and PDE4 activities in particulate fraction	0.748	Mongillo et al. [117]
$[PDE2]_{tot}$	Total cellular concentration of PDE2	0.034610 μM	Bondarenko [16]
$[PDE3]_{tot}$	Total cellular concentration of PDE3	0.010346 μM	Bondarenko [16]
$[PDE4]_{tot}$	Total cellular concentration of PDE4	0.026687 μM	Bondarenko [16]
f_{PDE2}^{cav}	Fraction of PDE2 located in caveolae	0.06608	Bondarenko [16]
f_{PDE2}^{ecav}	Fraction of PDE2 located in extracaveolae	$2 \cdot \mathrm{f}_{PDE2}^{cav}$	Bondarenko [16]
f_{PDE2}^{cyt}	Fraction of PDE2 located in cytosol	$1 - \mathrm{f}_{PDE2}^{cav} - \mathrm{f}_{PDE2}^{ecav}$	Bondarenko [16]
f_{PDE3}^{cav}	Fraction of PDE3 located in caveolae	0.29814	Bondarenko [16]
f_{PDE3}^{ecav}	Fraction of PDE3 located in extracaveolae	0.0	Bondarenko [16]
f_{PDE3}^{cyt}	Fraction of PDE3 located in cytosol	$1 - \mathrm{f}_{PDE3}^{cav} - \mathrm{f}_{PDE3}^{ecav}$	Bondarenko [16]
f_{PDE4}^{cav}	Fraction of PDE4 located in caveolae	0.05366	Bondarenko [16]
f_{PDE4}^{ecav}	Fraction of PDE4 located in extracaveolae	$2 \cdot \mathrm{f}_{PDE4}^{cav}$	Bondarenko [16]
f_{PDE4}^{cyt}	Fraction of PDE4 located in cytosol	$1 - \mathrm{f}_{PDE4}^{cav} - \mathrm{f}_{PDE4}^{ecav}$	Bondarenko [16]

Caveolae

$$[PDE2]_{tot}^{cav} = \left(1 - \frac{[IBMX]^{h_{IBMX,PDE2}}}{K_{m,PDE2}^{IBMX} + [IBMX]^{h_{IBMX,PDE2}}}\right) \cdot \mathrm{f}_{PDE2}^{cav} \cdot [PDE2]_{tot} \cdot \frac{V^{cell}}{V^{cav}} \tag{B.64}$$

$$[PDE3]_{tot}^{cav} = \left(1 - \frac{[IBMX]^{h_{IBMX,PDE3}}}{K_{m,PDE3}^{IBMX} + [IBMX]^{h_{IBMX,PDE3}}}\right) \cdot \mathrm{f}_{PDE3}^{cav} \cdot [PDE3]_{tot} \cdot \frac{V^{cell}}{V^{cav}} \tag{B.65}$$

$$[PDE4]_{tot}^{cav} = \left(1 - \frac{[IBMX]^{h_{IBMX,PDE4}}}{K_{m,PDE4}^{IBMX} + [IBMX]^{h_{IBMX,PDE4}}}\right) \cdot \mathrm{f}_{PDE4}^{cav} \cdot [PDE4]_{tot} \cdot \frac{V^{cell}}{V^{cav}} \tag{B.66}$$

$$\frac{d[PDE3]_{p}^{cav}}{dt} = k_{f,PDEp} \cdot [C]^{cav} \cdot ([PDE3]_{tot}^{cav} - [PDE3]_{p}^{cav}) - k_{b,PDEp} \cdot [PDE3]_{p}^{cav} \tag{B.67}$$

$$\frac{d[PDE4]_{p}^{cav}}{dt} = k_{f,PDEp} \cdot [C]^{cav} \cdot ([PDE4]_{tot}^{cav} - [PDE4]_{p}^{cav}) - k_{b,PDEp} \cdot [PDE4]_{p}^{cav} \tag{B.68}$$

$$\frac{d[cAMP]_{PDE2}^{cav}}{dt} = \frac{k_{PDE2} \cdot [PDE2]_{tot}^{cav} \cdot [cAMP]^{cav}}{K_{m,PDE2} + [cAMP]^{cav}} \tag{B.69}$$

$$\frac{d[cAMP]^{cav}_{PDE3}}{dt} = \frac{k_{PDE3}\cdot([PDE3]^{cav}_{tot} - [PDE3]^{cav}_{p})\cdot[cAMP]^{cav} + \Delta_{k,PDE3/4}\cdot k_{PDE3}\cdot[PDE3]^{cav}_{p}\cdot[cAMP]^{cav}}{K_{m,PDE3} + [cAMP]^{cav}} \quad \text{(B.70)}$$

$$\frac{d[cAMP]^{cav}_{PDE4}}{dt} = \frac{k_{PDE4}\cdot([PDE4]^{cav}_{tot} - [PDE4]^{cav}_{p})\cdot[cAMP]^{cav} + \Delta_{k,PDE3/4}\cdot k_{PDE4}\cdot[PDE4]^{cav}_{p}\cdot[cAMP]^{cav}}{K_{m,PDE4} + [cAMP]^{cav}} \quad \text{(B.71)}$$

Extracaveolae

$$[PDE2]^{ecav}_{tot} = \left(1 - \frac{[IBMX]^{h_{IBMX,PDE2}}}{K^{IBMX}_{m,PDE2} + [IBMX]^{h_{IBMX,PDE2}}}\right)\cdot \mathrm{f}^{ecav}_{PDE2}\cdot[PDE2]_{tot}\cdot\frac{V^{cell}}{V^{ecav}} \quad \text{(B.72)}$$

$$[PDE4]^{ecav}_{tot} = \left(1 - \frac{[IBMX]^{h_{IBMX,PDE4}}}{K^{IBMX}_{m,PDE4} + [IBMX]^{h_{IBMX,PDE4}}}\right)\cdot \mathrm{f}^{ecav}_{PDE4}\cdot[PDE4]_{tot}\cdot\frac{V^{cell}}{V^{ecav}} \quad \text{(B.73)}$$

$$\frac{d[PDE4]^{ecav}_{p}}{dt} = k_{f,PDEp}\cdot[C]^{ecav}\cdot([PDE4]^{ecav}_{tot} - [PDE4]^{ecav}_{p}) - k_{b,PDEp}\cdot[PDE4]^{ecav}_{p} \quad \text{(B.74)}$$

$$\frac{d[cAMP]^{ecav}_{PDE2}}{dt} = \frac{k_{PDE2}\cdot[PDE2]^{ecav}_{tot}\cdot[cAMP]^{ecav}}{K_{m,PDE2} + [cAMP]^{ecav}} \quad \text{(B.75)}$$

$$\frac{d[cAMP]^{ecav}_{PDE4}}{dt} = \frac{k_{PDE4}\cdot([PDE4]^{ecav}_{tot} - [PDE4]^{ecav}_{p})\cdot[cAMP]^{ecav} + \Delta_{k,PDE3/4}\cdot k_{PDE4}\cdot[PDE4]^{ecav}_{p}\cdot[cAMP]^{ecav}}{K_{m,PDE4} + [cAMP]^{ecav}} \quad \text{(B.76)}$$

Cytosol

$$[PDE2]^{cyt}_{tot} = \left(1 - \frac{[IBMX]^{h_{IBMX,PDE2}}}{K^{IBMX}_{m,PDE2} + [IBMX]^{h_{IBMX,PDE2}}}\right)\cdot \mathrm{f}^{cyt}_{PDE2}\cdot[PDE2]_{tot}\cdot\frac{V^{cell}}{V^{cyt}} \quad \text{(B.77)}$$

$$[PDE3]^{cyt}_{tot} = \left(1 - \frac{[IBMX]^{h_{IBMX,PDE3}}}{K^{IBMX}_{m,PDE3} + [IBMX]^{h_{IBMX,PDE3}}}\right)\cdot \mathrm{f}^{cyt}_{PDE3}\cdot[PDE3]_{tot}\cdot\frac{V^{cell}}{V^{cyt}} \quad \text{(B.78)}$$

$$[PDE4]^{cyt}_{tot} = \left(1 - \frac{[IBMX]^{h_{IBMX,PDE4}}}{K^{IBMX}_{m,PDE4} + [IBMX]^{h_{IBMX,PDE4}}}\right)\cdot \mathrm{f}^{cyt}_{PDE4}\cdot[PDE4]_{tot}\cdot\frac{V^{cell}}{V^{cyt}} \quad \text{(B.79)}$$

$$\frac{d[PDE3]^{cyt}_{p}}{dt} = k_{f,PDEp}\cdot[C]^{cyt}\cdot([PDE3]^{cyt}_{tot} - [PDE3]^{cyt}_{p}) - k_{b,PDEp}\cdot[PDE3]^{cyt}_{p} \quad \text{(B.80)}$$

$$\frac{d[PDE4]^{cyt}_{p}}{dt} = k_{f,PDEp}\cdot[C]^{cyt}\cdot([PDE4]^{cyt}_{tot} - [PDE4]^{cyt}_{p}) - k_{b,PDEp}\cdot[PDE4]^{cyt}_{p} \quad \text{(B.81)}$$

$$\frac{d[cAMP]^{cyt}_{PDE2}}{dt} = \frac{k_{PDE2} \cdot [PDE2]^{cyt}_{tot} \cdot [cAMP]^{cyt}}{K_{m,PDE2} + [cAMP]^{cyt}} \tag{B.82}$$

$$\frac{d[cAMP]^{cyt}_{PDE3}}{dt} = \frac{k_{PDE3} \cdot ([PDE3]^{cyt}_{tot} - [PDE3]^{cyt}_{p}) \cdot [cAMP]^{cyt} + \Delta_{k,PDE3/4} \cdot k_{PDE3} \cdot [PDE3]^{cyt}_{p} \cdot [cAMP]^{cyt}}{K_{m,PDE3} + [cAMP]^{cyt}} \tag{B.83}$$

$$\frac{d[cAMP]^{cyt}_{PDE4}}{dt} = \frac{k_{PDE4} \cdot ([PDE4]^{cyt}_{tot} - [PDE4]^{cyt}_{p}) \cdot [cAMP]^{cyt} + \Delta_{k,PDE3/4} \cdot k_{PDE4} \cdot [PDE4]^{cyt}_{p} \cdot [cAMP]^{cyt}}{K_{m,PDE4} + [cAMP]^{cyt}} \tag{B.84}$$

cAMP-PKA module

Parameter	Definition	Value	Reference
$[PKA]_{tot}$	Total cellular concentration of PKA holoenzyme	0.5176 μM	Bondarenko [16]
f^{cav}_{PKA}	Fraction of PKA located in caveolae	0.08	Bondarenko [16]
f^{ecav}_{PKA}	Fraction of PKA located in extracaveolae	0.20	Bondarenko [16]
f^{cyt}_{PKA}	Fraction of PKA located in cytosol	$1 - \mathrm{f}^{cav}_{PKA} - \mathrm{f}^{ecav}_{PKA}$	
$[PKI]_{tot}$	Total cellular concentration of PKA inhibitor	$2 \cdot 0.2 \cdot [PKA]_{\mathrm{tot}}$	Beavo et al. [118]
f^{cav}_{PKI}	Fraction of PKI located in caveolae	f^{cav}_{PKA}	
f^{ecav}_{PKI}	Fraction of PKI located in extracaveolae	f^{ecav}_{PKA}	
f^{cyt}_{PKI}	Fraction of PKI located in cytosol	f^{cyt}_{PKA}	
$k_{PKAI,f1}$	Forward rate for binding of the first cAMP to PKA	5.6 $\mu M^{-1}\ s^{-1}$	Bondarenko [16]
$K_{PKAI,1}$	Equilibrium value for the binding of the first cAMP to PKA	2.9 μM	Dao et al. [119]
$k_{PKAI,f2}$	Forward rate for binding of the second cAMP to PKA	$k_{PKAI,f1}$	Bondarenko [16]
$K_{PKAI,2}$	Equilibrium value for binding of the second cAMP to PKA	2.9 μM	Dao et al. [119]
$k_{PKAI,f3}$	Forward rate for dissociation of C subunit	2.6 s^{-1}	Bondarenko [16]
$K_{PKAI,3}$	Equilibrium value for dissociation of C subunit	1.3 μM	Bondarenko [16]
$k_{PKI,f}$	Forward rate for inhibition of C subunit by PKI	50 $\mu M^{-1}\ s^{-1}$	Heijman et al. [34]
K_{PKI}	Equilibrium value for inhibition of C subunit by PKI	$2.6 \cdot 10^{-4}$ μM	Bondarenko [16]
$k_{PKAII,f1}$	Forward rate for binding of the first cAMP to PKA	$k_{PKAI,f1}$	Heijman et al. [34]
$K_{PKAII,1}$	Equilibrium value for the binding of the first cAMP to PKA	2.5 μM	Heijman et al. [34]

$k_{PKAII,f2}$	Forward rate for binding of the second cAMP to PKA	$k_{PKAI,f1}$	Heijman et al. [34]
$K_{PKAII,2}$	Equilibrium value for binding of the second cAMP to PKA	2.5 μM	Heijman et al. [34]
$k_{PKAII,f3}$	Forward rate for dissociation of C subunit	$k_{PKAI,f3}$	Bondarenko [16]
$K_{PKAII,3}$	Equilibrium value for dissociation of C subunit	$K_{PKAI,3}$	Bondarenko [16]

Caveolae

$$[PKA]^{cav} = \mathrm{f}_{PKA}^{cav} \cdot [PKA]_{tot} \cdot \frac{V^{cell}}{V^{cav}} \tag{B.85}$$

$$[RC]_f^{cav} = 2 \cdot [PKA]^{cav} - [ARC]^{cav} - [A_2RC]^{cav} - [A_2R]^{cav} \tag{B.86}$$

$$[PKI]_f^{cav} = \mathrm{f}_{PKI}^{cav} \cdot [PKI]_{tot} \cdot \frac{V^{cell}}{V^{cav}} - [PKIC]^{cav} \tag{B.87}$$

$$k_{PKAII,b1} = k_{PKAII,f1} \cdot K_{PKAII,1} \tag{B.88}$$

$$k_{PKAII,b2} = k_{PKAII,f2} \cdot K_{PKAII,2} \tag{B.89}$$

$$k_{PKAII,b3} = k_{PKAII,f3} / K_{PKAII,3} \tag{B.90}$$

$$k_{PKI,b} = k_{PKI,f} \cdot K_{PKI} \tag{B.91}$$

$$\begin{aligned} \frac{d[cAMP]_{PKA}^{cav}}{dt} &= -k_{PKAII,f1} \cdot [RC]_f^{cav} \cdot [cAMP]^{cav} + k_{PKAII,b1} \cdot [ARC]^{cav} \\ &\quad - k_{PKAII,f2} \cdot [ARC]^{cav} \cdot [cAMP]^{cav} + k_{PKAII,b2} \cdot [A_2RC]^{cav} \end{aligned} \tag{B.92}$$

$$\begin{aligned} \frac{d[ARC]^{cav}}{dt} &= k_{PKAII,f1} \cdot [RC]_f^{cav} \cdot [cAMP]^{cav} - k_{PKAII,b1} \cdot [ARC]^{cav} \\ &\quad - k_{PKAII,f2} \cdot [ARC]^{cav} \cdot [cAMP]^{cav} + k_{PKAII,b2} \cdot [A_2RC]^{cav} \end{aligned} \tag{B.93}$$

$$\begin{aligned} \frac{d[A_2RC]^{cav}}{dt} &= k_{PKAII,f2} \cdot [ARC]^{cav} \cdot [cAMP]^{cav} - (k_{PKAII,b2} + k_{PKAII,f3}) \cdot [A_2RC]^{cav} \\ &\quad + k_{PKAII,b3} \cdot [A_2R]^{cav} \cdot [C]^{cav} \end{aligned} \tag{B.94}$$

$$\frac{d[A_2R]^{cav}}{dt} = k_{PKAII,f3} \cdot [A_2RC]^{cav} - k_{PKAII,b3} \cdot [A_2R]^{cav} \cdot [C]^{cav} \tag{B.95}$$

$$\frac{d[C]^{cav}}{dt} = k_{PKAII,f3} \cdot [A_2RC]^{cav} - k_{PKAII,b3} \cdot [A_2R]^{cav} \cdot [C]^{cav} + k_{PKI,b} \cdot [PKIC]^{cav} - k_{PKI,f} \cdot [PKI]_f^{cav} \cdot [C]^{cav} \quad \text{(B.96)}$$

$$\frac{d[PKIC]^{cav}}{dt} = -k_{PKI,b} \cdot [PKIC]^{cav} + k_{PKI,f} \cdot [PKI]_f^{cav} \cdot [C]^{cav} \quad \text{(B.97)}$$

Extracaveolae

$$[PKA]^{ecav} = \mathrm{f}_{PKA}^{ecav} \cdot [PKA]_{tot} \cdot \frac{V^{cell}}{V^{ecav}} \quad \text{(B.98)}$$

$$[RC]_f^{ecav} = 2 \cdot [PKA]^{ecav} - [ARC]^{ecav} - [A_2RC]^{ecav} - [A_2R]^{ecav} \quad \text{(B.99)}$$

$$[PKI]_f^{ecav} = \mathrm{f}_{PKI}^{ecav} \cdot [PKI]_{tot} \cdot \frac{V^{cell}}{V^{ecav}} - [PKIC]^{ecav} \quad \text{(B.100)}$$

$$k_{PKAII,b1} = k_{PKAII,f1} \cdot K_{PKAII,1} \quad \text{(B.101)}$$

$$k_{PKAII,b2} = k_{PKAII,f2} \cdot K_{PKAII,2} \quad \text{(B.102)}$$

$$k_{PKAII,b3} = k_{PKAII,f3} / K_{PKAII,3} \quad \text{(B.103)}$$

$$k_{PKI,b} = k_{PKI,f} \cdot K_{PKI} \quad \text{(B.104)}$$

$$\frac{d[cAMP]_{PKA}^{ecav}}{dt} = -k_{PKAII,f1} \cdot [RC]_f^{ecav} \cdot [cAMP]^{ecav} + k_{PKAII,b1} \cdot [ARC]^{ecav} - k_{PKAII,f2} \cdot [ARC]^{ecav} \cdot [cAMP]^{ecav} + k_{PKAII,b2} \cdot [A_2RC]^{ecav} \quad \text{(B.105)}$$

$$\frac{d[ARC]^{ecav}}{dt} = k_{PKAII,f1} \cdot [RC]_f^{ecav} \cdot [cAMP]^{ecav} - k_{PKAII,b1} \cdot [ARC]^{ecav} - k_{PKAII,f2} \cdot [ARC]^{ecav} \cdot [cAMP]^{ecav} + k_{PKAII,b2} \cdot [A_2RC]^{ecav} \quad \text{(B.106)}$$

$$\frac{d[A_2RC]^{ecav}}{dt} = k_{PKAII,f2} \cdot [ARC]^{ecav} \cdot [cAMP]^{ecav} - (k_{PKAII,b2} + k_{PKAII,f3}) \cdot [A_2RC]^{ecav} + k_{PKAII,b3} \cdot [A_2R]^{ecav} \cdot [C]^{ecav} \quad \text{(B.107)}$$

$$\frac{d[A_2R]^{ecav}}{dt} = k_{PKAII,f3} \cdot [A_2RC]^{ecav} - k_{PKAII,b3} \cdot [A_2R]^{ecav} \cdot [C]^{ecav} \quad \text{(B.108)}$$

$$\frac{d[C]^{ecav}}{dt} = k_{PKAII,f3} \cdot [A_2RC]^{ecav} - k_{PKAII,b3} \cdot [A_2R]^{ecav} \cdot [C]^{ecav} + k_{PKI,b} \cdot [PKIC]^{ecav} - k_{PKI,f} \cdot [PKI]_f^{ecav} \cdot [C]^{ecav} \quad \text{(B.109)}$$

$$\frac{d[PKIC]^{ecav}}{dt} = -k_{PKI,b} \cdot [PKIC]^{ecav} + k_{PKI,f} \cdot [PKI]_f^{ecav} \cdot [C]^{ecav} \quad \text{(B.110)}$$

Cytosol

$$[PKA]^{cyt} = \mathrm{f}_{PKA}^{cyt} \cdot [PKA]_{tot} \cdot \frac{V^{cell}}{V^{cyt}} \quad \text{(B.111)}$$

$$[RC]_f^{cyt} = 2 \cdot [PKA]^{cyt} - [ARC]^{cyt} - [A_2RC]^{cyt} - [A_2R]^{cyt} \quad \text{(B.112)}$$

$$[PKI]_f^{cyt} = \mathrm{f}_{PKI}^{cyt} \cdot [PKI]_{tot} \cdot \frac{V^{cell}}{V^{cyt}} - [PKIC]^{cyt} \quad \text{(B.113)}$$

$$k_{PKAI,b1} = k_{PKAI,f1} \cdot K_{PKAI,1} \quad \text{(B.114)}$$

$$k_{PKAI,b2} = k_{PKAI,f2} \cdot K_{PKAI,2} \quad \text{(B.115)}$$

$$k_{PKAI,b3} = k_{PKAI,f3} / K_{PKAI,3} \quad \text{(B.116)}$$

$$k_{PKI,b} = k_{PKI,f} \cdot K_{PKI} \quad \text{(B.117)}$$

$$\frac{d[cAMP]_{PKA}^{cyt}}{dt} = -k_{PKAI,f1} \cdot [RC]_f^{cyt} \cdot [cAMP]^{cyt} + k_{PKAI,b1} \cdot [ARC]^{cyt} - k_{PKAI,f2} \cdot [ARC]^{cyt} \cdot [cAMP]^{cyt} + k_{PKAI,b2} \cdot [A_2RC]^{cyt} \quad \text{(B.118)}$$

$$\frac{d[ARC]^{cyt}}{dt} = k_{PKAI,f1} \cdot [RC]_f^{cyt} \cdot [cAMP]^{cyt} - k_{PKAI,b1} \cdot [ARC]^{cyt} - k_{PKAI,f2} \cdot [ARC]^{cyt} \cdot [cAMP]^{cyt} + k_{PKAI,b2} \cdot [A_2RC]^{cyt} \quad \text{(B.119)}$$

$$\frac{d[A_2RC]^{cyt}}{dt} = k_{PKAI,f2} \cdot [ARC]^{cyt} \cdot [cAMP]^{cyt} - (k_{PKAI,b2} + k_{PKAI,f3}) \cdot [A_2RC]^{cyt} + k_{PKAI,b3} \cdot [A_2R]^{cyt} \cdot [C]^{cyt} \quad \text{(B.120)}$$

$$\frac{d[A_2R]^{cyt}}{dt} = k_{PKAI,f3} \cdot [A_2RC]^{cyt} - k_{PKAI,b3} \cdot [A_2R]^{cyt} \cdot [C]^{cyt} \quad \text{(B.121)}$$

$$\frac{d[C]^{cyt}}{dt} = k_{PKAI,f3} \cdot [A_2RC]^{cyt} - k_{PKAI,b3} \cdot [A_2R]^{cyt} \cdot [C]^{cyt} + k_{PKI,b} \cdot [PKIC]^{cyt} - k_{PKI,f} \cdot [PKI]_f^{cyt} \cdot [C]^{cyt} \quad \text{(B.122)}$$

$$\frac{d[PKIC]^{cyt}}{dt} = -k_{PKI,b} \cdot [PKIC]^{cyt} + k_{PKI,f} \cdot [PKI]_f^{cyt} \cdot [C]^{cyt} \quad \text{(B.123)}$$

Protein phosphatases and inhibitor-1 module

Parameter	Definition	Value	Reference
$[PP1]_{tot}^{cyt}$	Total concentration of PP1 in the cytosolic compartment	0.2 μM	Heijman et al. [34]
$[PP1]^{cyt}$	Cytosolic concentration of PP1	0.0607843 μM	This paper
$[PP2A]^{cyt}$	Cytosolic concentration of PP2A	0.0607843 μM	Bondarenko [16]
$[PP1]^{cav}$	Concentration of PP1 in the caveolae compartment	0.1 μM	Bondarenko [16]
$[PP2A]^{cav}$	Concentration of PP2A in the caveolae compartment	0.1 μM	Bondarenko [16]
$[PP]^{cav}$	Total phosphatase concentration in caveolae compartment $[PP1]^{cav} + [PP2A]^{cav}$	0.2 μM	Bondarenko [16]
$[PP1]^{ecav}$	Concentration of PP1 in the extracaveolae compartment	0.1 μM	Heijman et al. [34]
$[Inhib1]_{tot}^{cyt}$	Total concentration of inhibitor 1 in the cytosolic compartment	0.08543 μM	El-Armouche et al. [120]
K_{inhib1}	Affinity for PP1 – Inhibitor 1 binding	$1.0 \cdot 10^{-3}$ μM	Saucerman et al. [30]
k_{PKA_Inhib1}	Rate of phosphorylation of inhibitor 1 by PKA	1080.0 μM^{-1} s^{-1}	Bondarenko [16]
K_{mPKA_Inhib1}	Affinity of inhibitor 1 for PKA catalytic subunit	1.5 μM	Bondarenko [16]
k_{PP2A_Inhib1}	Rate of dephosphorylation of inhibitor 1	50.67 μM^{-1} s^{-1}	Bondarenko [16]
K_{mPP2A_Inhib1}	Affinity for PP2A – Inhibitor 1 binding	$1.0 \cdot 10^{-3}$ μM	Bondarenko [16]

$$[Inhib1]_f^{cyt} = [Inhib1]_{tot}^{cyt} - [Inhib1]_{p,tot}^{cyt} \quad \text{(B.124)}$$

$$a_{Inhib1} = 1.0 \quad \text{(B.125)}$$

$$b_{Inhib1} = K_{Inhib1} + [PP1]_{tot}^{cyt} - [Inhib1]_{p,tot}^{cyt} \quad \text{(B.126)}$$

$$c_{Inhib1} = -[Inhib1]_{p,tot}^{cyt} \cdot K_{Inhib1} \quad \text{(B.127)}$$

$$[Inhib1]_p^{cyt} = \frac{-b_{Inhib1} + \sqrt{[b_{Inhib1}]^2 - 4 \cdot a_{Inhib1} \cdot c_{Inhib1}}}{2 \cdot a_{Inhib1}} \tag{B.128}$$

$$[PP1]_f^{cyt} = \frac{[PP1]_{tot}^{cyt} \cdot K_{Inhib1}}{K_{Inhib1} + [Inhib1]_p^{cyt}} \tag{B.129}$$

$$\frac{d[Inhib1]_{p,tot}^{cyt}}{dt} = \frac{k_{PKA\_Inhib1} \cdot [C]^{cyt} \cdot [Inhib1]_f^{cyt}}{K_{mPKA\_Inhib1} + [Inhib1]_f^{cyt}} - \frac{k_{PP2A\_Inhib1} \cdot [PP2A]^{cyt} \cdot [Inhib1]_{p,tot}^{cyt}}{K_{mPP2A\_Inhib1} + [Inhib1]_{p,tot}^{cyt}} \tag{B.130}$$

cAMP fluxes

Parameter	Definition	Value	Reference
$J_{cav/ecav}$	Rate of cAMP diffusion between caveolae and extracaveolae compartments	$5.000 \cdot 10^{-9}$ μL s^{-1}	Iancu et al. [114]
$J_{cav/cyt}$	Rate of cAMP diffusion between caveolae and cytosolic compartments	$7.500 \cdot 10^{-8}$ μL s^{-1}	Iancu et al. [114]
$J_{ecav/cyt}$	Rate of cAMP diffusion between extracaveolae and cytosolic compartments	$9.000 \cdot 10^{-9}$ μL s^{-1}	Iancu et al. [114]

$$\begin{aligned}\frac{d[cAMP]^{cav}}{dt} = {} & \frac{d[cAMP]_{PKA}^{cav}}{dt} + \frac{d[cAMP]_{AC56}^{cav}}{dt} - \frac{d[cAMP]_{PDE2}^{cav}}{dt} - \frac{d[cAMP]_{PDE3}^{cav}}{dt} \\ & - \frac{d[cAMP]_{PDE4}^{cav}}{dt} - J_{cav/ecav} \cdot \frac{[cAMP]^{cav} - [cAMP]^{ecav}}{V_{cav}} \\ & - J_{cav/cyt} \cdot \frac{[cAMP]^{cav} - [cAMP]^{cyt}}{V_{cav}}\end{aligned} \tag{B.131}$$

$$\begin{aligned}\frac{d[cAMP]^{ecav}}{dt} = {} & \frac{d[cAMP]_{PKA}^{ecav}}{dt} + \frac{d[cAMP]_{AC47}^{ecav}}{dt} - \frac{d[cAMP]_{PDE2}^{ecav}}{dt} - \frac{d[cAMP]_{PDE4}^{ecav}}{dt} \\ & - J_{cav/ecav} \cdot \frac{[cAMP]^{ecav} - [cAMP]^{cav}}{V_{ecav}} - J_{ecav/cyt} \cdot \frac{[cAMP]^{ecav} - [cAMP]^{cyt}}{V_{ecav}}\end{aligned} \tag{B.132}$$

$$\begin{aligned}\frac{d[cAMP]^{cyt}}{dt} = {} & \frac{d[cAMP]_{PKA}^{cyt}}{dt} + \frac{d[cAMP]_{AC56}^{cyt}}{dt} + \frac{d[cAMP]_{AC47}^{cyt}}{dt} - \frac{d[cAMP]_{PDE2}^{cyt}}{dt} \\ & - \frac{d[cAMP]_{PDE3}^{cyt}}{dt} - \frac{d[cAMP]_{PDE4}^{cyt}}{dt} - J_{cav/cyt} \cdot \frac{[cAMP]^{cyt} - [cAMP]^{cav}}{V_{cyt}} \\ & - J_{ecav/cyt} \cdot \frac{[cAMP]^{cyt} - [cAMP]^{ecav}}{V_{cyt}}\end{aligned} \tag{B.133}$$

Electrophysiological part: PKA substrates

L-type Ca^{2+} current module

Para-meter	Definition	Value	Reference
$[I_{CaL}]_{tot}$	Total cellular concentration of the L-type Ca^{2+} channels	0.0273 μM	Chu et al. [121] Bers and Stiffel [122]
f_{ICaL}^{cav}	Fraction of the L-type Ca^{2+} channels located in caveolae	0.2	Scriven et al. [38]
f_{ICaL}^{ecav}	Fraction of the L-type Ca^{2+} channels located in extracaveolae	$1 - f_{ICaL}^{cav}$	Scriven et al. [38]
G_{CaL}	Specific maximum conductivity for L-type Ca^{2+} channel (non-phosphorylated)	0.3772 mS/μF	Bondarenko [16]
G_{CaLp}	Specific maximum conductivity for L-type Ca^{2+} channel (phosphorylated)	0.7875 mS/μF	Bondarenko [16]
E_{CaL}	Reversal potential for L-type Ca^{2+} channel	52.0 mV	Petkova-Kirova et al. [61]
$K_{pc,\max}$	Maximum rate constant for Ca^{2+}-induced inactivation	233.24 s^{-1}	Bondarenko [16]
$K_{pc,half}$	Half-saturation constant for Ca^{2+}-induced inactivation	10.0 μM	Bondarenko [16]
K_{pcf}	Forward voltage-insensitive rate constant for inactivation	40,000 s^{-1}	Bondarenko [16]
K_{pcb}	Backward voltage-insensitive rate constant for inactivation	2.4 s^{-1}	Bondarenko [16]
k_{co}	Forward voltage-insensitive rate constant for activation (non-phosphorylated)	1,000 s^{-1}	Bondarenko [16]
k_{cop}	Forward voltage-insensitive rate constant for activation (phosphorylated)	4,000 s^{-1}	Bondarenko [16]
k_{oc}	Backward voltage-insensitive rate constant for activation	1,000 s^{-1}	Bondarenko [16]
$I_{CaL,\max}$	Normalization constant for L-type Ca^{2+} current	7.0 pA/pF	Bondarenko et al. [29]
k_{ICaL_PKA}	Phosphorylation rate of the L-type Ca^{2+} channel by PKA	$1.74 \cdot 10^{-2}$ s^{-1}	Bondarenko [16]
k_{ICaL_PP}	Dephosphorylation rate of the L-type Ca^{2+} channel by PP1 and PP2A	$2.325 \cdot 10^{-4}$ s^{-1}	Bondarenko [16]
K_{ICaL_PKA}	Affinity of the L-type Ca^{2+} channel for PKA	0.5 μM	Bondarenko [16]
K_{ICaL_PP}	Affinity of the L-type Ca^{2+} channel for PP1 and PP2A	0.2 μM	Bondarenko [16]

$$I_{CaL} = I_{ICaL}^{cav} + I_{ICaL}^{ecav} \tag{B.134}$$

$$\alpha = 0.4e^{(V+15.0)/15.0} \tag{B.135}$$

$$\alpha_p = 0.4e^{(V+15.0+20.0)/15.0} \tag{B.136}$$

$$\beta = 0.13e^{-(V+15.0)/18.0} \tag{B.137}$$

Caveolae

$$[I_{CaL}]_{tot}^{cav} = \mathrm{f}_{ICaL}^{cav}[I_{CaL}]_{tot}\frac{V_{cell}}{V_{cav}} \tag{B.138}$$

$$I_{CaL}^{cav} = \mathrm{f}_{ICaL}^{cav}\cdot(G_{CaL}\cdot O^{cav} + G_{CaLp}\cdot O_p^{cav})(V - E_{CaL}) \tag{B.139}$$

$$\gamma^{cav} = \frac{K_{pc,\max}[Ca^{2+}]_i}{K_{pc,half} + [Ca^{2+}]_i} \tag{B.140}$$

$$\begin{aligned}\frac{dO^{cav}}{dt} &= k_{co}C_P^{cav} - k_{oc}O^{cav} + K_{pcb}I_1^{cav} - \gamma^{cav}O^{cav} + 0.001(\alpha I_2^{cav} - K_{pcf}O^{cav}) \\ &\quad - \frac{k_{ICaL\_PKA}[C]^{cav}O^{cav}}{K_{ICaL\_PKA} + [I_{CaL}]_{tot}^{cav}O^{cav}} + \frac{\alpha}{\alpha_p}\frac{k_{ICaL\_PP}[PP]^{cav}O_p^{cav}}{K_{ICaL\_PP} + [I_{CaL}]_{tot}^{cav}O_p^{cav}}\end{aligned} \tag{B.141}$$

$$\begin{aligned}C_1^{cav} = 1 - (&O^{cav} + C_2^{cav} + C_3^{cav} + C_4^{cav} + C_P^{cav} + I_1^{cav} + I_2^{cav} + I_3^{cav} \\ &+ O_p^{cav} + C_{1p}^{cav} + C_{2p}^{cav} + C_{3p}^{cav} + C_{4p}^{cav} + C_{Pp}^{cav} + I_{1p}^{cav} + I_{2p}^{cav} + I_{3p}^{cav})\end{aligned} \tag{B.142}$$

$$\begin{aligned}\frac{dC_2^{cav}}{dt} &= 4\alpha C_1^{cav} - \beta C_2^{cav} + 2\beta C_3^{cav} - 3\alpha C_2^{cav} \\ &\quad - \frac{k_{ICaL\_PKA}[C]^{cav}C_2^{cav}}{K_{ICaL\_PKA} + [I_{CaL}]_{tot}^{cav}C_2^{cav}} + \frac{\alpha_p^2 k_{cop}}{\alpha^2 k_{co}}\frac{k_{ICaL\_PP}[PP]^{cav}C_{2p}^{cav}}{K_{ICaL\_PP} + [I_{CaL}]_{tot}^{cav}C_{2p}^{cav}}\end{aligned} \tag{B.143}$$

$$\begin{aligned}\frac{dC_3^{cav}}{dt} &= 3\alpha C_2^{cav} - 2\beta C_3^{cav} + 3\beta C_4^{cav} - 2\alpha C_3^{cav} \\ &\quad - \frac{k_{ICaL\_PKA}[C]^{cav}C_3^{cav}}{K_{ICaL\_PKA} + [I_{CaL}]_{tot}^{cav}C_3^{cav}} + \frac{\alpha_p k_{cop}}{\alpha k_{co}}\frac{k_{ICaL\_PP}[PP]^{cav}C_{3p}^{cav}}{K_{ICaL\_PP} + [I_{CaL}]_{tot}^{cav}C_{3p}^{cav}}\end{aligned} \tag{B.144}$$

$$\begin{aligned}\frac{dC_4^{cav}}{dt} &= 2\alpha C_3^{cav} - 3\beta C_4^{cav} + 4\beta C_P^{cav} - \alpha C_4^{cav} + 0.01(4K_{pcb}\beta I_1^{cav} - \frac{k_{co}}{k_{oc}}\alpha\gamma^{cav}C_4^{cav}) \\ &\quad + 0.002(4\beta I_2^{cav} - \frac{k_{co}}{k_{oc}}K_{pcf}C_4^{cav}) + 4\beta K_{pcb}I_3^{cav} - \frac{k_{co}}{k_{oc}}\gamma^{cav}K_{pcf}C_4^{cav} \\ &\quad - \frac{k_{ICaL\_PKA}[C]^{cav}C_4^{cav}}{K_{ICaL\_PKA} + [I_{CaL}]_{tot}^{cav}C_4^{cav}} + \frac{k_{cop}}{k_{co}}\frac{k_{ICaL\_PP}[PP]^{cav}C_{4p}^{cav}}{K_{ICaL\_PP} + [I_{CaL}]_{tot}^{cav}C_{4p}^{cav}}\end{aligned} \tag{B.145}$$

$$\frac{dC_P^{cav}}{dt} = \alpha C_4^{cav} - 4\beta C_P^{cav} + k_{oc} O^{cav} - k_{co} C_P^{cav} \tag{B.146}$$
$$- \frac{k_{ICaL\_PKA}[C]^{cav} C_P^{cav}}{K_{ICaL\_PKA} + [I_{CaL}]_{tot}^{cav} C_P^{cav}} + \frac{\alpha k_{cop}}{\alpha_p k_{co}} \frac{k_{ICaL\_PP}[PP]^{cav} C_{Pp}^{cav}}{K_{ICaL\_PP} + [I_{CaL}]_{tot}^{cav} C_{Pp}^{cav}}$$

$$\frac{dI_1^{cav}}{dt} = \gamma^{cav} O^{cav} - K_{pcb} I_1^{cav} + 0.001(\alpha I_3^{cav} - K_{pcf} I_1^{cav}) + 0.01(\frac{k_{co}}{k_{oc}} \alpha \gamma^{cav} C_4^{cav} - 4\beta K_{pcb} I_1^{cav}) \tag{B.147}$$
$$- \frac{k_{ICaL\_PKA}[C]^{cav} I_1^{cav}}{K_{ICaL\_PKA} + [I_{CaL}]_{tot}^{cav} I_1^{cav}} + \frac{\alpha}{\alpha_p} \frac{k_{ICaL\_PP}[PP]^{cav} I_{1p}^{cav}}{K_{ICaL\_PP} + [I_{CaL}]_{tot}^{cav} I_{1p}^{cav}}$$

$$\frac{dI_2^{cav}}{dt} = 0.001(K_{pcf} O^{cav} - \alpha I_2^{cav}) + K_{pcb} I_3^{cav} - \gamma^{cav} I_2^{cav} + 0.002(\frac{k_{co}}{k_{oc}} K_{pcf} C_4^{cav} - 4\beta I_2^{cav}) \tag{B.148}$$
$$- \frac{k_{ICaL\_PKA}[C]^{cav} I_2^{cav}}{K_{ICaL\_PKA} + [I_{CaL}]_{tot}^{cav} I_2^{cav}} + \frac{k_{ICaL\_PP}[PP]^{cav} I_{2p}^{cav}}{K_{ICaL\_PP} + [I_{CaL}]_{tot}^{cav} I_{2p}^{cav}}$$

$$\frac{dI_3^{cav}}{dt} = 0.001(K_{pcf} I_1^{cav} - \alpha I_3^{cav}) + \gamma^{cav} I_2^{cav} - K_{pcb} I_3^{cav} + \frac{k_{co}}{k_{oc}} \gamma^{cav} K_{pcf} C_4^{cav} - 4\beta K_{pcb} I_3^{cav} \tag{B.149}$$
$$- \frac{k_{ICaL\_PKA}[C]^{cav} I_3^{cav}}{K_{ICaL\_PKA} + [I_{CaL}]_{tot}^{cav} I_3^{cav}} + \frac{k_{ICaL\_PP}[PP]^{cav} I_{3p}^{cav}}{K_{ICaL\_PP} + [I_{CaL}]_{tot}^{cav} I_{3p}^{cav}}$$

$$\frac{dO_p^{cav}}{dt} = k_{cop} C_{Pp}^{cav} - k_{oc} O_p^{cav} + K_{pcb} I_{1p}^{cav} - \gamma^{cav} O_p^{cav} + 0.001(\alpha_p I_{2p}^{cav} - K_{pcf} O_p^{cav}) \tag{B.150}$$
$$+ \frac{k_{ICaL\_PKA}[C]^{cav} O^{cav}}{K_{ICaL\_PKA} + [I_{CaL}]_{tot}^{cav} O^{cav}} - \frac{\alpha}{\alpha_p} \frac{k_{ICaL\_PP}[PP]^{cav} O_p^{cav}}{K_{ICaL\_PP} + [I_{CaL}]_{tot}^{cav} O_p^{cav}}$$

$$\frac{dC_{1p}^{cav}}{dt} = \beta C_{2p}^{cav} - 4\alpha_p C_{1p}^{cav} + \frac{k_{ICaL\_PKA}[C]^{cav} C_1^{cav}}{K_{ICaL\_PKA} + [I_{CaL}]_{tot}^{cav} C_1^{cav}} - \frac{\alpha_p^3 k_{cop}}{\alpha^3 k_{co}} \frac{k_{ICaL\_PP}[PP]^{cav} C_{1p}^{cav}}{K_{ICaL\_PP} + [I_{CaL}]_{tot}^{cav} C_{1p}^{cav}} \tag{B.151}$$

$$\frac{dC_{2p}^{cav}}{dt} = 4\alpha_p C_{1p}^{cav} - \beta C_{2p}^{cav} + 2\beta C_{3p}^{cav} - 3\alpha_p C_{2p}^{cav} \tag{B.152}$$
$$+ \frac{k_{ICaL\_PKA}[C]^{cav} C_2^{cav}}{K_{ICaL\_PKA} + [I_{CaL}]_{tot}^{cav} C_2^{cav}} - \frac{\alpha_p^2 k_{cop}}{\alpha^2 k_{co}} \frac{k_{ICaL\_PP}[PP]^{cav} C_{2p}^{cav}}{K_{ICaL\_PP} + [I_{CaL}]_{tot}^{cav} C_{2p}^{cav}}$$

$$\frac{dC_{3p}^{cav}}{dt} = 3\alpha_p C_{2p}^{cav} - 2\beta C_{3p}^{cav} + 3\beta C_{4p}^{cav} - 2\alpha_p C_{3p}^{cav} \tag{B.153}$$
$$+ \frac{k_{ICaL\_PKA}[C]^{cav} C_3^{cav}}{K_{ICaL\_PKA} + [I_{CaL}]_{tot}^{cav} C_3^{cav}} - \frac{\alpha_p k_{cop}}{\alpha k_{co}} \frac{k_{ICaL\_PP}[PP]^{cav} C_{3p}^{cav}}{K_{ICaL\_PP} + [I_{CaL}]_{tot}^{cav} C_{3p}^{cav}}$$

$$\frac{dC_{4p}^{cav}}{dt} = 2\alpha_p C_{3p}^{cav} - 3\beta C_{4p}^{cav} + 4\beta C_{Pp}^{cav} - \alpha_p C_{4p}^{cav} + 0.01(4K_{pcb}\beta I_{1p}^{cav} - \frac{k_{cop}}{k_{oc}}\alpha\gamma^{cav} C_{4p}^{cav}) \quad \text{(B.154)}$$
$$+ 0.002(4\beta I_{2p}^{cav} - \frac{k_{cop}}{k_{oc}} K_{pcf} C_{4p}^{cav}) + 4\beta K_{pcb} I_{3p}^{cav} - \frac{k_{cop}}{k_{oc}}\gamma^{cav} K_{pcf} C_{4p}^{cav}$$
$$+ \frac{k_{ICaL\_PKA}[C]^{cav} C_4^{cav}}{K_{ICaL\_PKA} + [I_{CaL}]_{tot}^{cav} C_4^{cav}} - \frac{k_{cop}}{k_{co}} \frac{k_{ICaL\_PP}[PP]^{cav} C_{4p}^{cav}}{K_{ICaL\_PP} + [I_{CaL}]_{tot}^{cav} C_{4p}^{cav}}$$

$$\frac{dC_{Pp}^{cav}}{dt} = \alpha_p C_{4p}^{cav} - 4\beta C_{Pp}^{cav} + k_{oc} O_p^{cav} - k_{cop} C_{Pp}^{cav} \quad \text{(B.155)}$$
$$+ \frac{k_{ICaL\_PKA}[C]^{cav} C_P^{cav}}{K_{ICaL\_PKA} + [I_{CaL}]_{tot}^{cav} C_P^{cav}} - \frac{\alpha k_{cop}}{\alpha_p k_{co}} \frac{k_{ICaL\_PP}[PP]^{cav} C_{Pp}^{cav}}{K_{ICaL\_PP} + [I_{CaL}]_{tot}^{cav} C_{Pp}^{cav}}$$

$$\frac{dI_{1p}^{cav}}{dt} = \gamma^{cav} O_p^{cav} - K_{pcb} I_{1p}^{cav} + 0.001(\alpha_p I_{3p}^{cav} - K_{pcf} I_{1p}^{cav}) + 0.01(\frac{k_{cop}}{k_{oc}}\alpha_p\gamma^{cav} C_{4p}^{cav} - 4\beta K_{pcb} I_{1p}^{cav}) \quad \text{(B.156)}$$
$$+ \frac{k_{ICaL\_PKA}[C]^{cav} I_1^{cav}}{K_{ICaL\_PKA} + [I_{CaL}]_{tot}^{cav} I_1^{cav}} - \frac{\alpha}{\alpha_p} \frac{k_{ICaL\_PP}[PP]^{cav} I_{1p}^{cav}}{K_{ICaL\_PP} + [I_{CaL}]_{tot}^{cav} I_{1p}^{cav}}$$

$$\frac{dI_{2p}^{cav}}{dt} = 0.001(K_{pcf} O_p^{cav} - \alpha_p I_{2p}^{cav}) + K_{pcb} I_{3p}^{cav} - \gamma^{cav} I_{2p}^{cav} + 0.002(\frac{k_{cop}}{k_{oc}} K_{pcf} C_{4p}^{cav} - 4\beta I_{2p}^{cav}) \quad \text{(B.157)}$$
$$+ \frac{k_{ICaL\_PKA}[C]^{cav} I_2^{cav}}{K_{ICaL\_PKA} + [I_{CaL}]_{tot}^{cav} I_2^{cav}} - \frac{k_{ICaL\_PP}[PP]^{cav} I_{2p}^{cav}}{K_{ICaL\_PP} + [I_{CaL}]_{tot}^{cav} I_{2p}^{cav}}$$

$$\frac{dI_{3p}^{cav}}{dt} = 0.001(K_{pcf} I_{1p}^{cav} - \alpha_p I_{3p}^{cav}) + \gamma^{cav} I_{2p}^{cav} - K_{pcb} I_{3p}^{cav} + \frac{k_{cop}}{k_{oc}}\gamma^{cav} K_{pcf} C_{4p}^{cav} - 4\beta K_{pcb} I_{3p}^{cav} \quad \text{(B.158)}$$
$$+ \frac{k_{ICaL\_PKA}[C]^{cav} I_3^{cav}}{K_{ICaL\_PKA} + [I_{CaL}]_{tot}^{cav} I_3^{cav}} - \frac{k_{ICaL\_PP}[PP]^{cav} I_{3p}^{cav}}{K_{ICaL\_PP} + [I_{CaL}]_{tot}^{cav} I_{3p}^{cav}}$$

Extracaveolae

$$[I_{CaL}]_{tot}^{ecav} = \mathrm{f}_{ICaL}^{ecav} [I_{CaL}]_{tot} \frac{V_{cell}}{V_{ecav}} \quad \text{(B.159)}$$

$$I_{CaL}^{ecav} = \mathrm{f}_{ICaL}^{ecav} \cdot (G_{CaL} \cdot O^{ecav} + G_{CaLp} \cdot O_p^{ecav})(V - E_{CaL}) \quad \text{(B.160)}$$

$$\gamma^{ecav} = \frac{K_{pc,\max}[Ca^{2+}]_{ss}}{K_{pc,half} + [Ca^{2+}]_{ss}} \quad \text{(B.161)}$$

$$\frac{dO^{ecav}}{dt} = k_{co}C_P^{ecav} - k_{oc}O^{ecav} + K_{pcb}I_1^{ecav} - \gamma^{ecav}O^{ecav} + 0.001(\alpha I_2^{ecav} - K_{pcf}O^{ecav}) \tag{B.162}$$
$$- \frac{k_{ICaL\_PKA}[C]^{ecav}O^{ecav}}{K_{ICaL\_PKA} + [I_{CaL}]_{tot}^{ecav}O^{ecav}} + \frac{\alpha}{\alpha_p}\frac{k_{ICaL\_PP}[PP1]^{ecav}O_p^{ecav}}{K_{ICaL\_PP} + [I_{CaL}]_{tot}^{ecav}O_p^{ecav}}$$

$$C_1^{ecav} = 1 - (O^{ecav} + C_2^{ecav} + C_3^{ecav} + C_4^{ecav} + C_P^{ecav} + I_1^{ecav} + I_2^{ecav} + I_3^{ecav} \tag{B.163}$$
$$+ O_p^{ecav} + C_{1p}^{ecav} + C_{2p}^{ecav} + C_{3p}^{ecav} + C_{4p}^{ecav} + C_{Pp}^{ecav} + I_{1p}^{ecav} + I_{2p}^{ecav} + I_{3p}^{ecav})$$

$$\frac{dC_2^{ecav}}{dt} = 4\alpha C_1^{ecav} - \beta C_2^{ecav} + 2\beta C_3^{ecav} - 3\alpha C_2^{ecav} \tag{B.164}$$
$$- \frac{k_{ICaL\_PKA}[C]^{ecav}C_2^{ecav}}{K_{ICaL\_PKA} + [I_{CaL}]_{tot}^{ecav}C_2^{ecav}} + \frac{\alpha_p^2 k_{cop}}{\alpha^2 k_{co}}\frac{k_{ICaL\_PP}[PP1]^{ecav}C_{2p}^{ecav}}{K_{ICaL\_PP} + [I_{CaL}]_{tot}^{ecav}C_{2p}^{ecav}}$$

$$\frac{dC_3^{ecav}}{dt} = 3\alpha C_2^{ecav} - 2\beta C_3^{ecav} + 3\beta C_4^{ecav} - 2\alpha C_3^{ecav} \tag{B.165}$$
$$- \frac{k_{ICaL\_PKA}[C]^{ecav}C_3^{ecav}}{K_{ICaL\_PKA} + [I_{CaL}]_{tot}^{ecav}C_3^{ecav}} + \frac{\alpha_p k_{cop}}{\alpha k_{co}}\frac{k_{ICaL\_PP}[PP1]^{ecav}C_{3p}^{ecav}}{K_{ICaL\_PP} + [I_{CaL}]_{tot}^{ecav}C_{3p}^{ecav}}$$

$$\frac{dC_4^{ecav}}{dt} = 2\alpha C_3^{ecav} - 3\beta C_4^{ecav} + 4\beta C_P^{ecav} - \alpha C_4^{ecav} + 0.01(4K_{pcb}\beta I_1^{ecav} - \frac{k_{co}}{k_{oc}}\alpha\gamma^{ecav}C_4^{ecav}) \tag{B.166}$$
$$+ 0.002(4\beta I_2^{ecav} - \frac{k_{co}}{k_{oc}}K_{pcf}C_4^{ecav}) + 4\beta K_{pcb}I_3^{ecav} - \frac{k_{co}}{k_{oc}}\gamma^{ecav}K_{pcf}C_4^{ecav}$$
$$- \frac{k_{ICaL\_PKA}[C]^{ecav}C_4^{ecav}}{K_{ICaL\_PKA} + [I_{CaL}]_{tot}^{ecav}C_4^{ecav}} + \frac{k_{cop}}{k_{co}}\frac{k_{ICaL\_PP}[PP1]^{ecav}C_{4p}^{ecav}}{K_{ICaL\_PP} + [I_{CaL}]_{tot}^{ecav}C_{4p}^{ecav}}$$

$$\frac{dC_P^{ecav}}{dt} = \alpha C_4^{ecav} - 4\beta C_P^{ecav} + k_{oc}O^{ecav} - k_{co}C_P^{ecav} \tag{B.167}$$
$$- \frac{k_{ICaL\_PKA}[C]^{ecav}C_P^{ecav}}{K_{ICaL\_PKA} + [I_{CaL}]_{tot}^{ecav}C_P^{ecav}} + \frac{\alpha k_{cop}}{\alpha_p k_{co}}\frac{k_{ICaL\_PP}[PP1]^{ecav}C_{Pp}^{ecav}}{K_{ICaL\_PP} + [I_{CaL}]_{tot}^{ecav}C_{Pp}^{ecav}}$$

$$\frac{dI_1^{ecav}}{dt} = \gamma^{ecav}O^{ecav} - K_{pcb}I_1^{ecav} + 0.001(\alpha I_3^{ecav} - K_{pcf}I_1^{ecav}) + 0.01(\frac{k_{co}}{k_{oc}}\alpha\gamma^{ecav}C_4^{ecav} - 4\beta K_{pcb}I_1^{ecav}) \tag{B.168}$$
$$- \frac{k_{ICaL\_PKA}[C]^{ecav}I_1^{ecav}}{K_{ICaL\_PKA} + [I_{CaL}]_{tot}^{ecav}I_1^{ecav}} + \frac{\alpha}{\alpha_p}\frac{k_{ICaL\_PP}[PP1]^{ecav}I_{1p}^{ecav}}{K_{ICaL\_PP} + [I_{CaL}]_{tot}^{ecav}I_{1p}^{ecav}}$$

$$\frac{dI_2^{ecav}}{dt} = 0.001(K_{pcf}O^{ecav} - \alpha I_2^{ecav}) + K_{pcb}I_3^{ecav} - \gamma^{ecav}I_2^{ecav} + 0.002(\frac{k_{co}}{k_{oc}}K_{pcf}C_4^{ecav} - 4\beta I_2^{ecav}) \quad \text{(B.169)}$$
$$- \frac{k_{ICaL\_PKA}[C]^{ecav}I_2^{ecav}}{K_{ICaL\_PKA} + [I_{CaL}]_{tot}^{ecav}I_2^{ecav}} + \frac{k_{ICaL\_PP}[PP1]^{ecav}I_{2p}^{ecav}}{K_{ICaL\_PP} + [I_{CaL}]_{tot}^{ecav}I_{2p}^{ecav}}$$

$$\frac{dI_3^{ecav}}{dt} = 0.001(K_{pcf}I_1^{ecav} - \alpha I_3^{ecav}) + \gamma^{ecav}I_2^{ecav} - K_{pcb}I_3^{ecav} + \frac{k_{co}}{k_{oc}}\gamma^{ecav}K_{pcf}C_4^{ecav} - 4\beta K_{pcb}I_3^{ecav} \quad \text{(B.170)}$$
$$- \frac{k_{ICaL\_PKA}[C]^{ecav}I_3^{ecav}}{K_{ICaL\_PKA} + [I_{CaL}]_{tot}^{ecav}I_3^{ecav}} + \frac{k_{ICaL\_PP}[PP1]^{ecav}I_{3p}^{ecav}}{K_{ICaL\_PP} + [I_{CaL}]_{tot}^{ecav}I_{3p}^{ecav}}$$

$$\frac{dO_p^{ecav}}{dt} = k_{cop}C_{Pp}^{ecav} - k_{oc}O_p^{ecav} + K_{pcb}I_{1p}^{ecav} - \gamma^{ecav}O_p^{ecav} + 0.001(\alpha_p I_{2p}^{ecav} - K_{pcf}O_p^{ecav}) \quad \text{(B.171)}$$
$$+ \frac{k_{ICaL\_PKA}[C]^{ecav}O^{ecav}}{K_{ICaL\_PKA} + [I_{CaL}]_{tot}^{ecav}O^{ecav}} - \frac{\alpha}{\alpha_p}\frac{k_{ICaL\_PP}[PP1]^{ecav}O_p^{ecav}}{K_{ICaL\_PP} + [I_{CaL}]_{tot}^{ecav}O_p^{ecav}}$$

$$\frac{dC_{1p}^{ecav}}{dt} = \beta C_{2p}^{ecav} - 4\alpha_p C_{1p}^{ecav} + \frac{k_{ICaL\_PKA}[C]^{ecav}C_1^{ecav}}{K_{ICaL\_PKA} + [I_{CaL}]_{tot}^{ecav}C_1^{ecav}} - \frac{\alpha_p^3 k_{cop}}{\alpha^3 k_{co}}\frac{k_{ICaL\_PP}[PP1]^{ecav}C_{1p}^{ecav}}{K_{ICaL\_PP} + [I_{CaL}]_{tot}^{ecav}C_{1p}^{ecav}} \quad \text{(B.172)}$$

$$\frac{dC_{2p}^{ecav}}{dt} = 4\alpha_p C_{1p}^{ecav} - \beta C_{2p}^{ecav} + 2\beta C_{3p}^{ecav} - 3\alpha_p C_{2p}^{ecav} \quad \text{(B.173)}$$
$$+ \frac{k_{ICaL\_PKA}[C]^{ecav}C_2^{ecav}}{K_{ICaL\_PKA} + [I_{CaL}]_{tot}^{ecav}C_2^{ecav}} - \frac{\alpha_p^2 k_{cop}}{\alpha^2 k_{co}}\frac{k_{ICaL\_PP}[PP1]^{ecav}C_{2p}^{ecav}}{K_{ICaL\_PP} + [I_{CaL}]_{tot}^{ecav}C_{2p}^{ecav}}$$

$$\frac{dC_{3p}^{ecav}}{dt} = 3\alpha_p C_{2p}^{ecav} - 2\beta C_{3p}^{ecav} + 3\beta C_{4p}^{ecav} - 2\alpha_p C_{3p}^{ecav} \quad \text{(B.174)}$$
$$+ \frac{k_{ICaL\_PKA}[C]^{ecav}C_3^{ecav}}{K_{ICaL\_PKA} + [I_{CaL}]_{tot}^{ecav}C_3^{ecav}} - \frac{\alpha_p k_{cop}}{\alpha k_{co}}\frac{k_{ICaL\_PP}[PP1]^{ecav}C_{3p}^{ecav}}{K_{ICaL\_PP} + [I_{CaL}]_{tot}^{ecav}C_{3p}^{ecav}}$$

$$\frac{dC_{4p}^{ecav}}{dt} = 2\alpha_p C_{3p}^{ecav} - 3\beta C_{4p}^{ecav} + 4\beta C_{Pp}^{ecav} - \alpha_p C_{4p}^{ecav} + 0.01(4K_{pcb}\beta I_{1p}^{ecav} - \frac{k_{cop}}{k_{oc}}\alpha\gamma^{ecav}C_{4p}^{ecav}) \quad \text{(B.175)}$$
$$+ 0.002(4\beta I_{2p}^{ecav} - \frac{k_{cop}}{k_{oc}}K_{pcf}C_{4p}^{ecav}) + 4\beta K_{pcb}I_{3p}^{ecav} - \frac{k_{cop}}{k_{oc}}\gamma^{ecav}K_{pcf}C_{4p}^{ecav}$$
$$+ \frac{k_{ICaL\_PKA}[C]^{ecav}C_4^{ecav}}{K_{ICaL\_PKA} + [I_{CaL}]_{tot}^{ecav}C_4^{ecav}} - \frac{k_{cop}}{k_{co}}\frac{k_{ICaL\_PP}[PP1]^{ecav}C_{4p}^{ecav}}{K_{ICaL\_PP} + [I_{CaL}]_{tot}^{ecav}C_{4p}^{ecav}}$$

$$\frac{dC_{Pp}^{ecav}}{dt} = \alpha_p C_{4p}^{ecav} - 4\beta C_{Pp}^{ecav} + k_{oc} O_p^{ecav} - k_{cop} C_{Pp}^{ecav} \tag{B.176}$$
$$+ \frac{k_{ICaL\_PKA}[C]^{ecav} C_P^{ecav}}{K_{ICaL\_PKA} + [I_{CaL}]_{tot}^{ecav} C_P^{ecav}} - \frac{\alpha k_{cop}}{\alpha_p k_{co}} \frac{k_{ICaL\_PP}[PP1]^{ecav} C_{Pp}^{ecav}}{K_{ICaL\_PP} + [I_{CaL}]_{tot}^{ecav} C_{Pp}^{ecav}}$$

$$\frac{dI_{1p}^{ecav}}{dt} = \gamma^{ecav} O_p^{ecav} - K_{pcb} I_{1p}^{ecav} + 0.001(\alpha_p I_{3p}^{ecav} - K_{pcf} I_{1p}^{ecav}) + 0.01(\frac{k_{cop}}{k_{oc}} \alpha_p \gamma^{ecav} C_{4p}^{ecav} - 4\beta K_{pcb} I_{1p}^{ecav}) \tag{B.177}$$
$$+ \frac{k_{ICaL\_PKA}[C]^{ecav} I_1^{ecav}}{K_{ICaL\_PKA} + [I_{CaL}]_{tot}^{ecav} I_1^{ecav}} - \frac{\alpha}{\alpha_p} \frac{k_{ICaL\_PP}[PP1]^{ecav} I_{1p}^{ecav}}{K_{ICaL\_PP} + [I_{CaL}]_{tot}^{ecav} I_{1p}^{ecav}}$$

$$\frac{dI_{2p}^{ecav}}{dt} = 0.001(K_{pcf} O_p^{ecav} - \alpha_p I_{2p}^{ecav}) + K_{pcb} I_{3p}^{ecav} - \gamma^{ecav} I_{2p}^{ecav} + 0.002(\frac{k_{cop}}{k_{oc}} K_{pcf} C_{4p}^{ecav} - 4\beta I_{2p}^{ecav}) \tag{B.178}$$
$$+ \frac{k_{ICaL\_PKA}[C]^{ecav} I_2^{ecav}}{K_{ICaL\_PKA} + [I_{CaL}]_{tot}^{ecav} I_2^{ecav}} - \frac{k_{ICaL\_PP}[PP1]^{ecav} I_{2p}^{ecav}}{K_{ICaL\_PP} + [I_{CaL}]_{tot}^{ecav} I_{2p}^{ecav}}$$

$$\frac{dI_{3p}^{ecav}}{dt} = 0.001(K_{pcf} I_{1p}^{ecav} - \alpha_p I_{3p}^{ecav}) + \gamma^{ecav} I_{2p}^{ecav} - K_{pcb} I_{3p}^{ecav} + \frac{k_{cop}}{k_{oc}} \gamma^{ecav} K_{pcf} C_{4p}^{ecav} - 4\beta K_{pcb} I_{3p}^{ecav} \tag{B.179}$$
$$+ \frac{k_{ICaL\_PKA}[C]^{ecav} I_3^{ecav}}{K_{ICaL\_PKA} + [I_{CaL}]_{tot}^{ecav} I_3^{ecav}} - \frac{k_{ICaL\_PP}[PP1]^{ecav} I_{3p}^{ecav}}{K_{ICaL\_PP} + [I_{CaL}]_{tot}^{ecav} I_{3p}^{ecav}}$$

Fast Na^+ current module

Para-meter	Definition	Value	Reference
G_{Na}	Specific maximum conductivity for the fast Na^+ channel (non-phosphorylated)	14.4 mS/μF	Bondarenko [16]
G_{Nap}	Specific maximum conductivity for the fast Na^+ channel (phosphorylated)	18.0 mS/μF	Bondarenko [16]
k_{INa_PKA}	Phosphorylation-traffiking rate of the fast Na^+ channel by PKA	$6.8400 \cdot 10^{-3}$ μM^{-1} s^{-1}	Bondarenko [16]
k_{INa_PP}	Dephosphorylation rate of the fast Na^+ channel by PP1 and PP2A	$1.9804 \cdot 10^{-2}$ μM^{-1} s^{-1}	Bondarenko [16]
K_{INa_PKA}	Affinity of the fast Na^+ channel for PKA	$5.49415 \cdot 10^{-3}$	Bondarenko [16]
K_{INa_PP}	Affinity of the fast Na^+ channel for PP1 and PP2A	0.393025	Bondarenko [16]

$$E_{Na} = \frac{RT}{F}\ln\left(\frac{0.9[Na^+]_o + 0.1[K^+]_o}{0.9[Na^+]_i + 0.1[K^+]_i}\right) \tag{B.180}$$

$$I_{Na} = (G_{Na}\cdot O_{Na} + G_{Nap}\cdot O_{Nap})(V - E_{Na}) \tag{B.181}$$

$$\begin{aligned} C_{Na3} = 1 - (&O_{Na} + C_{Na2} + C_{Na1} + IF_{Na} + I1_{Na} + I2_{Na} + IC_{Na2} + IC_{Na3} \\ &+ O_{Nap} + C_{Na3p} + C_{Na2p} + C_{Na1p} + IF_{Nap} + I1_{Nap} + I2_{Nap} + IC_{Na2p} + IC_{Na3p}) \end{aligned} \tag{B.182}$$

$$\begin{aligned} \frac{dC_{Na2}}{dt} = {} & \alpha_{Na11}C_{Na3} - \beta_{Na11}C_{Na2} + \beta_{Na12}C_{Na1} - \alpha_{Na12}C_{Na2} + \alpha_{Na3}IC_{Na2} - \beta_{Na3}C_{Na2} \\ & - \frac{k_{INa\_PKA}[C]^{cav}C_{Na2}}{K_{INa\_PKA} + C_{Na2}} + \frac{k_{INa\_PP}[PP]^{cav}C_{Na2p}}{K_{INa\_PP} + C_{Na2p}} \end{aligned} \tag{B.183}$$

$$\begin{aligned} \frac{dC_{Na1}}{dt} = {} & \alpha_{Na12}C_{Na2} - \beta_{Na12}C_{Na1} + \beta_{Na13}O_{Na} - \alpha_{Na13}C_{Na1} + \alpha_{Na3}IF_{Na} - \beta_{Na3}C_{Na1} \\ & - \frac{k_{INa\_PKA}[C]^{cav}C_{Na1}}{K_{INa\_PKA} + C_{Na1}} + \frac{k_{INa\_PP}[PP]^{cav}C_{Na1p}}{K_{INa\_PP} + C_{Na1p}} \end{aligned} \tag{B.184}$$

$$\begin{aligned} \frac{dO_{Na}}{dt} = {} & \alpha_{Na13}C_{Na1} - \beta_{Na13}O_{Na} + \beta_{Na2}IF_{Na} - \alpha_{Na2}O_{Na} \\ & - \frac{k_{INa\_PKA}[C]^{cav}O_{Na}}{K_{INa\_PKA} + O_{Na}} + \frac{k_{INa\_PP}[PP]^{cav}O_{Nap}}{K_{INa\_PP} + O_{Nap}} \end{aligned} \tag{B.185}$$

$$\begin{aligned} \frac{dIF_{Na}}{dt} = {} & \alpha_{Na2}O_{Na} - \beta_{Na2}IF_{Na} + \beta_{Na3}C_{Na1} - \alpha_{Na3}IF_{Na} + \beta_{Na4}I1_{Na} - \alpha_{Na4}IF_{Na} \\ & + \alpha_{Na12}IC_{Na2} - \beta_{Na12}IF_{Na} - \frac{k_{INa\_PKA}[C]^{cav}IF_{Na}}{K_{INa\_PKA} + IF_{Na}} + \frac{k_{INa\_PP}[PP]^{cav}IF_{Nap}}{K_{INa\_PP} + IF_{Nap}} \end{aligned} \tag{B.186}$$

$$\begin{aligned} \frac{dI1_{Na}}{dt} = {} & \alpha_{Na4}IF_{Na} - \beta_{Na4}I1_{Na} + \beta_{Na5}I2_{Na} - \alpha_{Na5}I1_{Na} \\ & - \frac{k_{INa\_PKA}[C]^{cav}I1_{Na}}{K_{INa\_PKA} + I1_{Na}} + \frac{k_{INa\_PP}[PP]^{cav}I1_{Nap}}{K_{INa\_PP} + I1_{Nap}} \end{aligned} \tag{B.187}$$

$$\frac{dI2_{Na}}{dt} = \alpha_{Na5}I1_{Na} - \beta_{Na5}I2_{Na} - \frac{k_{INa\_PKA}[C]^{cav}I2_{Na}}{K_{INa\_PKA} + I2_{Na}} + \frac{k_{INa\_PP}[PP]^{cav}I2_{Nap}}{K_{INa\_PP} + I2_{Nap}} \tag{B.188}$$

$$\frac{dIC_{Na2}}{dt} = \alpha_{Na11} IC_{Na3} - \beta_{Na11} IC_{Na2} + \beta_{Na12} IF_{Na} - \alpha_{Na12} IC_{Na2} + \beta_{Na3} C_{Na2} - \alpha_{Na3} IC_{Na2} \quad \text{(B.189)}$$
$$- \frac{k_{INa\_PKA}[C]^{cav} IC_{Na2}}{K_{INa\_PKA} + IC_{Na2}} + \frac{k_{INa\_PP}[PP]^{cav} IC_{Na2p}}{K_{INa\_PP} + IC_{Na2p}}$$

$$\frac{dIC_{Na3}}{dt} = \beta_{Na11} IC_{Na2} - \alpha_{Na11} IC_{Na3} + \beta_{Na3} C_{Na3} - \alpha_{Na3} IC_{Na3} \quad \text{(B.190)}$$
$$- \frac{k_{INa\_PKA}[C]^{cav} IC_{Na3}}{K_{INa\_PKA} + IC_{Na3}} + \frac{k_{INa\_PP}[PP]^{cav} IC_{Na3p}}{K_{INa\_PP} + IC_{Na3p}}$$

$$\frac{dC_{Na3p}}{dt} = \beta_{Na11} C_{Na2p} - \alpha_{Na11} C_{Na3p} + \alpha_{Na3} IC_{Na3p} - \beta_{Na3} C_{Na3p} \quad \text{(B.191)}$$
$$+ \frac{k_{INa\_PKA}[C]^{cav} C_{Na3}}{K_{INa\_PKA} + C_{Na3}} - \frac{k_{INa\_PP}[PP]^{cav} C_{Na3p}}{K_{INa\_PP} + C_{Na3p}}$$

$$\frac{dC_{Na2p}}{dt} = \alpha_{Na11} C_{Na3p} - \beta_{Na11} C_{Na2p} + \beta_{Na12} C_{Na1p} - \alpha_{Na12} C_{Na2p} + \alpha_{Na3} IC_{Na2p} - \beta_{Na3} C_{Na2p} \quad \text{(B.192)}$$
$$+ \frac{k_{INa\_PKA}[C]^{cav} C_{Na2}}{K_{INa\_PKA} + C_{Na2}} - \frac{k_{INa\_PP}[PP]^{cav} C_{Na2p}}{K_{INa\_PP} + C_{Na2p}}$$

$$\frac{dC_{Na1p}}{dt} = \alpha_{Na12} C_{Na2p} - \beta_{Na12} C_{Na1p} + \beta_{Na13} O_{Nap} - \alpha_{Na13} C_{Na1p} + \alpha_{Na3} IF_{Nap} - \beta_{Na3} C_{Na1p} \quad \text{(B.193)}$$
$$+ \frac{k_{INa\_PKA}[C]^{cav} C_{Na1}}{K_{INa\_PKA} + C_{Na1}} - \frac{k_{INa\_PP}[PP]^{cav} C_{Na1p}}{K_{INa\_PP} + C_{Na1p}}$$

$$\frac{dO_{Nap}}{dt} = \alpha_{Na13} C_{Na1p} - \beta_{Na13} O_{Nap} + \beta_{Na2} IF_{Nap} - \alpha_{Na2} O_{Nap} \quad \text{(B.194)}$$
$$+ \frac{k_{INa\_PKA}[C]^{cav} O_{Na}}{K_{INa\_PKA} + O_{Na}} - \frac{k_{INa\_PP}[PP]^{cav} O_{Nap}}{K_{INa\_PP} + O_{Nap}}$$

$$\frac{dIF_{Nap}}{dt} = \alpha_{Na2} O_{Nap} - \beta_{Na2} IF_{Nap} + \beta_{Na3} C_{Na1p} - \alpha_{Na3} IF_{Nap} + \beta_{Na4} I1_{Nap} - \alpha_{Na4} IF_{Nap} \quad \text{(B.195)}$$
$$+ \alpha_{Na12} IC_{Na2p} - \beta_{Na12} IF_{Nap} + \frac{k_{INa\_PKA}[C]^{cav} IF_{Na}}{K_{INa\_PKA} + IF_{Na}} - \frac{k_{INa\_PP}[PP]^{cav} IF_{Nap}}{K_{INa\_PP} + IF_{Nap}}$$

$$\frac{dI1_{Nap}}{dt} = \alpha_{Na4} IF_{Nap} - \beta_{Na4} I1_{Nap} + \beta_{Na5} I2_{Nap} - \alpha_{Na5} I1_{Nap} + \frac{k_{INa\_PKA}[C]^{cav} I1_{Na}}{K_{INa\_PKA} + I1_{Na}} - \frac{k_{INa\_PP}[PP]^{cav} I1_{Nap}}{K_{INa\_PP} + I1_{Nap}} \tag{B.196}$$

$$\frac{dI2_{Nap}}{dt} = \alpha_{Na5} I1_{Nap} - \beta_{Na5} I2_{Nap} + \frac{k_{INa\_PKA}[C]^{cav} I2_{Na}}{K_{INa\_PKA} + I2_{Na}} - \frac{k_{INa\_PP}[PP]^{cav} I2_{Nap}}{K_{INa\_PP} + I2_{Nap}} \tag{B.197}$$

$$\frac{dIC_{Na2p}}{dt} = \alpha_{Na11} IC_{Na3p} - \beta_{Na11} IC_{Na2p} + \beta_{Na12} IF_{Nap} - \alpha_{Na12} IC_{Na2p} + \beta_{Na3} C_{Na2p} - \alpha_{Na3} IC_{Na2p} + \frac{k_{INa\_PKA}[C]^{cav} IC_{Na2}}{K_{INa\_PKA} + IC_{Na2}} - \frac{k_{INa\_PP}[PP]^{cav} IC_{Na2p}}{K_{INa\_PP} + IC_{Na2p}} \tag{B.198}$$

$$\frac{dIC_{Na3p}}{dt} = \beta_{Na11} IC_{Na2p} - \alpha_{Na11} IC_{Na3p} + \beta_{Na3} C_{Na3p} - \alpha_{Na3} IC_{Na3p} + \frac{k_{INa\_PKA}[C]^{cav} IC_{Na3}}{K_{INa\_PKA} + IC_{Na3}} - \frac{k_{INa\_PP}[PP]^{cav} IC_{Na3p}}{K_{INa\_PP} + IC_{Na3p}} \tag{B.199}$$

$$\alpha_{Na11} = \frac{3.802}{0.1027 e^{-(V-2.5)/17.0} + 0.20 e^{-(V-2.5)/150.0}} \tag{B.200}$$

$$\alpha_{Na12} = \frac{3.802}{0.1027 e^{-(V-2.5)/15.0} + 0.23 e^{-(V-2.5)/150.0}} \tag{B.201}$$

$$\alpha_{Na13} = \frac{3.802}{0.1027 e^{-(V-2.5)/12.0} + 0.25 e^{-(V-2.5)/150.0}} \tag{B.202}$$

$$\beta_{Na11} = 0.1917 e^{-(V-2.5)/20.3} \tag{B.203}$$

$$\beta_{Na12} = 0.20 e^{-(V-7.5)/20.3} \tag{B.204}$$

$$\beta_{Na13} = 0.22 e^{-(V-12.5)/20.3} \tag{B.205}$$

$$\alpha_{Na3} = 7.0 \times 10^{-7} e^{-(V+7.0)/7.7} \tag{B.206}$$

$$\beta_{Na3} = 0.0084 + 0.00002(V + 7.0) \tag{B.207}$$

$$\alpha_{Na2} = \frac{1.0}{0.188495e^{-(V+7.0)/16.6} + 0.393956} \tag{B.208}$$

$$\beta_{Na2} = \alpha_{Na13}\alpha_{Na2}\alpha_{Na3}/(\beta_{Na13}\beta_{Na3}) \tag{B.209}$$

$$\alpha_{Na4} = \alpha_{Na2}/100.0 \tag{B.210}$$

$$\beta_{Na4} = \alpha_{Na3} \tag{B.211}$$

$$\alpha_{Na5} = \alpha_{Na2}/95000 \tag{B.212}$$

$$\beta_{Na5} = \alpha_{Na3}/50.0 \tag{B.213}$$

Ryanodine receptor module

Para-meter	Definition	Value	Reference
$[RyR]_{tot}$	Total cellular concentration of ryanodine receptors	0.1993 μM	Chu et al. [121]
ν_1	Maximum RyR channel Ca^{2+} permeability	4,500 s^{-1}	Bondarenko et al. [29]
n	RyR Ca^{2+} cooperativity parameter $P_{C1} - P_{O1}$	4	Bondarenko et al. [29]
m	RyR Ca^{2+} cooperativity parameter $P_{O1} - P_{O2}$	3	Bondarenko et al. [29]
k_a^+	RyR $P_{C1} - P_{O1}$ rate constant	6.075 μM^{-4} s^{-1}	Bondarenko et al. [29]
k_a^-	RyR $P_{O1} - P_{C1}$ rate constant	71.25 s^{-1}	Bondarenko et al. [29]
k_b^+	RyR $P_{O1} - P_{O2}$ rate constant	4.05 μM^{-3} s^{-1}	Bondarenko et al. [29]
k_b^-	RyR $P_{O2} - P_{O1}$ rate constant	965.0 s^{-1}	Bondarenko et al. [29]
k_c^+	RyR $P_{O1} - P_{C2}$ rate constant	9.0 s^{-1}	Bondarenko et al. [29]
k_c^-	RyR $P_{C2} - P_{O1}$ rate constant	0.8 s^{-1}	Bondarenko et al. [29]
k_{ap}^+	RyR $P_{C1p} - P_{O1p}$ rate constant	$5k_a^+$	Bondarenko [16]
k_{ap}^-	RyR $P_{O1p} - P_{C1p}$ rate constant	$3k_a^-$	Bondarenko [16]
k_{bp}^+	RyR $P_{O1p} - P_{O2p}$ rate constant	$5k_b^+$	Bondarenko [16]
k_{bp}^-	RyR $P_{O2p} - P_{O1p}$ rate constant	$3k_b^-$	Bondarenko [16]

k_{cp}^{+}	RyR $P_{O1p} - P_{C2p}$ rate constant	$50k_c^{+}$	Bondarenko [16]
k_{cp}^{-}	RyR $P_{C2p} - P_{O1p}$ rate constant	$30k_c^{-}$	Bondarenko [16]
f_{RyR}	Allosteric factor for RyR	0.001	Bondarenko [16]
k_{RyR_PKA}	Phosphorylation rate of ryanodine receptors by PKA	$5.775 \cdot 10^{-2}$ μM^{-1} s^{-1}	Bondarenko [16]
k_{RyR_PP}	Dephosphorylation rate of ryanodine receptors by PP1	0.28875 μM^{-1} s^{-1}	Bondarenko [16]
K_{RyR_PKA}	Affinity of ryanodine receptors for PKA	0.5 μM	Bondarenko [16]
K_{RyR_PP}	Affinity of ryanodine receptors for PP1	0.05 μM	Bondarenko [16]

$$[RyR]^{ecav} = [RyR]_{tot} \frac{V_{cell}}{V_{ecav}} \tag{B.214}$$

$$C_1 = 1 - (C_2 + O_1 + O_2 + C_{1p} + C_{2p} + O_{1p} + O_{2p}) \tag{B.215}$$

$$\frac{dP_{O1}}{dt} = k_a^{+}[Ca^{2+}]_{ss}^{n} P_{C1} - k_a^{-} P_{O1} - k_b^{+}[Ca^{2+}]_{ss}^{m} P_{O1} + k_b^{-} P_{O2} - k_c^{+} P_{O1} + k_c^{-} P_{C2} \tag{B.216}$$
$$- \frac{f_{RyR} k_{RyR\_PKA} [C]^{ecav} P_{O1}}{K_{RyR\_PKA} + [RyR]^{ecav} P_{O1}} + \frac{k_a^{+} k_{ap}^{-}}{k_{ap}^{+} k_a^{-}} \frac{f_{RyR} k_{RyR\_PP} [PP1]^{ecav} P_{O1p}}{K_{RyR\_PP} + [RyR]^{ecav} P_{O1p}}$$

$$\frac{dP_{O2}}{dt} = k_b^{+}[Ca^{2+}]_{ss}^{m} P_{O1} - k_b^{-} P_{O2} \tag{B.217}$$
$$- \frac{f_{RyR} k_{RyR\_PKA} [C]^{ecav} P_{O2}}{K_{RyR\_PKA} + [RyR]^{ecav} P_{O2}} + \frac{k_a^{+} k_{ap}^{-} k_b^{+} k_{bp}^{-}}{k_{ap}^{+} k_a^{-} k_{bp}^{+} k_b^{-}} \frac{f_{RyR} k_{RyR\_PP} [PP1]^{ecav} P_{O2p}}{K_{RyR\_PP} + [RyR]^{ecav} P_{O2p}}$$

$$\frac{dP_{C2}}{dt} = k_c^{+} P_{O1} - k_c^{-} P_{C2} \tag{B.218}$$
$$- \frac{f_{RyR} k_{RyR\_PKA} [C]^{ecav} P_{C2}}{K_{RyR\_PKA} + [RyR]^{ecav} P_{C2}} + \frac{k_a^{+} k_{ap}^{-} k_c^{+} k_{cp}^{-}}{k_{ap}^{+} k_a^{-} k_{cp}^{+} k_c^{-}} \frac{f_{RyR} k_{RyR\_PP} [PP1]^{ecav} P_{C2p}}{K_{RyR\_PP} + [RyR]^{ecav} P_{C2p}}$$

$$\frac{dP_{C1p}}{dt} = -k_{ap}^{+}[Ca^{2+}]_{ss}^{n} P_{C1p} + k_{ap}^{-} P_{O1p} \tag{B.219}$$
$$+ \frac{k_{RyR\_PKA} [C]^{ecav} P_{C1}}{K_{RyR\_PKA} + [RyR]^{ecav} P_{C1}} - \frac{k_{RyR\_PP} [PP1]^{ecav} P_{C1p}}{K_{RyR\_PP} + [RyR]^{ecav} P_{C1p}}$$

$$\frac{dP_{O1p}}{dt} = k_{ap}^{+}[Ca^{2+}]_{ss}^{n} P_{C1p} - k_{ap}^{-} P_{O1p} - k_{bp}^{+}[Ca^{2+}]_{ss}^{m} P_{O1p} + k_{bp}^{-} P_{O2p} - k_{cp}^{+} P_{O1p} + k_{cp}^{-} P_{C2p} \quad \text{(B.220)}$$
$$+ \frac{f_{RyR} k_{RyR\_PKA}[C]^{ecav} P_{O1}}{K_{RyR\_PKA} + [RyR]^{ecav} P_{O1}} - \frac{k_a^{+} k_{ap}^{-}}{k_{ap}^{+} k_a^{-}} \frac{f_{RyR} k_{RyR\_PP}[PP1]^{ecav} P_{O1p}}{K_{RyR\_PP} + [RyR]^{ecav} P_{O1p}}$$

$$\frac{dP_{O2p}}{dt} = k_{bp}^{+}[Ca^{2+}]_{ss}^{m} P_{O1p} - k_{bp}^{-} P_{O2p} \quad \text{(B.221)}$$
$$+ \frac{f_{RyR} k_{RyR\_PKA}[C]^{ecav} P_{O2}}{K_{RyR\_PKA} + [RyR]^{ecav} P_{O2}} - \frac{k_a^{+} k_{ap}^{-} k_b^{+} k_{bp}^{-}}{k_{ap}^{+} k_a^{-} k_{bp}^{+} k_b^{-}} \frac{f_{RyR} k_{RyR\_PP}[PP1]^{ecav} P_{O2p}}{K_{RyR\_PP} + [RyR]^{ecav} P_{O2p}}$$

$$\frac{dP_{C2p}}{dt} = k_{cp}^{+} P_{O1p} - k_{cp}^{-} P_{C2p} \quad \text{(B.222)}$$
$$+ \frac{f_{RyR} k_{RyR\_PKA}[C]^{ecav} P_{C2}}{K_{RyR\_PKA} + [RyR]^{ecav} P_{C2}} - \frac{k_a^{+} k_{ap}^{-} k_c^{+} k_{cp}^{-}}{k_{ap}^{+} k_a^{-} k_{cp}^{+} k_c^{-}} \frac{f_{RyR} k_{RyR\_PP}[PP1]^{ecav} P_{C2p}}{K_{RyR\_PP} + [RyR]^{ecav} P_{C2p}}$$

Na^+-K^+ pump module

Para-meter	Definition	Value	Reference
$I_{NaK}^{\max}$	Maximum Na^+-K^+ pump current	4.0 pA/pF	Bondarenko [16]
$K_{m,Nai}^{np}$	Na^+ half-saturation constant for Na^+-K^+ pump current (non-phosphorylated PLM)	18,800 μM	Despa et al. [123]
$K_{m,Nai}^{p}$	Na^+ half-saturation constant for Na^+-K^+ pump current (phosphorylated PLM)	13,600 μM	Despa et al. [123]
$K_{m,Ko}$	K+ half-saturation constant Na^+-K^+ pump current	1,500 μM	Bondarenko et al. [29]
k_{PLM_PKA}	Rate of PLM phosphorylation by PKA	$3.053 \cdot 10^{-3}$ μM^{-1} s^{-1}	Bondarenko [16]
K_{PLM_PKA}	Relative affinity for PLM phosphorylation by PKA	0.0011001	Heijman et al. [34]
k_{PLM_PP}	Rate of PLM dephosphorylation by PP1 and PP2A	$1.8491 \cdot 10^{-2}$ μM^{-1} s^{-1}	Bondarenko [16]
K_{PLM_PP}	Relative affinity for PLM dephosphorylation by PP1 and PP2A	5.7392	Heijman et al. [34]

$$\frac{df_{PLM,p}^{cav}}{dt} = \frac{k_{PLM\_PKA}[C]^{cav}(1 - f_{PLM,p}^{cav})}{K_{PLM\_PKA} + (1 - f_{PLM,p}^{cav})} - \frac{k_{PLM\_PP}[PP]^{cav} f_{PLM,p}^{cav}}{K_{PLM\_PP} + f_{PLM,p}^{cav}} \quad \text{(B.223)}$$

$$I_{NaK} = I_{NaK}^{\max} f_{NaK} \frac{1}{1+(K_{m,Nai}/[Na^+]_i)^3} \frac{[K^+]_0}{[K^+]_0 + K_{m,Ko}} \tag{B.224}$$

$$f_{NaK} = \frac{1}{1+0.1245e^{-0.1VF/RT} + 0.0365\sigma e^{-VF/RT}} \tag{B.225}$$

$$\sigma = \frac{1}{7}(e^{[Na^+]_0/67300} - 1) \tag{B.226}$$

$$K_{m,Nai} = K_{m,Nai}^{np}(1 - f_{PLM,p}^{cav}) + K_{m,Nai}^{p} f_{PLM,p}^{cav} \tag{B.227}$$

Ultra-rapidly activating delayed rectifier K^+ current module

Para-meter	Definition	Value	Reference
G_{Kur}	Specific maximum conductivity for the ultra-rapidly activating delayed rectifier K^+ current (non-phosphorylated)	0.3424 pA/pF	Petkova-Kirova et al. [61]
G_{Kurp}	Specific maximum conductivity for the ultra-rapidly activating delayed rectifier K^+ current (phosphorylated)	0.53307 pA/pF	Bondarenko [16]
k_{IKur_PKA}	Rate of I_{Kur} phosphorylation by PKA	$6.9537 \cdot 10^{-3}$ μM^{-1} s^{-1}	Bondarenko [16]
K_{IKur_PKA}	Relative affinity for I_{Kur} phosphorylation by PKA	0.138115	Bondarenko [16]
k_{IKur_PP}	Rate of I_{Kur} dephosphorylation by PP1	$3.170 \cdot 10^{-2}$ μM^{-1} s^{-1}	Bondarenko [16]
K_{IKur_PP}	Relative affinity for I_{Kur} dephosphorylation by PP1	0.23310	Bondarenko [16]

$$E_K = \frac{RT}{F} \ln\left(\frac{[K^+]_o}{[K^+]_i}\right) \tag{B.228}$$

$$I_{Kur} = (G_{Kur} a_{ur} i_{ur} f_{IKur}^{ecav} + G_{Kurp} a_{urp} i_{urp} (1 - f_{IKur}^{ecav}))(V - E_K) \tag{B.229}$$

$$\frac{df_{IKur}^{ecav}}{dt} = \frac{k_{IKur\_PP}[PP1]^{ecav}(1 - f_{IKur}^{ecav})}{K_{IKur\_PP} + (1 - f_{IKur}^{ecav})} - \frac{k_{IKur\_PKA}[C]^{ecav} f_{IKur}^{ecav}}{K_{IKur\_PKA} + f_{IKur}^{ecav}} \tag{B.230}$$

$$a_{ss} = \frac{1}{1+e^{-(V+22.5)/7.7}} \tag{B.231}$$

$$i_{ss} = \frac{1}{1+e^{(V+45.2)/5.7}} \tag{B.232}$$

$$\tau_{aur} = \frac{6.1}{e^{0.0629(V+40.0)}+e^{-0.0629(V+40.0)}} + 2.058 \tag{B.233}$$

$$\tau_{iur} = 1200.0 - \frac{170.0}{1+e^{(V+45.2)/5.7}} \tag{B.234}$$

$$\frac{da_{ur}}{dt} = \frac{a_{ss}-a_{ur}}{\tau_{aur}} \tag{B.235}$$

$$\frac{di_{ur}}{dt} = \frac{i_{ss}-i_{ur}}{\tau_{iur}} \tag{B.236}$$

$$\frac{da_{urp}}{dt} = \frac{a_{ss}-a_{urp}}{\tau_{aur}} \tag{B.237}$$

$$\frac{di_{urp}}{dt} = \frac{i_{ss}-i_{urp}}{\tau_{iur}} \tag{B.238}$$

Rapidly inactivating transient outward K^+ current module

Para-meter	Definition	Value	Reference
$G_{Kto,f}$	Specific maximum conductivity for the rapidly inactivating transient outward K^+ current (non-phosphorylated)	0.3846 pA/pF	Petkova-Kirova et al. [61]
$G_{Kto,fp}$	Specific maximum conductivity for the rapidly inactivating transient outward K^+ current (phosphorylated)	$G_{Kto,f}$	Petkova-Kirova et al. [61]
k_{IKto,f_PKA}	Rate of $I_{Kto,f}$ phosphorylation by PKA	$4.38983 \cdot 10^{-2}$ μM^{-1} s^{-1}	Bondarenko [16]
K_{IKto,f_PKA}	Relative affinity for $I_{Kto,f}$ phosphorylation by PKA	0.27623	Bondarenko [16]
k_{IKto,f_PP}	Rate of $I_{Kto,f}$ dephosphorylation by PP1	$9.09678 \cdot 10^{-2}$ μM^{-1} s^{-1}	Bondarenko [16]
K_{IKto,f_PP}	Relative affinity for $I_{Kto,f}$ dephosphorylation by PP1	0.23310	Bondarenko [16]

$$I_{Kto,f} = (G_{Kto,f} a_{to,f}^3 i_{to,f} f_{IKto,f}^{ecav} + G_{Kto,fp} a_{to,fp}^3 i_{to,fp} (1 - f_{IKto,f}^{ecav}))(V - E_K) \quad \text{(B.239)}$$

$$\frac{df_{IKto,f}^{ecav}}{dt} = \frac{k_{IKto,f\_PP}[PP1]^{ecav}(1 - f_{IKto,f}^{ecav})}{K_{IKto,f\_PP} + (1 - f_{IKto,f}^{ecav})} - \frac{k_{IKto,f\_PKA}[C]^{ecav} f_{IKto,f}^{ecav}}{K_{IKto,f\_PKA} + f_{IKto,f}^{ecav}} \quad \text{(B.240)}$$

$$\frac{da_{to,f}}{dt} = \alpha_a (1 - a_{to,f}) - \beta_a a_{to,f} \quad \text{(B.241)}$$

$$\frac{di_{to,f}}{dt} = \alpha_i (1 - i_{to,f}) - \beta_i i_{to,f} \quad \text{(B.242)}$$

$$\frac{da_{to,fp}}{dt} = \alpha_{ap} (1 - a_{to,fp}) - \beta_{ap} a_{to,fp} \quad \text{(B.243)}$$

$$\frac{di_{to,fp}}{dt} = \alpha_{ip} (1 - i_{to,fp}) - \beta_{ip} i_{to,fp} \quad \text{(B.244)}$$

$$\alpha_a = 0.18064 e^{0.03577(V+33.0)} \quad \text{(B.245)}$$

$$\beta_a = 0.3956 e^{-0.06237(V+33.0)} \quad \text{(B.246)}$$

$$\alpha_i = \frac{0.000152 e^{-(V+15.5)/7.0}}{0.067083 e^{-(V+35.5)/7.0} + 1} \quad \text{(B.247)}$$

$$\beta_i = \frac{0.00095 e^{(V+35.5)/7.0}}{0.051335 e^{(V+35.5)/7.0} + 1} \quad \text{(B.248)}$$

$$\alpha_{ap} = 0.18064 e^{0.03577(V+17.0)} \quad \text{(B.249)}$$

$$\beta_{ap} = 0.3956 e^{-0.06237(V+17.0)} \quad \text{(B.250)}$$

$$\alpha_{ip} = \frac{0.000152 e^{-(V+7.5)/7.0}}{0.067083 e^{-(V+27.5)/7.0} + 1} \quad \text{(B.251)}$$

$$\beta_{ip} = \frac{0.00095 e^{(V+27.5)/7.0}}{0.051335 e^{(V+27.5)/7.0} + 1} \quad \text{(B.252)}$$

Time-independent K^+ current module

$$\alpha_{K1} = \frac{1.02}{1+\exp(0.2385(V - E_K - 59.215))} \tag{B.253}$$

$$\beta_{K1} = \frac{0.8\exp(0.08032(V - E_K + 5.476)) + \exp(0.06175(V - E_K - 594.31))}{1+\exp(-0.5143(V - E_K + 4.753))} \tag{B.254}$$

$$I_{K1} = 0.27\sqrt{\frac{[K^+]_o}{5400}}\frac{\alpha_{K1}}{\alpha_{K1}+\beta_{K1}}(V - E_K) \tag{B.255}$$

Phospholamban module

Para-meter	Definition	Value	Reference
$K_{m,up}^{np}$	Half-saturation constant for SR Ca^{2+}-ATPase pump (non-phosphorylated)	0.41 μM	Bondarenko [16]
$K_{m,up}^{p}$	Half-saturation constant for SR Ca^{2+}-ATPase pump (phosphorylated)	0.37 μM	Bondarenko [16]
v_3	SR Ca^{2+}-ATPase maximum pump rate	306.0 μM s^{-1}	Bondarenko [16]
k_{PLB_PKA}	Rate of PLB phosphorylation by PKA	0.108917 μM^{-1} s^{-1}	Bondarenko [16]
K_{PLB_PKA}	Relative affinity for PLB phosphorylation by PKA	$4.90970 \cdot 10^{-4}$	Heijman et al. [34]
k_{PLB_PP1}	Rate of PLB dephosphorylation by PP1	$4.41956 \cdot 10^{-2}$ μM^{-1} s^{-1}	Bondarenko [16]
K_{PLB_PP1}	Relative affinity for PLB dephosphorylation by PP1	$1.69376 \cdot 10^{-2}$	Bondarenko [16]

$$K_{m,up} = K_{m,up}^{np}(1 - f_{PLB,p}^{cyt}) + K_{m,up}^{p} f_{PLB,p}^{cyt} \tag{B.256}$$

$$\frac{df_{PLB,p}^{cyt}}{dt} = \frac{k_{PLB\_PKA}\cdot[C]^{cyt}\cdot(1 - f_{PLB,p}^{cyt})}{K_{PLB\_PKA} + (1 - f_{PLB,p}^{cyt})} - \frac{k_{PLB\_PP1}\cdot[PP1]_f^{cyt}\cdot f_{PLB,p}^{cyt}}{K_{PLB\_PP1} + f_{PLB,p}^{cyt}} \tag{B.257}$$

Troponin I module

Parameter	Definition	Value	Reference
$[\mathrm{LTRPN}]_{\mathrm{tot}}$	Total cytosolic troponin low-affinity site concentration	70.0 μM	Bondarenko et al. [29]
$[\mathrm{HTRPN}]_{\mathrm{tot}}$	Total cytosolic troponin high-affinity site concentration	140.0 μM	Bondarenko et al. [29]
k^{+}_{htrpn}	Ca^{2+} on rate constant for troponin high-affinity sites	2.37 μM s^{-1}	Bondarenko et al. [29]
k^{-}_{htrpn}	Ca^{2+} off rate constant for troponin high-affinity sites	0.032 s^{-1}	Bondarenko et al. [29]
k^{+}_{ltrpn}	Ca^{2+} on rate constant for troponin low-affinity sites	32.7 μM s^{-1}	Bondarenko et al. [29]
$k^{-}_{ltrpn,np}$	Ca^{2+} off rate constant for troponin low-affinity sites (non-phosphorylated)	19.6 s^{-1}	Bondarenko et al. [29]
$k^{-}_{ltrpn,p}$	Ca^{2+} off rate constant for troponin low-affinity sites (phosphorylated)	29.4 s^{-1}	Bondarenko [16]
k_{TnI_PKA}	Rate of TnI phosphorylation by PKA	0.0247254 μM^{-1} s^{-1}	Bondarenko [16]
K_{TnI_PKA}	Relative affinity for TnI phosphorylation by PKA	$2.71430 \cdot 10^{-5}$	Heijman et al. [34]
k_{TnI_PP2A}	Rate of TnI dephosphorylation by PP2A	0.0865898 μM^{-1} s^{-1}	Bondarenko [16]
K_{TnI_PP2A}	Relative affinity for TnI dephosphorylation by PP2A	0.801420	Bondarenko [16]

$$k^{-}_{ltrpn} = k^{-}_{ltrpn,np}(1 - f^{cyt}_{TnI,p}) + k^{-}_{ltrpn,p} f^{cyt}_{TnI,p} \tag{B.258}$$

$$\frac{df^{cyt}_{TnI,p}}{dt} = \frac{k_{TnI\_PKA} \cdot [C]^{cyt} \cdot (1 - f^{cyt}_{TnI,p})}{K_{TnI\_PKA} + (1 - f^{cyt}_{TnI,p})} - \frac{k_{TnI\_PP2A} \cdot [PP2A]^{cyt} \cdot f^{cyt}_{TnI,p}}{K_{TnI\_PP2A} + f^{cyt}_{TnI,p}} \tag{B.259}$$

$$\frac{d[LTRPNCa]}{dt} = k^{+}_{ltrpn}[Ca^{2+}]_i([LTRPN]_{tot} - [LTRPNCa]) - k^{-}_{ltrpn}[LTRPNCa] \tag{B.260}$$

$$\frac{d[HTRPNCa]}{dt} = k^{+}_{htrpn}[Ca^{2+}]_i([HTRPN]_{tot} - [HTRPNCa]) - k^{-}_{htrpn}[HTRPNCa] \tag{B.261}$$

MyBP-C module

Parameter	Definition	Value	Reference
$[\mathrm{MyBPC}]_{\mathrm{tot}}$	Total cytosolic myosin binding protein C concentration	50.0 μM	This paper
k_{MyBPC_PKA}	Rate of MyBP-C phosphorylation by PKA	$7.0 \cdot 10^{-3}$ μM^{-1} s^{-1}	This paper
K_{MyBPC_PKA}	Relative affinity for MyBP-C phosphorylation by PKA	0.5	This paper
k_{MyBPC_PP}	Rate of MyBP-C dephosphorylation by PP1 and PP2A	$1.3985 \cdot 10^{-3}$ μM^{-1} s^{-1}	This paper
K_{MyBPC_PP}	Relative affinity for MyBP-C dephosphorylation by PP1 and PP2A	0.4	This paper

$$\frac{df_{MyBPC,p}^{cyt}}{dt} = \frac{k_{MyBPC\_PKA} \cdot [C]^{cyt} \cdot (1 - f_{MyBPC,p}^{cyt})}{K_{MyBPC\_PKA} + (1 - f_{MyBPC,p}^{cyt})} - \frac{k_{MyBPC\_PP} \cdot \left([PP1]^{cyt} + [PP2A]^{cyt}\right) \cdot f_{MyBPC,p}^{cyt}}{K_{MyBPC\_PP} + f_{MyBPC,p}^{cyt}} \tag{B.262}$$

Electrophysiological part: unaffected by PKA

Membrane potential

$$\frac{dV}{dt} = -\frac{1}{C_m}(I_{CaL} + I_{p(Ca)} + I_{NaCa} + I_{Cab} + I_{Na} + I_{Nab} + I_{NaK} + I_{Kto,f} + I_{K1} + I_{Kur} + I_{Kss} + I_{Kr} + I_{Cl,Ca} - I_{stim}) \tag{B.263}$$

Calcium dynamics: Calcium concentrations

$$\frac{d[Ca^{2+}]_i}{dt} = B_i \left\{ J_{leak} + J_{xfer} - J_{up} - J_{trpn} - (I_{Cab} - 2I_{NaCa} + I_{p(Ca)} + I_{CaL}^{cav}) \frac{A_{cap} C_m}{2V^{cyt} F} \right\} \tag{B.264}$$

$$\frac{d[Ca^{2+}]_{ss}}{dt} = B_{ss} \left\{ J_{rel} \frac{V_{JSR}}{V_{ss}} - J_{xfer} \frac{V^{cyt}}{V_{ss}} - I_{CaL}^{ecav} \frac{A_{cap} C_m}{2V_{ss} F} \right\} \tag{B.265}$$

$$\frac{d[Ca^{2+}]_{JSR}}{dt} = B_{JSR} \left\{ J_{tr} - J_{rel} \right\} \tag{B.266}$$

$$\frac{d[Ca^{2+}]_{NSR}}{dt} = \left\{ J_{up} - J_{leak} \right\} \frac{V^{cyt}}{V_{NSR}} - J_{tr} \frac{V_{JSR}}{V_{NSR}} \tag{B.267}$$

$$B_i = \left\{1 + \frac{[CMDN]_{tot} K_m^{CMDN}}{(K_m^{CMDN} + [Ca^{2+}]_i)^2}\right\}^{-1} \tag{B.268}$$

$$B_{ss} = \left\{1 + \frac{[CMDN]_{tot} K_m^{CMDN}}{(K_m^{CMDN} + [Ca^{2+}]_{ss})^2}\right\}^{-1} \tag{B.269}$$

$$B_{JSR} = \left\{1 + \frac{[CSQN]_{tot} K_m^{CSQN}}{(K_m^{CSQN} + [Ca^{2+}]_{JSR})^2}\right\}^{-1} \tag{B.270}$$

Calcium dynamics: Calcium fluxes

$$J_{rel} = v_1 (P_{O1} + P_{O2} + P_{O1p} + P_{O2p})([Ca^{2+}]_{JSR} - [Ca^{2+}]_{ss} P_{RyR}) \tag{B.271}$$

$$J_{tr} = \frac{[Ca^{2+}]_{NSR} - [Ca^{2+}]_{JSR}}{\tau_{tr}} \tag{B.272}$$

$$J_{xfer} = \frac{[Ca^{2+}]_{ss} - [Ca^{2+}]_i}{\tau_{xfer}} \tag{B.273}$$

$$J_{leak} = v_2([Ca^{2+}]_{NSR} - [Ca^{2+}]_i) \tag{B.274}$$

$$J_{up} = v_3 \frac{[Ca^{2+}]_i^2}{K_{m,up}^2 + [Ca^{2+}]_i^2} \tag{B.275}$$

$$\begin{aligned} J_{trpn} = {} & k_{htrpn}^{+}[Ca^{2+}]_i([HTRPN]_{tot} - [HTRPNCa]) - k_{htrpn}^{-}[HTRPNCa] \\ & + k_{ltrpn}^{+}[Ca^{2+}]_i([LTRPN]_{tot} - [LTRPNCa]) - k_{ltrpn}^{-}[LTRPNCa] \end{aligned} \tag{B.276}$$

$$\frac{dP_{RyR}}{dt} = -0.04 P_{RyR} - 0.1 \frac{I_{CaL}^{ecav}}{I_{CaL,\max}} e^{-\frac{(V+5.0)^2}{648.0}} \tag{B.277}$$

Calcium pump current

$$I_{p(Ca)} = I_{p(Ca)}^{\max} \frac{[Ca^{2+}]_i^2}{K_{m,p(Ca)}^2 + [Ca^{2+}]_i^2} \tag{B.278}$$

Na^+/Ca^{2+} exchanger current

$$I_{NaCa} = k_{NaCa} \frac{1}{K_{m,Na}^3 + [Na^+]_o^3} \frac{1}{K_{m,Ca} + [Ca^{2+}]_o} \frac{1}{1 + k_{sat} e^{(\eta-1)VF/RT}} \times (e^{\eta VF/RT} [Na^+]_i^3 [Ca^{2+}]_o - 2.0 e^{(\eta-1)VF/RT} [Na^+]_o^3 [Ca^{2+}]_i) \quad \text{(B.279)}$$

Calcium background current

$$I_{Cab} = G_{Cab}(V - E_{CaN}) \quad \text{(B.280)}$$

$$E_{CaN} = \frac{RT}{2F} \ln\left(\frac{[Ca^{2+}]_o}{[Ca^{2+}]_i}\right) \quad \text{(B.281)}$$

Sodium dynamics: Sodium concentration

$$\frac{d[Na^+]_i}{dt} = -(I_{Na} + + I_{Nab} + 3I_{NaCa} + 3I_{NaK}) \frac{A_{cap} C_m}{V^{cyt} F} \quad \text{(B.282)}$$

Sodium background current

$$I_{Nab} = G_{Nab}(V - E_{Na}) \quad \text{(B.283)}$$

Potassium dynamics: Potassium concentration

$$\frac{d[K^+]_i}{dt} = -(I_{Kto,f} + I_{Kto,s} + I_{Kur} + I_{Kss} + I_{K1} + I_{Kr} + I_{Ks} - 2I_{NaK}) \frac{A_{cap} C_m}{V^{cyt} F} \quad \text{(B.284)}$$

Non-inactivating steady-state K^+ current

$$I_{Kss} = G_{Kss} a_{Kss} (V - E_K) \quad \text{(B.285)}$$

$$\frac{da_{Kss}}{dt} = \frac{a_{ss} - a_{Kss}}{\tau_{Kss}} \quad \text{(B.286)}$$

$$\tau_{Kss} = \frac{1235.5}{e^{0.0862(V+40.0)} + e^{-0.0862(V+40.0)}} + 13.17 \quad \text{(B.287)}$$

Rapid delayed rectifier K^+ current

$$I_{Kr} = G_{Kr} O_{Kr} (V - E_{Kr}) \tag{B.288}$$

$$E_{Kr} = \frac{RT}{F} \ln\left(\frac{0.98[K^+]_o + 0.02[Na^+]_o}{0.98[K^+]_i + 0.02[Na^+]_i} \right) \tag{B.289}$$

$$C_{Kr0} = 1 - (C_{Kr1} + C_{Kr2} + O_{Kr} + I_{Kr1}) \tag{B.290}$$

$$\frac{dC_{Kr1}}{dt} = \alpha_{a0} C_{Kr0} - \beta_{a0} C_{Kr1} + k_b C_{Kr2} - k_f C_{Kr1} \tag{B.291}$$

$$\frac{dC_{Kr2}}{dt} = k_f C_{Kr1} - k_b C_{Kr2} + \beta_{a1} O_{Kr} - \alpha_{a1} C_{Kr2} \tag{B.292}$$

$$\frac{dO_{Kr}}{dt} = \alpha_{a1} C_{Kr2} - \beta_{a1} O_{Kr} + \beta_{ir} I_{Kr1} - \alpha_{ir} O_{Kr} \tag{B.293}$$

$$\frac{dI_{Kr1}}{dt} = \alpha_{ir} O_{Kr} + \beta_{ir} I_{Kr1} \tag{B.294}$$

$$\alpha_{a0} = 0.022348 e^{0.01176V} \tag{B.295}$$

$$\beta_{a0} = 0.047002 e^{-0.0631V} \tag{B.296}$$

$$\alpha_{a1} = 0.013733 e^{0.038198V} \tag{B.297}$$

$$\beta_{a1} = 0.0000689 e^{-0.04178V} \tag{B.298}$$

$$\alpha_{ir} = 0.090821 e^{0.023391(V+5.0)} \tag{B.299}$$

$$\beta_{ir} = 0.006497 e^{-0.03268(V+5.0)} \tag{B.300}$$

Ca^{2+}-activated Cl^- current

$$I_{Cl,Ca} = G_{Cl,Ca} O_{Cl,Ca} \frac{[Ca^{2+}]_i}{[Ca^{2+}]_i + K_{m,Cl}} (V - E_{Cl}) \quad \text{(B.301)}$$

$$O_{Cl,Ca} = \frac{0.2}{1 + e^{-(V-46.7)/7.8}} \quad \text{(B.302)}$$

Extracellular ion concentrations

Parameter	Definition	Value	Reference
$[K^+]_o$	Extracellular K^+ concentration	5,400 μM	Bondarenko et al. [29]
$[Na^+]_o$	Extracellular Na^+ concentration	140,000 μM	Bondarenko et al. [29]
$[Ca^{2+}]_o$	Extracellular Ca^{2+} concentration	1,800 μM	Bondarenko et al. [29]

Sarcoplasmic reticulum parameters

Parameter	Definition	Value	Reference
v_2	Ca^{2+} leak rate constant from the NSR	$1.74 \cdot 10^{-2}$ s^{-1}	Bondarenko et al. [29]
τ_{tr}	Time constant for transfer from NSR to JSR	0.02 s	Bondarenko et al. [29]
τ_{xfer}	Time constant for transfer from subspace to cytosol	0.008 s	Bondarenko et al. [29]

Calmodulin and calsequestrin parameters

Parameter	Definition	Value	Reference
$[CMDN]_{tot}$	Total cytosolic calmodulin concentration	50.0 μM	Bondarenko et al. [29]
$[CSQN]_{tot}$	Total JSR calsequestrin concentration	15,000.0 μM	Bondarenko et al. [29]
K_m^{CMDN}	Ca^{2+} half-saturation constant for calmodulin	0.238 μM	Bondarenko et al. [29]
K_m^{CSQN}	Ca^{2+} half-saturation constant for calsequestrin	800.0 μM	Bondarenko et al. [29]

Membrane current parameters

Parameter	Definition	Value	Reference
C_m	Specific membrane capacitance	1.0 μF/cm^2	Bondarenko et al. [29]
F	Faraday constant	96.5 C/mmol	Bondarenko et al. [29]
T	Absolute temperature	298 K	Bondarenko et al. [29]
R	Ideal gas constant	8.314 J mol^{-1} K^{-1}	Bondarenko et al. [29]
k_{NaCa}	Scaling factor for Na^+/Ca^{2+} exchanger	275 pA/pF	Bondarenko [16]
$K_{m,Na}$	Na^+ half-saturation constant for Na^+/Ca^{2+} exchanger	87,500 μM	Bondarenko et al. [29]
$K_{m,Ca}$	Ca^{2+} half-saturation constant for Na^+/Ca^{2+} exchanger	1,380 μM	Bondarenko et al. [29]
k_{sat}	Na^+/Ca^{2+} exchanger saturation factor at very negative potentials	0.27	Bondarenko [16]
η	Controls voltage dependence of Na^+/Ca^{2+} exchanger	0.35	Bondarenko et al. [29]
$I_{p(Ca)}^{\max}$	Maximum sarcolemmal Ca^{2+} pump current	0.051	Bondarenko [16]
$K_{m,p(Ca)}$	Ca^{2+} half-saturation constant for sarcolemmal Ca^{2+} pump current	0.5 μM	Bondarenko et al. [29]
G_{Cab}	Maximum background Ca^{2+} current conductance	0.000284 mS/μF	Bondarenko [16]
G_{Nab}	Maximum background Na^+ current conductance	0.0063 mS/μF	Bondarenko [16]
$G_{Kto,s}$	Specific maximum conductivity for the slowly inactivating transient outward K^+ current	0.0 mS/μF	Bondarenko et al. [29]
G_{Kss}	Specific maximum conductivity for the noninactivating steady-state K^+ current	0.0611 mS/μF	Petkova-Kirova et al. [61]
G_{Ks}	Specific maximum conductivity for the slow delayed rectifier K^+ current	0.00575 mS/μF	Bondarenko et al. [29]
G_{Kr}	Specific maximum conductivity for the rapid delayed rectifier K^+ current	0.078 mS/μF	Bondarenko et al. [29]
k_f	Rate constant for the rapid delayed rectifier K^+ current	23.761 s^{-1}	Bondarenko et al. [29]
k_b	Rate constant for the rapid delayed rectifier K^+ current	36.778 s^{-1}	Bondarenko et al. [29]
$G_{Cl,Ca}$	Specific maximum conductivity for the Ca^{2+}-activated Cl^- current	10.0 mS/μF	Bondarenko et al. [29]
$K_{m,Cl}$	Half-saturation constant for the Ca^{2+}-activated Cl^- current	10.0 μM	Bondarenko et al. [29]
E_{Cl}	Reversal potential for the Ca^{2+}-activated Cl^- current	−40 mV	Bondarenko et al. [29]

Contraction part

Contraction Parameters

Parameter	Definition	Value	Reference
SL_0	Initial sarcomere length	1.9 – 2.3 μm	
SL_{rest}	Resting sarcomere length	1.9 μm	Rice et al. [43]
k_{PN}	Transition rate from permissive to non-permissive state	1,350 s^{-1}	This paper
$PCon_{titin}$	Titin passive force amplitude	0.002	Rice et al. [43]
$PExp_{titin}$	Titin passive force exponent	10.0	Rice et al. [43]
$SL_{collagen}$	Collagen sarcomere length	2.25 μm	Rice et al. [43]
$PCon_{collagen}$	Collagen passive force amplitude	0.0005	This paper
$PExp_{collagen}$	Collagen passive force exponent	14.0	This paper
$mass$	Sarcomere mass	$15.0 \cdot 10^{-6}$ s^2 μm^{-1}	This paper
KSE	Stiffness	1.0 μm^{-1}	This paper
f_{XB0}	Basic transition rate from weak to strong crossbridge	18.0 s^{-1}	This paper
g_{minxb0}	Minimum detachment rate from strong to weak crossbridge	12.348 s^{-1}	This paper
$visc_0$	Effective viscosity without β_1-adrenergic stimulation	0.0141 s μm^{-1}	This paper
a_{fx0}	Non-linear correction to effective viscosity without β_1-adrenergic stimulation	0.040 s μm^{-1}	This paper

Permissive states

$$\frac{dN0}{dt} = k_{PN}P0 + g_{10SL}N1 - k_{NP}N0 \tag{B.303}$$

$$\frac{dN1}{dt} = k_{PN}P1 - \left(k_{NP} + g_{10SL}\right)N1 \tag{B.304}$$

$$\frac{dP0}{dt} = g_{10SL}P1 + k_{NP}N0 - \left(k_{PN} + f_{01}\right)P0 \tag{B.305}$$

$$\frac{dP1}{dt} = g_{21SL}P2 + f_{01}P0 + k_{NP}N1 - \left(f_{12} + g_{10SL} + k_{PN}\right)P1 \tag{B.306}$$

$$\frac{dP2}{dt} = g_{32SL}P3 + f_{12}P1 - \left(f_{23} + g_{21SL}\right)P2 \tag{B.307}$$

$$\frac{dP3}{dt} = f_{23}P2 - g_{32SL}P3 \tag{B.308}$$

$$f_{XB} = f_{XB0}\left(1+0.45\left(f_{TnI,p}^{cyt}-0.364\right)\right)^{-1}\left(1+1.5\left(f_{MyBPC,p}^{cyt}-0.575\right)\right)^{-1} \tag{B.309}$$

$$g_{minxb} = g_{minxb0}\left(1+0.3\left(f_{TnI,p}^{cyt}-0.364\right)\right)\left(1+1.0\left(f_{MyBPC,p}^{cyt}-0.575\right)\right) \tag{B.310}$$

$$f_{01} = 15 f_{XB} \tag{B.311}$$

$$f_{12} = 30 f_{XB} \tag{B.312}$$

$$f_{23} = 7 f_{XB} \tag{B.313}$$

$$g_{10SL} = g_{xbSL} \tag{B.314}$$

$$g_{21SL} = 2 g_{xbSL} \tag{B.315}$$

$$g_{32SL} = 3 g_{xbSL} \tag{B.316}$$

$$g_{xbSL} = g_{minxb}\left(2-\left(SL_{norm}\right)^{1.6}\right) \tag{B.317}$$

$$SL_{norm} = \frac{SL-1.3\mu\text{m}}{2.5\mu\text{m}-1.3\mu\text{m}} \tag{B.318}$$

$$k_{NP} = k_{PN}\left(\frac{\left[LTRPNCa\right]}{\left[LTRPNCa\right]_{tot}\times K_{half}}\right)^{Ntm} \tag{B.319}$$

$$Ntm = 5+3\ SL_{norm} \tag{B.320}$$

$$K_{half} = 1/\left(1+\frac{K_{Ca}}{1.5\mu\text{M}-SL_{norm}\times 1.0\mu\text{M}}\right) \tag{B.321}$$

$$K_{Ca} = \frac{k_{ltrpn}^{-}}{k_{ltrpn}^{+}} \tag{B.322}$$

Active Contraction Force

$$F_{contr} = 58.0\ F_{contrn} \tag{B.323}$$

$$F_{contrn} = \frac{P1+N1+2\left(P2\right)+3\left(P3\right)}{F_{\max}} \tag{B.324}$$

$$F_{\max} = P1_{\max} + 2\left(P2_{\max}\right) + 3\left(P3_{\max}\right) \tag{B.325}$$

$$P1_{\max} = \frac{f_{01}\left(2g_{\min xb}\right)\left(3g_{\min xb}\right)}{\Sigma} \tag{B.326}$$

$$P2_{\max} = \frac{f_{01}f_{12}\left(3g_{\min xb}\right)}{\Sigma} \tag{B.327}$$

$$P3_{\max} = \frac{f_{01}f_{12}f_{23}}{\Sigma} \tag{B.328}$$

$$\Sigma = \left(g_{\min xb}\right)\left(2g_{\min xb}\right)\left(3g_{\min xb}\right) + f_{01}\left(2g_{\min xb}\right)\left(3g_{\min xb}\right) + f_{01}f_{12}\left(3g_{\min xb}\right) + f_{01}f_{12}f_{23} \tag{B.329}$$

Passive Contraction Force

$$F_{passive}\left(SL\right) = F_{titin}\left(SL\right) + F_{collagen}\left(SL\right) \tag{B.330}$$

$$F_{titin}\left(SL\right) = \begin{cases} PCon_{titin}\left(\exp\left(PExp_{titin}\left(SL - SL_{rest}\right)\right) - 1\right) & \text{if} \quad SL \geq SL_{rest} \\ -PCon_{titin}\left(\exp\left(PExp_{titin}\left(SL_{rest} - SL\right)\right) - 1\right) & \text{if} \quad SL < SL_{rest} \end{cases} \tag{B.331}$$

$$F_{collagen}\left(SL\right) = \begin{cases} PCon_{collagen}\left(\exp\left(PExp_{collagen}\left(SL - SL_{collagen}\right)\right) - 1\right) & \text{if} \quad SL \geq SL_{collagen} \\ 0 & \text{if} \quad SL < SL_{collagen} \end{cases} \tag{B.332}$$

Viscous and flexible forces

$$F_{visc} = -visc \cdot v\left(1 - a_{fx} \cdot v\right) \tag{B.333}$$

$$visc = visc_0\left(1 + 0.33\left(f_{TnI,p}^{cyt} - 0.364\right)\right)^{-1}\left(1 + 1.1\left(f_{MyBPC,p}^{cyt} - 0.575\right)\right)^{-1} \tag{B.334}$$

$$a_{fx} = a_{fx0}\left(1 + 0.2\left(f_{TnI,p}^{cyt} - 0.364\right)\right)^{-1}\left(1 + 0.6\left(f_{MyBPC,p}^{cyt} - 0.575\right)\right)^{-1} \tag{B.335}$$

$$F_{flex} = KSE\left(SL - SL_0\right) \tag{B.336}$$

Sarcomere length

$$\frac{dSL}{dt} = -v \tag{B.337}$$

$$\frac{dv}{dt} = \frac{F_{contrn} + F_{passive} + F_{visc} + F_{flex}}{mass} \tag{B.338}$$

Initial Conditions

Parameter	Definition	Value
t	Time	0.0 ms
V	Membrane potential	−78.2807 mV
$[Ca^{2+}]_i$	Myoplasmic Ca^{2+} concentration	0.100156 μM
$[Ca^{2+}]_{ss}$	Subspace SR Ca^{2+} concentration	0.100156 μM
$[Ca^{2+}]_{JSR}$	Junctional SR Ca^{2+} concentration	1025.35 μM
$[Ca^{2+}]_{NSR}$	Network SR Ca^{2+} concentration	1025.35 μM
$[LTRPNCa]$	Concentration Ca^{2+} bound low-affinity troponin-binding sites	8.66973 μM
$[HTRPNCa]$	Concentration Ca^{2+} bound high-affinity troponin-binding sites	123.369 μM
O^{cav}	L-type Ca^{2+} channel conducting state (non-phosphorylated, caveolae)	0.319908×10^{-11}
C_1^{cav}	L-type Ca^{2+} channel closed state (non-phosphorylated, caveolae)	0.973686
C_2^{cav}	L-type Ca^{2+} channel closed state (non-phosphorylated, caveolae)	0.524361×10^{-2}
C_3^{cav}	L-type Ca^{2+} channel closed state (non-phosphorylated, caveolae)	0.105895×10^{-4}
C_4^{cav}	L-type Ca^{2+} channel closed state (non-phosphorylated, caveolae)	0.950461×10^{-8}
C_P^{cav}	L-type Ca^{2+} channel closed state (non-phosphorylated, caveolae)	0.319909×10^{-11}
I_1^{cav}	L-type Ca^{2+} channel inactivated state (non-phosphorylated, caveolae)	0.308287×10^{-11}
I_2^{cav}	L-type Ca^{2+} channel inactivated state (non-phosphorylated, caveolae)	0.217361×10^{-7}
I_3^{cav}	L-type Ca^{2+} channel inactivated state (non-phosphorylated, caveolae)	0.209470×10^{-7}
O_p^{cav}	L-type Ca^{2+} channel conducting state (phosphorylated, caveolae)	0.561698×10^{-10}
C_{1p}^{cav}	L-type Ca^{2+} channel closed state (phosphorylated, caveolae)	0.206347×10^{-1}
C_{2p}^{cav}	L-type Ca^{2+} channel closed state (phosphorylated, caveolae)	0.421569×10^{-3}
C_{3p}^{cav}	L-type Ca^{2+} channel closed state (phosphorylated, caveolae)	0.322977×10^{-5}
C_{4p}^{cav}	L-type Ca^{2+} channel closed state (phosphorylated, caveolae)	0.109974×10^{-7}
C_{Pp}^{cav}	L-type Ca^{2+} channel closed state (phosphorylated, caveolae)	0.140424×10^{-10}

I_{1p}^{cav}	L-type Ca^{2+} channel inactivated state (phosphorylated, caveolae)	0.541306×10^{-10}
I_{2p}^{cav}	L-type Ca^{2+} channel inactivated state (phosphorylated, caveolae)	0.100602×10^{-6}
I_{3p}^{cav}	L-type Ca^{2+} channel inactivated state (phosphorylated, caveolae)	0.969496×10^{-7}
O^{ecav}	L-type Ca^{2+} channel conducting state (non-phosphorylated, extracaveolae)	0.286584×10^{-11}
C_1^{ecav}	L-type Ca^{2+} channel closed state (non-phosphorylated, extracaveolae)	0.872263
C_2^{ecav}	L-type Ca^{2+} channel closed state (non-phosphorylated, extracaveolae)	0.469741×10^{-2}
C_3^{ecav}	L-type Ca^{2+} channel closed state (non-phosphorylated, extracaveolae)	0.948641×10^{-5}
C_4^{ecav}	L-type Ca^{2+} channel closed state (non-phosphorylated, extracaveolae)	0.851456×10^{-8}
C_P^{ecav}	L-type Ca^{2+} channel closed state (non-phosphorylated, extracaveolae)	0.286585×10^{-11}
I_1^{ecav}	L-type Ca^{2+} channel inactivated state (non-phosphorylated, extracaveolae)	0.276160×10^{-11}
I_2^{ecav}	L-type Ca^{2+} channel inactivated state (non-phosphorylated, extracaveolae)	0.194714×10^{-7}
I_3^{ecav}	L-type Ca^{2+} channel inactivated state (non-phosphorylated, extracaveolae)	0.187646×10^{-7}
O_p^{ecav}	L-type Ca^{2+} channel conducting state (phosphorylated, extracaveolae)	0.328143×10^{-9}
C_{1p}^{ecav}	L-type Ca^{2+} channel closed state (phosphorylated, extracaveolae)	0.120548
C_{2p}^{ecav}	L-type Ca^{2+} channel closed state (phosphorylated, extracaveolae)	0.246280×10^{-2}
C_{3p}^{ecav}	L-type Ca^{2+} channel closed state (phosphorylated, extracaveolae)	0.188683×10^{-4}
C_{4p}^{ecav}	L-type Ca^{2+} channel closed state (phosphorylated, extracaveolae)	0.642469×10^{-7}
C_{Pp}^{ecav}	L-type Ca^{2+} channel closed state (phosphorylated, extracaveolae)	0.820358×10^{-10}
I_{1p}^{ecav}	L-type Ca^{2+} channel inactivated state (phosphorylated, extracaveolae)	0.316230×10^{-9}
I_{2p}^{ecav}	L-type Ca^{2+} channel inactivated state (phosphorylated, extracaveolae)	0.587716×10^{-6}
I_{3p}^{ecav}	L-type Ca^{2+} channel inactivated state (phosphorylated, extracaveolae)	0.566378×10^{-6}
C_{Na3}	Fast Na^+ channel closed state (non-phosphorylated)	0.436281
C_{Na2}	Fast Na^+ channel closed state (non-phosphorylated)	0.132239×10^{-1}
C_{Na1}	Fast Na^+ channel closed state (non-phosphorylated)	0.161132×10^{-3}
O_{Na}	Fast Na^+ channel open state (non-phosphorylated)	0.367578×10^{-6}
IF_{Na}	Fast Na^+ channel inactivated state (non-phosphorylated)	0.153188×10^{-3}
$I1_{Na}$	Fast Na^+ channel inactivated state (non-phosphorylated)	0.145913×10^{-4}
$I2_{Na}$	Fast Na^+ channel inactivated state (non-phosphorylated)	0.545220×10^{-7}
IC_{Na2}	Fast Na^+ channel inactivated state (non-phosphorylated)	0.125719×10^{-1}

IC_{Na3}	Fast Na^+ channel inactivated state (non-phosphorylated)	0.414772
C_{Na3p}	Fast Na^+ channel closed state (phosphorylated)	0.610868×10^{-1}
C_{Na2p}	Fast Na^+ channel closed state (phosphorylated)	0.185159×10^{-2}
C_{Na1p}	Fast Na^+ channel closed state (phosphorylated)	0.225622×10^{-4}
O_{Nap}	Fast Na^+ channel open state (phosphorylated)	0.514708×10^{-7}
IF_{Nap}	Fast Na^+ channel inactivated state (phosphorylated)	0.214505×10^{-4}
$I1_{Nap}$	Fast Na^+ channel inactivated state (phosphorylated)	0.216956×10^{-5}
$I2_{Nap}$	Fast Na^+ channel inactivated state (phosphorylated)	0.301417×10^{-7}
IC_{Na2p}	Fast Na^+ channel inactivated state (phosphorylated)	0.176035×10^{-2}
IC_{Na3p}	Fast Na^+ channel inactivated state (phosphorylated)	0.580768×10^{-1}
P_{C1}	RyR channel closed state (non-phosphorylated)	0.996216
P_{C2}	RyR channel closed state (non-phosphorylated)	0.961523×10^{-4}
P_{O1}	RyR channel open state (non-phosphorylated)	0.854703×10^{-5}
P_{O2}	RyR channel open state (non-phosphorylated)	0.360387×10^{-10}
P_{C1p}	RyR channel closed state (phosphorylated)	0.367832×10^{-2}
P_{C2p}	RyR channel closed state (phosphorylated)	0.986391×10^{-6}
P_{O1p}	RyR channel open state (phosphorylated)	0.526043×10^{-7}
P_{O2p}	RyR channel open state (phosphorylated)	0.369679×10^{-12}
$[Na^+]_i$	Myoplasmic Na^+ concentration	10,508.7 μM
$[K^+]_i$	Myoplasmic K^+ concentration	145,411 μM
a_{ur}	Activation gate of non-phosphorylated I_{Kur}	0.713766×10^{-3}
i_{ur}	Inactivation gate of non-phosphorylated I_{Kur}	0.996992
$f^{ecav}_{IKto,f}$	Fraction of phosphorylated $I_{Kto,f}$	0.252661
$a_{to,f}$	Activation gate of non-phosphorylated $I_{Kto,f}$	0.533700×10^{-2}
$i_{to,f}$	Inactivation gate of non-phosphorylated $I_{Kto,f}$	0.999945
$a_{to,fp}$	Activation gate of phosphorylated $I_{Kto,f}$	0.111478×10^{-2}
$i_{to,fp}$	Inactivation gate of phosphorylated $I_{Kto,f}$	0.999983
$f^{cyt}_{PLB,p}$	Fraction of phosphorylated phospholamban	0.186637
$f^{cyt}_{TnI,p}$	Fraction of phosphorylated troponin I	0.364102
$f^{cyt}_{MyBPC,p}$	Fraction of phosphorylated myosin binding protein C	0.572184
P_{RyR}	RyR modulation factor	0.253809×10^{-11}
a_{Kss}	Activation gate of I_{Kss}	0.921658×10^{-3}
C_{K0}	*m*ERG channel closed state	0.997366
C_{K1}	*m*ERG channel closed state	0.135199×10^{-2}
C_{K2}	*m*ERG channel closed state	0.873471×10^{-3}

O_K	*m*ERG channel open state	0.332502×10^{-3}
I_K	*m*ERG channel inactivated state	0.763460×10^{-4}
$\left[R_{\beta 1}\right]_{PKA,tot}^{cav}$	Concentration of total β_1-ARs phosphorylated by PKA (caveolae)	0.799452×10^{-3} μM
$\left[R_{\beta 1}\right]_{GRK2,tot}^{cav}$	Concentration of total β_1-ARs phosphorylated by GRK2 (caveolae)	0.165971×10^{-29} μM
$\left[G_s\right]_{\alpha,GTP}^{cav}$	Concentration of active $G_{s\alpha}$ subunit (caveolae)	0.132189×10^{-2} μM
$\left[G_s\right]_{\beta\gamma}^{cav}$	Concentration of active $G_{s\beta\gamma}$ subunit (caveolae)	0.180824×10^{-2} μM
$\left[G_s\right]_{\alpha,GDP}^{cav}$	Concentration of inactive $G_{s\alpha}$ subunit (caveolae)	0.487356×10^{-3} μM
$\left[R_{\beta 1}\right]_{PKA,tot}^{ecav}$	Concentration of total β_1-ARs phosphorylated by PKA (extracaveolae)	0.478002×10^{-1} μM
$\left[R_{\beta 1}\right]_{GRK2,tot}^{ecav}$	Concentration of total β_1-ARs phosphorylated by GRK2 (extracaveolae)	0.165971×10^{-29} μM
$\left[G_s\right]_{\alpha,GTP}^{ecav}$	Concentration of active $G_{s\alpha}$ subunit (extracaveolae)	0.230801×10^{-1} μM
$\left[G_s\right]_{\beta\gamma}^{ecav}$	Concentration of active $G_{s\beta\gamma}$ subunit (extracaveolae)	0.237276×10^{-1} μM
$\left[G_s\right]_{\alpha,GDP}^{ecav}$	Concentration of inactive $G_{s\alpha}$ subunit (extracaveolae)	0.648475×10^{-3} μM
$\left[R_{\beta 1}\right]_{PKA,tot}^{cyt}$	Concentration of total β_1-ARs phosphorylated by PKA (cytosol)	0.155949×10^{-2} μM
$\left[R_{\beta 1}\right]_{GRK2,tot}^{cyt}$	Concentration of total β_1-ARs phosphorylated by GRK2 (cytosol)	0.165971×10^{-29} μM
$\left[G_s\right]_{\alpha,GTP}^{cyt}$	Concentration of active $G_{s\alpha}$ subunit (cytosol)	0.331511×10^{-3} μM
$\left[G_s\right]_{\beta\gamma}^{cyt}$	Concentration of active $G_{s\beta\gamma}$ subunit (cytosol)	0.663570×10^{-3} μM
$\left[G_s\right]_{\alpha,GDP}^{cyt}$	Concentration of inactive $G_{s\alpha}$ subunit (cytosol)	0.333058×10^{-3} μM
$\left[cAMP\right]_{AC56}^{cav}$	cAMP concentration produced by AC5/6 (caveolae)	0.1 μM
$\left[cAMP\right]_{AC47}^{ecav}$	cAMP concentration produced by AC4/7 (extracaveolae)	0.1 μM
$\left[cAMP\right]_{AC56}^{cyt}$	cAMP concentration produced by AC5/6 (cytosol)	0.1 μM
$\left[cAMP\right]_{AC47}^{cyt}$	cAMP concentration produced by AC4/7 (cytosol)	0.1 μM
$\left[PDE3\right]_{p}^{cav}$	Concentration of phosphorylated PDE3 (caveolae)	0.125103×10^{-1} μM
$\left[PDE4\right]_{p}^{cav}$	Concentration of phosphorylated PDE4 (caveolae)	0.580798×10^{-2} μM
$\left[cAMP\right]_{PDE2}^{cav}$	cAMP concentration degraded by PDE2 (caveolae)	0.1 μM
$\left[cAMP\right]_{PDE3}^{cav}$	cAMP concentration degraded by PDE3 (caveolae)	0.1 μM

$[cAMP]_{PDE4}^{cav}$	cAMP concentration degraded by PDE4 (caveolae)	0.1 μM
$[PDE4]_{p}^{ecav}$	Concentration of phosphorylated PDE4 (extracaveolae)	0.158226×10^{-1} μM
$[cAMP]_{PDE2}^{ecav}$	cAMP concentration degraded by PDE2 (extracaveolae)	0.1 μM
$[cAMP]_{PDE4}^{ecav}$	cAMP concentration degraded by PDE4 (extracaveolae)	0.1 μM
$[PDE3]_{p}^{cyt}$	Concentration of phosphorylated PDE3 (cytosol)	0.120998×10^{-2} μM
$[PDE4]_{p}^{cyt}$	Concentration of phosphorylated PDE4 (cytosol)	0.373102×10^{-2} μM
$[cAMP]_{PDE2}^{cyt}$	cAMP concentration degraded by PDE2 (cytosol)	0.1 μM
$[cAMP]_{PDE3}^{cyt}$	cAMP concentration degraded by PDE3 (cytosol)	0.1 μM
$[cAMP]_{PDE4}^{cyt}$	cAMP concentration degraded by PDE4 (cytosol)	0.1 μM
$[cAMP]_{PKA}^{cav}$	cAMP concentration change due to binding to PKA (caveolae)	7.92317 μM
$[ARC]^{cav}$	Concentration of PKA RC dimer with 1 cAMP molecule bound (caveolae)	0.299288 μM
$[A_2RC]^{cav}$	Concentration of PKA RC dimer with 2 cAMP molecules bound (caveolae)	0.303358×10^{-1} μM
$[A_2R]^{cav}$	Concentration of PKA R subunit with 2 cAMP molecules bound (caveolae)	0.858440 μM
$[C]^{cav}$	Concentration of free PKA catalytic subunit (caveolae)	0.459397×10^{-1} μM
$[PKIC]^{cav}$	Concentration of PKI inactivated PKA catalytic subunit (caveolae)	0.823499 μM
$[cAMP]_{PKA}^{ecav}$	cAMP concentration change due to binding to PKA (extracaveolae)	6.74029 μM
$[ARC]^{ecav}$	Concentration of PKA RC dimer with 1 cAMP molecule bound (extracaveolae)	0.653988 μM
$[A_2RC]^{ecav}$	Concentration of PKA RC dimer with 2 cAMP molecules bound (extracaveolae)	0.132861 μM
$[A_2R]^{ecav}$	Concentration of PKA R subunit with 2 cAMP molecules bound (extracaveolae)	1.17000 μM
$[C]^{ecav}$	Concentration of free PKA catalytic subunit (extracaveolae)	0.147623 μM
$[PKIC]^{ecav}$	Concentration of PKI inactivated PKA catalytic subunit (extracaveolae)	1.03338 μM
$[cAMP]_{PKA}^{cyt}$	cAMP concentration change due to binding to PKA (cytosol)	9.32461 μM
$[ARC]^{cyt}$	Concentration of PKA RC dimer with 1 cAMP molecule bound (cytosol)	0.996350×10^{-1} μM
$[A_2RC]^{cyt}$	Concentration of PKA RC dimer with 2 cAMP molecules bound (cytosol)	0.140099×10^{-1} μM
$[A_2R]^{cyt}$	Concentration of PKA R subunit with 2 cAMP molecules bound (cytosol)	0.273868 μM
$[C]^{cyt}$	Concentration of free PKA catalytic subunit (cytosol)	0.665022×10^{-1} μM

$[PKIC]^{cyt}$	Concentration of PKI inactivated PKA catalytic subunit (cytosol)	0.218365 μM
$[Inhib1]^{cyt}_{p,tot}$	Concentration of total phosphorylated PP1 inhibitor 1 (cytosol)	0.213571×10^{-1} μM
$[cAMP]^{cav}$	Concentration of cAMP in caveolae	0.253399 μM
$[cAMP]^{ecav}$	Concentration of cAMP in extracaveolae	0.507889 μM
$[cAMP]^{cyt}$	Concentration of cAMP in cytosol	0.407775 μM
SL	Sarcomere length	1.89958 μm
v	Shortening velocity	0.110974×10^{-14} μm ms^{-1}
N0	Nonpermissive tropomyosin with 0 crossbridges	0.999236
N1	Nonpermissive tropomyosin with 1 crossbridge	0.447564×10^{-3}
P0	Permissive tropomyosin with 0 crossbridges	0.344737×10^{-4}
P1	Permissive tropomyosin with 1 crossbridge	0.683798×10^{-5}
P2	Permissive tropomyosin with 2 crossbridges	0.901321×10^{-4}
P3	Permissive tropomyosin with 3 crossbridges	0.184806×10^{-3}

Appendix C Derivation of F_{visc}

We start from Hill's Equation [101] (see equation (3.17)):

$$(v+b)(F+a)=b(F_0+a)$$

Using algebraic manipulations, we can obtain an equation for F/F_0:

$$v+b=b\frac{F_0+a}{F+a}$$

$$v=b\frac{F_0+a}{F+a}-b\frac{F+a}{F+a}$$

$$v=b\left(\frac{F_0+a-F-a}{F+a}\right)$$

$$v=b\left(\frac{F_0-F}{F+a}\right)$$

$$v=b\left(\frac{1-\frac{F}{F_0}}{\frac{F}{F_0}+\frac{a}{F_0}}\right)$$

$$\frac{v}{b}=\frac{1-\frac{F}{F_0}}{\frac{a}{F_0}+\frac{F}{F_0}}$$

$$\frac{v}{b}\left(\frac{a}{F_0}+\frac{F}{F_0}\right)=1-\frac{F}{F_0}$$

$$\frac{av}{bF_0}+\frac{v}{b}\frac{F}{F_0}=1-\frac{F}{F_0}$$

$$\frac{F}{F_0}\left(1+\frac{v}{b}\right)=1-\frac{av}{bF_0}$$

$$\frac{F}{F_0} = \frac{1 - \frac{av}{bF_0}}{1 + \frac{v}{b}}$$

With the assumption that the ratio v/b is small, we can use the Taylor Expansion of

$$f(v) = \left(1 + \frac{v}{b}\right)^{-1}$$

at $v = 0$:

$$f(v) = \left(1 + \frac{v}{b}\right)^{-1},\ f'(v) = \frac{-1}{b}\left(1 + \frac{v}{b}\right)^{-2},\ f''(v) = \frac{2}{b^2}\left(1 + \frac{v}{b}\right)^{-3},\ f''(v) = \frac{-6}{b^3}\left(1 + \frac{v}{b}\right)^{-3}$$

$$f(0) = 1,\ f'(0) = \frac{-1}{b},\ f''(0) = \frac{2}{b^2},\ f''(0) = \frac{-6}{b^3}$$

Therefore

$$f(v) = f(0) + f'(0)v + \frac{1}{2}f''(0)v^2 + \frac{1}{6}f'''(0) + \cdots$$

$$= 1 + \left(\frac{-1}{b}\right)v + \frac{1}{2}\left(\frac{2}{b^2}\right)v^2 + \frac{1}{6}\left(\frac{-6}{b^3}\right) + \cdots$$

$$= 1 - \frac{v}{b} + \frac{v^2}{b^2} - \frac{v^3}{b^3} + \cdots$$

Since $\frac{v}{b}$ is small, $\left(1 + \frac{v}{b}\right)^{-1} \approx 1 - \frac{v}{b}$, and we obtain equation (3.19):

$$\frac{F}{F_0} \approx \left(1 - \frac{av}{bF_0}\right)\left(1 - \frac{v}{b}\right).$$